SELF-ASSEMBLY BEHAVIOR OF MODULATED ELEMENTAL REACTANTS

by

DMITRI LEO M. CORDOVA

A DISSERTATION

Presented to the Department of Chemistry and Biochemistry
and the Graduate School of the University of Oregon
in partial fulfillment of the requirements
for the degree of
Doctor of Philosophy

June 2020

DISSERTATION APPROVAL PAGE

Student: Dmitri Leo M. Cordova

Title: Self-assembly Behavior of Modulated Elemental Reactants

This dissertation has been accepted and approved in partial fulfillment of the requirements for the Doctor of Philosophy degree in the Department of Chemistry and Biochemistry by:

Dr. Mark C. Lonergan	Chairperson
Dr. David C. Johnson	Advisor
Dr. Christopher H. Hendon	Core Member
Dr. Richard Taylor	Institutional Representative

and

Kate Mondloch	Interim Vice Provost and Dean of the Graduate School

Original approval signatures are on file with the University of Oregon Graduate School.

Degree awarded June 2020

DISSERTATION ABSTRACT

Dmitri Leo M. Cordova

Doctor of Philosophy

Department of Chemistry and Biochemistry

June 2020

Title: Self-Assembly Behavior of Modulated Elemental Reactants

Diverse bulk-derived layered structures have been made via Modulated Elemental Reactants (MER) synthesis despite only superficial understanding of its mechanism. The premise behind this approach is that an elemental multilayer precursor self-assembles in an almost diffusionless process if it has the correct number of atoms per layer and its nanoarchitecture closely resembles the target product. The work presented here is concentrated on developing a deeper understanding of the reaction mechanism of Modulated Elemental Reactants, prompted by developments in analysis methods for thin films.

A new method for analyzing X-ray Florescence (XRF) data was developed to measure the number of atoms per square Angstrom (areal density) in a thin film with sub-monolayer accuracy. With this advancement, precursors can be made so that the two conditions set by the simple MER mechanism are satisfied. The crystallographic alignment of thick PbSe layers on VSe_2 demonstrated a strong non-epitaxial relationship between the two constituents, suggesting that compatibility of two layered constituents in a heterostructure can be determined by testing for preferred alignment. A new class of charge density wave containing heterostructures, $[(PbSe)_{1+\delta}]_m(VSe_2)_1$, where m = 1-4 and the number of PbSe bilayers, was synthesized by precisely controlling the element areal

density and nanoarchitecture of the precursor. Alternate reaction pathways were explored when the areal density of the precursor was modified. Next, a similar class of heterostructures, $[(PbSe)_{1+\delta}]_1(VSe_2)_1$, where q = 1-11 and the number of PbSe monolayers, was investigated. When a small odd number of PbSe monolayers (q = 1, 3, and 5) was targeted for synthesis, the precursors exhibited unexpected long range lateral surface diffusion during the deposition process, uncovering a new aspect of MER synthesis. Computational studies confirmed that the low temperature rearrangement is driven by the stability of PbSe bilayers compared to monolayers. Lastly, the growth mechanism of a new heterostructure, $[(SnSe_2)_{1+d}]_1(VSe_2)_1$ was elucidated from Laue oscillations in x-ray reflectivity data and in-plane x-ray diffraction and precursor nanoarchitecture, and was used as a guide to direct reaction pathways toward the synthesis of a new alloy, $Sn_xV_{1-x}Se_2$.

This dissertation contains previously published and unpublished coauthored material.

CURRICULUM VITAE

NAME OF AUTHOR: Dmitri Leo M. Cordova

GRADUATE AND UNDERGRADUATE SCHOOLS ATTENDED:

University of Oregon, Eugene

University of the Philippines, Manila

DEGREES AWARDED:

Doctor of Philosophy, Chemistry, 2020, University of Oregon

Bachelor of Science, Biochemistry, 2013, University of the Philippines Manila

AREAS OF SPECIAL INTEREST:

Solid State Chemistry

Materials Chemistry

PROFESSIONAL EXPERIENCE:

Graduate Employee, University of Oregon, September 2016 - December 2018

Instructor III, University of the Philippines Manila, June 2013 - July 2016

GRANTS, AWARDS, AND HONORS:

Merit Scholarship, Science Education Institute, Department of Science and Technology, Republic of the Philippines, 2013

Cum laude, University of the Philippines, Manila, 2013

PUBLICATIONS:

Cordova, D. L. M.; Kam, T. M.; Gannon, R. N.; Lu, P.; Johnson, D. C.; Controlling the self-assembly of new metastable tin vanadium selenides

using composition and nanoarchitecture of precursors, *J. Am. Chem. Soc.*, Submitted.

Cordova, D. L. M.; Johnson, D. C.; Synthesis of Metastable Inorganic Solids with Extended Structures. *ChemPhysChem*, Accepted. DOI 10.1002/cphc.202000199

Hamann, D. M.; Rudin, S; Asaba, T.; Ronning, F.; **Cordova, D. L. M.**; Lu, P.; Johnson, D. C.; Emergent Structure and Properties in Interface Stabilized 2D-Layers. *ACS Nano*. Submitted.

Cordova, D. L. M.; Fender, S. S.; Kam, T. M.; Seyd, J.; Albrecht, M.; Lu, P.; Fischer, R.; Johnson, D. C. Designed Synthesis and Structure-Property Relationships of Kinetically Stable $[(PbSe)_{1+\delta}]_m(VSe_2)_1$ (m = 1, 2, 3, 4) Heterostructures. *Chem. Mater.* **2019**, *31* (20), 8473–8483.

Cordova, D. L. M.; Kam, T. M.; Fender, S. S.; Tsai, Y. H.; Johnson, D. C. Strong Non-Epitaxial Interactions: Crystallographically Aligned PbSe on VSe_2. *Phys. Status Solidi* **2019**, *1800896*, 1800896.

Choffel, M. A.; Hamann, D. M.; Joke, J. A.; **Cordova, D. L. M.**; Johnson, D. C. The Reaction between Mn and Se Layers. *Zeitschrift fur Anorg. und Allg. Chemie* **2018**, *644* (24), 1875–1880.

Hamann, D. M.; Bardgett, D.; **Cordova, D. L. M.**; Maynard, L. A.; Hadland, E. C.; Lygo, A. C.; Wood, S. R.; Esters, M.; Johnson, D. C. Sub-Monolayer Accuracy in Determining the Number of Atoms per Unit Area in Ultrathin Films Using X-Ray Fluorescence. *Chem. Mater.* **2018**, *30* (18), 6209–6216.

Cordova, D. L. M.; Abuel, R. J. D.; Galingana, M. O.; Villanueva, L. A.; Billones, J. B. Piggyback Drug Development: (Molecular Docking of Entacapone Analogues as Direct M. Tuberculosis InhA Inhibitors). *J. Chem. Pharm. Res.* **2015**, *7* (5), 636–642.

ACKNOWLEDGMENTS

I wish to express my sincere appreciation to Dr. David Johnson, for welcoming me into his lab and allowing me make mistakes and learn from them. I am forever grateful for the advice and encouragement you have given me and for affording me the freedom to pursue research paths that truly interests and challenges me. I am thankful to the members of my committee, Dr. Mark Lonergan, Dr. Chris Hendon, and Dr. Richard Taylor, for the words of encouragement they have given me along the way. I am especially thankful to Dr. Cathy Page, for introducing me to the wonderful world of solid state chemistry and for serving as an inspirational educator. I am thankful for the kindness of the staff at the Chemistry offices, Janet Macha, Kathy Noakes, Christi Mabinuori, and Jim Rasmussen, for the tiny things they do that make student's lives easier amidst the chaos of doing science.

My colleagues from the Johnson lab have been absolutely essential during my time in Oregon, I am forever grateful for them. Dr. Dani Hamann has been a valuable part of my journey, she is a trusted friend, mentor, and like a big sister to me. I am glad to have experienced both the highs and lows of science alongside her. I have had the distinct pleasure of working with incredible undergraduates who always inspire me to do better. I am glad that Shannon Fender, Taryn Kam, Mina Buchanan, and Terence Tsai have been part of the team for the past three years. I am thankful for the other members of the Johnson lab, Marisa Choffel, Renae Gannon, Alex Lygo, Dylan Bardgett, Jake Logan, Jordan Joke, Dr. Erik Hadland, Dr. Marco Esters, Aaron Miller, Alex Skochko, and Coleman Johnson for the fruitful conversations and fond memories.

My work would not have been possible without the help of the talented people from the UO TSA Machine Shop. Jeffrey Garman, Cliff Dax, Julien McAdams, and Kris

Johnson have gotten us out of dire situations more than I can remember. I am thankful to the CAMCOR staff for making it possible to pursue high quality research; namely Steve Weimholt, Kurt Langworthy, Becky Beach, Mark Adams, and Robert Fischer.

I am glad to have forged valuable connections with different collaborators from all over the world whose insight have opened my eyes to different facets of solid state chemistry. I am thankful to Dr. Kirsten Jensen and her group at Copenhagen for helping me collect and analyze total scattering data. I am thankful to Dr. Ping Lu from Sandia for collecting HAADF-STEM data that literally adds another dimension to how we visualize our materials. I am thankful to Dr. Mark Asta, Dr. Ben Hanken, and Dr. Shahriar Hooshmand from UC Berkeley for the insightful calculations that explained the experimental phenomena we were observing. I am thankful for Dr. Vedran Vonk from DESY for discovering interesting structural correlations in our materials and Jenia Karapetrova from APS for making our beamline experience quite memorable. I am thankful for collaborators with the finest instrumentation that have made our materials more interesting by uncovering interesting properties; Dr. Manfred Albrecht and Johannes Seyd from Augsburg, Dr. Dietrich Zahn and Fabian Gohler from TU Chemnitz, Dr. Stephen Cronin and Yu Wang from USC, Dr. Matt Beekman from Cal Ply SLO, Dr. Sage Bauers and Dr. Dennice Roberts from NREL, and Dr. Wolfgang Bensch from Kiel.

Finally, I am thankful for my family and friends for being there to hold me up when I think nothing else can. I am thankful for my parents, Chie and Leo, and sister, Hannah, for the never-ending support. I am thankful for my family here in the US, Tita Iah, Lola, Tito Jay, Tito Abong, and families, who have made the transition for me quite easy and have been a constant source of inspiration for me.

For my family, friends, and teachers

TABLE OF CONTENTS

Chapter Page

Chapter Page

Chapter Page

LIST OF FIGURES

Figure Page

Figure Page

Figure Page

Figure Page

Figure Page

Figure Page

Figure Page

LIST OF TABLES

LIST OF TABLES

Table Page

CHAPTER I

SYNTHESIS OF METASTABLE SOLIDS WITH EXTENDED STRUCTURES

Authorship Statement

At the time of writing, this chapter has been accepted as a review article to ChemPhysChem (DOI 10.1002/cphc.202000199). Dr. David C. Johnson is my advisor and group leader, and I am the primary author.

I.1. Introduction

The number of known inorganic compounds with extended structures is dramatically less than the number predicted based on the number of potential systems of n elements out of the 86 known stable elements.[1] In Figure I.1, the number of known compounds, estimated based on databases of known compounds, is plotted versus the number expected for each value of n, which was estimated based on the number of possible

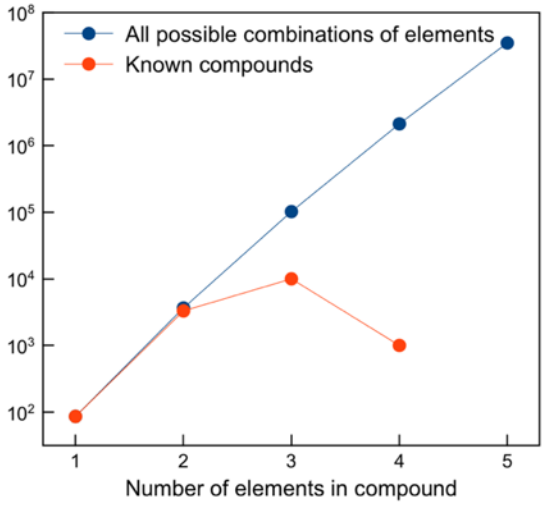

Figure I.1. The number of known compounds and possible combinations of the elements plotted versus the number of elements in the compound.

elemental combinations. The large difference between them results from the constraints of traditional approaches to prepare inorganic compounds with extended structures. There have been many proposed compounds predicted to be thermodynamically stable and structural homologies suggest many other potential compounds.[2–4] The challenge is the synthesis of these unknown compounds, as many of these compounds cannot be prepared using classical synthesis approaches.[5] The synthetic challenge is especially difficult if the unknown compounds are metastable with respect to mixtures of known thermodynamically stable phases.[6] Chemists and material scientists have historically not been able to design synthetic routes that avoid thermodynamic traps, limiting the ability to prepare compounds with desired structures.[7] Indeed *the holy grail of solid-state synthesis is a design and mechanism based approach to the synthesis of targeted compounds.*[8]

The concept of an energy landscape on which a reactant moves as it lowers its free energy in the process of eventually forming the thermodynamic product is a useful, but underutilized tool to discuss synthetic approaches to metastable compounds.[9] An energy landscape describes the complex relationship between the stability of different atomic configurations as a function of a variety of system parameters such as temperature, pressure, and overall composition. The energy landscape provides a framework where the relationships between different compounds and the reaction trajectories between them can be discussed.[10] There are two types of energy minima in energy landscapes, local and global free energy minima. There are, of course, many more local free energy minima, defined here as a position in the free energy landscape that requires an activation energy for the system to move to a different state of lower free energy. Reaction barriers inherent in the energy landscape pertinent to the synthesis of inorganic compounds with extended

structures include nucleation energies and the activation energy required for diffusion. This is schematically illustrated in Figure I.2, where two different starting points on an energy

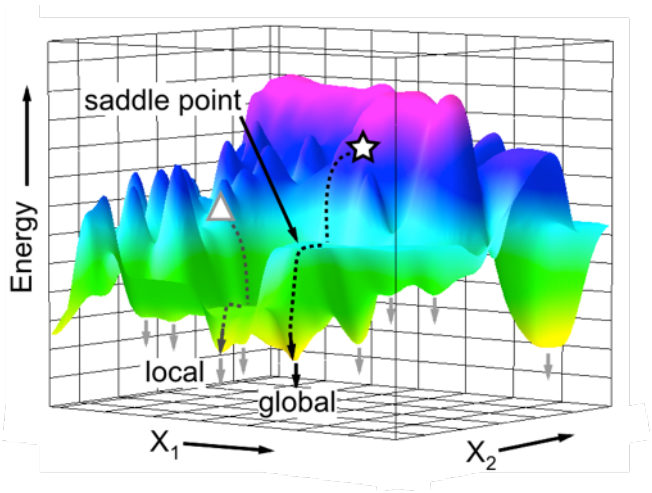

Figure I.2. Free energy surface with a number of local minima and a global minimum. Shown are two different starting points resulting in two different reaction trajectories and two different products.

landscape are chosen, resulting in two different reaction pathways. The two starting points, while taking different reaction pathways, both lower the free energy as rapidly as possible. The system moves into different free energy basins and passes through saddle points in the landscape that are associated with reaction barriers.

Nucleation is the self-assembly of atoms or molecules to form a new thermodynamically more stable phase. The interface between the new phase and the prior phase is typically higher in free energy, resulting in an initially higher energy for the new phase when it is small in physical size. This increase in free energy for small nuclei creates an activation energy for the new phase even though the bulk phase is thermodynamically more stable.

Diffusion is the movement of atoms in a solid, typically driven by concentration gradients. It is an activated process, as atoms typically move out of a locally stable bonding environment through a less stable bonding state before arriving in another stable bonding site. The rate of diffusion typically depends on the concentration of defects, with each specific defect having a different activation energy for diffusion.

The small number of known compounds shown in Figure I.1 reflects the state of the art: researchers have not discovered how to move across the energy landscape in a controlled manner. Each local free energy minima is a potential new compound, which is kinetically stable but thermodynamically unstable relative to the known compounds in the phase diagram. Two key questions for chemists are "Where are the minima?" and "How can the metastable compounds at these minima be synthesized?".

I.2. Selective Overview of Solid State Synthesis Techniques

I.2.1 Direct Solid State Reaction of Elements or Compounds

Probably the most common technique to synthesize new solids with extended structures is the direct reaction of solid reactants at elevated temperatures, shown schematically in Figure 3. These reaction conditions involve a complicated mixture of

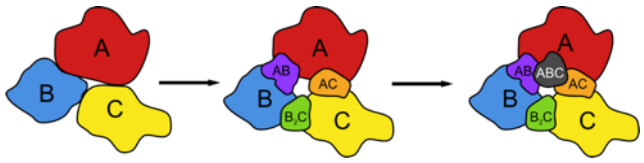

Figure I.3. Schematic of the reaction of elements to form a ternary compound showing the formation of binary compounds before the nucleation of the first ternary phase.

atomic configurations as reactants convert to products via heterogeneous intermediate mixtures containing elements and binary compounds.[11] The reaction rates are typically limited by slow solid state diffusion. To increase diffusion rates, high temperatures are typically used. Consequently, all phases in the relevant phase diagram can form as reaction intermediates. The relative amounts of each compound during the reaction process is related to the diffusion rates of the different elements through or around the different phases formed. Binary compounds typically form as reaction intermediates on the way to ternary compounds. Since products form at the interfaces between reactants, reaction rates slow as the thickness of the product layer increases.

To obtain reasonable reaction rates in traditional solid state synthesis one needs to increase diffusion rates and/or decrease diffusion distances. There are two general approaches to increasing diffusion rates. One is to increase temperature, as mentioned earlier, because diffusion is an activated process. However, long reaction times are still needed due to long diffusion lengths and the need to diffuse through product layers. This typically results in the formation of thermodynamic products. A second approach to increase diffusion rates is to add a flux so atoms can move through a fluid phase. Adding a flux changes the reacting system, sometimes making compounds thermodynamically stable that would be metastable without the flux. Reactions in a fluid phase will be discussed more in subsequent paragraphs.

There are also several approaches to decrease reaction time by decreasing the distance atoms need to diffuse during the reaction. The simplest approach is the physical grinding or ball milling of the reacting mixture, before and/or during a sequence of annealing steps, to decrease particle size and pulverize the product layers on the outside of

particles. A second approach is to prepare precursor in which the atoms of the desired product are already intimately mixed. An example would be preparing an alloy to react with a third element rather than reacting the three elements directly. Ideally the atoms in the precursor are bound to one another via strong bonding interactions, such that they remain bonded during the reaction to form products. With many molecular precursors, there is still the challenge of removing atoms present in the precursor but not in the desired product. The excess atoms will typically have long range diffusion path lengths to get out of the solid as the precursor converts to product. A third approach is to prepare a homogenous amorphous phase with a composition that matches that of the targeted compound, which will be discussed in section I.3.5.

An important aspect of solid state reactions is the choice of starting reactants, which will impact reaction times, reaction pathway and the temperatures required for conversion of reactants into products. An elegant example of this is the formation of pyrite, FeS_2 from the reaction between Na_2S and $FeCl_2$ explored by Neilson and coworkers.[12] Pyrite is thermodynamically stable and can be formed directly from the elements via a high temperature reaction. Gaseous sulfur reacts with iron to form a surface skin of FeS_2 around the metallic iron particles. The reaction rate depends on the diffusion of species through the surface layer of FeS_2, and the reaction must be done carefully to prevent high pressures of sulfur vapor at the high reaction temperatures required for diffusion. Neilson and coworkers showed that $NaFeS_2$ forms as a reaction intermediate at low temperature (100-175°C) as Na_2S reacts with $FeCl_2$. The thermodynamic products, NaCl and FeS_2, form as $NaFeS_2$ decomposes at higher temperatures. The temperatures and times required are less than needed for the direct reaction of the elements. Attempts to make metastable pyrites

via using this approach as a synthetic pathway were unfortunately unsuccessful. The increased use of in situ and operando probes will result in the discovery of many other unexpected reaction intermediates in solid state reactions.[13] These reaction pathways may enable the synthesis of targeted metastable compounds.

I.2.2 Synthesis in a Fluid Phase

It is very common in solid state synthesis to use a fluid phase to increase diffusion rates and lower reaction temperatures. The fluid phase goes by a variety of different names, including a melt, a solvent, a flux, a mineralizer, a eutectic flux or a reactive flux, as researchers adjust the fluid phase's composition and resulting properties to hopefully obtain desired products. A fluid phase could also be a supercritical fluid by raising the temperature and pressure above the critical point, such as in hydro- and solvothermal syntheses. A common property of all fluid phases is a much higher diffusion rate than found in solids, and potentially further enhanced diffusion rates due to convection effects or active stirring. The net result is that these systems can explore large areas of the free energy landscape. The rate-limiting step in forming a solid crystalline phase from a fluid phase is typically nucleation. Since the compound that will nucleate is one with the lowest activation energy for nucleation, what nucleates is not necessarily the thermodynamically most stable phase. In contrast to the typical reaction between bulk elements, the fluid phase approach can directly form ternary compounds without forming binary compounds as reaction intermediates.

Phase evolution often occurs in fluid reactions, as initial products react with flux to make more stable compounds.[14,15] In situ studies have found kinetically stable compounds

that form at short times (Figure I.4), presumably because they are easier to nucleate.[16] A sequence of nucleation events can occur as more stable compounds nucleate and grow at the expense of earlier compounds. During the growth of new phases, the concentration of some species in solution drops. This can result in previously formed compounds dissolving in the flux. Understanding what factors influence the sequence of nucleation events or the time required for the next compound to nucleate from a mixture

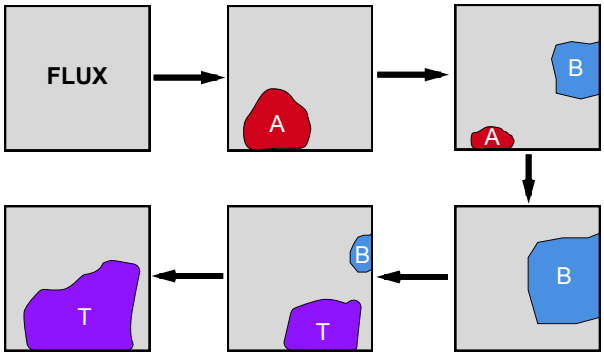

Figure I.4. A schematic illustration of the evolution of crystalline phases from a flux reaction due to the changes in concentration of different species in solution. The initial product (A) is the easiest to nucleate from the flux given the species and their respective concentrations. The growth of phase A depletes the concentration of some species in solution and the species continue to evolve with time. This can lead to the nucleation and growth of a second phase (B), which again depletes the concentration of some species in solution. This can lead to phase A dissolving. This process can continue forming phase T. Typically the density of the compounds increase during the reaction, with the density of T greater than B, which has a density greater than A.

at a specific temperature is challenging.[17] There is unfortunately little understanding of speciation in the complex mixtures and solvents used synthetically and hardly any knowledge of speciation in fluxes.[18] How species evolve in the reaction mixtures is also not known. An additional challenge in fluid phase synthesis is that most often there is no knowledge of the relative solubility of the various potential products or what the likely potential products are. In general, the composition of the system, temperature and time are

the main parameters used to steer reaction towards a desired product. Fast diffusion rates mean that the system can explore many configurations as it proceeds towards the thermodynamic minimum. The net result is that serendipity plays a large part in what compounds form.[19]

I.2.3. The Experimental Procedure to Discover New Compounds

Solid state reaction and fluid phase synthesis approaches are by far the most common techniques used to prepare new solid state compounds as they are experimentally relatively easy to perform. Additional synthesis approaches, such as “soft” chemistry and topochemical approaches, will be discussed in the following section. The products of initial reactions in all of these synthetic approaches are typically examined via powder x-ray diffraction, looking for "new" reflections that cannot be explained by existing compounds. Reaction conditions are then varied to try to increase the intensity of the "new" reflections at the expense of "known" reflections, indicating that more of the new product is being formed. Since both solid state and fluid phase synthesis approaches suffer from the inability to understand how to control the reaction pathway, the changes made in the reacting systems depend mainly on experience and intuition. There are typically a limited number of experimental parameters that can be varied to either steer the reaction down a particular pathway or to change the relative free energies to make a desired product more stable than a competing phase. Without the ability to avoid binary compounds as reaction intermediates, any multinary compound has to be more stable than a mix of the binary compounds to be discovered (see Figure I.3). This is a tremendous limitation on what can

be prepared and probably the underlying reason for the difficulty in preparing new ternary and higher order compounds.

I.3. Energy Landscape Description of Synthetic Pathways.

The energy landscape concept is a useful platform to compare and contrast different solid state synthesis approaches. It is instructive to introduce the energy landscape by using it to describe the synthesis of organic compounds. Chemists are used to graphs of energy along a reaction coordinate linking reactants to products, which is a line along a particular trajectory in the energy landscape. The maxima on an energy versus reaction

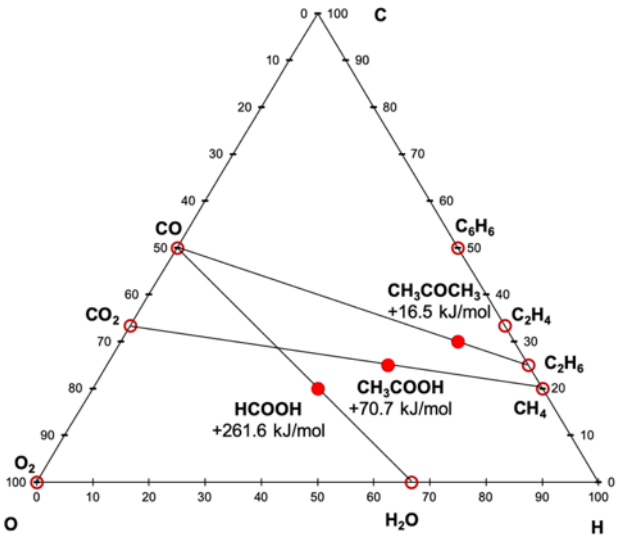

Figure I.5. The C-H-O ternary phase diagram showing the thermodynamically stable binary compounds. A select few ternary compounds are shown on tie lines between binary compounds. They are all metastable with respect to a mixture of the binary compounds.

coordinate plot is a saddle point between two adjacent minima on the energy landscape. To focus this discussion toward the synthesis of compounds in local free energy minima - kinetically stable compounds - Figure I.5 contains a ternary phase diagram for the elements

C, H and O. In addition to the thermodynamically stable compounds (shown as red unfilled circles) there are an enormous number of kinetically stable compounds that have been made. We show only a couple on tie lines between two stable binary compounds. The amount of energy that would be released by the decomposition of the ternary compound to a mix of binary compounds is shown underneath the chemical formula. Most, if not all. of the ternary compounds in this phase diagram are metastable. A key to chemists preparing these metastable compounds has been the development of reaction mechanisms to understand the rate limiting steps in product formation and the discovery of different reagents and reaction sequences that enable a desired kinetic product to be formed. While many of the specifics of these reaction mechanisms are not directly translatable into the synthesis of extended solids, the underlying principles are, and the concept of an energy landscape is a useful common platform for this comparison. After the synthesis of molecules, we will discuss four solid state chemistry approaches to metastable solids in the context of energy landscapes, focusing on what makes them work, what limits their more general implementation and what key features need to be combined in new synthesis approaches.

I.3.1. Molecular Synthesis

Organic chemists have developed a number of concepts and tools used to control chemical reactions to obtain specific products.[20] They have developed "protecting groups" that are used to control the reaction pathway by limiting diffusion of reactant molecules to the sites blocked by the protecting group.[21] We attempt to show this schematically in Figure I.6, which shows a probably energy landscape for a system containing two sites that could

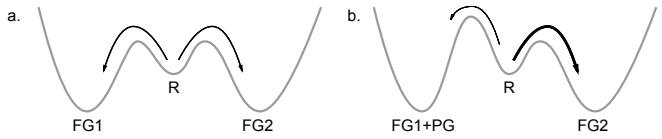

Figure I.6. Reaction coordinate diagram for a molecule containing two sites with the same functional group. This results in very similar reaction energies for either site (6a). If a protecting group is installed at one site, then this favors the reaction at the other site (6b).

react with the same reagent. If they are similar (I.6a), there will be two nearly equivalent saddle points in energy, one towards the reaction of each of the groups leading to different products. Attaching a protecting group raises the energy of one of the saddle points relative to the other one (I.6b), as diffusional access to the reacting bond by reactants is blocked. With the protecting group in place, therefore, the majority of the reactant molecules will react at the site without the protecting group if the reaction temperature is adjusted to be above that required to form the product without the protecting group and below that required for the site with the protecting group to react. Chemists have also developed catalysts for specific reactions, which lower the activation energy for one reaction while leaving other activation energies unaffected. Catalysts and the manipulation of the identity and concentration of chemical species in the system permit molecular chemists to favor reaction of one functional group over another. Organic chemists have also learned how to use concentration to favor inter- versus intra-molecule reactions. These and other approaches enable chemists to steer molecular reactions across the energy landscape, avoiding unwanted molecules by favoring a particular reaction pathway instead of another. The reactions in general preserve most of the structure of the reactants, with changes only occurring at specific locations. It is important to note that controlling molecular reactions is different than forming an extended structure. Organic chemists, like solid state chemists, still cannot control the crystal structure of the product formed.[22,23]

A second key to the success of organic chemistry is the ability to predict potential free energy minima in the energy landscape via a set of local coordination rules for elements: carbon needs four bonds, oxygen two and hydrogen one.[24] Given a formula, say $C_4H_8O_2$, undergraduate chemists are expected to be able to use these rules to come up with the structures of all of the compounds - isomers of one another - that follow these rules. This ability to predict structures of compounds does not exist in extended inorganic systems. The reasons include elements in the rest of the periodic table existing in several possible oxidation states, being stable in a number of different local coordination environments, and having several different possible coordination numbers. This situation is even more complex because many elements can exist in different oxidation states, even in the same compound, and extended inorganic compounds can be non-stoichiometric and/or have a composition range due to vacancies. As DiSalvo pointed out for intermetallic compounds, there are no general rules that predict or make understandable the stoichiometries, although ideas by Zintl and others make the composition of subsets of these materials reasonable if their structures are examined.[25]

I.3.2 Synthesis Using a Fluid Phase

It is useful to begin our discussion of solid state synthesis with respect to the energy landscape by focusing on fluid phase synthesis and how this approach is able to prepare metastable compounds. The initial system in fluid phase synthesis typically involves one or more solids that dissolve and react in the liquid phase as temperature is raised.[26] As the concentration of species in solution increase as A and B dissolve, the solution can become supersaturated with respect to a solid compound, which will nucleate and grow. This is

shown schematically in Figure I.7. As the solution evolves, the concentration of species evolves, potentially forming one or more complex fluid phase species (for example A_2). The increases in concentration of these species as a function of time can result in the solubility limits for another compound to be exceeded. If this occurs, then a second phase will nucleate and grow. As the amount of the second phase increases, the amount of the first phase may decrease as it either dissolves as concentrations decrease due to the growth of the second phase or is a reactant in the formation of the second phase. The evolution of the solution as a function of time, the species formed and the solid compounds that might nucleate are typically not known. A hypothetical set of chemical equilibria and the resulting concentration changes as a function of time corresponding to the schematic are also shown

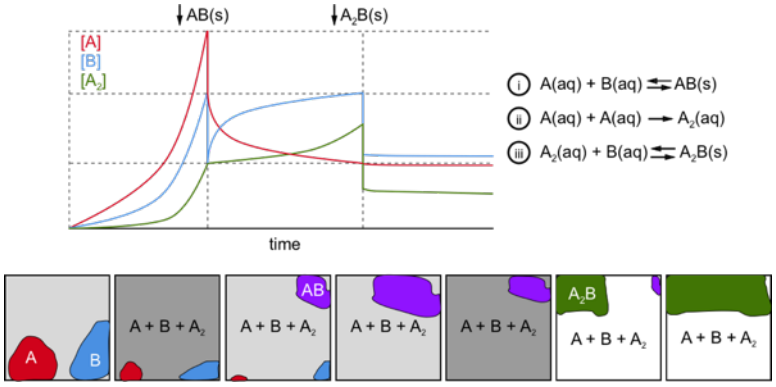

Figure I.7. A schematic diagram showing solids A and B dissolving in a flux. The major species in solution are A, B and A_2. As the concentration of A and B increase, the solution becomes supersaturated with respect to solid AB, which then nucleates and grows. As the concentration of A_2 increases, decreasing the concentration of A, solid AB begins to dissolve. Eventually the solution becomes supersaturated with respect to solid A_2B, which nucleates.

in Figure I.7. This sequential formation of solid phases, each typically more dense than the preceding phase, is known as the Ostwald step rule.[27,28]

Viewing this reaction in the context of an energy landscape (Figure I.8) involves the system continuously decreasing its free energy as a function of time as species in the

fluid react to form intermediates and the concentrations of different species in solution evolve. The high diffusion rates in the solution allow the system to explore a large fraction of the energy landscape in the local basin in which it resides. To form a solid compound, the system needs to move though a saddle point in the energy landscape where the saddle point is related to the activation energy required to nucleate the solid phase.[29] There are typically more than one saddle point in any free energy basin with different activation energies with respect to the state of the system at each point in time. Each saddle point corresponds to a different solid compound that could form. What nucleates first depends on the activation energies, which depend on the concentration of different species, the solubility constants of the different compounds and the size of the critical nucleus required.

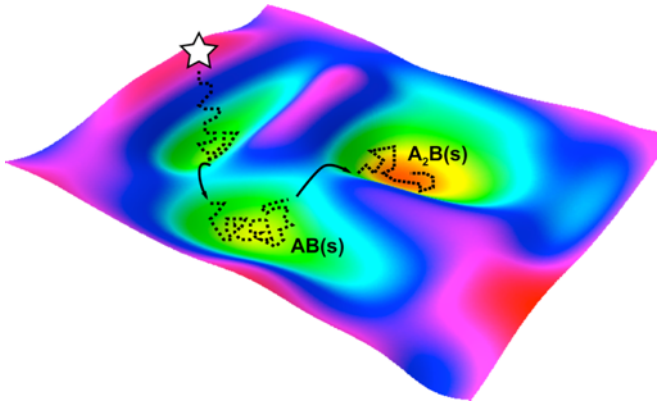

Figure I.8. A schematic free energy landscape showing the trajectory of an initial system (the star) through the free energy landscape as a function of time. The system initially lands in a basin where the saddle point to the crystalline phase AB is the lowest energy path. From this basin the system nucleates the compound A_2B through the lowest energy pathway to a lower free energy state of the system.

The system needs to become supersaturated in order to nucleate a compound. The location of the saddle points, the activation energy for the system to exit through the different saddle points, and the location of the system in the free energy landscape all change as a function

of time as species and their concentrations evolve and experimental parameters such as temperature are varied.

A key point is that the first phase to nucleate is the easiest to nucleate, not necessarily the thermodynamically most stable compound that could form. In the free energy landscape, the first compound typically forms by the system moving through the lowest energy saddle point. After the first phase nucleates, the free energy of the system decreases as the volume of the first phase to nucleate increases to eliminate the supersaturation. This causes the concentrations of other species in solution evolve and remaining solid reactants to dissolve. The evolving concentrations may lead to a second phase nucleating if the solution becomes supersaturated. As the amount of the second phase increases, the concentration of species in solution again evolves. The amount of the first phase may decrease as it dissolves in response to the concentration changes or if it is a reactant in the formation of the second phase.

The major challenge in planning a fluid phase synthesis is that the concentration of different species as a function of temperature and time, the solubility constants of the different compounds and the effect of adding different species to the system on the concentrations of all of the different species are typically not known.[30] The structure of the products is often unrelated to the structure of the reactants. Structural motifs in the solids state structure of reactants may not exist in the solution. It is a complicated problem. The ability to change concentrations and add additional species to the solution provide experimental parameters that can be used to influence the reaction pathway by changing the concentration and species in solution, which will impact the relative energies of the saddle points and the free energy minima. This has enabled chemists to prepare compounds

with amazingly complex structures containing elements with a wide range of bond lengths, bond angles, and coordination environments. The lack of knowledge about the intermediates and relationships between them and potential products, however, has resulted in the synthesis of novel solids being described as being "as much an art as a science".[25]

I.3.3. Synthesis Using Molecular Beam Epitaxy

Molecular beam epitaxy (MBE), initially developed by Cho and Arthur at Bell Laboratories, is an interesting contrast to synthesis in a fluid phase for the production of kinetically stable products.[31] Briefly MBE involves bombarding a surface, held at a specific temperature, with controlled fluxes of a number of different elements. This is done in a high vacuum to prevent contamination and to create long mean free paths for the molecular beams. MBE takes advantage of different activation energies for bulk and surface diffusion, working in a regime where surface diffusion is possible but bulk diffusion is not. Essentially the structure that forms on the surface is buried by subsequent layers and is unable to rearrange into a more stable structure because the temperature is too low for bulk diffusion to occur.

A schematic of a MBE deposition system is shown in Figure I.9. The surface of the substrate provides a template for the desired structure, having an epitaxial or near epitaxial relationship with the structure being grown. In the energy landscape picture of this synthesis method, the structural relationship between the surface and the target phase reduces or eliminates the activation energy required to nucleate the targeted compound. The temperature of the substrate needs to be high enough that atoms can explore the surface to find optimal locations but needs to be low enough to maintain a critical concentration of

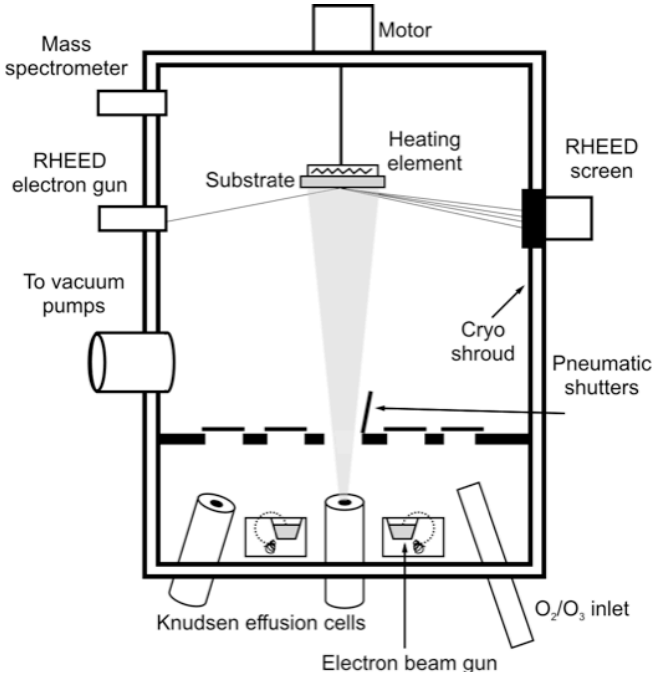

Figure I.9. A schematic diagram of an MBE growth chamber. Several deposition sources provide fluxes of different elements aimed towards a heated substrate. In-situ analysis tools (reflection high-energy electron diffraction and deposition rate monitors) are used to control the process.

the most volatile element. The substrate temperature also must be low enough that the atoms remain trapped long enough in optimal bonding sites for other atoms being deposited to bind to the edges of the growing next layer. The mobility of atoms is significantly reduced once additional atoms attach to the edge of the growing layer, and their mobility is reduced further as subsequent layers bury them.[32] The required reaction conditions to nucleate and grow a targeted compound are often very challenging to find.[33] A schematic of the MBE growth process on a surface is shown in Figure I.10.

There are a number of different MBE film growth modes depending on the relative flux rates, surface mobility and activation energy required to nucleate the next layer. The three major growth modes are island formation (Volmer–Weber[34]), layer-by-layer growth (Frank–van der Merwe[35]) and simultaneous layer growth and island formation (Stranski–

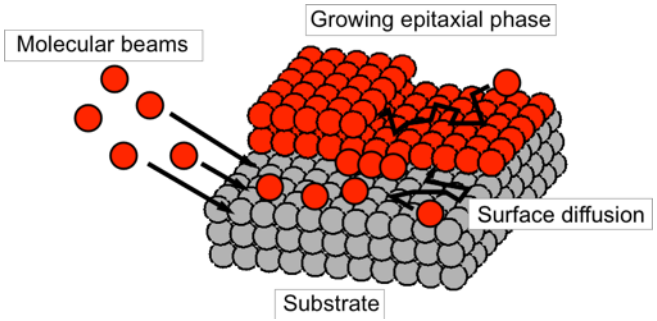

Figure I.10. Schematic of MBE growth, showing arriving atoms, evaporating atoms, a growing epitaxial island and atoms moving on the growth surface.

Krastanov[36]). The rate limiting steps are different in each of these growth modes. In the Volmer-Weber growth mode, the interaction between the atoms being deposited is stronger than their interaction with the surface, which results in nucleation and vertical growth of islands to limit the amount of interface. This results in a rough surface topography of the growing film. In the Frank- van der Merwe growth mode, the interaction of the depositing atoms with the surface is larger than the interaction with the surface. Hence any island that nucleates preferentially grows until the layer is completed. This results in the layer-by-layer growth of atomically smooth films. In the Stranski–Krastanov growth mode, the interaction energy between the depositing atoms is comparable to the interaction of the atoms with the substrate. Hence layer formation competes with nuclei formation. The growth mode may change with film thickness, with notable differences between the initial layer and subsequent layers. For example, island growth may dominate the initial deposition of A on B, but once B is covered by A there may be a switch to a layer by layer growth mode.

The energy landscape provides an interesting frame of reference to compare MBE experiments with solution synthesis methods used by molecular chemists. An MBE experiment can be tuned to many different locations on the energy landscape by varying

substrates, substrate temperature and atomic fluxes of the different sources. When one is in a stable growth mode for a particular compound on a particular substrate, the growth of the compound is kinetically favored. The temperature needs to be high enough to permit surface diffusion but low enough to prevent bulk diffusion. The interdiffusion of the growing film with previously deposited layers, would be a saddle point in the free energy landscape at higher temperature, since bulk diffusion has a higher activation energy than surface diffusion. Bulk diffusion requires point defects, the existence of dislocations, and/or grain boundaries to occur at reasonable rates at lower temperatures. The quality of the growing film therefore impacts the upper temperature limit before mixing via bulk diffusion occurs. Changing the substrate temperature changes the diffusion rates of atoms across the surface and also changes the surface composition as different species have different residency times on the surface due to the different temperature dependencies of sublimation into the gas phase. A change in surface concentration potentially reduces the energy for nucleating a different phase – crossing a different saddle point in the free energy diagram. Changes in the ratio of reactant fluxes may be used to maintain growth of the target phase. The change in surface temperature and reactant fluxes, however, may result in a different growth mechanism as surface diffusion and sublimation rates change.

The ability to change the identity of the flux of atoms impinging the surface provides a means to jump from one spot on the free energy surface to another. The ability to stop the fluxes required to form A and start the fluxes required to form B enables researchers to prepare metastable superlattice structures with arbitrary, but controlled nanoarchitecture. The ability to toggle sources many times in complex sequences while maintaining growth modes is a unique ability of the MBE approach to synthesize complex

nanoarchitectures. Preparing superlattice structures using MBE is challenging and the number of systems where it is possible is limited, however, because the proper conditions need to be found to achieve the desired growth mode with a common substrate temperature. The need for a common, or at least similar substrate growth temperature for the different constituents often prevents layer-by-layer growth of both A on B and B on A. The different constituents also need to be lattice matched for epitaxy to occur. The ability to toggle sources and manipulate growth conditions enables MBE growers to synthesize designed structures - the holy grail of solid-state chemistry.

The ability of MBE to jump from one spot on the free energy surface to another by toggling sources is analogous to adding an additional reactant to a solution reaction to transform an intermediate into a desired product. The ability to abruptly remove a reactant is analogous to separations (via solubility differences, growth of crystals, etc.) used in multistep solution phase synthesis of molecules to purify an intermediate product. Similar addition or subtraction of reagents is key to the topotactic approaches to metastable compounds, discussed next, where the product from one reaction is removed from one solution and immersed in another.

I.3.4. Synthesis via Topotactic Reactions.

Another approach to synthesizing metastable compounds is topotactic (also called topochemical) reactions.[37] The term "topotactic" refers to reactions in which specific motifs within the structure of the reacting solid phase are maintained in the product. These reactions are often reversible. Well known example of topotactic reactions include intercalation and deintercalation reactions that form the basis of lithium battery

technology.[38] The first step of this synthesis approach is the preparation of a precursor (host lattice) - typically a thermodynamically stable compound. The precursor usually has a strong, covalent, spatially directed bonding network between the elements of the structure that are preserved in the topochemical reaction. The structure of the precursor also needs an empty system of interconnected lattice sites sharing polyhedral faces, and the lattice sites must be large enough for the transport of cations - either into or out of the host lattice - at temperatures low enough that the host structure is preserved. For high ionic mobility of the species moving into or out of the precursor structure at low temperature, the lattice sites along the diffusion path should be of similar energies and the increase in energy of the saddle points between the lattice sites along the diffusion path relative to the lattice sites should be small. The precursor needs to be able to be oxidized or reduced, and have an energetically suitable conduction band for the reversible transport of electrons to the redox active element(s). Given this set of constraints, this synthesis approach is obviously limited to a small fraction of known compounds that would be suitable precursors.

The constraints on a precursor to survive the chemical or electrochemical conditions required for a topochemical reaction define a topology for the surrounding energy landscape. The cations must have high enough diffusion rates for reasonable reaction rates at temperatures low enough to maintain the structural integrity of the precursor. The energy landscape therefore has a "basin" containing the precursor and all of the possible topochemical products where the structural moiety is preserved. The system stays within this "basin" with the addition of reagents or applying the potentials required to intercalate or deintercalate the host lattice.

Intercalation is accomplished by exposing the precursor to high enough concentrations of reactive cations - via a reactive organometallic compound, electrochemically by applying a potential, or by the direct reaction with an element at low temperatures. Deintercalation is typically done electrochemically, by exposing the precursor to a solution containing a species that reacts with the cation (an anion such as iodide, a cyclic mutidentate ligand such as crown ether or a polycyclic multidentate ligands such as a cryptand), or by gas transport reactions where a product formed with the cation can be condensed at the cold end of the reaction vessel (such as a metal iodide). A schematic of a system undergoing intercalation/deintercalation reactions is shown in Figure I.11.

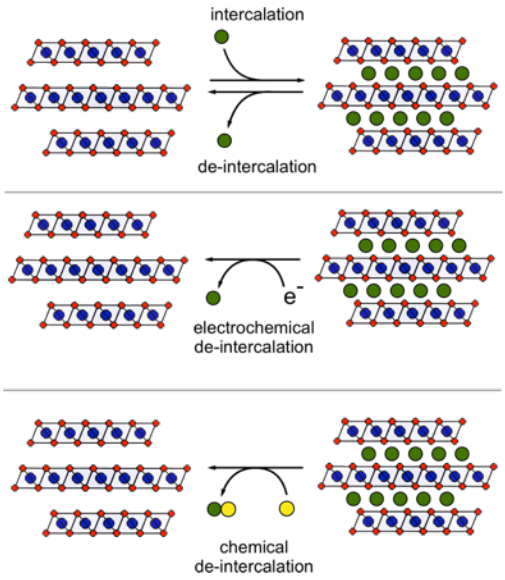

Figure I.11. Schematic of idealized model of intercalation-deintercalation topochemical reactions where the layered moiety is preserved.

Topotactic reactions can be sequentially used to prepare targeted compounds that cannot be prepared in a single step, much in the manner that organic reactions can be

sequentially performed to prepare targeted molecules.[39] When reactants are added to the precursor, the free energy of the resulting system can be higher than that of the precursor alone. The resulting product can therefore be higher in free energy than the original precursor. By separating the product of a first topochemical reaction from the resulting by-products, it is possible to repeat the process, again forming a compound that is higher in free energy than the intermediate product. This is shown schematically in Figure I.12. The key to these transformations is that a large fraction of the original structure remains intact during the reactions.

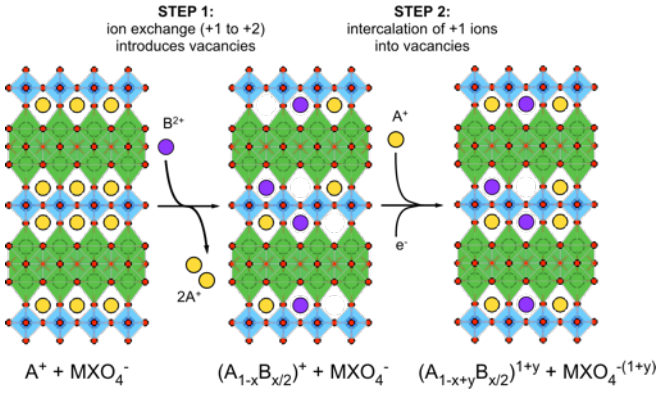

Figure I.12. Schematic of a series of sequential topochemical reactions where the addition of reactants results in the formation of products that are higher in energy than the precursor.

I.3.5. Synthesis via Amorphous Intermediates.

As mentioned earlier in section I.2.1, the reaction of ultra-thin elemental layers - a special case of a bulk reaction where diffusion distances are short enough that the system interdiffuses before nucleation occurs - can result in the formation of metastable compounds. It is instructive to examine the changes in the sequence of phase formation as thickness is reduced. In a bulk planar diffusion couple, two elements are placed in contact with one another and heated for extended times at an elevated temperature. If the binary phase diagram contains compounds, all of the compounds stable at the annealing

temperature will form at the reacting interface as illustrated in Figure I.13.[40] Parallel layers of single phase compounds in a sequence dictated by the phase diagram will form, assuming that only volume diffusion occurs. Wavy interfaces or precipitate structures are thermodynamically forbidden by the phase rule. While the phase diagram dictates what compounds will exist, the relative amounts of the different compounds depend on the diffusion rates of A and B through the compounds.

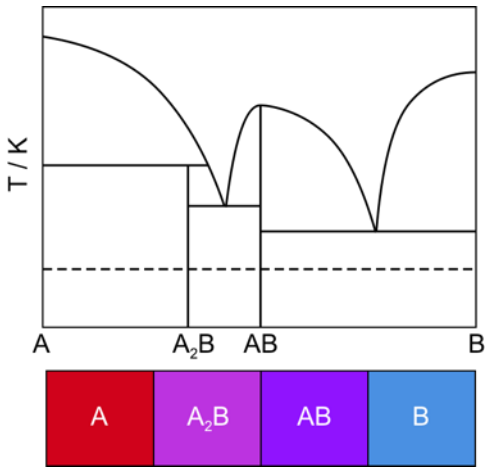

Figure I.13. Schematic of a binary diffusion couple of A and B after annealing for sufficient time at the temperature of the dashed horizontal line. The phase diagram for A and B is shown above the diffusion couple.

When the elemental layers are decreased in thickness, the reaction pathway changes. For thin enough layers, a sequential evolution of phases occurs during annealing as the formation of crystalline compounds is alternately limited by diffusion and nucleation as shown in Figure I.14.[41] This sequence of phase growth in this "thin film regime" results from the elemental layers first intermixing at the interfaces forming a composition gradient spanning all compositions. As this intermixed region becomes thicker, the rate of change of local compositions decreases, enabling nucleation to occur. The compound that nucleates first is determined by which phase has the lowest nucleation energy. It has been

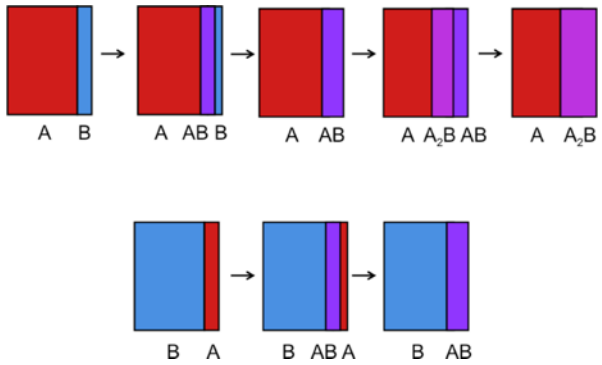

Figure I.14. Schematic of thin film diffusion couples of A and B shown as a function of annealing time. The top case is where B is the limiting reagent. The bottom case is where A is the limiting reagent. The hypothetical phase diagram for A and B is shown in Figure I.13.

suggested that the composition gradient between the elemental layers may develop composition plateaus, as all amorphous compositions will not have the same stability nor the same diffusion rates for the constituent elements. The formation of these composition plateaus may determine which compound nucleates first.[42] This first compound grows, limited by the diffusion rates of the elements through the compound, until one of the elemental reactants is totally consumed. A composition gradient then begins to develop between the first compound and the remaining element. Composition plateaus may also develop in this second interface region, influencing which compound is the second to nucleate. A second compound then nucleates in this second interface. The thickness of the second compound will grow at the expense of the amount of the first compound and the remaining element till one of them is exhausted. The sequence of compounds that forms is determined by the nucleation energies, and the sequence can skip compounds on phase diagram that have high nucleation energies.

If the elemental layer thicknesses are made thinner, a point can usually be reached where the system interdiffuses completely before any nucleation occurs at the reacting interface, resulting in a homogeneous amorphous intermediate.[43] The "critical thickness" to avoid interfacial nucleation depends on the relative activation energies for interdiffusion, nucleation energies and the rate of change of the composition gradient as a function of time.[44] The composition of the amorphous intermediate is determined by the relative thicknesses of the initial elemental layers. The composition of the amorphous intermediate controls what compound nucleates first.[45] If a metastable compound has the lowest nucleation energy, then it will be the first compound to form.[46] If the composition of the homogenous amorphous phase matches that of a metastable compound, then the nucleation and growth of the metastable compound will be a nearly diffusionless process. A schematic of the reaction of ultrathin layers, also called nanolaminates, is shown in Figure I.15. This approach has been used to prepare a number of new, metastable binary compounds.

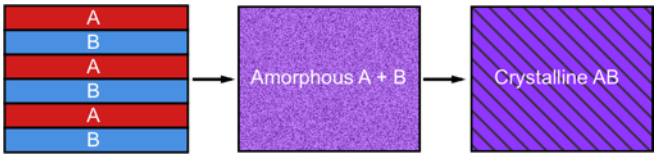

Figure I.15. Schematic of an ultra thin film diffusion couple. The system progresses through a homogenous amorphous intermediate before nucleation occurs.

Bene connected the formation of an amorphous intermediate at the interface between two reacting elements to the formation of the first phase in thin film diffusion couples, suggesting in both cases that the first phase that forms is that which leads to a maximum decrease of the Gibbs free energy - dG/dt.[47] If the thickness of the elemental layers are thin enough and the diffusion rate high enough, then the elemental layers can

completely interdiffuse. Bene also suggested that the reaction rate is proportional to diffusion rates, so the rate of decrease of the free energy is related to $D\Delta g$ where D is the diffusion rates and Δg is the change in the Gibbs free energy per atom. Since diffusion rates tend to be higher in amorphous phases than bulk diffusion in crystalline phases, the higher diffusion rates can compensate for the higher Gibbs free energy of the crystalline phases relative to the amorphous intermediate(s).

The homogenous amorphous intermediates obtained from the interdiffusion of nanolaminates are ideal precursors for the synthesis of compounds with targeted structures, such as those that might have been predicted by a theoretical investigation of stability. For binary systems, there are several experimental parameters available to control what compound nucleates. The most important are the bilayer thickness, which needs to be thin enough to avoid interfacial nucleation before the homogenous amorphous intermediate is formed, and the composition, which is controlled by the relative thicknesses of the elemental layers.[46] The processing conditions, time and temperature, and the substrate also influence what compound nucleates first. If the desired phase does not nucleate from the amorphous intermediate, additional experimental parameters to influence what compound nucleates would be useful. One concept that needs to be further explored in the future is seeding nucleation with isostructural analogs of the desired compound.

When three elements are in the repeating sequence of layers, the order of the layers provides another experimental parameter to control the reaction path.[48] Binary compounds can be avoided as reaction intermediates by using sequences of layers to control what layers are adjacent to one another. For example, suppose the compound AB nucleates at a reacting interface even when the layer thicknesses are at an atomic scale. In this case, it is

not possible to prepare an amorphous alloy of A and B by inter diffusing A and B layers. In a ternary system, as shown in Figure I.16, the layer sequence ACBC places the element

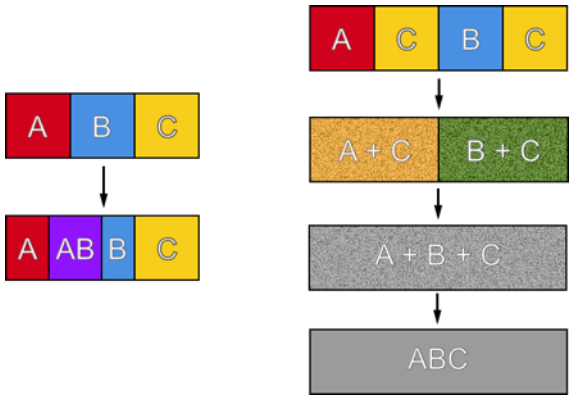

Figure I.16. Schematic of the two different reaction pathways taken by precursors with layer sequences ABC and ABCB.

C between the A and B layers. This forces A and B to both intermix with C before they can begin to interdiffuse. This can prevent AB from forming before the system forms an amorphous ternary intermediate.[48] It is more challenging to form a binary compound from a ternary amorphous intermediate because it requires disproportionation.

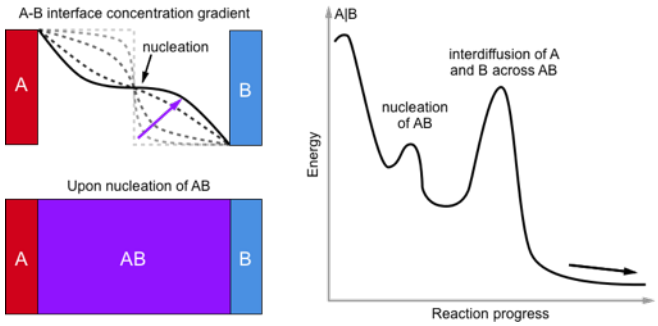

Figure I.17. Schematic of the free energy reaction pathway taken by a precursor with thick elemental layers of A and B.

It is instructive to examine the evolution of an energy landscape picture of the reaction between solids as a function of layer thickness and on the layer sequence of the precursor. For thick elemental layers, diffusion and nucleation alternate as the rate-limiting step as shown in Figure I.17. The initial layers initially interdiffuse to form a thin amorphous region between the elements. The change in local concentration slows with time as the concentration gradients decrease. Eventually the movement of a region of constant composition is slow enough that there is enough time for an embryonic nucleus of a binary compound to grow to the critical nucleus size, resulting in the nucleation and rapid growth of the binary compound along the constant composition region along the diffusion front. Diffusion of the two elements through the compound to the two growth surfaces then becomes the rate limiting step. New composition gradients become established at the growth fronts and the process repeats as nuclei of other binary compounds begin to form at the interfaces.

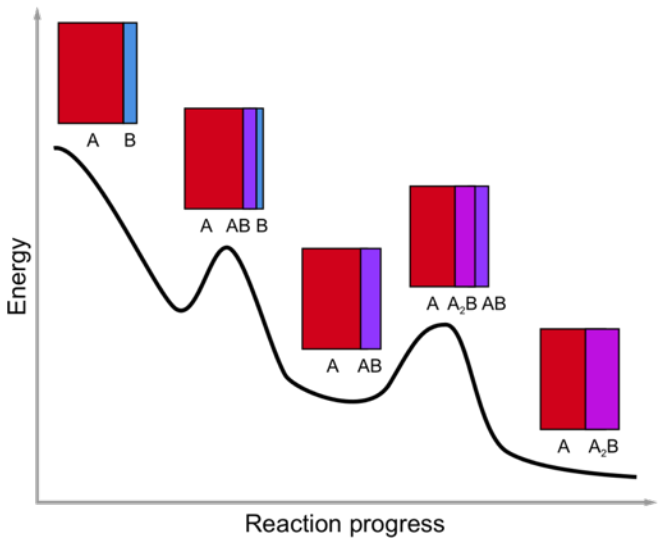

Figure I.18. Schematic of the free energy reaction pathway taken by a precursor with thin elemental layers of A and B.

For precursors containing thin elemental layers, diffusion and nucleation also alternate as the rate-limiting step as shown in Figure I.18, but the growth of the first phase to nucleate stops when one of the elemental layers is exhausted. The rate of free energy decrease is then determined by the establishment of the composition gradient at the interface between the element and the compound, until the equilibrium solubility is reached. This decrease is slower than in the thick film case because there is no more of the compound being formed. Nucleation of the next compound to form is the only way for the system to further decrease its free energy. Once the second compound nucleates, it will grow until either the first compound to form or the elemental layer is exhausted. The process can then repeat if there is another compound in the equilibrium phase diagram that can form. Compounds can be skipped in this sequential nucleation and growth process, if they have higher nucleation energies.

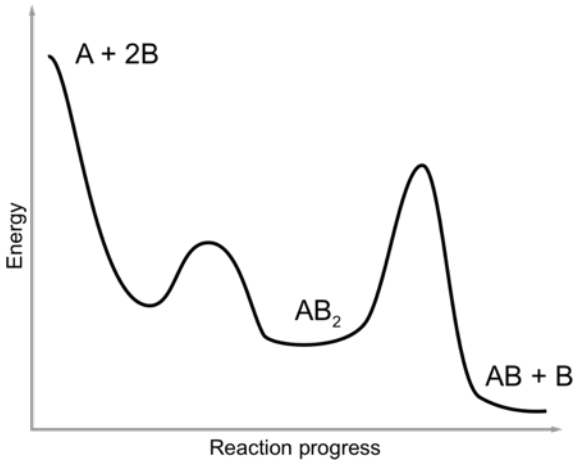

Figure I.19. Schematic of the free energy reaction pathway taken by a precursor of ultrathin elemental layers of A and B at a 1 to 2 ratio of the elements. An amorphous intermediate is formed from which the metastable compound AB_2 nucleates first. This compound decomposes at higher temperatures to form the equilibrium mixture of AB and B.

For ultrathin layers which interdiffuse completely without nucleating a compound, diffusion is the initial rate limiting step. The amorphous solid that forms at low enough temperatures is kinetically stable and hence is a local free energy minimum in the energy landscape. The crystalline solid that is easiest to nucleate will form first from this amorphous alloy. The pathways to potential compounds that could nucleate from the amorphous allow are saddle points connecting the minimum of the amorphous alloy to other minima containing potential crystalline products. The difference in energies between the amorphous alloy and the saddle points are directly related to the activation energy for nucleation of the different compounds. This is illustrated schematically in Figure I.19. The transformation of the amorphous solid to a crystalline compound does not require long range diffusion if the composition of the amorphous solid matches that of the compound. Only local rearrangements to form nuclei with the structure of the targeted compound are required, which explains why composition is a powerful tool to control what forms.[49–51] This constant composition transformation is shown schematically in Figure I.19 as the lowest energy saddle point. The transformation of the intermediate to a mixture of two compounds with different compositions is not kinetically favored at low temperatures because it requires a local disproportionation that is a large enough fluctuation to form critical nuclei of at least one of the compounds in the more stable mixture. This disproportionation is also unfavorable with respect to the associated decrease in entropy from the unmixing of the amorphous alloy.

Since amorphous alloys yield only the easiest solid to nucleate at each composition, they have been a very useful reaction intermediate to form metastable crystalline solids. Unfortunately, there are no methods currently known to control the nucleation event to

form a specific structure. New approaches to control nucleation need to be developed to form different polymorphs at the same composition. Pressure or substrate structure are experimental parameters that could be used to control what forms, by altering the relative nucleation energies of competing compounds. Creating thin regions with a composition that nucleate a known structure might seed the growth of adjacent layers with compositions that do not nucleate this structure. There is much to be explored. The inability to predict what nucleates first results in a familiar serendipity concerning what compounds are actually prepared.

I.4. Predicting Undiscovered Compounds

A challenge for all of the experimental approaches to metastable compounds with extended structure is predicting what compounds might be possible local free energy minima in a quantitative way. The simple local coordination rules that enable organic chemists to predict the structure and composition of plausible compounds does not exist for extended inorganic solids. Synthesizing compounds with specific properties is even more challenging. In the last decade, the search for new, potentially stable compounds using high-throughput machinery has emerged as a rapidly evolving field of materials science.[3,4] The basic idea of this new field is straight forward - create and then examine a database containing calculated and experimental thermodynamic and electronic properties of existing and potentially yet to be discovered compounds to find materials with specific properties. The most common theoretical approach to predict undiscovered materials is to calculate the energy of known compounds, enabling the energy of mixtures to be

calculated. The formation energies of undiscovered compounds are then calculated, usually by starting with placing atoms into a known structure type and allowing the system to relax to a minimum in the calculated energy. If the energy of the compound is lower or close to the energy of a mixture of known compounds with the same composition, then the compound is reported as a potentially stable compound. This is shown schematically in Figure I.20. A large number of synthetic targets can now be found in these computational repositories.[4,52–55] For this high throughput machinery to be ultimately useful, however, the properties of the existing and proposed materials must be predicted correctly and researchers need to be able to synthesize the proposed undiscovered compounds.

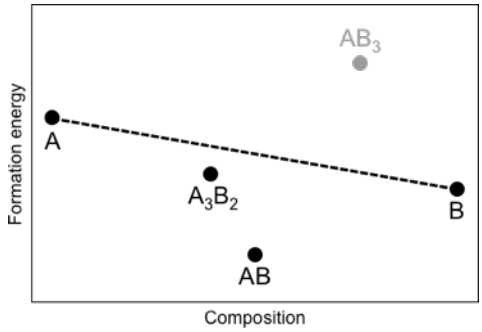

Figure I.20. Schematic of a free energy diagram in a binary system of elements showing the energy of thermodynamically stable compounds, with lines showing the energy of physical mixtures of adjacent compounds. If the free energy of a compound is above this line, it is thermodynamically unstable with respect to disproportionation. If below the line, it is thermodynamically stable

The limited number of new compounds made relative to the number of synthetic targets predicted, highlights the challenges in choosing the correct functionals to accurately calculate stability using density functional theory and the limitations of traditional synthetic approaches. A common result of experimentalists trying to prepare unknown compounds predicted to be thermodynamically stable are reaction products that consist of mixtures of

known compounds as expected from existing phase diagrams.[5] While some of the reason undoubtedly lies on assumptions implicit in the predictions, a significant factor is the inability to control reaction pathways to avoid known thermodynamically stable compounds. If the predicted compounds are metastable, the traditional high temperature reaction of the elements will result in a mixture of binary compounds as they form first in the reaction.

An alternative approach to theoretically predicting compounds that might be stable is to use structural homologies to predict compounds that might be local free energy minima. The rules in organic chemistry to predict the structure of compounds are simple and based on the local coordination of atoms which needs to be maintained as atoms are used as building blocks to create molecules. For example, potential synthetic targets need to have all carbon atoms making 4 bonds, oxygen two bonds and hydrogen one. In extended inorganic systems, the situation is more complicated as even the same element can assume different coordination environments in the same compound based on stoichiometry and the chemical nature of neighboring elements. To predict potential undiscovered compounds, researchers can identify structural building blocks in a compound and then create new compounds by either assembling them in different arrangements or extending them in one or more dimensions. The compounds created by extending the size or number of structural units are called a homologous family of compounds. A simple example of a homologous family of compounds is shown in Figure I.21. The simplest compound in this family is $[(PbSe)_{1.14}]_1(NbSe_2)_1$, referred to as $(PbSe)_1(NbSe_2)_1$ or simply as the 1:1 compound of this family. It contains a bilayer of a distorted rock salt structured PbSe alternating with a $NbSe_2$ trilayer with an octahedral transition metal dichalcogenide structure. In addition to the 1:1

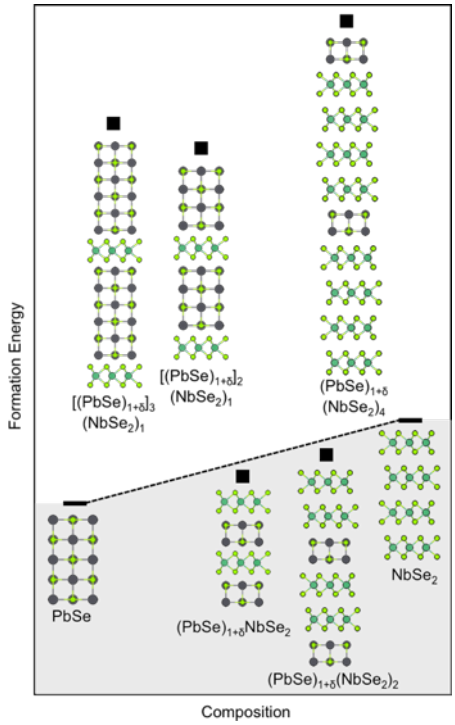

Figure I.21. Schematic of a free energy diagram in a binary system of compounds showing the energy of thermodynamically stable compounds, with lines showing the energy of physical mixtures of adjacent compounds. If the free energy of a compound is above this line, it is thermodynamically unstable with respect to disproportionation. If below the line, it is thermodynamically stable.

compound, the 1:2 and 1:3 compounds, containing one, two and three $NbSe_2$ layers alternating with a PbSe bilayer are thermodynamically stable ternary compounds and have been prepared by directly reacting the elements. The remaining members of this family are metastable, and cannot be prepared using traditional approaches. Quite a few members of this family of compounds have been prepared using modulated elemental reactants as described later in this review. More complicated homologous series are known as described in an excellent article by Kanatzidis.[2]

I.5. Modulated Elemental Reactants – An Approach to Control Reaction Pathway using Designed Precursors.

For the remainder of this chapter we focus on synthesis using solid amorphous or mostly amorphous mixtures containing just the elements required for the structure that forms as reaction intermediates, as they are perhaps the simplest and most general reaction system of the four approaches discussed previously. In these neat systems, there is no solvent or flux that remains after an extended structure nucleates and grows from the amorphous solid. Indeed, if the homogenous amorphous solid has a composition that matches the stoichiometry of the nucleating compound, there can be 100% conversion of the precursor into the final crystalline product via a near diffusionless process.[56] In the self-assembly process only short range diffusion is necessary, making nucleation the rate limiting step in the formation of a crystalline product.

Amorphous solids can be formed with most of the periodic table over a wide variety of compositions using a variety of approaches. In the early 1980's, W. Johnson's group discovered a way to form amorphous alloys at low temperatures from crystalline foils. They showed that amorphous metals are formed by the spontaneous mixing of crystalline metal foils driven by a large ΔH of mixing.[43] Annealing the amorphous alloys formed by the mixing at higher temperatures nucleated crystalline compounds. Novet and coworkers extended this work, showing that this approach for forming amorphous alloys at low temperatures works in a wide variety of systems if the thickness of the reacting layers is below a critical thickness. They also showed that the composition of the amorphous intermediate can control which compound nucleates first. Another key result of Novet's work was demonstrating the nucleation of a compound from an amorphous intermediate

under conditions where it is thermodynamically metastable.[45] They showed that the activation energy to nucleate a metastable phase from an amorphous intermediate with a composition corresponding to the stoichiometry of the compound can be lower than that required to disproportionate and nucleate a thermodynamically more stable mixture of two compounds. Figure I.22 shows a schematic energy landscape picture of the reaction pathway of a precursor designed to form Fe_5Si_3 at temperatures where it is metastable.

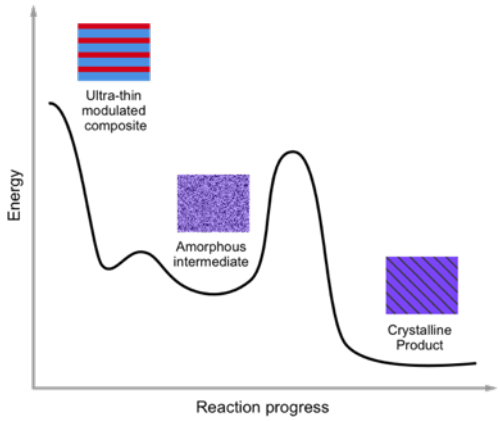

Figure I.22. Schematic of the free energy reaction pathway taken by a precursor designed to form Fe_3Si_5.

Several research groups followed up on these initial studies, demonstrating the utility in using homogeneous amorphous solids as versatile intermediates in synthesis. D. Johnson's group prepared a number of metastable binary and ternary antimonide compounds with the skutterudite structure by controlling the composition of amorphous intermediates.[46] Subsequent studies showed that the nucleation energies of compounds depended on the composition, and it was necessary to find the range of compositions in which the desired compound had the lowest nucleation energy with respect to competing compounds.[50] Adding a third element to a binary amorphous solid resulted in an increase

in the nucleation energy of the binary compounds.[51,57] Jansen's group directly prepared amorphous intermediates by co-evaporation onto a cooled substrate. They showed that metastable halides could be kinetically trapped as the temperature of the intermediates was increased. These studies showed the importance of controlling substrate temperature during the evaporation, especially when one of the elements being deposited has a high vapor pressure or high surface mobility during the deposition.[57] Bensch's group used amorphous intemediates to prepare a number of new binary compounds and showed via temperature dependent operando diffraction experiments that this is a consequence of avoiding more stable compounds.[58] Bensch's group also attacked the significant challenge of determining the structure of new compounds formed as films using a variety of diffraction techniques. A key recent advance in this area is the use of electron microscopy techniques to create models for subsequent refinement of x-ray diffraction data.[59]

With several groups demonstrating the ability to prepare new binary compounds and metastable polymorphs of known compounds, the fundamental basis of controlling the composition of an amorphous intermediate to prepare new compounds seems established. The time and activation energy required to nucleate a compound of similar composition via a diffusionless transformation is less than the time and activation energy required to disproportionate the precursor and nucleate a more stable compound. While the main experimental parameter explored in these initial studies to control which compound nucleated was the average composition, other parameters, for example pressure, could provide additional experimental tools to control what nucleates first. Pressure would change the relative saddle point energies of the different potential nucleation events,

permitting compounds to nucleate that are different than the one that forms at one atmosphere of pressure.

The energy minimum in the free energy landscape for the amorphous phase has been proposed to be a useful guide to determine if predicted compounds can be made.[60,61] Compounds that are higher in free energy than the amorphous intermediate will be unstable with respect to forming an amorphous structure at the same composition. Therefore, they cannot nucleate from the amorphous phase, as this would increase the free energy of the system. Compounds that are lower in free energy than the amorphous phase can potentially be formed by manipulating experimental conditions so that the saddle point leading to them in the energy landscape is the lowest available to the amorphous phase. Amorphous intermediates that have compositions that match the stoichiometry of targeted compounds are perhaps the best initial approach to prepare the many compounds predicted to be stable via theory. An example of this is the free energy diagram in Figure I.23 for the Fe-Sb

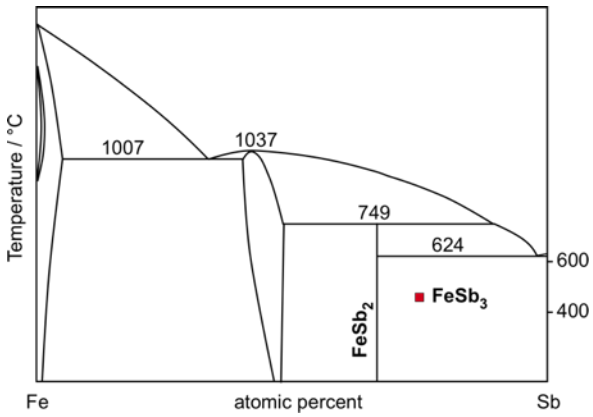

Figure I.23. The Fe-Sb phase diagram with the metastable compound $FeSb_3$ shown in red. $FeSb_3$ decomposes exothermically to a mixture of $FeSb_2$ and Sb.

system. The binary compound $FeSb_3$ is thermodynamically less stable than a mixture of $FeSb_2$ and Sb. $FeSb_3$ is, however, more stable than an amorphous solid with a one to three ratio of Fe to Sb.[46] Hence it can be formed by controlling annealing conditions.

I.5.1. More Complex Precursors - Composition Modulation

A challenging issue in utilizing designed precursors is finding synthetic targets where there are experimental parameters besides the composition of the amorphous intermediate that can be used to control the synthetic pathway to compounds with targeted structures. Homologous compounds are logical first synthetic targets. A family of homologous compounds all contain the same fundamental structural units, or building blocks.[2,62] The compounds within the family differ from one another by the size and/or stacking sequence of the different building blocks. The structural relationship between the different building blocks is maintained within the family of homologous compounds.

Layered homologous compounds are ideal synthetic targets for the modulated elemental reactants (MER) synthesis approach. Consider two building blocks, A and B, that both represent the thinnest two-dimensional layer of two different structures that maintains the essence of each structure. Conceptually these blocks can be stacked in an infinite number of layer sequences where the thickness and/or stacking sequence is varied. The thinnest layer sequence would contain two layers, AB. There are two sequences with three layers, AAB and ABB. There are three sequences with four layers ABBB, AABB, and AAAB. There are six different sequences with five layers {ABBBB, AABBB, ABBAB, AAABB, AABAB, and AAAAB} and eight different sequences with 6 layers {ABBBBB, AABBBB, ABABBB, AAABBB, ABAABB, AAAABB, AAABAB, and

AAAAAB}. The number of sequences increases very rapidly above this point, with sixteen different sequences with seven layers, twenty four different sequences with eight layers, and forty two different sequences with 9 layers. Keeping the total number of layers less than 20, there are over 60,000 possible sequences with just two building blocks, and the number of possible sequences increases rapidly as the number of constituents increases as shown in Figure I.24.[63] In a homologous family with three building blocks, there are over

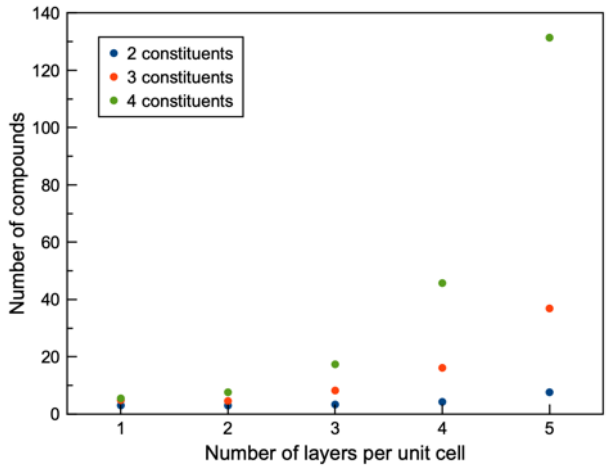

Figure I.24. The increase in the number of possible homologous compounds as the number of layers in the unit cell is increased. The increase is much greater as the number of distinct constituent layers increases.

130 million possible sequences with a total number of layers less than 20. In a homologous family with four building blocks, there are over 35 billion possible sequences with a total number of layers less than 20. The number of potential new compounds generated by homologous relationships is staggering. The challenge is developing synthetic strategies that are able to selectively prepare specific sequences of layers.

The misfit layer compounds are thermodynamically stable examples of compounds that have the desired layered motif.[64] The misfit layer compounds contain alternating layers

of a dichalcogenide structured and a rock salt structured constituent. The misfit layer compounds are unusual due to an incommensurate relationship between their constituent layers, resulting in a non-integer stoichiometry $(MX)_{1+y}(TX_2)_1$. The magnitude of y reflects the difference in the atom density of the two formula units in their common plane. It takes 1+y units of MX to cover the same area as 1 unit of TX_2 for the respective planes that are parallel to the interface between them. Thermodynamically stable misfit layer compounds are known with M = Sn, Pb, Bi, Sb and rare earth metals, X = S and Se, and T = Ti, V, Cr, Nb and Ta.[64] Many more sulfides are known than selenides. Most of the misfit layer compounds contain a single layer of both the rock salt constituent and the dichalcogenide. There are a few examples of compounds containing a single rock salt layer and two or three layer thick dichalcogenide layers that are prepared by changing the composition of the initial reactant mixture. The rock salt layer thickness is almost always a single bilayer thick. Since these compounds are stable at the high temperature synthesis temperatures, it suggests that the interaction between layers must be stronger than the interaction between the same structural units in the respective binary compounds. If one tries to make the MX layer thicker by changing the composition of the initial reaction mixture, one obtains a mixture of $(MX)_{1+y}(TX_2)_1$ and MX rather than $[(MX)_{1+y}]_m(TX_2)_1$ where m is an integer greater than one.

Layered homologous compounds related to known misfit layer compounds are a natural synthetic target using MER. The strong interaction between the rock salt layer and dichalcogenide is responsible for the thermodynamic stability of the known misfit layer compounds relative to mixtures of the binary compounds. This strong interaction should help stabilize homologs of the known $(MX)_{1+y}(TX_2)_1$ compounds. One can adjust the

deposition conditions when preparing MER precursors so that there are the correct number of atoms in an M|X bilayer to form a single structural unit of MX and, likewise, a T|X bilayer can be deposited with the required number of atoms to form a single structural layer of TX_2. If an initial sequence of layers M|X|T|X is used as the repeating structure of a precursor, a layered heterostructure $(MX)_{1+y}(TX_2)_1$ can form in a nearly diffusionless process. This will make this compound the kinetically favored product if diffusion is limited. The known misfit layer compounds will be more stable than two amorphous layers as the M-X and T-X bonding will be maximized in forming MX and TX_2 layers. The other two possibilities are the M|X|T|X repeat can completely interdiffuse to form an amorphous M-T-X alloy intermediate or the M|X|T|X precursor can disproportionate into macroscopic domains of MX and TX_2. In the case of known misfit layer compounds, both of these possibilities will be higher in energy than the $(MX)_{1+y}(TX_2)_1$ misfit layer compound. A precursor with repeating M|X|M|X|T|X elemental layers will be kinetically favored to form $[(MX)_{1+y}]_2(TX_2)_1$, because the M|X|M|X|T|X precursor structure provides very similar initial composition profiles to $[(MX)_{1+y}]_2(TX_2)_1$, enabling a near diffusionless transformation. While annealing may result in changing concentration gradients during annealing before nucleation occurs due to the thicker M|X region, it is reasonable to expect local compositions to control what nucleates. Indeed, this approach works, producing heterostructures with amazing fidelity due to the large stability difference between the precursor and the targeted heterostructures.[65–67] Appropriately designed precursors have enabled the synthesis of compounds with specific sequences of layers as shown in Figure I.25.[68] This approach enables the synthesis of extensive families of homologous compounds, because the criteria for formation is to be more stable than the precursor. This

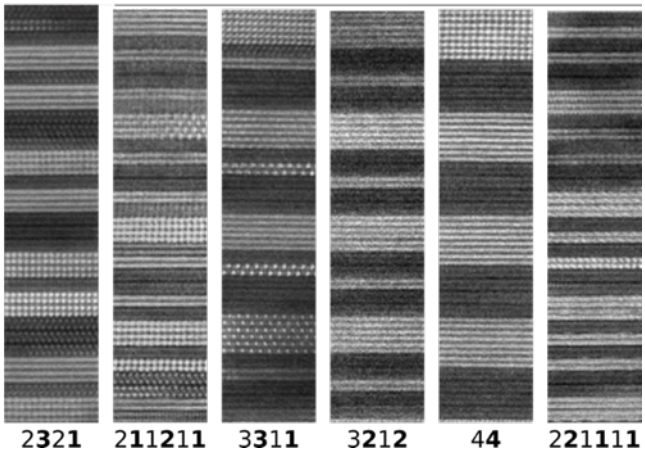

Figure I.25. HAADF-STEM images of structural isomers containing four bilayers of PbSe and four $TiSe_2$ trilayers. The notation on the bottom of the images provides the number of PbSe bilayers in bold and the number of $TiSe_2$ layers in normal font. The sequence of numbers matches the sequence of layers in each isomer.

differs from traditional synthetic techniques, where the uncontrolled formation of intermediates requires products to be more stable than any mixture of thermodynamically stable compounds and the elements.

Families of compounds of rock salt structured constituents alternating with transition metal dichalcogenide blocks have also been prepared using designed precursors where no family members were previously reported via direct reaction of the elements. Of the Group 6 metals (Cr, Mo or W), only Cr containing misfits have been reported to form as thermodynamically stable misfit compounds and only with trivalent cations.[69,70] Lin et al reported the synthesis of over a hundred new compounds in the $[(PbSe)_{0.99}]_m(WSe_2)_n$ homologous family.[71] Heideman et al reported the synthesis of analogous family of homologous compounds, $[(PbSe)_{1.00}]_m(MoSe_2)_n$.[72] Beekman et al reported the synthesis from designed precursors of a homologous family of $[(SnSe)_{1.04}]_m(MoSe_2)_n$ compounds, where $0 < m, n < 32$.[73] There have been no reports of additional $[(MSe)_{1.23}]_m[CrSe_2]_n$ compounds, but to our knowledge the use of designed precursors to prepare them has yet

to be attempted. The first reported telluride misfit layer compounds containing rock salt structured PbTe with a layered $TiTe_2$ were also prepared using modulated elemental reactants.[74] Other examples are expected with different dichalcogenides or rock satl structures, as there are many potential rock salt structured compounds that have yet to be explored using designed precursors. More complicated sequences have also been created with two different dichalcogenides and a rock salt structured layer in ordered sequences.[63,75] Specific layers within layering sequences have also been alloyed, with the nanoarchitecture of the precursor preserved as it self assembles into the desired compound.[59,76–78] There appears to be an unlimited number of combinations that can be prepared.

Designed precursors have also enabled synthesis of new layered solids with a wide variety of constituents having different structures than the rock salt structure and transition metal dichalcogenides found in misfit layer compounds. New families of homologous compounds have been prepared by layering two different dichalcogenides, including

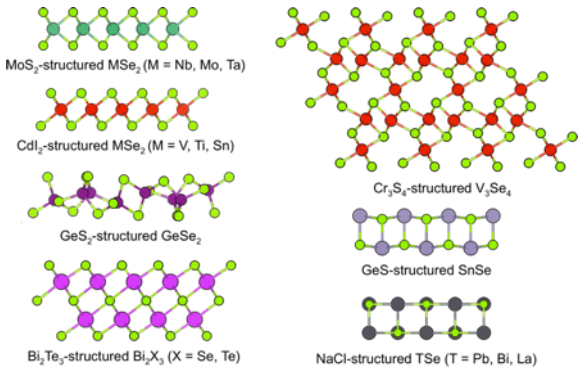

Figure I.26. The different layered constituents that can be used as building blocks to prepare heterostructures via designed precursors.

$SnSe_2$.[79–84] New families of homologous compounds (shown in Figure I.26) have been prepared with transition metal dichalcogenide layers alternating with layers of Bi_2Se_3 and Bi_2Te_3,[85,86] $GeSe_2$,[87] and V_3Se_4.[88] These metastable compounds are prepared using precursors as described for misfit layer homologs discussed previously. Key to the synthesis is preparing the precursors such that each elemental bilayer contains the appropriate number of atoms to form a structural unit of the desired constituent. Gently heating the precursor caused the individual layers to nucleate the desired structures through a near diffusionless reaction which maintains the nanoarchitecture of the precursor.

Designed precursors also permit the formation of compounds containing three or more different constituents and the different constituents can each have a different structure. An example of a heterostructure containing 3 different structures is $(BiSe)_{1+\delta}(Bi_2Se_3)_{1+\gamma}(BiSe)_{1+\delta}(TiSe_2)_1$,[89] while an example of a heterostructure containing three different compounds is $[(PbSe)_{1+\delta}]_m(TiSe_2)_n[(SnSe_2)_{1+\gamma}]_m(TiSe_2)_n$.[63] As mentioned earlier, this greatly expands the number of potential compounds that can be prepared. All of the compounds in a family of homologous compounds containing two constituents fall on the compositional tie line between the two compounds as shown schematically in the phase diagram in Figure I.27. In a family of homologous compounds containing three constituents, the compounds fall in an area bounded by the 3 tie lines between the three constituents, also represented in the phase diagram in Figure I.28 for a case where two of the structures contain the same elements but have different stoichiometries. In a family of homologous compounds containing four constituents, the compounds are in a volume bounded by the areas of the four combinations of three constituents Figure I.29.

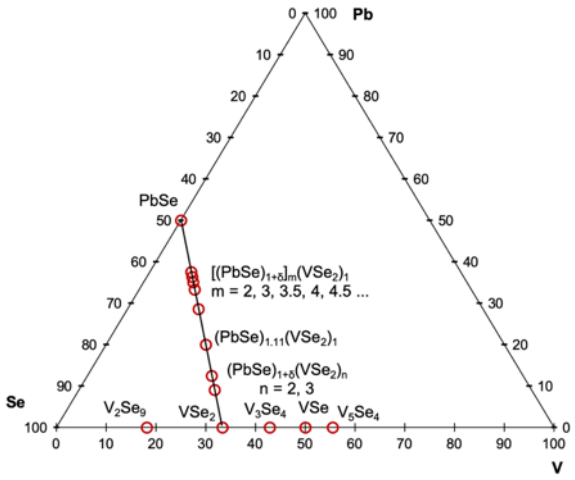

Figure I.27. The ternary phase diagram of Pb-V-Se. The three elements do not have a ternary thermodynamically stable compound. However, using designed precursors, metastable heterostructures containing PbSe and VSe_2 have been made and are contained as red circles in the ternary phase diagrams. For two constituent heterostructures, the metastable heterostructures lie on the tie line (black line) connecting the two building blocks.

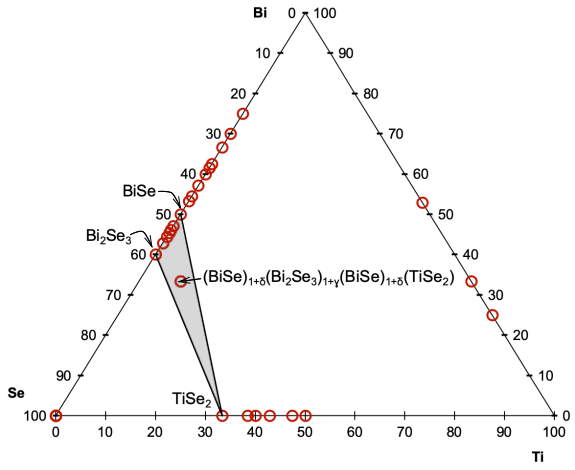

Figure I.28. The ternary phase diagram of Bi-Ti-Se. A three-component heterostructure containing BiSe, Bi_2Se_3, and $TiSe_2$ will be contained in an area enclosed by the tie lines connecting Bi_2Se_3 and $TiSe_2$, and BiSe and $TiSe_2$. Shown as a red circile in that area is metastable three-component heterostructure $(BiSe)_{1+\delta}(Bi_2Se_3)_{1+\gamma}(BiSe)_{1+\delta}(TiSe_2)_1$, first synthesized by Lygo et al. via MER.[89]

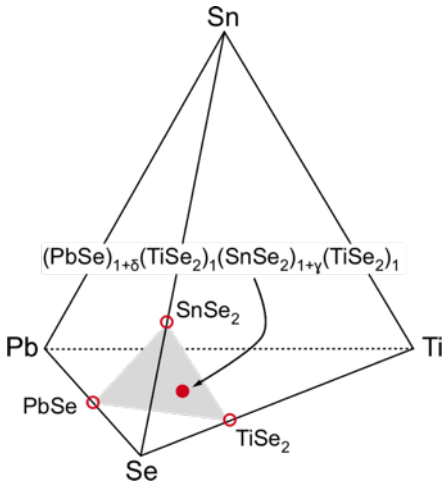

Figure I.29. The quaternary phase diagram of Pb-Sn-Ti-Se. Each phase in the tetrahedron represents a ternary phase diagram containing 3 elements. The three-component heterostructure is contained in the area defined by the tie lines connecting the three components in three different ternary phase diagram.

Both the shortfall in the number of ternary compounds and the inability to prepare a significant fraction of compounds predicted to be stable result from the inability of materials scientists, solid state chemists and physicists to control the reaction pathway to obtain specific kinetically stable products. Developing approaches to control reaction intermediates is one of the keys to enabling the synthesis of targeted and other yet to be prepared solids.

I.5.2 Ideas Concerning the Reaction Mechanism of the Self-Assembly of Precursors into Products

While many compounds have been prepared via designed precursors, why this approach works is not really understood. The simplest mechanism presented to date is schematically shown in Figure I.30. Consider a precursor containing a chosen sequence of

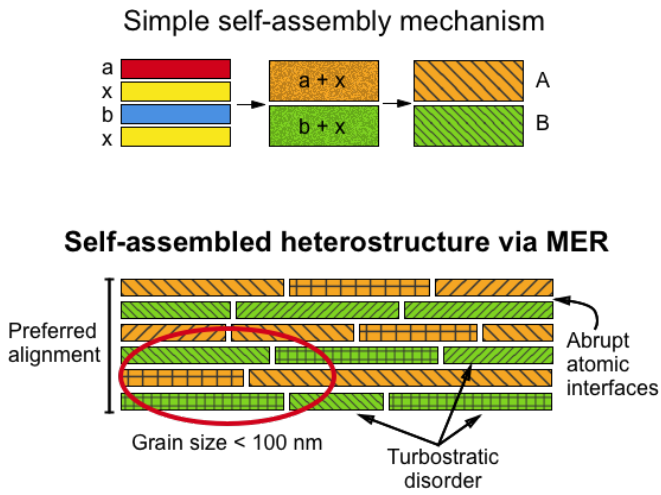

Figure I.30. A schematic representation of the a|x and b|x bilayers interdifusing to form amorphous layers of a-x and b-x before nucleation and growth of crystalline A and B layers (top). The density of the nucleation sites determines the laterial grain sizes and the random orientation of the different nucleation sites results in the turbostratic disorder found in the self-assembled product.

elemental a|x and b|x bilayers, each with the number of atoms per unit area required to form a single structural unit of the targeted constituents. If the thicknesses of the elemental bilayers are lower than the critical thickness for the binary a-x and b-x systems at the targeted compositions, the bilayers are expected to interdiffuse on annealing to form an amorphous intermediate. At low temperatures and short times, the composition modulation of a and b will be maintained if a-x and b-x interdiffuse faster than a into b-x or b into a-x. Nucleation of the target compounds AX and BX must occur before the composition modulation diffuses away in order for the final product to maintain the nanoarchitecture of the precursor.

The nucleation rates of A and B along with the order of nucleation play important roles as revealed by the microstructure of final products. In all of the compounds prepared to date using an elementally modulated precursor, the same common plane is found at all the interfaces between two constituents. This suggests that one constituent nucleates first

and grows with a preferred orientation, perhaps partially as a result of the anisotropic, layered morphology of the compositionally modulated amorphous a|x|b|x precursor. In almost all of the compounds prepared to date, there is extensive rotational disorder between the constituent layers.[90] This turbostratic disorder, as it is called in the clay literature, may be a consequence of multiple nucleation sites in each ax and bx layer, with subsequent lateral growth resulting in a random mosaic of different relative orientations of the two compounds. The observed disorder suggests that there is not a strong preferred, rotational orientation for heterogeneous nucleation of A on B or B on A. The lateral grain size of the constituents A and B tend to be less than 100 nm, suggesting that there are many nucleation sites. Presumably the extensive nucleation sites result from the high extent of supersaturation of the layers in the precursor, leading to a low activation energy for nucleation. Finally, the final structures have long coherence lengths perpendicular to the substrate, remarkably consistent layers in STEM images with structurally abrupt interfaces, and high carrier mobility that suggests a low concentration of defects that scatter the carriers.[71,91] Since the precursors have larger variations in local composition and layer thicknesses than the final products, lateral and/or vertical diffusion must occur during growth to average out local variation.

The proposed reaction mechanism involves both nucleation and diffusion, both of which are challenging to control. Nucleation can be controlled by the absolute composition and thickness of the sequences of layers in the elemental precursors. Very thin a|x and b|x bilayers results in very large local super saturation in the as deposited precursor if the compositions are close to that of a known binary compound. The thin elemental layers typically interdiffuse extensively during the deposition process or at low temperatures. The

extent of lateral diffusion across the surface of the precursor during deposition can be considerable, even for nominally room temperature substrates with deposition via evaporation. The large surface area of the different elemental bilayers in the precursor, which have relatively constant composition, results in many potential nucleation sites either during the deposition process or during annealing at low temperatures. A key question in this simplified mechanism is why the same crystalline surfaces are parallel to the interface between constituents. Atkins proposed that an initial nucleation event results in subsequent heterogeneous templated nucleation off of the first formed crystalline region by adjacent layers.[92] He tested this hypothesis by looking at the structure of binary dichalcogenides formed from layered a|x precursors, and found that ordered crystals formed if the dichalcogenide only existed as a 1T polytype and disordered layers formed if the dichalcogenide existed as a multilayer polytype, for example 2H, because of the choice of different orientations for the next layer (see Figure I.31). Additional studies on $MoSe_2$ were consistent with this proposed mechanism. $MoSe_2$ forms a disordered polymorph from Mo|Se precursors and exists as a 2H polymorph in the bulk.[56] When there are two different constituents that are not structurally related, the orientation of the template nucleation of the second phase to crystalize is expected to be random.[84]

A large number of compounds homologous to misfit layer compounds have been investigated using HAADF-STEM, providing a considerable library of images to explore the proposed mechanism of Atkins. In heterostructures containing only one layer of each constituent, turbostratic disorder is observed between all MSe layers and TSe_2 layers.[93] If the rock salt layers contain multiple bilayers, the entire layer within a grain usually has the same crystallographic orientation. This suggests that 3 dimensional growth occurs from a

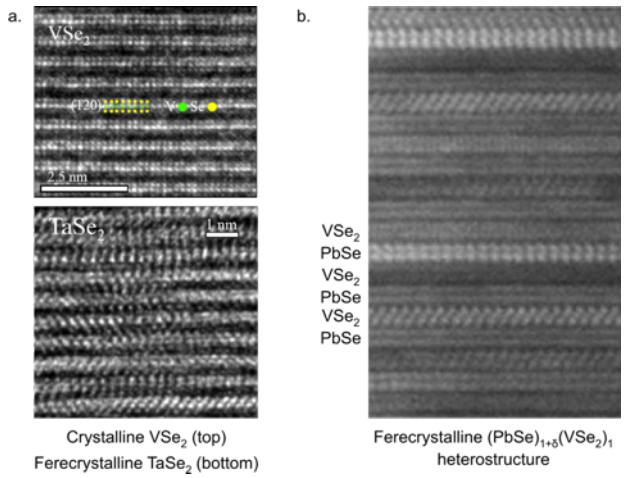

Figure I.31. Differences in structure between crystalline and ferecrystalline phases from HAADF-STEM. Crystalline VSe_2 have the same orientation across several layers. Ferecrystalline $TaSe_2$ exhibits multiple zone axes across multiple layers. The ferecrystalline heterostructure $[(PbSe)_{1+\delta}]_1(VSe_2)_1$ exhibits different zone axes across adjacent repeat units.

nucleation site, although the rate of growth might be different along and perpendicular to the substrate. If the dichalcogenide layer contains multiple TSe_2 layers, it follows the Atkins model. Moderately thick $TiSe_2$ and VSe_2 layers (2 – 6 layers) typically have the same orientation for each TSe_2 layer. For $TaSe_2$, $NbSe_2$, WSe_2 and $MoSe_2$, the different TSe_2 units within a layer have different orientations, even in bilayers.[66,90,94] In special cases, where there is an accidental epitaxial relationship between the two constituents, preferred orientations over multiple unit cells can be observed, consistent with heterogeneous nucleation of subsequent layers off of an initially nucleated layer.[95] Figure I.32 shows different STEM images illustrating the variety of behaviors observed depending on the identity of the constituents. Adjacent rock salt bilayers form with the same orientation as observed in $[(PbSe)_{1+\delta}]_2(WSe_2)$ in Figure I.32a. Dichalcogenides that have only one polytype in the bulk, like $TiSe_2$ and VSe_2 have a single orientation when multiple layers are present in a repeating unit in the heterostructure. Dichalcogenides with multiple

polytypes in the bulk like $NbSe_2$ and $MoSe_2$ can have multiple orientations. These observations are consistent with Atkin's suggestion of heterogenous nucleation.

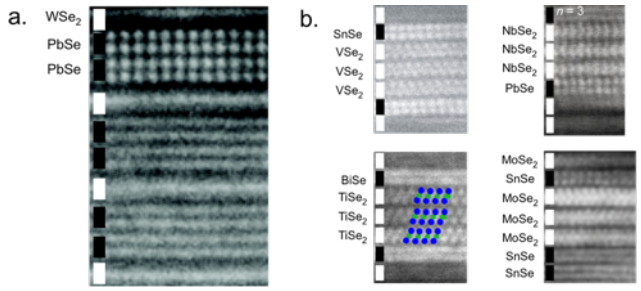

Figure I.32. The structural coherence of between planes of atoms in different crystallographic layers depends on their crystal structure and the structure of the layers adjacent to them. In (a), the adjacent rock salt structured bilayers of PbSe have the same crystallographic orientation. In (b) the adjacent layers of VSe_2, $TISe_2$ and $NbSe_2$ with the same block have the same crystallographic alignment while the alignment of the $MoSe_2$ layers in the same block are different.

Controlling the extent and rate of diffusion in the deposition of the precursor and during the annealing process is also challenging. Diffusion is driven by the free energy decrease associated with the enthalpy and entropy changes during the mixing of the elemental layers. The rate of diffusion also depends on the concentration and type of defects that are present in the layers. An as deposited precursor is typically amorphous with a density that is 5 to 10 % less dense than expected if the layers were crystalline elements. As temperature is increased, defects that are mobile enable the elemental layers to mix and there is a concomitant increase in the density as the mobile defect is eliminated. When temperature is increased, new defects become mobile leading to a jump in the diffusion rate.[96] If one or more of the other elements in the precursor are not miscible in a binary compound that has nucleated, the growth of the binary compound will drive a disproportionation as the immiscible elements are excluded. Conversely, the nucleation of

a thermodynamically stable ternary compound can drive interdiffusion and mixing of layers in the precursor.

Two experimental parameters in the design of a precursor that can be used to modify the interdiffusion of layers in a precursor are the thickness of the elemental layers and the sequence of elemental layers. The rate of mixing of elemental layers depends on the thickness of the elemental layers in the precursor, with thicker layers taking longer to interdiffuse as concentration gradients are more gradual and the distance between the elemental layers increase as the interdiffused region becomes thicker.[81] For example, if one compares the relative rates of mixing of the elemental layers two precursors, a|x|a|x|a|x|b|x versus 3a|3x|b|x, the a-x layer with a single bilayer that is three times thicker, [3a|3x], will mix 9 times slower relative to the layer with three layers that are 1/3 of the thickness if Fick's laws for diffusion hold.[97] This difference in thickness can be used to control which layer nucleates and grows first. The layer sequence in a precursor can also have dramatic effects on the sequence of compounds that form, particularly if there are large differences in the interdiffusion rates of the elements through similar matrices. For example, Cu diffuses very quickly through Se at low temperatures while Cr and In diffuse much slower at similar temperatures. Hence, Cu|M|Se layer sequences, where M = Cr and In, will evolve on annealing to form CuSe|M structures, leading to the formation of binary copper selenides. Creating precursors with M|Cu|M|Se layer sequences eliminates the interfaces between Cu and Se, resulting in the initial mixing of M and Se. This leads to the formation of an amorphous M-Cu-Se alloy, which directly nucleate ternary compounds ($CuInSe_2$ or $CuCr_2Se_4$), avoiding the formation of intermediate $CuSe_x$ as an intermediate binary compound (Figure I.33)

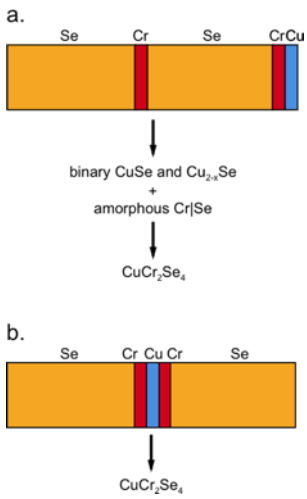

Figure I.33. Synthesis of $CuCr_2Se_4$ can be accomplished without the formation of CuSe as a reaction intermediate by controlling the sequence of Cu, Cr, and Se layers.

Mixing of elements in the precursor and the subsequent formation of alloys is an aspect of MER synthesis that needs to be carefully controlled since it impacts the properties of the heterostructures. Significant mixing and alloying can take place in heterostructures that consists of constituents that have the same coordination and/or similar in-plane lattice parameters. For example, in $(TiSe_2)_6(NbSe_2)_6$ the extent of metal cross-substitution is more than 35% at the $NbSe_2$-$TiSe_2$ interface.[79] Different strategies have been employed in attempts to control the extent of alloying. The individual building blocks for heterostructures can be strategically chosen to have vastly different crystal structures. Transition metal dichalcogenides and rock salt bilayers are an obvious example of this strategy, as the differences in their basal plane shape (hexagonal vs square) and coordination favors the post transition metal cations being in the rock salt structured constituent. To form heterostructures that consists solely of a single structure, for example hexagonal transition metal dichalcogenides, the building blocks must have drastically different 2D crystal structures or large difference in their lattice parameters. Compositional

and structural analysis via HAADF-STEM and EDS have demonstrated the formation of distinct layers of GeS_2-structured $GeSe_2$ and CdI_2-structured VSe_2 as a heterostructure with no mixing of metals across layers.[87] Similarly structured dichalcogenides have been made as heterostructures, such as $(SnSe_2)_1(MoSe_2)_{1.32}$ with minimal intermixing of the cations due to the large misfit between their respective in-plane lattice parameters.[84] In the case of $(SnSe_2)_1(MoSe_2)_{1.32}$, islands of $SnSe_2$ within a $MoSe_2$ layer can occur, however, if the initial precursor does not contain the correct number of atoms of each constituent. An intervening constituent can act as diffusion barriers to prevent metals in different layers from mixing. A $MoSe_2$-$NbSe_2$ heterostructure exhibits alloying of up to 20% at the interfaces, but this interdiffusion can be reduced to near zero when 4 bilayers of SnSe are present between the two different dichalcogenides.[98] Alloying can be deliberately done to achieve modulation doping between rock salt or transition metal dichalcogenide layers. This is accomplished by depositing a trilayer of a|b|x where b is the dopant and the total number of atoms of a and b is that required to completely occupy the crystallographic site in the building block., The rock salt alloyed heterostructure $(Bi_xSn_{1-x}Se)_{1+y}]_1(TiSe_2)_1$[99] and transition metal dichalcogenide alloyed heterostructure $[(SnSe)_{1+y}]_1(Ta_xV_{1-x}Se_2)_1$[100] have been synthesized using this synthetic strategy. These compounds obey Vegard's law and the amount of the dopant atom can be very large because of the closely similar basal plane sizes of (SnSe and BiSe) and ($TaSe_2$ and VSe_2).

While traditional inorganic chemists usually rely on controlling the composition of the initial reactant mixture to drive what products form, the MER route depends on composition, the exact number of atoms in the precursor and where the atoms are located in the precursor. Having the correct number of atoms in each repeating period results in the

low temperature self- assembly of targeted compounds via an essentially diffusionless process.[56,84] Key to discovering this effect was the ability to determine the number of atoms of each element in a film using x- fluorescence,[101] which greatly simplified the calibration of the deposition process. A significant amount of the self-assembly can occur during the deposition process. When there is a slight deviation from the targeted area density of the elements, partial layers, extra layers, or incomplete repeat units need to be fixed during the self-assembly, a process that requires longer range diffusion. If the measured amount of each element deviates enough from the target, a mixture of the thermodynamic products can form as the extent of long-range diffusion eliminates the kinetic advantages of the nanoarchitecture of the precursor. The ability to conveniently measure the area density of elements in designed precursor,[102] has expedited the discovery of new heterostructures. Which structure forms when there are competing compounds in a phase diagram is dictated by the area density of the precursor. For example, the two compounds present in the Sn-Se phase diagram, SnSe and $SnSe_2$, can each be made as heterostructure building blocks by depositing Sn|Se with the correct area density for either the basal plane of tetragonal SnSe or hexagonal $SnSe_2$.

I.6. Next Steps in Materials Synthesis

The ability to prepare new solids with designed structure and properties has historically been limited by the lack of analytical techniques to follow the course of reactions on the atomic scale. How experimental variables impact the reaction pathways during many of the synthesis approaches used to make extended solids, described earlier

in the review, is not known. The heterogeneous intermediate states in typical solid state reactions enhances the difficulty of obtaining information about key reaction events and what experimental parameters control them. When the system being investigated is near equilibrium, phase diagrams greatly assist the logical development of processing conditions towards particular compounds or microstructures. A great example of this is the precipitation hardening of metal alloys. When a system is far from equilibrium or when the system is very complex, we have much to learn. In the next sections we briefly discuss currently developing analytical techniques that may provide insight into the reaction mechanisms of several of the synthesis approaches discussed in this review.

I.6.1 Pair Distribution Function Analysis

Pair distribution function analysis (PDF) of total scattering data provides structural information from disordered materials by analyzing both the Bragg scattering and the underlying diffuse scattering. The long range order of the atoms is determined from the position and intensities of the Bragg reflections. The local atomic structure is deduced from the less well- defined features of the diffuse scattering. This local structure is described quantitatively by the atomic pair distribution function. The pair distribution function analysis of X-ray total scattering measurements of amorphous materials has yielded important information about local structure and the spatial extent of long range order which has been correlated with physical properties.[103] Similar information about the reaction intermediates would be a valuable asset in the development of systematic methods to prepare targeted solid-state compounds from the techniques discussed in this review. The challenge is to remove the scattering background from those parts of the sample that are

not of interest. As an example, the diffuse scattering from the solvent in a reaction occurring in a liquid media dominates because it makes up most of the sample. This scattering needs to be subtracted to leave the diffuse scattering from the reacting molecules. If possible, such total scattering studies as a function of temperature and time provide information about the species in solution. These types of investigations are just appearing in the literature. For example, Iversen's group has published a number of in situ synchrotron small-angle X-ray scattering/wide-angle X-ray scattering/pair distribution function studies of the formation and growth of compounds in solution and in supercritical fluid conditions.[18,104,105] While similar studies of the direction reaction of solids would be difficult, studying the structure of amorphous thin films as a function of composition and/or nanoarchitecture may enable correlations between the structure and composition of the amorphous phase and the structures that nucleate. Several approaches to obtaining and analyzing total scattering data from thin films on a substrate have been developed, which has enabled studies addressing the evolution of structure in amorphous films as a function of annealing temperatures and time.[106,107] The grazing incidence geometry requires complicated data analysis procedures and assumptions about the sample volume and geometry, but the signal of the sample relative to the background from the substrate is high.[103,108] The normal incidence thin film PDF approach simplifies the data processing and allows for quantitative analysis of the total scattering data, however subtracting the large background signal to obtain the scattering from the thin film is challenging. Total scattering pair distribution analysis has have been used to follow the chemical transformation and structural evolution of sol gel films and during processing and the crystallization of the metastable compound, $FeSb_3$ from an amorphous intermediate.[109,110]

PDF and difference PDF were also used to examine other solid state reactions.[111–113] While these experiments show the promise of using total scattering investigations to follow solid state reactions, there remain significant experimental challenges. The most significant are the subtraction of background scattering and the lack of a method to analyze total scattering from samples that are textured.

I.6.2 In-situ studies

Time and temperature dependent in situ studies of reactions by NMR, thermal analysis, diffraction techniques, EXAFS and different spectroscopies have played an important role in unravelling reaction pathways in both molecular and solid synthesis, often discovering new compounds formed as intermediates during the transformation of reactants into the final products.[30,114–116] Advances in detectors, enhanced intensity and energy resolution of synchrotron facilities and advances in analysis software packages provide new opportunities to rapidly obtain and analyze data obtained during reactions. Simultaneously using multiple probes during in-situ and operando investigations is becoming increasingly common, as the additional constraints imposed by the different techniques eliminate possible interpretations of the data.[30] It is important to recognize that different techniques may be looking at different parts of the sample, for example x-ray techniques may probe the entire sample volume while spectroscopies based on lower energy radiation may probe mainly the surface of the sample. Continued development of experimental configurations that permit simultaneous measurements via multiple techniques will provide insights to the key transformations that lead to the formation of targeted compounds.

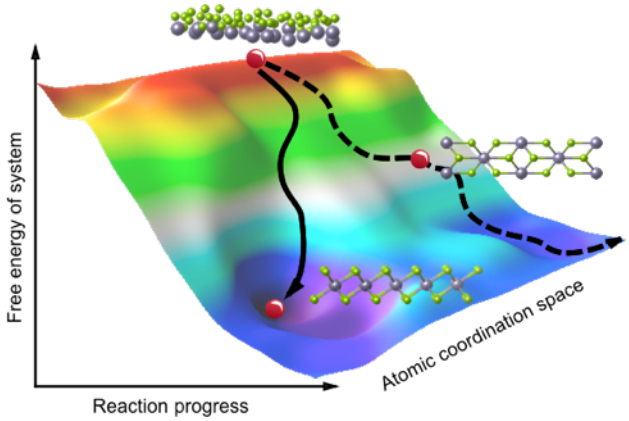

Figure I.34. Local minima within the energy landscape of an Sn|Se|V|Se precursor can be determined by constraining Sn and Se atoms between layers of VSe_2. Calculations demonstrate that the formation of CdI_2-structured $SnSe_2$ is favored while $MoSi_2$-structured $SnSe_2$ is not.

In parallel with these experimental probes, theoretical efforts are beginning to probe aspects of the energy landscape to provide guidance to synthetic efforts. The pioneering work of Schon and Jensen, combining experimental investigations of amorphous precursors with theoretical modeling of the evolution of atoms placed in unit cells with arbitrary configurations, illustrates the challenges and the promise of pairing theory and experiment.[9] More recently Rudin has proposed a model to mimic the evolution of modulated elemental layer precursors, exploring the stability of islands constrained between crystalline layers.[117] This method determines what atomic configurations are local minima in the energy landscape (Figure I.34). New models for nucleation and growth via agglomeration are providing insights to solution phase growth. As more in-situ data is published additional ideas will be created.

I.6.3 EDX and other STEM techniques

The continued development of electron microscopy techniques with enhanced capabilities combined with the advances in the ability to prepare cross sectioned samples from chosen locations via focused ion beam approaches is providing unprecedented information about structure and composition on a sub Ångstrom scale. Resolution of better than 0.5Å can be reached on modern aberration correction scanning transmission electron microscopes.[118] Increased energy resolution in electron energy loss spectroscopy enable measurements of small energy differences caused by local structure and even measurements of phonon spectra.[119] Coincident electron, ion and optical beams in plasma assisted dual beam focused ion beam instruments provide unprecedented ability to prepare cross sections from bulk samples quickly and efficiently with minimum damage from the focused beams.[120] Clever liquid flow and electrochemical cells enable in situ investigations of chemical reactions such as the nucleation and growth of precipitates or electrochemical intercalation/deintercalation.[121,122] Enhanced detectors enable the determination of local composition using energy dispersed fluorescence measurements of atoms excited by the electron beam with increased sensitivity.[123] These advances create opportunities to reexamine systems studied in the 1970's and 80's, probing the evolution of structure and composition at reacting interfaces. This will provide new insights on the development of composition gradients and nucleation of compounds at reacting interfaces. The information about local structure and composition will be very useful to develop models for complementary experiments that probe larger sample volumes, such as x-ray diffraction experiments.

I.7 Conclusions

The next decade promises to yield a much greater understanding of the energy landscape involved in the synthesis of compounds due to advances in experimental techniques and theory. The need to integrate new materials into devices will further increase the push to understand how processing conditions impact reaction mechanisms and rates. We anticipate a new era of solid state synthesis, inspired in part by physical preparation of precisely layered solids via the "scotch tape approach", the continued expansion of new operando approaches to following solid state reactions, and new analytical techniques to probe reacting condensed phase systems. This will have a dramatic impact on the rate of discovery of new materials, and increase the importance of theoretical approaches to discover synthesizable materials with properties of technological or practical importance.

I.8 Dissertation Overview

The introduction highlights a widely underappreciated aspect of solid state synthesis: the reaction mechanism. This dissertation focuses on developing tools and concepts designed to understand how modulated elemental reactants self-assemble to form ferecrystalline structures with the goal of rational synthesis in mind. More specifically, it emphasizes the role of the precursor in defining the energy landscape of a potential compound. Chapter II discusses important structural, compositional, and physical characterization techniques utilized throughout this dissertation. A large section of this chapter is dedicated to a new method of XRF metrology the group has developed that is a groundbreaking innovation in thin film synthesis. This is based on published work that is

done in collaboration with Danielle M. Hamman, Dylan Bardgett, Liese A. Maynard, Dr. Erik C. Hadland, Alexander C. Lygo, Dr. Suzannah R. Wood, Dr. Marco Esters, and Dr. David C. Johnson. Experimental work on dropcast calibration was done in collaboration with Sarah Chu, Dylan Galutera, and Jack Congel. Chapter III talks about the strong interaction between PbSe and VSe_2 and the development of a test for the feasibility of two constituents as misfit layer compounds. This work was published in collaboration with Shannon S. Fender, Taryn M. Kam, Yu Hsin Tsai, and Dr. David C. Johnson.

Chapter IV expands on Chapter III and describes the synthesis and characterization of $[(PbSe)_{1+\delta}]_m(VSe_2)_1$ compounds with charge density waves published in collaboration with Shannon S. Fender, Taryn M. Kam, Robert Fischer, Johann Seyd, Dr. Manfred Albrecht, and Dr. David C. Johnson. Chapter V expands on Chapters III and IV by demonstrating the limit of the strength of the interaction between PbSe and VSe_2. The work describes the instability of monolayer thick PbSe on VSe_2 using $[(PbSe)_{1+\delta}]_q(VSe_2)_1$ heterostructures where q is the number of PbSe monolayers and equal to 1 to 11. This chapter was written in collaboration with Mina Buchanan, Taryn M. Kam, Shannon S. Fender, Renae F. Gannon, Robert Fischer, Dr. Benjamin Hanken, Dr. Mark Asta, and Dr. David C. Johnson. Finally, Chapter VI demonstrates the use of a reaction monitoring based on XRR and XRD to track lateral and perpendicular film growth in order to study reeaction mechanisms. It also highlights how precise control over precursor composition and nanoarchitecture can direct the formation of $[(SnSe_2)_{1+\delta}]_1(VSe_2)_1$ over a thermodynamically stable compound, $[(SnSe)_{1+\delta}]_1(VSe_2)_1$ and the uncovering a reaction pathway towards a new alloy, $Sn_xV_{1-x}Se_2$. This chapter was written in collaboration with Taryn M. Kam, Renae F. Gannon, Robert Fischer, and Dr. David C. Johnson.

Overall this dissertation attempts to address a long-standing problem in solid state chemistry: the reliance on serendipity to control a solid state reaction. Here, we provide a systematic approach on how to drive a MER reaction towards a specific pathway in its energy landscape by precisely controlling the number of atoms and the nanoarchitecture in the multilayer precursor. The ability to control these two parameters also allow mechanistic aspects of the synthesis method to be unmasked.

CHAPTER II

STRUCTURCAL, COMPOSITIONAL, AND ELECTRICAL CHARACTERIZATION TECHNIQUES

Authorship Statement

Parts of Section 2 were based a paper published in Chemistry of Materials, volume 30, issue 18, pp. 6209-6216. This work was done in collaboration with Danielle Hamann (as first author), Dylan Bardgett, Liese Maynard, Dr. Erik C. Hadland, Alexander C. Lygo, Dr. Suzannah R. Wood, and Dr. Marco Esters. Dropcast calibration section of Section 2 is based on unpublished data from experimental work done in collaboration with Sarah Chu, Dylan Galutera, and Jack Congel. Dr. David C. Johnson is my advisor and was consulted in the preparation of this chapter.

II.1 Structural Characterization via X-ray Diffraction

In solid state synthesis, structure determination plays a crucial role in developing new materials with novel functionalities. The products of solid state chemistry are distinctly different from molecular chemistry - they contain different structural features that are essential in structure determination. In molecular/organic chemistry, molecules are an assembly of atoms linked together in a specific manner via bonds. The way they are connected to each other defines the structure. Molecular chemists rely on methods like mass spectrometry (MS), infrared spectroscopy (IR), and nuclear magnetic resonance (NMR) techniques to determine the identity and number of elements, the type of bonds, and the connectivity of the bonds. Each piece of information from the various methods mentioned serves as a puzzle piece to the overall structure. The way the structure of solids are elucidated also fits this puzzle analogy. The extended structure of solids can be

conceptualized as an assembly or collection of coherent atomic planes with various orientations. How these atomic planes orient with each other dictates what the overall structure is. Solid state structure of powders and thin films is typically elucidated by studying how a material interacts, or more specifically, diffracts incident x-rays. This section is dedicated to discussing the various x-ray diffraction (XRD) techniques applied to the structure elucidation of thin films.

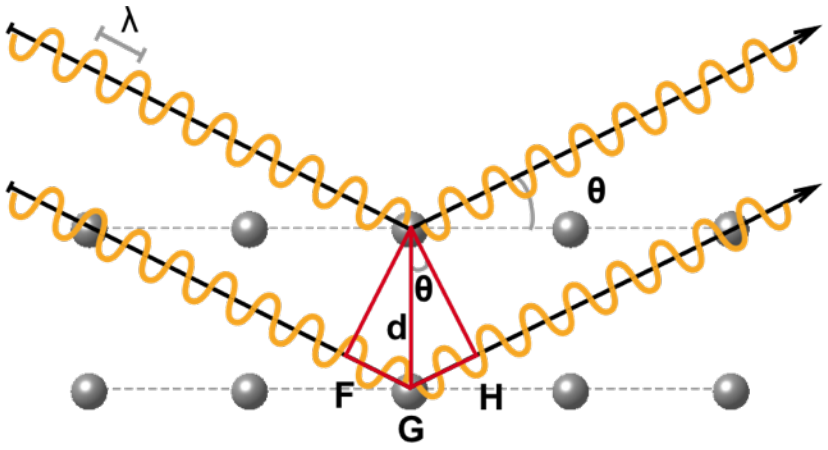

Figure II.1. Schematic of an atomic lattice describing the conditions required for Bragg's law.

Bragg's law is a mathematical equation that relates interplanar spacings with the relative directions of incident and scattered radiation.[1] It is the quantitative basis of structural characterization via x-ray diffraction. Consider a set of parallel planes that consists of arrays of atoms shown in Figure II1. Each plane is separated by a perpendicular distance of d and the system is irradiated by x-rays at a glancing angle, θ. When atoms are irradiated with x-rays, the electron cloud oscillates such that electromagnetic waves with the same frequency as the incident radiation is re-emitted (elastic scattering). Scattered

radiation is emitted in all directions and can interact with each other to produce interference phenomena.

Figure II.1 illustrates the conditions required for constructive interference. When atoms from two adjacent planes scatter simultaneously, two x-ray beams with the same wavelength are produced. The x-ray radiation can either interfere constructively or destructively depending on the path difference between the two. If the path difference, shown as the segment FGH, is equal to $n\lambda$, where n is an integer and called the diffraction order, the waves will interfere constructively. Mathematically, the segment FGH is can be expressed in terms of the incident angle, θ, and the interplanar spacing, d.

$$FGH = 2d \sin \theta$$

$$n\lambda = 2d \sin \theta \quad \text{"Bragg's Law"} \qquad \text{Equation II.1}$$

d = interplanar spacing

θ = angle of Bragg peak

n = diffraction order

λ = wavelength of incident radiation

When Bragg's law is satisfied, there is constructive interference and high intensity is observed at the incident angle. If Bragg's law is not satisfied, there is destructive interference and no intensity observed at the incident angle. X-ray diffraction experiments are performed by irradiating a sample with x-rays at different incident angles and collecting intensity information from the angular scans.

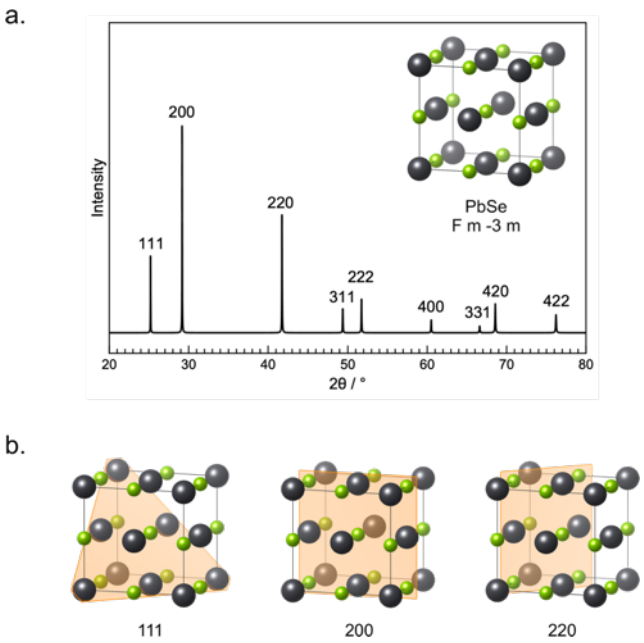

Figure II.2. (a) A simulated x-ray diffraction pattern of powder PbSe. (b) Atomic planes and their Miller indices represented in the simulated x-ray diffraction pattern.

A simple x-ray diffraction experiment can be performed on powdered samples. A simulated diffraction pattern of powdered PbSe is shown in Figure II.2a. Reflections (peaks) can be observed at specific angles where Bragg's Law is satisfied and each peak can be correlated to atomic planes that can be observed in the PbSe crystal structure (inset of Figure II2a). These atomic planes can be defined by their Miller indices (hkl). For every crystal structure, there are a specific set of atomic planes that lead to constructive interference of the incident beam. A crystal structure can be elucidated by analyzing the observed peaks, correlating them to the Miller indices of the atomic planes, and constructing the crystal structure from that information. For PbSe, the only allowed reflections by the structure are those with Miller indices where h, k, and l are either all even or all odd. Models for some of the atomic planes elucidated from powdered PbSe are shown in Figure II.2b. Other rules apply to different structures. One can refer to any standard solid

state chemistry text for more information on Miller indices and allowed reflections of different crystal structures.

Thin films synthesized via modulated elemental reactants (MER) require more specialized x-ray diffraction experiments to account for the preferred alignment. MER thin films exhibit crystallographic alignment parallel to the substrate and turbostratic disorder.[2] The turbostratic disorder does not permit any atomic planes with an x, y, and z component to be present, so *hkl* reflections cannot be observed. Because of this orientation constraint, there is order in the x-y plane that is independent of the order in the z-axis. To account for this, two x-ray diffraction geometries are used to probe independent crystallinity in the x-y plane and the z-axis. To probe order in the z-axis, specular geometry is used. To probe order in the x-y plane, grazing incidence in-plane geometry is utilized. The combination of these two methods permits the structural characterization of MER thin films.

Specular x-ray diffraction and x-ray reflectivity are executed using the same configuration and are used to probe crystallinity in the z-axis direction of MER thin films. For specular x-ray diffraction and x-ray reflectivity experiments, a locked coupled θ-2θ scan is collected. In this experiment, the sample moves simultaneously with the detector such that the detector angle, 2θ, is always twice the incident angle, θ. With this configuration, only planes that are parallel to the substrate are probed. The magnitude of the order that can be probed can be controlled by modifying the angular range used in this experiment. X-ray reflectivity data is collected over a small angular range (0-15° 2θ) and provides information on the overall structure of the entirety of the film. Specular x-ray diffraction data is collected over a large angular range (5-70° 2θ) and provides more well-resolved information on the atomic positions in the z-direction.

II.1.1 X-ray Reflectivity

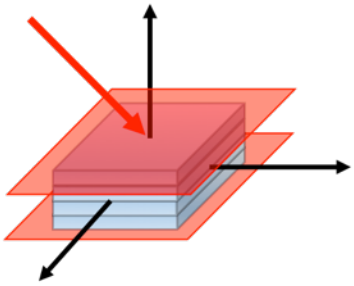

Figure II.3. Schematic of the geometry for x-ray reflectivity.

An x-ray reflectivity experiment follows Bragg's law, however, the reflected x-rays come from the top and bottom of the entirety of the film (Figure II.3). To maximize the information that can be gathered from x-ray reflectivity data, a film with reasonable smoothness is required. The constructive and destructive interference of the reflected x-rays from the film causes oscillations in the x-ray reflectivity patterns called Kiessig fringes.[3] These oscillations can be used to determine the period or the thickness of the film by using a modified form of Bragg's law that includes critical angle of the film. Bragg's law needs to be modified at low angles to account for the difference between the index of refraction occurring at the interface due to Snell's law.[4]

$$m\lambda = 2t\,[\sin^2(\theta_i) - \sin^2(\theta_f)]^{1/2} \qquad \text{Equation II.2}$$

Modified Bragg's Law

t = film thickness

θ_i = angle of Kiessig fringe

θ_f = critical angle

m = Kiessig fringe index

λ = wavelength of radiation

Kiessig fringes provide valuable information on the thickness uniformity or the "smoothness" of a film. Generally, the higher the angle the Keissig fringes extend to, the smoother the film. Quantitatively, the thickness uniformity (Δt) or smoothness of a thin film is described by Parrat's equation.[5]

$$\Delta t = \lambda/[4(\theta_n - \theta_c)]^{1/2} \qquad \text{Equation II.3}$$

Parrat's Equation

λ = wavelength of incident radiation

θ_n = angle of last Kiessig fringe

θ_c = critical angle

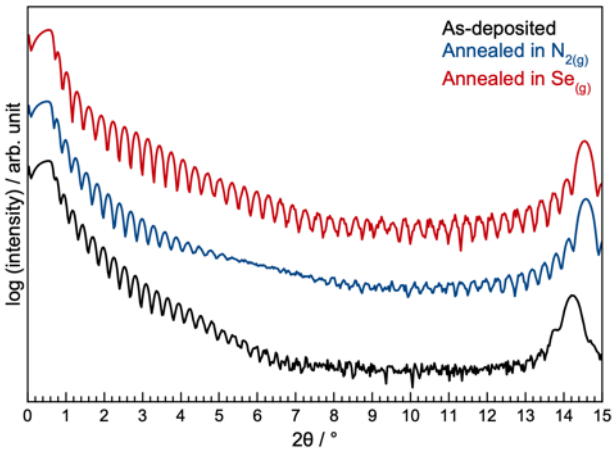

Figure II.4. X-ray reflectivity patterns of V|Se precursors annealed in different conditions demonstrating changes in film structures during self-assembly.

XRR patterns of VSe_2 films annealed in different conditions are shown in Figure II.4. There are clear changes in the thickness and smoothness of the film as the precursor is annealed. Annealing increases the smoothness of the film, apparent from the appearance of Kiessig fringes close to 15°. The increase in the period of the Kiessig fringe suggests that the film also decreases in thickness as it is annealed. This demonstrates how XRR can be used both qualitatively and quantitatively to describe MER thin films.

II.1.2 Specular X-ray Diffraction

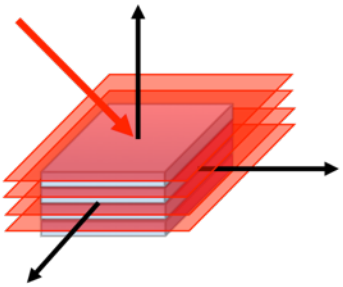

Figure II.5. Schematic of the geometry for specular x-ray diffraction.

A specular/out-of-plane x-ray diffraction experiment follows Bragg's law, but only planes that are parallel to the substrate are examined (Figure II.5). This configuration is especially suitable for MER films that have preferred alignment to the *001* plane.[6] In a specular x-ray diffraction pattern of MER films, only Bragg peaks of type 00*l* can be observed. Atomic planes that have an x or y component will not be parallel to the surface. The c-lattice parameter can be calculated from the interplanar spacing, calculated via Bragg's law. Since this experiment treats the film as a one-dimensional system, the c-lattice parameter and interplanar spacing are related through the following expression.

$$1/d^2 = l^2/c^2 \qquad \text{Equation II.4}$$

d = interplanar spacing

l = z-axis Miller index

c = c-lattice parameter

An example of a specular pattern of VSe_2 is shown in Figure II.6. Some of the reflections that are normally allowed in randomly oriented (powder) VSe_2 is not observed in the specular pattern. This is a result of a specular scan selectively enhancing the 00*l* reflections because of the experiment geometry.

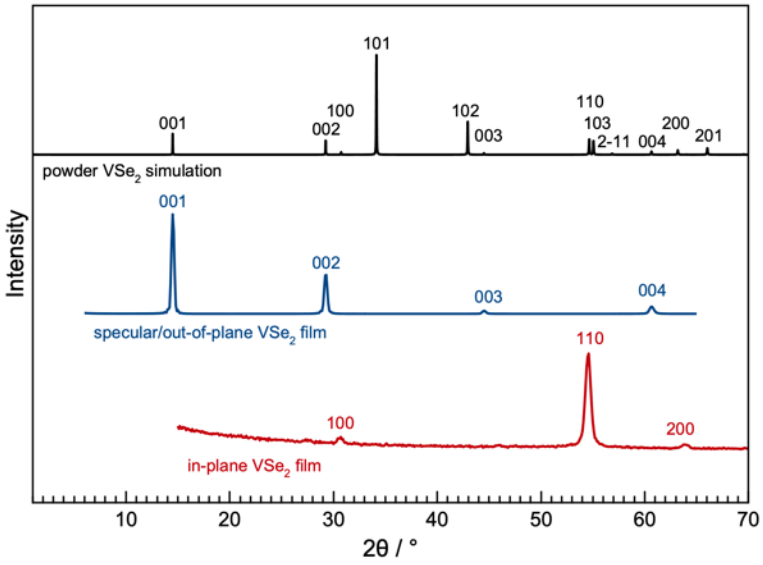

Figure II.6. X-ray diffraction patterns of VSe_2 with various orientations. (red) powder simulation, (blue) specular MER film, (red) in-plane MER film.

II.1.3 Grazing Incidence In-plane X-ray Diffraction

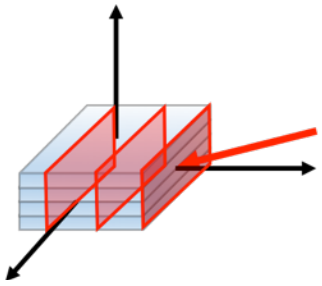

Figure II.7. Schematic of the geometry for grazing incidence in-plane x-ray diffraction.

Similar to specular diffraction experiments, in-plane x-ray diffraction is performed with a geometry that constrains what structural features can be probed. In this configuration the detector is positioned in the plane of the thin film sample, while the incident x-ray is set at a low angle (Figure II.7). Only planes that are perpendicular to the surface are probed, so only *hk*0 Bragg peaks can be observed.[7] This type of analysis is particularly useful for MER films since it can determine the different 2D constituents of a heterostructure that

diffract independently.[6] An example of an in-plane x-ray diffraction pattern of VSe_2 is also shown in Figure II.6. Bragg's law can be used to show that the VSe_2 film consists of a hexagonal basal plane based on the reflections present. This experiment is particularly powerful in the analysis of MER heterostructures, where it has been demonstrated to resolve up to 3 different xy lattices.[8]

II.2 X-ray Fluorescence

Controlling composition plays a vital part in conventional solid state synthesis. Starting materials are carefully weighed out and combined to match the composition of the desired product. In MER synthesis, however, the actual number of atoms deposited is a more important factor and more useful metric compared to the composition of the precursor. X-ray fluorescence (XRF) is used to determine the number of atoms per unit area in a thin film. In a typical XRF setup (Figure II.8), the sample is initially irradiated with high energy x-rays to knock off electrons in its inner shell, generating a hole. An electron from a higher energy level, relaxes and occupies the generated hole. During this transition, energy is released in the form of x-ray radiation. The energy of these fluorescent

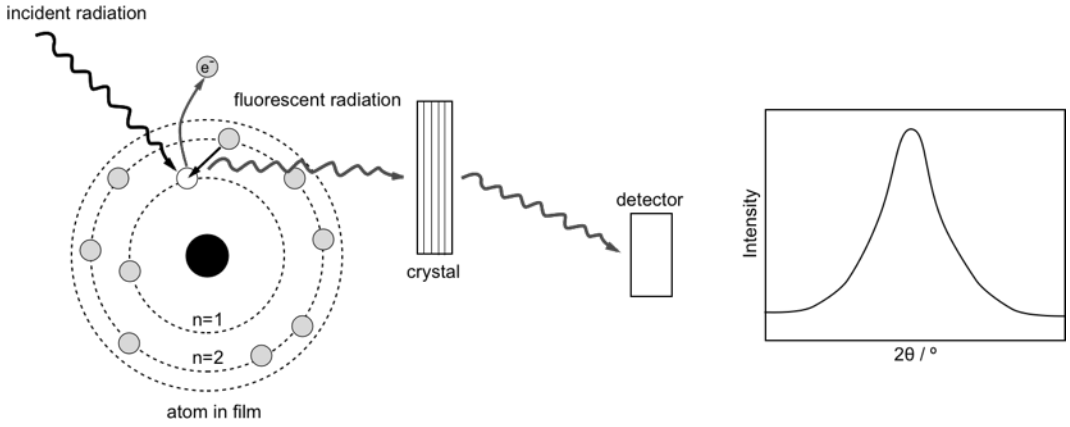

Figure II.8. Schematic of x-ray fluorescence analysis.

x-rays is related to the atomic number of the elements in the sample. Fluorescent x-rays are resolved using analyzer crystals with fixed d-spacings to yield an x-ray diffraction pattern. The peak angle and the d-spacing of the analyzer crystal is used to determine the wavelength and energy of the fluorescent x-rays. This is the mechanism by which elements can be identified using XRF.[9]

II.2.1 X-ray Fluorescence Analysis of Thin Films

The intensities of the fluorescent x-rays are related to the number of atoms of each element in the sample (Figure II.9). This correlation is difficult to apply to bulk samples because the large volumes involved make it prone to re-absorption, hence, not all fluorescent x-rays from the sample may reach the detector. However, it has been determined that there is a linear relationship between the amount of material present and intensity for thin film samples by assuming there is no re-absorption. Mathematically, the XRF intensity is dependent on several factors.

$$I_{ij} = \{K_j(\lambda_s)C_i/\mu_T(\lambda_{ij})\}\{1-\exp[-\mu_T(\lambda_{ij})\rho d]\} \qquad \text{Equation II.5}$$

Iij = XRF intensity from specific line, j, or element, i

C_i = mass fraction of element i in film

λ_{ij} = wavelength

ρ = average film density

d = film thickness

$\mu_T(\lambda_{ij})$ = total mass absorption coefficient at λ_{ij}

$K_j(\lambda_s)$ = product of constants related to experiment

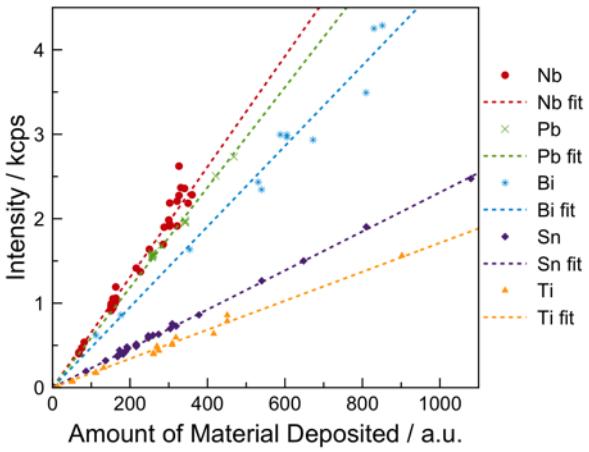

Figure II.9. The linear relationship of amount of material deposited and intensity for different elements deposited on Si substrate. All linear fits pass through zero.

For very thin films, the term $\mu_T(\lambda_{ij})\rho d$ becomes small and the expression can be simplified to,

$$I_{ij} = K_j(\lambda_s)C_i\rho d \qquad \text{Equation II.6}$$

at low thickness regimes. In this more simple form, the XRF intensity is only directly proportional to $C_i\rho d$, which is the number of atoms of element i per unit area of the film that is probed. This equation typically applies to films that are less than 100 nm in thickness.[10]

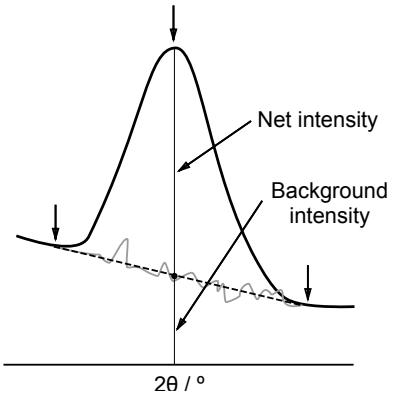

Figure II.10. Background correction (dashed line) using pre-installed software.

The XRF measurement of thin films deals with intensities that are very low in magnitude, making the analysis extremely sensitive to background effects. Programmed background correction pre-installed in XRF instruments are not completely adequate for very thin films because it assumes a functional background form. For example, one method defines the background by connecting a two points at the shoulder of an XRF peak and measures the net intensity for analysis (Figure II.10).

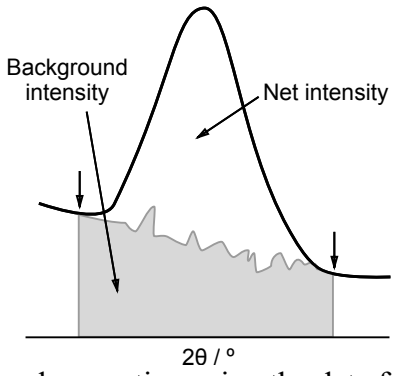

Figure II.11. Manual background correction using the data from a blank substrate.

In reality, XRF backgrounds are more complicated, schematically shown in Figure II11. To account for the true background, a blank substrate must be analyzed alongside the actual sample. To increase the magnitude of the signal, the integrated area under the curves are measured instead of intensity at one specific point. Subtracting the measured integrated intensity of the background from the sample provides a more representative measurement. This type of XRF analysis and background correction has proven useful for investigating elements that yield low magnitude signals.[10]

II.2.2 X-ray Fluorescence Calibration Methods

Two methods have been developed to construct calibration curves for XRF analysis of elements. Each method relies on depositing a known amount of material within the analytical area of a substrate. The first method requires the synthesis of thin films of heterostructures or dichalcogenides that are well-characterized with XRR, specular XRD, and in-plane XRD. The calibration samples must have a known phase (with known stoichiometry), known number of layers and basal plane area. Information from x-ray diffraction data is used to calculate the number of atoms per unit area of each element in a calibration sample. The total number of atoms per unit area (area density, AD) of an element, i, can be calculated via the equation,

$$AD_i = r * (Z/A_{ip}) \qquad \text{Equation II.7}$$

r = number of layers/repeating units in the film

Z = number of atoms of each element in unit cell

A_{ip} = basal plane area

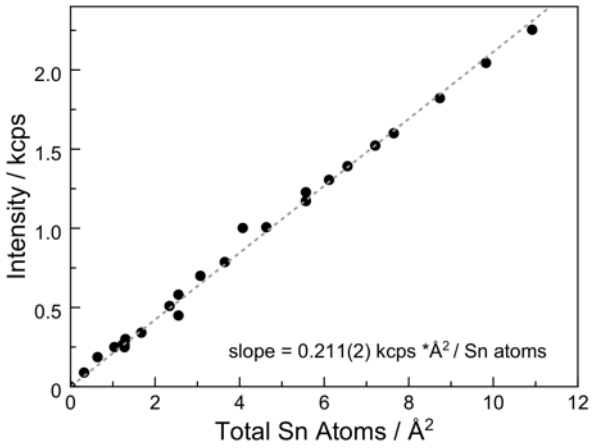

Figure II.12. The linear relationship between the total number of Sn atoms per square Angstrom and background corrected integrated intensity.

There will be a linear relationship between the area density of the films and intensity (Figure II.12) as long as the films do not pass the thickness threshold and the analytical area remains constant.[10]

A second, more convenient method was developed if well-characterized thin films are not available. Dropcast film samples were used to construct the calibration curve. These samples were made by drop casting a very small volume of a salt solution with known concentration containing the element of interest on the analytical area of the substrate. The number atoms per unit area can be calculated from the moles of salt deposited and the analytical area.

A representative calibration curve for Pb is shown in Figure II.13. There is only a 10% difference in the slope derived from dropcast samples and thin film samples (Figure II13). Replicate calibration points from dropcast samples have a large spread presumably due to the non-uniformity of the films. Table II.1 shows the proportionality constants obtained from different elements.

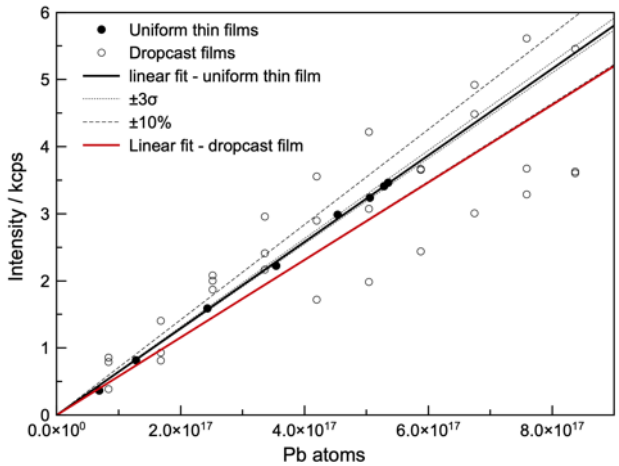

Figure II.13. Calibration curve for Pb obtained using thin film and dropcast samples. The linear fits for both methods agree with each other with 10% error.

Table II.1. Comparison of the proportionality constants of different elements

Element	Slope (kcps/atom)		Slope (kcps/atom per square Angstrom)	
	Dropcast	Uniform thin film	Dropcast	Uniform thin film
Pb	$5.8(3) \times 10^{-17}$	$6.45(4) \times 10^{-17}$	0.454	0.507(3)
Cu	$1.23(2) \times 10^{-17}$		0.0966	
Cr	$3.6(1) \times 10^{-18}$		0.0283	

X-ray fluorescence is a versatile and valuable tool in MER synthesis as a way to determine if precursors have the correct number of atoms. Additionally, it can also be used to optimized deposition conditions. Routine analysis of thickness-normalized XRF intensities informs one about the behavior of the deposition and make appropriate adjustments as necessary. XRF monitoring serves as a guide to establishing more reproducible depositions, which is the key to concise synthesis.

II.3 Electrical Transport Measurements

Thin films have found a place in modern technology as a means to enhance the properties of solid interfaces.[11] Electronic devices contain thin films with different properties that enable control over current flow through a system. Two important properties of thin films that dictates their use in electronics are resistivity and carrier density. Resistivity is related to how well a material permits a current flow and the carrier density is the number of charge carriers normalized to the volume.[12]

II.3.1 Van der Pauw Method for Measuring Resistivity

A simple method of obtaining resistivity is by running a current across a bar of material through two contacts and measuring the resulting voltage. However, a two-point probe measurement can have large contribution from contact resistance.[13] A four-point probe measurement like the van der Pauw method permits the resistivity to be collected from a lamella of arbitrary shape without significant influence from contact resistance.[14] Thin film materials can be analyzed using the van der Paw method if the following conditions are met:

1. The thin film is uniform in thickness and free of holes.
2. The contacts are small.
3. The contacts are at the edges of the sample.

For the MER samples discussed in this work, the thin films were deposited to form a highly symmetric cross-shaped lamella and indium contacts were pressed onto the four vertices (FigureII.14).

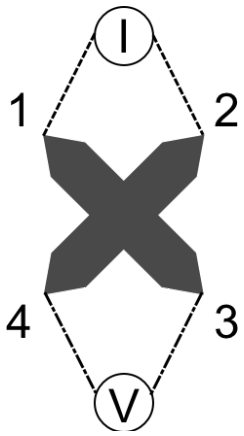

Figure II.14. Thin film sample shape, and current and voltage contact configuration for a van der Pauw resistivity measurement.

To measure resistivity, a current is sourced through two adjacent contacts (e.g. 1 to

2, I_{12}) while the generated voltage is measured across the other two adjacent contacts (e.g. 3 to 4, $R_{34,12}$). The resistivity is related to the current and voltage through the equation,

$$\rho = (\pi t/\ln 2)R_{34,12.} \qquad \text{Equation II.8}$$

t = film thickness

R = measured voltage

There are four different ways to connect the contacts and 8 different combinations to source a current and measure a resistance. Because the shape of the lamella is symmetric, the calculated resistivity should not change when the connections are changed. For example, the horizontal line of symmetry indicates that $R_{34,12} = R_{21,43}$. If the ratio $R_{34,12}/R_{21,43}$ is not unity because of asymmetry in contact placement, a geometry factor, f, must be considered.

$$\rho = \frac{\pi t}{\ln(2)} \frac{R_{34,12}+R_{21,43}}{2} f \qquad \text{Equation II.9}$$

The geometry factor is a function of $R_{34,12}/R_{21,43}$.

II.3.2 Van der Pauw Method for Measuring Carrier Density

The carrier density, n, is an important thin film property that can be calculated from the Hall coefficient (R_H), which can also be obtained using a van der Pauw experiment.[14] The sign of the Hall coefficient is dependent on the type of carrier present, negative for electrons and positive for holes. Carrier densities can be calculated from the Hall coefficient using the equation,

$$R_H = -1/qn \text{ (electrons)} \qquad \text{Equation II.10}$$

$$R_H = 1/qp \text{ (holes)} \qquad \text{Equation II.11}$$

n = carrier (electron) density OR p = carrier (hole) density

q = charge.

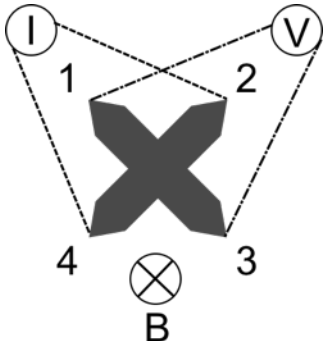

Figure II.15. Thin film sample shape, and current and voltage contact configuration for a van der Pauw carrier density measurement.

To measure the Hall coefficient (Figure II.15), a magnetic field normal to the sample is applied, then, a current is sourced across two opposite contacts (e.g. 2 to 4, I_{24}) and the voltage is measured across the other two opposite contacts (e.g. $R_{1,3}$). The measured voltage, called the Hall voltage, is a result of the deflection of electrons from a Lorenz force. The Hall voltage (V_H) is shown mathematically as,

$$V_H = R_H B \frac{I}{t} \qquad \text{Equation II.12}$$

B = applied magnetic field

t = thickness

In this work, a constant current was sourced across a sample and the voltage was measured while the magnetic field is varied. The slope of the best fit line of the V_H vs BI/t data gives the calculated Hall coefficient.

CHAPTER III

STRONG NON-EPITAXIAL INTERACTION: CRYSTALLOGRAPHICALLY ALIGNED PbSe ON VSe_2

Authorship Statement

This chapter was published in Physica Status Solidi A: Applications and Materials Science, volume 2019, page 1800896. I am the primary author of this work. Taryn Kam, Shannon Fender, and Yu Hsin Tsai assisted with analysis of x-ray diffraction and x-ray fluorescence data. Dr. David C. Johnson is my advisor and group leader, consulted in preparation of the manuscript.

III.1 Introduction

The number of known ternary and multinary compounds is much less than expected.[1] There are many ternary systems that do not contain any known ternary compounds. Traditional solid-state synthesis techniques that directly react elements or mixes of elements and binary compounds evolve through complex mixtures of elements, binary compounds and/or ternary compounds as diffusion occurs. The search for new compounds is often difficult, because only trace amounts of a new compound are formed using the initial reaction conditions. Potential new compounds are found by identifying reflections in diffraction patterns of mixtures that cannot be explained by known phases. Reaction conditions are then modified to increase the amount of the new compound. For a new ternary or multinary compound to be the primary product in this reaction after long times at high temperatures, they need to be more stable than any of the intermediate mixtures. Other approaches have been developed that use a fluid phase to increase diffusion

rates and make nucleation the rate-limiting step in the synthesis (flux-based growth techniques, vapor phase transport, molecular beam epitaxy, etc.). While there has been recent progress in understanding the speciation in fluids that control product formation, serendipity controls what forms.[2] The reacting systems are more complicated and there is little fundamental understanding of how to adjust the composition of the system to change speciation and impact which compound nucleates.

In an attempt to increase the rate of discovery of new materials, a variety of high throughput methods have been developed in projects such as the Materials Genome Initiative.[3–5] Typically these methods combine information in databases and computational approaches to predict the stability and properties of materials that have yet to be synthesized in the lab. Unfortunately, attempted syntheses of many of the new compounds that have been predicted to be stable have failed. For example, a recent paper predicted 24 likely new compounds in phase diagrams that did not contain any known ternary compounds.[6] The authors tried to prepare these predicted compounds, containing a cation, a transition metal and a chalcogen, using several synthesis approaches. The products of the reactions were mixes of known binary compounds and the elements. While the predicted compounds are potential local free energy minima in the energy landscape based on the calculations, the synthetic protocols used could not prevent the formation of binary compounds as reaction intermediates. In three systems, a compound forms with a stoichiometry close to that of a predicted compound, but the structure that forms is a misfit layer compound rather than the predicted structure. Calculating the formation energy of misfit layer compounds is challenging due to the incommensurate interface between the constituents. The surprising thermodynamic stability of misfit layer structures has long

puzzled researchers.[7] Misfit layer structures consist of two interwoven lattices that are commensurately stacked along the crystallographic *c* axis. A common pairing of structures is a transition metal dichalcogenide such as $NbSe_2$ with a rock salt structured layer such as PbSe.[8] In the *a-b* plane, there is a size mismatch between the constituents and often a symmetry difference that results in an incommensurate relationship between the constituent layers. The atoms at the interface in each layer are displaced from their average position due to the interaction with the atoms of the other layer. This results in a structurally incoherent interface between the two layers. Given the varying and irregular local coordination environment between the atoms at the interface that results from the structural incoherence, one would expect that a mix of the binary compounds (for example $NbSe_2$ + PbSe) to be more stable than the misfit layered compound $(PbSe)_{1.14}NbSe_2$, which contains alternating planes of the dichalcogenide trilayer (Se-Nb-Se) with bilayers of PbSe. The misfit compound $(PbSe)_{1.14}NbSe_2$, however, is the product that is formed on heating a stoichiometric mix of the elements at 1000°C for an extended time.[9] This indicates that the interaction between the PbSe and $NbSe_2$ at the interface must be stronger than the sum of the interactions between $NbSe_2$ layers in $NbSe_2$ and between (001) planes of PbSe.

There have been several explanations presented in the literature for the surprising stability of misfit layer compounds. While van der Waals forces certainly exist between the two structures, the interaction between the layers needs to be much stronger. For misfit layer compounds containing trivalent cations such as rare earth metals in the rock salt layer, there is abundant evidence that there is electron transfer from the rock salt layer to the dichalcogenide. Such charge transfer would result in a strong enough ionic interaction between the layers $(LnX)_{1+d}^{\delta+}(TX_2)^{\delta-}$ to stabilize the misfit layer structure.[8,10] There is

significant controversy in the literature, however, about whether charge transfer occurs in misfit layer compounds containing a semiconducting divalent rock salt structure (such as SnX or PbX where X = S or Se) paired with a transition metal dichalcogenide. Ohno performed x-ray photoemission, x-ray absorption and reflection electron energy loss spectroscopy on misfit layer compounds containing alternating layers of PbS and TiS_2 and SnS and NbS_2. He concluded that a small amount of charge transfer occurs from the rock salt layer to the dichalcogenide.[11] A subsequent photoelectron spectroscopy study of the misfit compounds $(MS)_{1+d}(TS_2)$ where M = Sn and Pb and T = Ti, Nb and Ta indicated that there was no, or only a very small amount of charge transfer and that the Pb and Sn were divalent.[12] Band structure calculations also suggest that there is no charge transfer.[13] If only a very small amount of charge transfer occurs, then the amount of ionic stabilization will be small. A subsequent study of several misfit layer compounds indicated that there was a systematic excess of the transition metal dichalcogenide cation (T) and a systematic shortfall in the rock salt cation (M). The authors suggested that T cations were substituting for M cations in the rock salt structure, resulting in layers that have high enough charges to stabilize the misfit layer structure via an ionic interaction between the constituents.[14] They also suggested that these deviations from stoichiometry are necessary to stabilize the misfit layer structure. The cross substitution of M and T cations was supported by a subsequent photoelectron spectroscopy investigation.[7]

In this work we probe the interaction between a rock salt compound, PbSe, and the surface of a dichalcogenide (VSe_2). We examine the formation and structure of PbSe, VSe_2, $(PbSe)_{1.11}VSe_2$ and PbSe on a layer of VSe_2 from precursors prepared by depositing sequences of ultrathin layers of the respective elements to form films of varying

thicknesses. The ultrathin layer thicknesses eliminate diffusion as a rate limiting step, while constraining the extent of long range diffusion because low reaction temperatures can be used. In all of the precursors, the respective crystalline compounds nucleated and grew during the deposition process. Post deposition annealing increased both crystallite size and the amount of material crystalized in all films. The PbSe precursors deposited on a SiO_2 surface formed rough films with randomly oriented PbSe crystals. The VSe_2 precursors deposited on a SiO_2 surface formed a crystallographically aligned films, with the basal plane of VSe_2 parallel to the substrate. In plane diffraction scans indicated a random rotational orientation of the VSe_2 crystallites. The precursor to the metastable misfit layer compound $[(PbSe)_{1.11}]_1(VSe_2)_1$ deposited on SiO_2 formed a crystallographically aligned film, with the basal plane of VSe_2 parallel to the substrate. In plane diffraction scans indicated a random rotational in plane orientation of both the PbSe and VSe_2. The PbSe precursor deposited on thin film of VSe_2 was also crystallographically aligned, with the (001) surface of the PbSe crystallites parallel with the basal plane of the VSe_2 substrate. This is an indication of a strong interaction between PbSe and VSe_2 at the interface. At the low reaction temperatures, it is unlikely that there is sufficient energy to exchange Pb with V cations from the VSe_2 substrate. This suggests a simple test to see if it is likely that a misfit layer compound can be formed between a new constituent and a dichalcogenide. If there is not crystallographic alignment of a proposed new constituent on a dichalcogenide, a new misfit layer compound is unlikely. If there is crystallographic alignment of a proposed new constituent on the dichalcogenide, it is much more likely that a new misfit layer compound can be formed.

III.2 Experimental

Thin film precursors consisting of elemental Pb (99.8%, Alfa Aesar), V (99.995%, Alfa Aesar), and Se (99.99%, Alfa Aesar) were deposited on silicon substrates with a native oxide layer using a low pressure (< 3 x 10^{-7} torr) physical deposition chamber. The elements were evaporated by using Thermionics 6 kW electron beam guns or custom-built Knudsen effusion cells producing a plume of atoms that deposit on the substrate. The thickness of each element deposited is controlled by opening and closing a pneumatic shutter that blocks the plume for a specific time. The deposition time is determined by the measured Angstrom thickness by a quartz crystal microbalance and custom-made LabView software. Crystallization of the films was accomplished by annealing the precursor in an inert N_2 atmosphere (O_2 < 0.8 ppm).

Out-of-plane specular diffraction and x-ray reflectivity were collected using a Bruker D8 Discover diffractometer to determine the lattice parameters and degree of crystallographic alignment of the film constituents. Grazing incidence in-plane diffraction was collected on a Rigaku Smartlab diffractometer to assess the crystallized constituents in the film. X-ray fluorescence measurements were taken using a Rigaku Primus II ZSX spectrometer to determine the elemental composition of the films.

III.3 Results and Discussion

The precursors designed to self-assemble the PbSe, VSe_2, $(PbSe)_{1.11}VSe_2$, and PbSe on a few layers of VSe_2 films were made by sequentially depositing alternating layers of either Pb and Se or V and Se. The number of M|Se pairs deposited was varied to obtain the desired total film thickness. The thickness of the Pb and Se layers in each Pb|Se pair

contained the number of atoms required to form a single rock salt structured PbSe bilayer. The thickness of the V and Se layers in each V|Se pair contained the appropriate number of atoms to form a single trilayer of VSe_2. The number of atoms of each element was calculated from the lattice parameters of PbSe[15] and VSe_2.[16] For example, the number of Pb atoms per unit area in a PbSe bilayer is given by the product of the number of Pb atoms per unit cell divided by the basal plane area of the unit cell [4 Pb atoms / 6.112 $Å^2$ = 0.107 Pb atoms $Å^{-2}$]. X-ray fluorescence analysis was used to determine the number of atoms per square Angstrom in the total film thickness.[17] Dividing the number of atoms per square Angstrom in the total film thickness by the number of layers deposited yields the average number of atoms deposited in each bilayer. We investigated what structure is formed as the precursors are deposited and how the structure evolves as the film is annealed using x-ray diffraction.

Figure III.1 contains specular x-ray diffraction data of as deposited and annealed PbSe films of various thicknesses (16, 32, and 82 layers) deposited on SiO_2. The measured number of Pb and Se atoms per bilayer in each film are given in Table III.1. In the high angle specular diffraction scans of the as deposited precursors (Figure III.1a), Bragg reflections consistent with the known rock salt structure of PbSe are observed in all of the films. This indicates that the Pb and Se atoms self-assemble during the deposition process forming PbSe. The *a*-axis lattice parameters are given in Table III.2. The degree of crystallographic alignment in the as deposited films is similar, based on the ratios of the intensities of the (111), (200) and (220) reflections. Crystallographic alignment increases as the films are annealed, with significant growth of the intensity of the (002) and (004) reflections in all of the films. In the 16 layer film the only non-00*l* reflection visible after

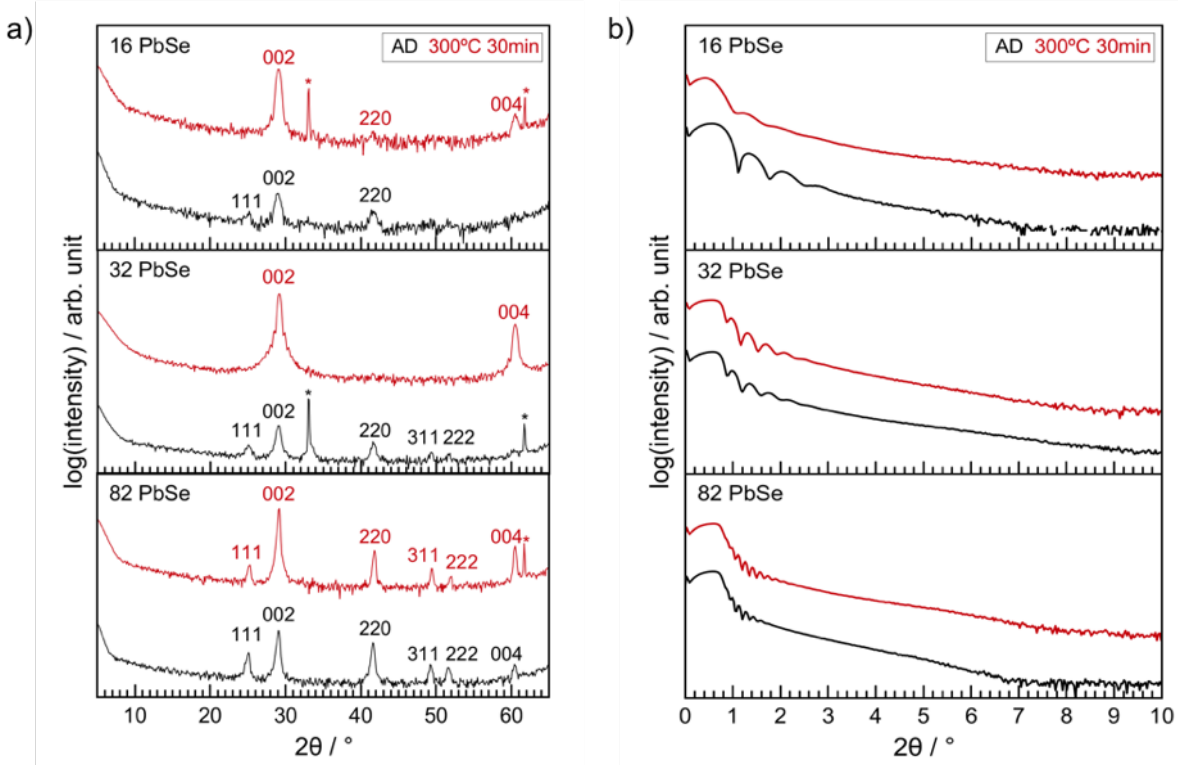

Figure III.1. (a) Specular x-ray diffraction and (b) x-ray reflectivity patterns of various thicknesses of PbSe films on SiO_2 as deposited (black) and annealed at 300°C for 30 minutes (red). The presence of non-00l reflections in the specular diffraction patterns indicate that PbSe is randomly oriented. Kiessig fringes that extend only up to ~2° suggest that the film is rough. *substrate

annealing is a weak (220) reflection. In the 82 layer film, the intensity of the (002) reflection increases 5 fold after annealing, but other non-00*l* reflections remain prominent. The x-ray reflectivity patterns of these films (Figure III.1b) suggest that the roughness increases as the film thickness increases, as the angle where Kiessig fringes are no longer resolvable decreases with increasing film thickness.[18] Table III.2 summarizes the measured lattice parameters of the three PbSe films both before and after annealing.

Table III.1. The number of Pb and Se atoms in the different PbSe precursors determined by x-ray fluorescence. The target composition to obtain a bilayer of PbSe is: Pb and Se: 0.107 atoms per Å^2

# layers Pb|Se	Pb atoms per Å^2		Se atoms per Å^2		Composition ratio (Se/Pb)
	total	per layer	total	per layer	
16	1.62	0.101	1.63	0.102	1.01
32	3.15	0.098	3.10	0.097	0.98
82	8.44	0.103	8.14	0.099	0.96

Table III.2. Lattice parameters calculated from specular x-ray diffraction patterns of PbSe on SiO_2. AD = as deposited, AN = annealed

# layers Pb|Se		a-lattice parameter [Å]
16	AD	6.08(1)
	AN	6.10(1)
32	AD	6.11(1)
	AN	6.11(1)
82	AD	6.08(1)
	AN	6.10(1)

Table III.3. The number of V and Se atoms in the different VSe_2 precursors determined by x-ray fluorescence. The target composition to obtain a trilayer of VSe_2 is: V = 0.103 atoms per Å^2 and Se = 0.205 atoms per Å^2

# layers Pb|Se	V atoms per Å^2		Se atoms per Å^2		Composition ratio (Se/Pb)
	total	per layer	total	per layer	
49	5.08	0.104	11.0	0.224	2.17
82	9.18	0.112	17.6	0.215	1.92

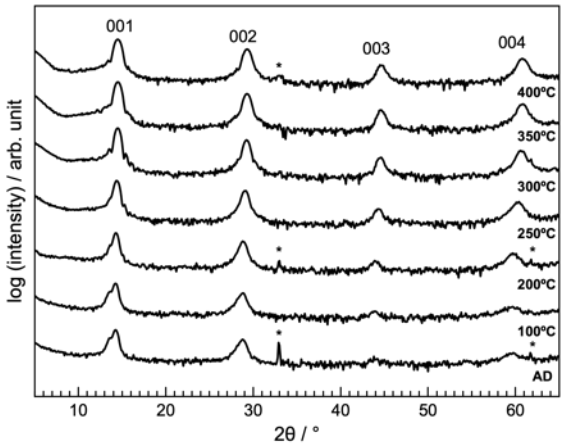

Figure III.2. Specular x-ray diffraction of representative V|Se precursors after annealing at each of the indicated temperatures for 30 minutes. The prominent 00l reflections appearing in the as deposited sample indicates that crystallographically aligned VSe_2 forms upon deposition and becomes more ordered as the film is annealed.

An annealing study was carried out on several V|Se precursors to investigate how the structure evolves as the temperature is increased. Table III.3 summarizes the amount of each element in each of the as deposited films. The slight excess of Se in one as deposited film is lost through evaporation as the sample is annealed. The specular x-ray patterns of a representative sample collected after annealing at several temperatures is shown in Figure III.2. The diffraction pattern of the as deposited precursor contains four 00*l* reflections indicating that VSe_2 self assembles during the deposition, crystallographically-aligned to the SiO_2 substrate. The (001) reflection at around 15º, however, has a shoulder at low angles from the artificial layering of the precursor. This suggests that only part of the film has formed VSe_2. As the annealing temperature increases, the intensity of this low angle shoulder decreases while the 00*l* reflections become more intense and have narrower line widths. The increased intensity suggests that more of the film becomes VSe_2 and/or the VSe_2 is becoming more crystallographically-aligned to the substrate. The decreasing line widths indicate that the structural coherence of the VSe_2 perpendicular to the substrate is

increasing. At 300°C Laue fringes were observed on either side of the (001) reflection of the thinner sample due to the finite number of unit cells, suggesting a uniform thickness exists over a significant portion of the film. In plane diffraction patterns, done on a subset of samples, contained only *hk*0 reflections, which gives further support that the VSe_2 film is crystallographically aligned to the substrate. Table III.4 contains a summary of the structural parameters derived from the diffraction studies of the VSe_2 films.

Table III.4. Structural parameters (c and a lattice constants) calculated from specular and in-plane x-ray diffraction patterns of VSe_2 on SiO_2. AD = as deposited, AN = annealed 350°C for 30 minutes

# layers V|Se		c-lattice parameter [Å]	a-lattice parameter [Å]
49	AD	6.20(1)	-
	AN	6.07(1)	3.37(1)
82	AD	6.10(1)	-
	AN	6.03(1)	-

Table III.5. The total number of Pb, V, and Se atoms in the different Pb|Se|V|Se precursors determined by x-ray fluorescence.

# layers Pb|Se|V|Se	Pb atoms per Å^2		Se atoms per Å^2		V atoms per Å^2	
	total	per layer	total	per layer	total	per layer
41*	4.39	0.107	12.6	0.308	4.67	0.114
24	2.66	0.111	8.21	0.342	2.09	0.087

*(sample used in annealing study)

A similar annealing study was carried out on Pb|Se|V|Se precursors to compare the formation of $(PbSe)_{1.11}(VSe_2)_1$ relative to that of the individual constituents. Table III.5

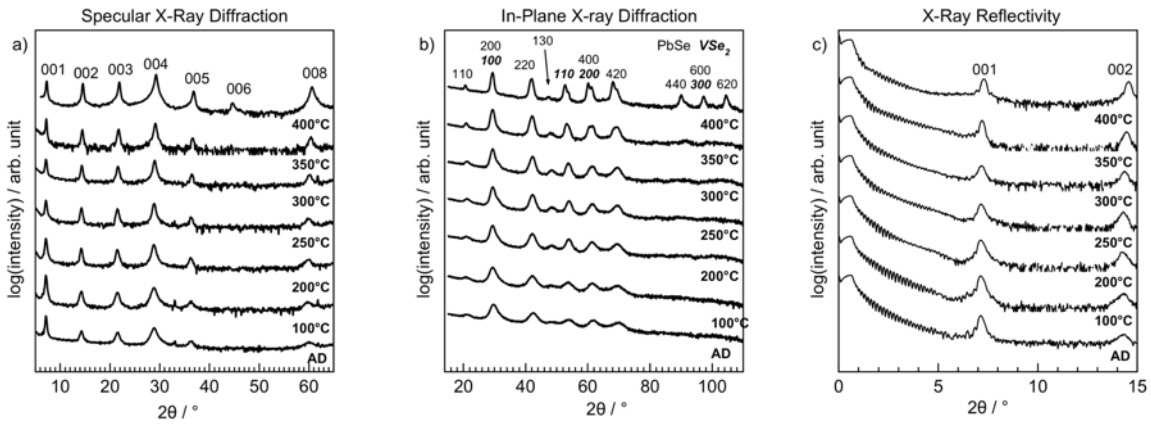

Figure III.3. (a) Specular x-ray diffraction of $[(PbSe)_{1.11}]_1(VSe_2)_1$, (b) in-plane diffraction of $[(PbSe)_{1.11}]_1(VSe_2)_1$, and (c) x-ray reflectivity patterns of of $[(PbSe)_{1.11}]_1(VSe_2)_1$ after annealing at the indicated temperatures for 30 minutes. Since the film is crystallographically aligned to the substrate, only 00l reflections are observed in the specular scans. The higher order 00l reflections observed in the as deposited film suggest crystallization of the superlattice taking place upon deposition. Reflections for independent lattices of PbSe and VSe_2 are observed in the in-plane diffraction pattern show that both constituents are present starting at the as deposited state. Kiessig fringes are retained in the x-ray reflectivity pattern even after multiple steps of annealing suggest that the film remains smooth throughout the self-assembly process.

summarizes the amount of each element in each of the as deposited films. Figure III.3 contains the diffraction patterns collected in the annealing study of a representative film. The appearance of higher order 00*l* reflections in the specular diffraction pattern, (Figure III.3a), indicates that a superstructure forms during the deposition. Since only 00*l* reflections are observed, it is crystallographically-aligned to the substrate. The *c*-axis lattice parameter determined from the 00*l* reflections (12.28(1) Å) is close to the previously reported value for $[(PbSe)_{1.11}]_1(VSe_2)_1$,12.25(1) Å.[19] The in-plane diffraction pattern of the as deposited sample (Figure III.3b) contains broad reflections of both PbSe and VSe_2, further indicating that $[(PbSe)_{1.11}]_1(VSe_2)_1$ forms during the deposition. Only *hk*0 reflections are observed for PbSe and VSe_2 in the in plane diffraction pattern, indicating strong crystallographic alignment of each constituent with respect to the substrate. X-ray

Table III.6. Structural parameters (superlattice d-spacing and a-lattice consants) calculated from specular and in-plane x-ray diffraction patterns of Pb|Se|V|Se precursor annealed at various temperatures. AD = as deposited

Temperature [°C]	d-spacing [Å]	PbSe a-lattice parameter [Å]	VSe_2 a-lattice parameter [Å]
AD	12.28(1)	-	-
100	12.38(1)	-	-
200	12.38(1)	-	-
250	12.36(1)	-	-
300	12.31(1)	6.03(1)	3.43(1)
350	12.25(1)	-	-
400	12.17(1)	-	-

reflectivity of the as deposited sample indicates that the Pb|Se|V|Se precursor is much smoother than the films of PbSe or VSe_2. The as deposited Pb|Se|V|Se precursor contains significantly more order than the corresponding films of the individual constituents. As the annealing temperature is increased, the 00*l* and *hk*0 reflections become more intense and narrow as atoms diffuse forming a more coherent structure perpendicular to the substrate and larger domains of PbSe and VSe_2 in the plane of the substrate. While the misfit layer compound $[(PbSe)_{1.11}]_1(VSe_2)_1$ has not been reported in the literature, the $[(PbSe)_{1.11}]_1(VSe_2)_1$ formed from the ordered precursor is at least kinetically stable at 400°C. Table III.6 contains a summary of the structural parameters derived from the diffraction studies of Pb|Se|V|Se precursors. Precursors that have around the targeted layering thickness and composition also form $[(PbSe)_{1.11}]_1(VSe_2)_1$, although a variety of defects (extra PbSe or VSe_2 layers between $[(PbSe)_{1.11}]_1(VSe_2)_1$ crystals, partial

replacement of a PbSe (or VSe_2) layer with VSe_2 (or PbSe), extra PbSe or VSe_2 on the surface) are present. This suggests that $[(PbSe)_{1.11}]_1(VSe_2)_1$ is at least a significant local free energy minimum in the free energy landscape. The large difference in the degree of order observed in Pb|Se|V|Se versus either Pb|Se or V|Se precursors in both as deposited and annealed states indicates a strong interaction must be present between bilayers of PbSe and trilayers of VSe_2.

We prepared precursor films with different thicknesses of PbSe on a thin layer of VSe_2 to determine if the PbSe layer was different than that found when PbSe was deposited on SiO_2 coated silicon described earlier. Table III.7 summarizes the amounts of each element in the as deposited films. Figure III.4 contains diffraction data collected on two samples. For both films, PbSe forms during the deposition process. For the 20 layer PbSe sample on 4 layers of VSe_2, only 00*l* reflections of PbSe are present, indicating that the PbSe is crystallographically aligned. After annealing, there is a relatively small change in the intensity (about 1.5x) of the 002 reflection suggesting that the as deposited film was already mostly crystalline and/or that the extent of crystallographic alignment increases. Kiessig fringes extending up to 5º, suggesting that the film is smooth, with calculated roughness of ~10Å. In the as deposited 82-layer PbSe on 8 layer VSe_2 film, weak non-00*l* reflections of PbSe are observed indicating that some grains are randomly oriented. However, since the intensity ratio of these reflections are low compared to the expected values of a randomly oriented powder, the majority of the film is crystallographically aligned. After annealing, the non-00*l* reflections disappear completely and the intensity of the 00*l* reflections increase. The amount of the intensity increase is significantly less than was observed in a similar thickness film of PbSe on SiO_2, suggesting that the as deposited

Table III.7. The total number of Pb, V, and Se atoms in the different PbSe precursors on VSe_2 determined by x-ray fluorescence. Exact composition ratio of Pb/Se cannot be determine because of the presence of Se in both constituents

# layers PbSe:VSe_2	Pb atoms per Å^2		Se atoms per Å^2		V atoms per Å^2	
	total	per layer	total	per layer	total	per layer
20:4	2.66	0.133	3.05	-	0.450	0.113
82:8	8.76	0.107	8.40	-	0.953	0.119

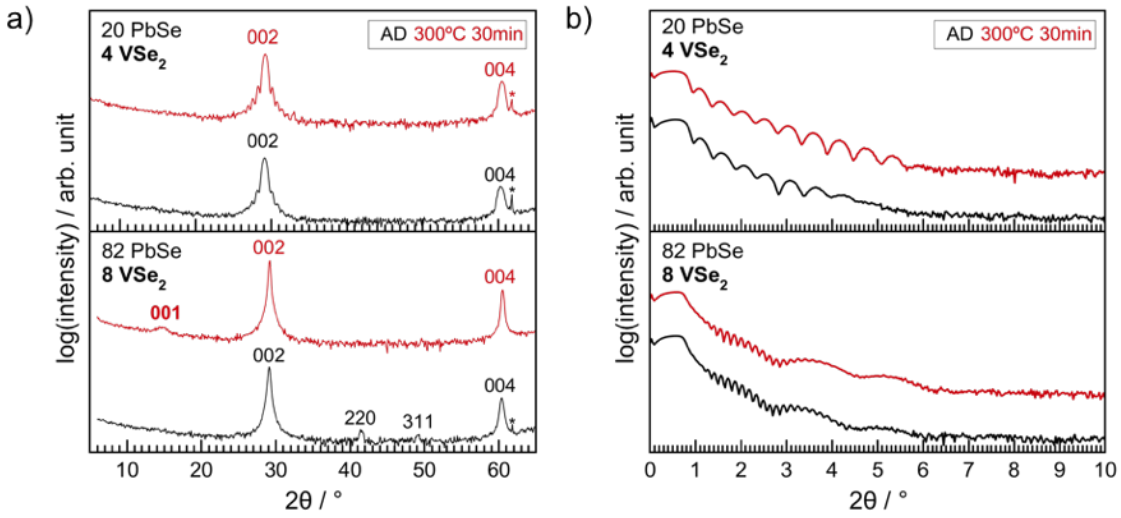

Figure III.4. (a) Specular x-ray diffraction and (b) x-ray reflectivity patterns of 20 layers of PbSe on 4 layers of VSe_2 (20:4) and 82 layers of PbSe on 8 layers of VSe_2 (82:8) films as deposited (black) and annealed at 300°C for 30 minutes (red). The thicker (82:8) film has weak non-00l reflections implying that there is a small fraction of randomly oriented grains. Annealed film samples have very strong 00l reflections indicating crystallographic alignment to the substrate due to the presence of the intervening layers of smooth VSe_2. The films are exceptionally smooth compared to PbSe on SiO_2 because the Kiessig fringes extending to higher angles.

film on VSe_2 is mostly crystalline and aligned as deposited. The (001) reflection of VSe_2 also appears after annealing. The thicker film on VSe_2 is significantly smoother than the film on SiO_2. The x-ray reflectivity scan of the thicker PbSe film on VSe_2 contains high

Table III.8. Lattice constants calculated from specular x-ray diffraction PbSe on VSe_2. AD = as deposited, AN = annealed

# layers Pb|Se:V|Se		a-lattice parameter [Å]
20:4	AD	6.13(1)
	AN	6.12(1)
82:8	AD	6.12(1)
	AN	6.11(1)

frequency fringes coming from the thick PbSe layer and broader low frequency fringes due to the VSe_2 layers beneath the PbSe. Table III.8 contains a summary of the structural parameters derived from the diffraction studies of Pb|Se precursors deposited on thin VSe_2 layers. The difference between the diffraction data of films of PbSe deposited on VSe_2 and on SiO_2 reflects the presence of a strong interaction between the PbSe and VSe_2.

III.4 Conclusions

There are a large number of potential misfit layer compounds, especially because there is not a requirement for lattice matching at the interface between different constituents. The incoherent interfaces and the lack of an understanding why the interactions between constituents at the interfaces is strong make it difficult to theoretically predict which misfit layer compounds might be thermodynamically stable or at least local free energy minima in the free energy landscape. Figure III.5 compares grazing incidence in-plane diffraction patterns of PbSe on SiO_2, PbSe on VSe_2, and $(PbSe)_{1.11}VSe_2$ annealed

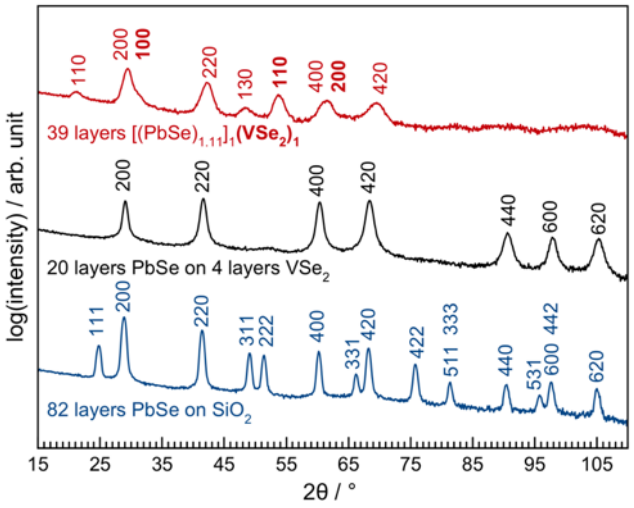

Figure III.5. Grazing incidence in-plane diffraction patterns of 82 layers of PbSe on SiO_2, 20 layers of PbSe on 4 layers of VSe_2, and $[(PbSe)_{1.11}]_1(VSe_2)_1$. The PbSe films have reflections that can be indexed to rock salt PbSe. All possible hkl reflections are observed in PbSe in SiO_2 film, indicating that the grains are randomly oriented. The absence of hkl reflections in the 20:4 film indicates that grains are parallel to the substrate.

at 300ºC for 30 min. The difference in the degree of crystallographic alignment reflects the strong interaction between the PbSe and VSe_2 layers. This suggests that comparing the degree of crystallographic alignment of films of A and B on SiO_2 or another convenient substrate with films of A on B (and/or B on A) may provide a way to quickly determine whether a misfit layer compound will form from a designed precursor with repeating layers of A and B. Since there are many possible potential combinations of constituents, such a fast screening test would save a significant amount of time.

III.5 Bridge

The crystallographic alignment of PbSe on VSe_2 suggests that there is a strong non-epitaxial relationship between PbSe and VSe_2 that is likely responsible for the stability of misfit layered compounds or ferecrystals containing the two constituents. The results

presented here promotes the idea that the compatibility of two constituents as misfit layered compound combination can be tested by checking for crystallographic alignment. The strong interaction between PbSe and VSe_2 shows that other misfit layered compounds between containing the two constituents can be synthesized. The next chapter focuses on the synthesis of $[(PbSe)_{1+\delta}]_m(VSe_2)_1$, where m = 1-4, heterostructures, a new family of PbSe and VSe_2 heterostructures with charge density wave (CDW) properties

.

CHAPTER IV

DESIGNED SYNTHESIS AND STRUCTURE-PROPERTY RELATIONSHIPS OF KINETICALLY STABLE $[(PbSe)_{1+\delta}]_m(VSe_2)_1$ (m = 1, 2, 3, 4) HETEROSTRUCTURES

Authorship Statement

This work was published in Chemistry of Materials, volume 31, issue 20, pages 8473-8483. I am the primary author of this work. Shannon Fender and Taryn Kam collected and analyzed x-ray diffraction and x-ray fluorescence data, and in the preparation of the manuscript. Johann Seyd and Dr. Manfred Albrecht assisted in the collection of electrical transport measurements. Robert Fischer and Dr. Ping Lu collected HAADF-STEM data. Dr. David C. Johnson is my advisor and consulted in preparation of this manuscript.

IV.1 Introduction

The discovery of emergent properties in single layer and very thin layers of quasi-two-dimensional systems has resulted in many reports of new systems and heterostructures.[1] Initially the majority of the systems being investigated were semiconducting because large changes in properties were discovered in semiconducting systems and because single sheets of metallic systems were found to be unstable in air.[2] More recently, a number of interesting properties of metallic system have been explored as a function of thickness including superconductivity and charge density waves (CDW).[3–5] The trends with layer thickness and/or layer separation depend on the specific property and compounds being investigated. The onset temperature of superconductivity is lowered when the thickness of $NbSe_2$ layers is reduced[6] or the separation between $NbSe_2$ layers in a heterostructure is increased.[7] Varying the layer thickness of different dichalcogenides

produced opposite effects on the onset temperature of charge density wave transitions. Studies on mechanically-exfoliated $TiSe_2$ have shown that as thickness of the exfoliated $TiSe_2$ is decreased, the onset temperature of the CDW increased.[8] The opposite has been found for $TaSe_2$, with the onset temperature of the CDW decreasing as the thickness of the mechanically-exfoliated film is decreased.[9] Unraveling the relationships between physical properties and the interaction between constituents at interfaces, the structure of the constituents, and/or the electronic or magnetic properties of the constituents is a focus of continued interest.

The electrical and magnetic properties of vanadium dichalcogenides have been extensively investigated both computationally and experimentally, with a variety of contradictory results presented as the number of layers of VSe_2 are reduced. Bulk VSe_2 has vanadium in octahedral coordination in a 1T structure and is metallic. It also has a small Pauli paramagnetism due to the conduction electrons and exhibits a CDW transition. Density functional theory calculations predict the ground state of undistorted VSe_2 layers to be the ferromagnetic 2H-polytype with a metal to semimetal/semiconductor transition when going from the bilayer to the monolayer.[10–12] There are contradictory reports on how the CDW changes as the number of VSe_2 layers are reduced in this n-type metal and how magnetic behavior changes as the sample is thinned to a monolayer. The onset of the CDW in bulk single crystals of VSe_2 is 100 K[13] and it has been reported that this increases to 135 K as thickness is reduced to 4-8 trilayers of VSe_2 prepared via liquid exfoliation.[14] An opposite trend was reported for micromechanically-exfoliated nanoflakes, where the onset temperature decreases to 81 K at the lowest thickness measured, 11.6 nm.[5] The thin nanoflakes are n-type conductors, as is bulk VSe_2, but the carrier concentration increases

as the nanoflake thickness is decreased. Both solvent-aided and mechanical exfoliation techniques were not able to precisely control the thickness of the VSe_2 flakes or reach the monolayer limit.[14,15]

Monolayer VSe_2 has been reported to have a charge density wave with a different distortion than found in the bulk.[16–18] The transition temperature is higher in the monolayer, and the transition temperature depends on both the material below it and the relative orientation of the adjacent layer. Monolayers of VSe_2 have also been reported to be ferromagnetic.[19] Other reports present data showing that their VSe_2 monolayers are non-magnetic and suggest that the ferromagnetism results from oxide impurities.[20] Studies of $[(SnSe)_{1+\delta}]_m(VSe_2)_1$ and $[(PbSe)_{1+\delta}]_1(VSe_2)_1$ prepared by annealing designed precursors show that they are p-type metals with a CDW that depends on the thickness of the rock salt constituent.[21,22] The changes in electrical resistivity and charge carrier concentration at the CDW transition temperature are much larger than that observed in bulk VSe_2. Compounds with thicker VSe_2 layers, $[(SnSe)_{1+\delta}]_1(VSe_2)_n$ and $[(PbSe)_{1+\delta}]_1(VSe_2)_n$ where n is larger than two, are n-type metals and CDW transition and transition temperature are similar to that found in bulk VSe_2.[22,23]

In this paper we probe the effect of changing the PbSe layer thickness on the CDW found in $[(PbSe)_{1+\delta}]_1(VSe_2)_1$. The synthesis, structure and electrical properties of a family of new, metastable compounds, $[(PbSe)_{1+\delta}]_m(VSe_2)_1$ are discussed. [22] The synthesis of $[(PbSe)_{1+\delta}]_m(VSe_2)_1$ with m = 2, 3, and 4 was more challenging than the synthesis of the m = 1 compound because the higher m compounds have smaller barriers towards disproportionation into PbSe and VSe_2. Deviations in the composition of the precursor from the stoichiometry of the desired products result in disproportionation of the precursor

during low temperature annealing. The structure of the PbSe layers in $[(PbSe)_{1+\delta}]_m(VSe_2)_1$ compounds is significantly less distorted than found in the analogous semiconducting $[(PbSe)_{0.99}]_m(WSe_2)_n$[24] and $[(PbSe)_{1.00}]_m(MoSe_2)_n$[25] compounds. The electrical resistivity data of all of the $[(PbSe)_{1+\delta}]_m(VSe_2)_1$ compounds contain a CDW transition at ~100 K that is distinctly different than that found in bulk VSe_2. The electrical resistivity can be successfully modeled using a parallel resistor circuit when m is three or greater, indicating composite behavior. These findings are very different from that previously reported for the isoelectronic $[(SnSe)_{1+\delta}]_m(VSe_2)_1$ compounds, where the CDW transition temperature changes systematically with m.[21] This suggests that the interaction between the constituent layers is more important than the separation of VSe_2 layers in determining the CDW transition temperature. The differences between these two sets of isoelectronic compounds demonstrate the sensitivity of emergent properties in heterostructures to the identity of the constituent layers.

IV.2 Experimental

Precursors designed to form the compounds $[(PbSe)_{1+\delta}]_m(VSe_2)_1$ where $1 \leq m \leq 4$, were synthesized using the modulated elemental reactants (MER) technique. Pb (99.8% Alfa Aesar), V (99.995% Alfa Aesar), and Se (99.99% Alfa Aesar) were deposited using 6 kW electron beam guns (Pb and V) and a custom-made Knudsen effusion cell (Se) under high vacuum ($< 3 \times 10^{-7}$ torr). The precursors were prepared by sequentially evaporating elemental sources in the sequence $[Pb|Se]_mV|Se$ onto Si wafers or quartz substrates. The mass of each element deposited was monitored using quartz crystal monitors. A LabView-based program opened and closed pneumatic shutters that control the amount of material

deposited using either the integrated thickness or the product of the deposition rate and time. A more detailed explanation of the chamber and the deposition procedure is described by Fister, et al..[26] The amount of each element deposited in each sample was measured using X-ray Fluorescence (XRF) on a Rigaku Primus II ZSX spectrometer. The proportionality factor between the measured fluorescence intensity and the number of atoms per unit area of each element in the film was determined as described by Hamann, et al..[27] The deposition conditions were iteratively adjusted to obtain precursors with the desired amounts of each element.

The layered precursors were crystalized by annealing in an inert N_2 atmosphere with an O_2 concentration less than 1 ppm. Out-of-plane specular x-ray diffraction (XRD), x-ray reflectivity (XRR), and x-ray rocking curve data were performed on a Bruker D8 Discover diffractometer with Cu Kα radiation (λ = 0.15418 nm). Grazing incidence in-plane x-ray diffraction scans (GIXRD) were performed on a Rigaku Smartlab diffractometer. Le Bail fitting of the diffraction patterns was used to determine the in-plane lattice parameters using FullProf and GSAS software.[28,29] Rietveld refinement of the specular x-ray diffraction patterns was done to determine the position of the atomic planes along the c-axis also using GSAS software.[29,30] High-angle annular dark-field scanning transmission electron microscopy (HAADF-STEM) images were collected by a FEI Titan^{TM} G2 80-200 STEM with a Cs probe corrector, operated at 200 kV, using an annular detector with a collection range of 60-160 mrad. STEM samples were prepared by focused ion beam technique.

Resistivity and Hall coefficients were measured as a function of temperature on a film deposited on a quartz substrate using the van der Pauw technique. Data was collected

at a temperature range between 25 K and 295 K. Seebeck coefficients were measured using a custom measurement system in which Cu and constantan thermocouples were used to measure temperature and the voltage created by a small temperature difference in a film.

IV.3 Results and Discussion

The MER precursors were designed to have the correct composition and nanoarchitecture necessary to crystallize the target compounds. The number of atoms per square Angstrom necessary to form the individual building blocks (PbSe and VSe_2) was calculated from the in-plane lattice parameters of the bulk structures of PbSe[31] and VSe_2[32] by dividing the number of atoms per unit cell by the basal plan area. The solid lines in Figure 1 give the calculated number of atoms of each element per unit area per repeating unit of the precursor for each targeted compound. The target number of V atoms per unit area per repeating sequence is constant since there is one VSe_2 trilayer in each repeat unit, while the number of atoms per unit area of Pb and Se increase linearly as the number of PbSe bilayer units (*m*) are increased. To prepare each of the compounds, *m* Pb|Se layers and a single V|Se layer were sequentially deposited. For example, the precursor for $[(PbSe)_{1+\delta}]_2(VSe_2)_1$ was made by repeatedly depositing the following sequence of elemental layers: V|Se|Pb|Se|Pb|Se. The amount or each element in the Pb|Se and V|Se bilayers was iteratively adjusted to obtain the desired number of atoms per unit area make a single unit cell thick layer of PbSe and VSe_2, respectively. The number of atoms/Å^2 per repeating unit for each element in the precursors were measured using XRF.[27] There is good agreement between the experimental and targeted number of atoms/Å^2 of each element in each precursor (Figure IV.1).

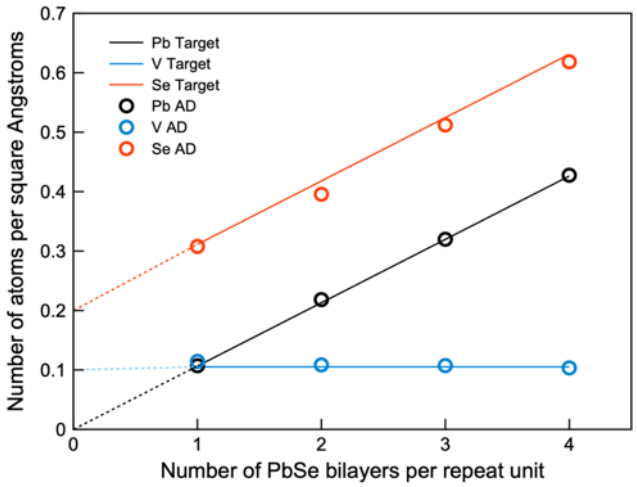

Figure IV.1. The calculated number of atoms per square Angstrom for V, Pb, and Se based on bulk lattice parameters are shown as solid lines. The measured amounts of each element in the precursors are shown as filled circles. The deviations from the calculated number reflect the experimental challenges of controlling the deposition process to fractions of a monolayer. AD: as-deposited precursor.

The nanoarchitecture of the precursors was measured using XRR and the data is presented in Figure IV.2. The XRR scans of each of the precursors contain Bragg reflections from the artificial layering of the elements and weaker subsidiary maxima from the finite thickness of the film. The first order Bragg reflections shift to lower angles as the number of Pb|Se building blocks increases due to the increased thickness of the repeating structure. Precursor modulation lengths (λ) calculated from the first order reflection linearly increase with the number of Pb|Se building blocks in the precursor (Figure IV.2 inset) and the measured thicknesses are all reasonable for the targeted heterostructures. The presence of the subsidiary maxima (Keissig fringes[33]) to greater than 5° 2θ indicates that the films are smooth, with roughness calculated using the formula derived by Parratt of less than 6-8 Å across the analytical area.[34] The combination of the XRF and XRR data

indicate that each precursor has close to the targeted amount of each element per unit area and the desired nanoarchitecture to form the targeted $[(PbSe)_{1+\delta}]_m(VSe_2)_1$ heterostructures.

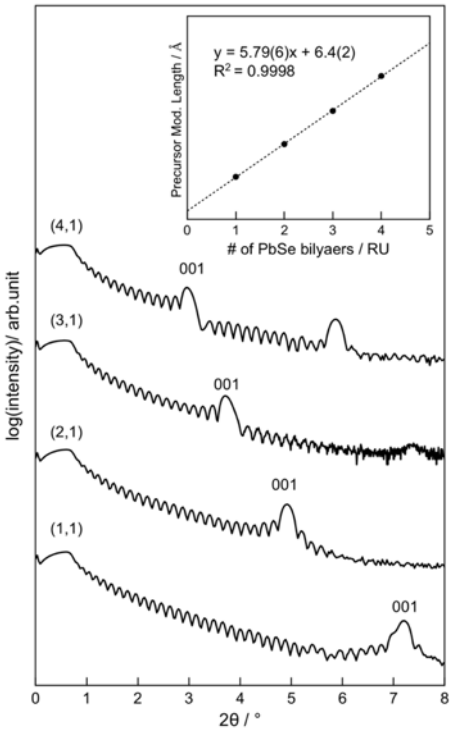

Figure IV.2. The x-ray reflectivity patterns of the precursors designed to form the targeted $[(PbSe)_{1+\delta}]_m(VSe_2)_1$ compounds. The modulation length of the $(Pb|Se)_mV|Se$ layer sequence determined from the position of the first order Bragg reflection is graphed versus the number of Pb|Se layers (m) in the repeating layer sequence in the inset.

The optimum annealing conditions to self-assemble the target heterostructures from the precursors were determined by an annealing study of the precursor with a 4(Pb|Se) + (V|Se) repeating sequence. The sample was annealed at a sequence of increasing temperatures for 1 hour in an inert atmosphere and changes in structure was followed by collecting specular and in-plane x-ray diffraction scans after each annealing temperature. Specular x-ray diffraction scans (Figure IV.3) were used to track changes in long range order in the *c*-axis direction in the film. The as-deposited diffraction pattern contains low

angle reflections from the artificial modulation of the deposited elemental layers and broad high order reflections (20-40° 2θ) indicating the film has begun to self-assemble with a period consistent with the targeted heterostructure. The reflections from both phenomena

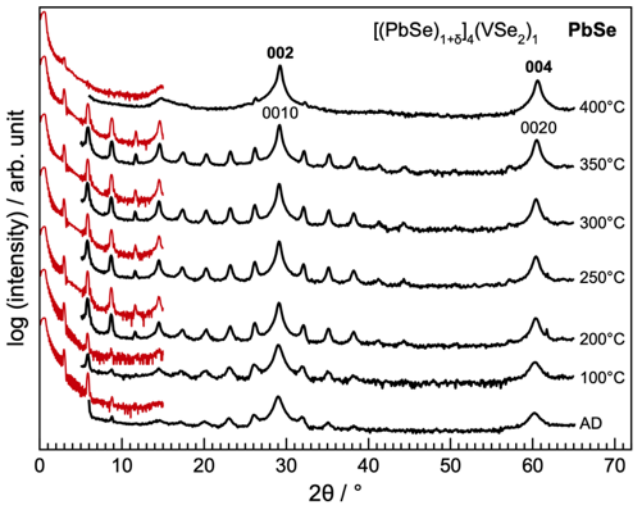

Figure IV.3. X-ray reflectivity and specular x-ray diffraction patterns collected as a function of increasing temperature after annealing a 4(Pb|Se)(V|Se) precursor at the indicated temperatures for 1 hour.

can be indexed as 00*l* reflections. The period of the low angle reflections (30.21(1) Å) is reasonably close to that expected from the repeating structure deposited. The *c*-axis lattice parameter of the developing heterostructure is slightly larger, 30.67(3) Å. The higher angle reflections become narrower and more intense after the sample is annealed at 200°C, indicating the start of crystal growth of one or both constituent layers at this temperature, resulting in a more coherent structure. After the 250, 300 and 350°C annealing periods, the intensity of the reflections increase, indicating continued crystal growth. There are only small changes in the peak locations, however, indicating a near constant *c*-axis lattice parameter. The low angle reflections become broader and shift to higher angle as annealing temperature is increased, becoming consistent in line width and *c*-axis lattice parameter

with the higher angle reflections of the heterostructures after the 300°C anneal. The Laue reflections from the finite number of unit cells in the film also increase in intensity, indicating that a coherent structure is forming with a uniform number of unit cells across the analytical area. After the 400°C annealing, the superlattice reflections are almost completely absent, suggesting that the heterostructure has decomposed. The two intense reflections remaining can be indexed as *002* and *004* reflections of PbSe. The broad reflection at ~14° 2θ is consistent with the *001* reflection of small VSe_2 crystallites. This suggests that at 400°C there is enough energy to disproportionate the heterostructures into a mixture of the binary constituents. The targeted heterostructures with thicker PbSe layers are less thermally stable than $[(PbSe)_{1+\delta}]_1(VSe_2)_1$ which was reported to be stable at 400°C.[35]

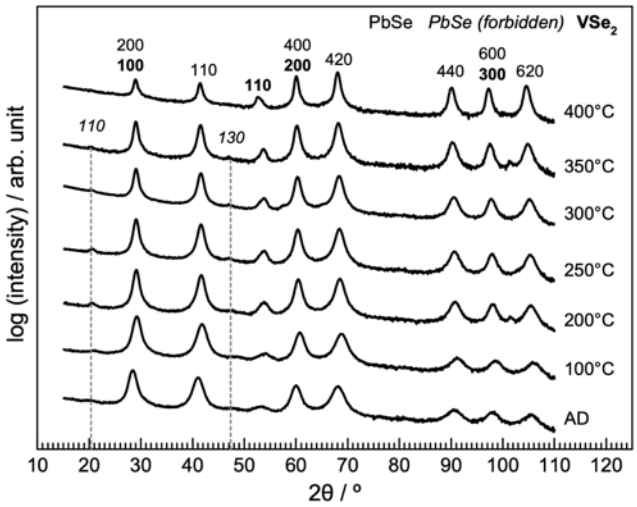

Figure IV.4. In-plane X-ray diffraction patterns collected as a function of increasing temperature after annealing a (V|Se) + 4(Pb|Se) precursor at the indicated temperatures for 1 hour.

In-plane diffraction patterns were collected during the annealing study to follow the evolution of the in-plane structure of the films and are shown in Figure IV.4. In the as-deposited precursor, broad reflections are present that can be indexed as *hk*0 reflections of

a hexagonal and a square lattice. The reflections shift to slightly higher angles after the sample is annealed at 100°C. The lattice parameters of the hexagonal (a = 3.393(4) Å) and square lattices (a = 6.0891(2) Å) above 100°C are close to the lattice parameters of bulk VSe_2[32] and PbSe.[31] There is a significant increase in the intensity of the *110* VSe_2 peak after annealing at 200°C, suggesting that significant crystal growth of VSe_2 occurs at this temperature. Intensities of both the VSe_2 and PbSe reflections continue to increase as the annealing temperature is increased up to 350°C. Weak reflections are present with odd indices for the square constituent. The reflections are consistent with the condition that $h + k = 2n$, indicating that the PbSe bilayer is distorted from the bulk face centered cubic structure. Both constituents are still present at 400°C, although the intensity of all reflections are lower and the reflections with odd indices in the square lattice are no longer detectable. This suggests that the loss of the heterostructure reflections in the specular diffraction data after annealing at 400°C results from disproportionation of the heterostructure into PbSe and VSe_2 regions. The broad 00*l* reflections for VSe_2 in the specular scan indicate that large crystallographically-aligned domains of VSe_2 do not form. The specular and in-plane diffraction data collected as a function of annealing temperature suggest that optimal processing conditions to convert the 4(Pb|Se)-(V|Se) precursor into $[(PbSe)_{1+\delta}]_4(VSe_2)_1$ is 300°C for 1 hour.

The absolute amounts of each element in each layer were found to be very important in controlling whether the targeted compounds self-assembled. The low temperature of the substrate during the deposition limits surface diffusion rates, so atoms cannot move far before being buried by the incoming flux of atoms. The diffraction data

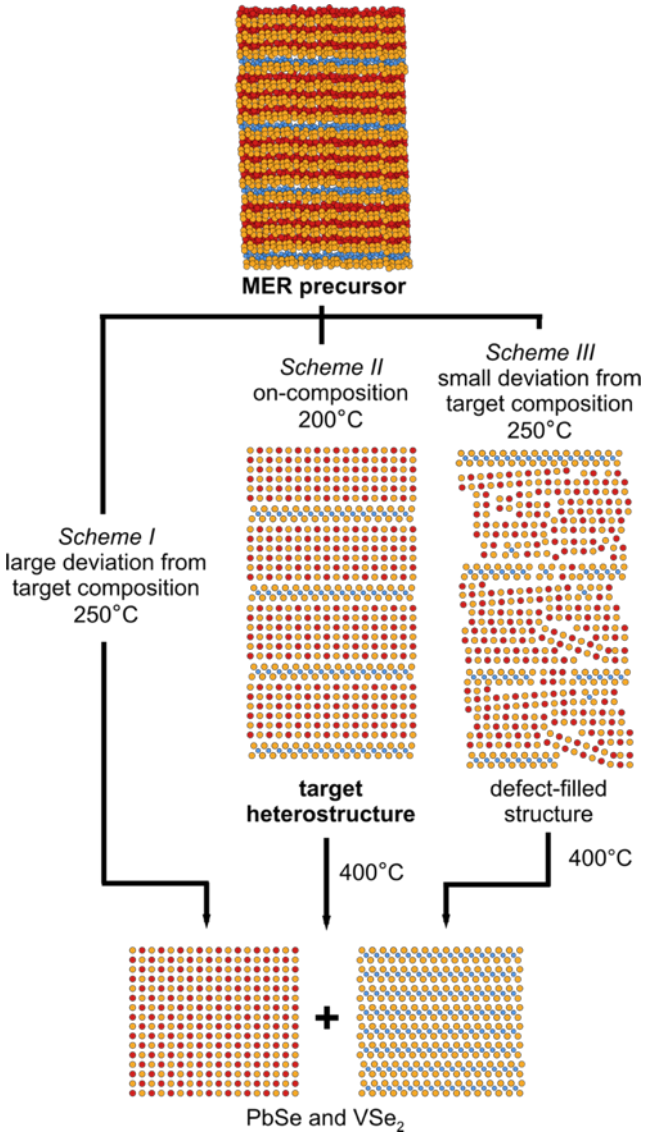

Figure IV.5. Proposed reaction pathway for the formation of products from a 3(Pb|Se) + 1(V|Se) precursor. The pathway depends on the absolute number of atoms per repeat unit of the precursor. The thermodynamic product is a disproportionation of the precursor into isolated regions of PbSe and VSe_2.

in the annealing study indicate that both PbSe and VSe_2 nucleate and grow during the deposition. If the amount of each bilayer (Pb|Se or V|Se) deposited corresponds to a complete single structural unit and nucleation occurs during the deposition, then the precursor layers develop significant long range order during the deposition (Figure IV.5, Scheme II). If the amount of a deposited element deviates from the targeted value, then the

extra (or missing) atoms result in partial layers. This increases the roughness in the layers and causes nucleation of the binary structures at different heights relative to the substrate. Annealing the sample at elevated temperatures activates diffusion, enabling atoms to move around to lower the free energy by eliminating defects and optimizing local coordination geometries Off-composition samples have partial layers in addition to interstitials and/or vacancies in the heterostructures (Figure IV.5, Scheme III). If the number of atoms in each layer deviates significantly from that required for an integer number of layers, then disproportionation occurs during annealing (Figure IV.5, Scheme I). The ability to determine the number of atoms of each element per repeating layer in the precursor using XRF is a critical advance, as it speeds up optimization of the deposition process and also enables us to predict which precursors are likely to form the targeted compounds.

Our assumption in this study is that precursors with the correct composition and nanoarchitecture, when annealed in the right conditions, should assemble to the target structure. We annealed the four precursors whose data is contained in Figures IV.1 and IV.2 using the optimized processing parameters and the specular diffraction patterns of the resulting compounds are shown in Figure IV.6. All the peaks in the diffraction patterns can be indexed as 00*l* reflections, consistent with heterostructures forming with their *c* axis perpendicular to the substrate. The *c*-axis lattice parameters of the annealed sample have a linear relationship with the number of PbSe bilayers in each repeat unit, which is consistent with the modulation length of the as precursors being preserved as they crystallize. The average change in *c*-axis lattice parameter per PbSe bilayer added (6.12(1) Å) is within error of the c-lattice parameter of bulk rock salt PbSe (6.1213(8) Å)[31] and equivalent PbSe

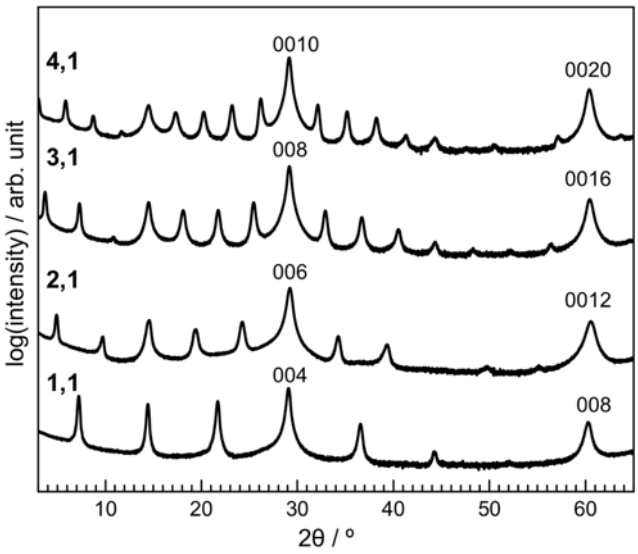

Figure IV.6. Specular x-ray diffraction patterns of $[(PbSe)_{1+\delta}]_m(VSe_2)_1$ (m = 1, 2, 3, 4) heterostructures.

bilayer thicknesses found in other heterostructures ($[(PbSe)_{1+\delta}]_m(NbSe_2)_1$) (6.12) and ($[(PbSe)_{1+\delta}]_1(TiSe_2)_n$)), (6.13(6) Å).[36,37] PbSe bilayer thicknesses in $[(PbSe)_{1+\delta}]_1(NbSe_2)_n$ and $[(PbSe)_{1+\delta}]_m(MoSe_2)_n$ are slightly greater than found in this work.[7,38] Since there is only one VSe_2 in each repeat unit, the y-intercept of a graph of the c-axis lattice parameter versus the number of PbSe bilayers (Figure IV.SI1) is greater than observed in bulk VSe_2, as the intercept is the sum of the average thickness of each VSe_2 trilayer and the thickness of the van der Waals gap. The PbSe and VSe_2 thicknesses obtained from this graph are close to their respective bulk equivalents and previous work on PbSe- and VSe_2-containing heterostructures. The *c*-axis lattice parameters of the PbSe-containing heterostructures are very close to those reported previously for analogous SnSe containing heterostructures (Figure A.1), and the change in inter-VSe_2 distances as m increases are similar.

The low angle x-ray reflectivity patterns (Figure IV.7) contain Kiessig fringes / Laue reflections between Bragg reflections extending to high angles, indicating that the

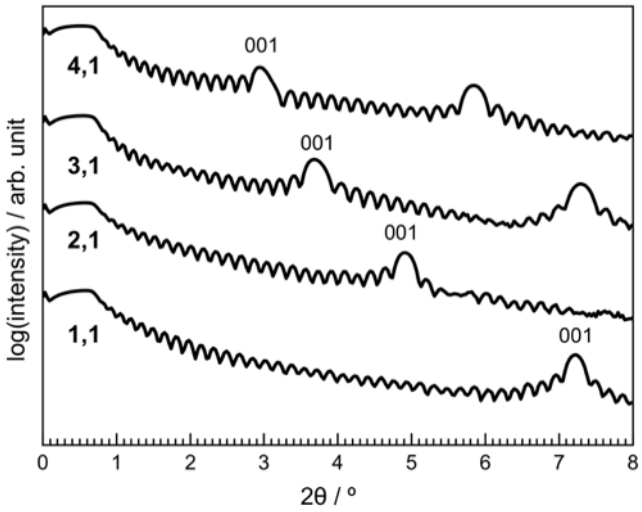

Figure IV.7. Low angle x-ray reflectivity patterns of $[(PbSe)_{1+\delta}]_m(VSe_2)_1$ (m = 1, 2, 3, 4) heterostructures.

films consist of a consistent number of unit cells over the analytical volume. The films become smoother after annealing, with roughness decreasing to 4-6 Å, as evidenced by the increase in the number of observed Kiessig fringes. Indexing the low angle Kiessig fringes and using a modified version of Bragg's law corrected for refraction enabled us to calculate the total film thicknesses. Each film has a total thickness of approximately 50 nm, consistent with the targeted thicknesses. Dividing the total film thickness by the calculated *c*-axis lattice parameter of the heterostructures yields the integral number of unit cells in the films. The number of repeat units formed calculated from the number of Kiessig fringes between Bragg peaks (Table IV.1) and the number of repeat units deposited are equal to one another, except in the $m = 1$ sample, where the number of unit cells formed is two less than the number of deposited layers. XRF data show that there is an increase in oxygen in this film after annealing; suggesting that the two layers might have been lost to oxidation at the top of the film. The specular diffraction data indicate that each Pb|Se and V|Se bilayer

in the deposited precursors crystallizes a PbSe bilayer or VSe_2 layer in the targeted structures.

Table IV.1: Structural parameters calculated from the x-ray reflectivity and specular x-ray diffraction patterns.

m,n	*c*-axis lattice parameter (Å)	Total film thickness (Å)	# of layers	targeted # of layers
1,1	12.273(4)	481.3(3)	39	41
2,1	18.343(8)	492.5(2)	27	27
3,1	24.486(9)	491.8(3)	20	20
4,1	30.617(9)	493.3(4)	16	16

The in-plane diffraction patterns of the $[(PbSe)_{1+\delta}]_m(VSe_2)_1$ (m = 1, 2, 3, 4) heterostructures are shown in Figure IV.8. All of the reflections can be indexed as *hk*0 reflections of a hexagonal and a square in-plane unit cell, consistent with the formation of VSe_2 and PbSe layers in the heterostructures. This indicates that the film has a preferred alignment with the *c*-axis perpendicular to the substrate, consistent with the specular diffraction data. The hexagonal basal plane unit cell with a lattice parameter of 3.40-3.43 Å is consistent with that reported for VSe_2.[32] The square basal plane unit cell is smaller for the m = 1 compound (6.03 Å)) than for the m = 2 - 4 compounds (6.11-6.13 Å), but all are close to that reported for PbSe.[31] However, the *hk*0 Bragg reflections where h and k are both odd, forbidden in an undistorted rock salt structure, are observed. The presence of *110* and *130* reflections indicates that Pb and Se are not located at (0,0) and (½,½) respectively in the intergrowth. A possible distortion that may give rise to these forbidden reflections is

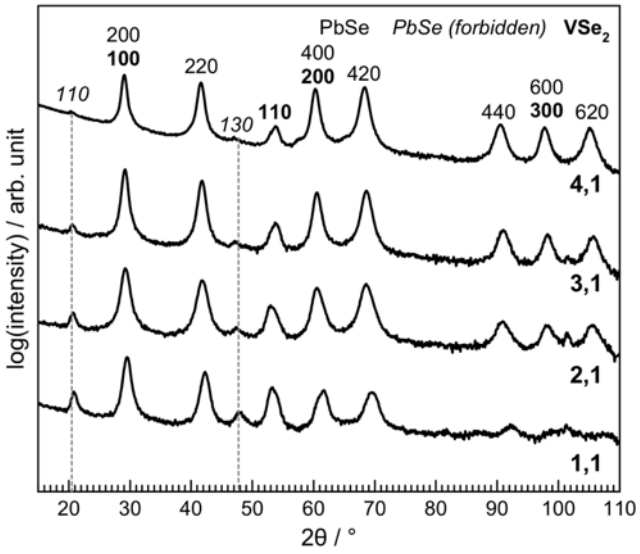

Figure IV.8. Grazing incidence in-plane diffraction of self-assembled $[(PbSe)_{1+\delta}]_m(VSe_2)_1$ (m = 1, 2, 3, 4) heterostructures.

Table IV.2: In-plane lattice parameters derived from the diffraction patterns via LeBail fitting. Misfit lattice parameters were calculated using the lattice parameters and the stoichiometric coefficients of each constituent.

m,n	a-axis lattice parameter, VSe_2 (Å)	a-axis lattice parameter, PbSe (Å)	Misfit parameter, δ
1,1	3.425(1)	6.030(1)	1.12
2,1	3.447(1)	6.116(1)	1.10
3,1	3.404(1)	6.106(5)	1.08
4,1	3.408(1)	6.130(1)	1.07

a lateral translation of one of the PbSe layers relative to one another. The intensities of the forbidden reflections decrease as the thickness of the PbSe constituent is increased, indicating that the magnitude of the distortion decreases. Forbidden reflections have also been observed in the in-plane diffraction patterns of $[(PbSe)_{1.14}]_1(NbSe_2)_n$

heterostructures,[39] suggesting that a distortion is a common feature of PbSe bilayers flanked by dichalcogenides in ferecrystals.

HAADF-STEM was collected to show the bonding arrangement of the atoms in the film and the relationship between the PbSe and VSe_2 layers in the heterostructures. This information is not present in the specular and in-plane diffraction patterns due to the preferred alignment in the films. The HAADF-STEM image of a representative portion of the $[(PbSe)_{1+\delta}]_3(VSe_2)_1$ sample is shown in Figure IV.9a. Both constituents are clearly distinguishable from each other because the PbSe layers are significantly brighter than the VSe_2 layers. The microscopy data confirms that the film consists of alternating layers of PbSe (6 planes or three bilayers) and one VSe_2 trilayer. Defects are clearly present, presumably due to different nucleation sites that grow together during the self-assembly process. The atoms in the VSe_2 layers, when viewed down the *<110>* zone axis, appear along a diagonal line, indicating that the V atoms are octahedrally coordinated, similar to the bulk binary compound.[40] The PbSe layers, observed down *<100>* and off-axis zones, both show that it has a structure similar to the rock salt structure found in the analogous $[(PbSe)_{1+\delta}]_m(WSe_2)_n$ heterostructure.[41] The integrated intensity profile across the slice of the image provides the positions of the atomic planes along the *c*-axis as shown in Figure IV.9b. The average atomic plane distances between Pb/Se planes, shown in the right of Figure IV.9b, are all within error of each other. This is different from what was observed in the analogous compound $[(PbSe)_{1+\delta}]_3(MoSe_2)_1$, where the PbSe planes had alternating short and long distances indicating discrete bilayers.[42] The lack of this distortion in $[(PbSe)_{1+\delta}]_3(VSe_2)_1$ perhaps results from a change in the interaction between the PbSe and

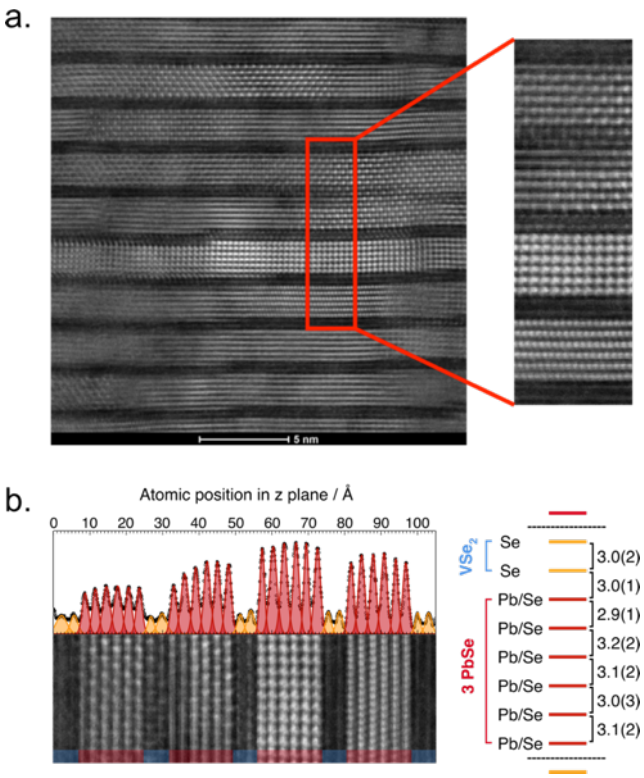

Figure IV.9. (a) HAADF-STEM image of the $[(PbSe)_{1+\delta}]_3(VSe_2)_1$ heterostructure showing the film consists of PbSe (bright rows) and VSe_2.

dichalcogenide layers due to the change in electronic properties of the dichalcogenide (trigonal prismatic $MoSe_2$ is semiconducting[43] while octahedral VSe_2 is metallic[44]). The availability of available states in metallic VSe_2 will result in virtual states between PbSe and VSe_2 as found at metal-semiconductor interfaces.[45] The reduced distortion in the PbSe layer in $[(PbSe)_{1+\delta}]_3(VSe_2)_1$ relative to $[(PbSe)_{1+\delta}]_3(MoSe_2)_1$ indicates a weaker interaction, consistent with the reduced kinetic stability of $[(PbSe)_{1+\delta}]_3(VSe_2)_1$ relative to $[(PbSe)_{1+\delta}]_3(MoSe_2)_1$.[42] The distance between the metal plane in the dichalcogenide to the average position of Pb/Se distance in the V-compound is 10% smaller (4.5(1) Å) than in the Mo-compound (5.0 Å), reflecting both the different coordination in the dichalcogenide and the different interaction between PbSe and the different dichalcogenides. In Figure 9a,

multiple zone axes for the PbSe layers are observed, indicating rotational disorder between the constituents.

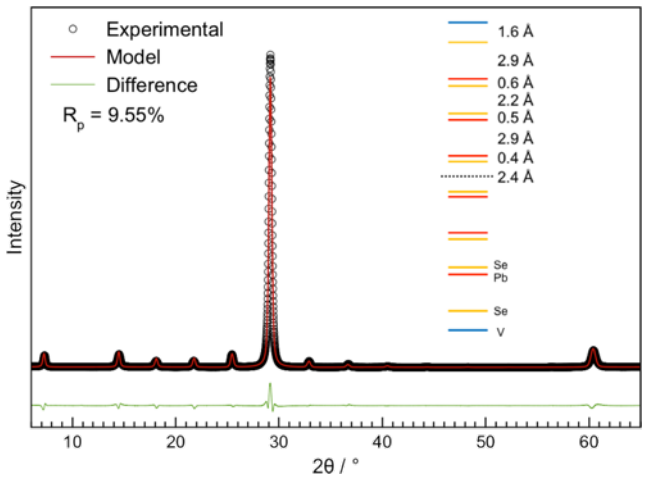

Figure IV.10. Results of a Rietveld refinement of the corresponding specular x-ray diffraction of the heterostructure and a comparison of the structural model refined to the HAADF-STEM-derived atomic positions.

Fractional z-axis coordinates obtained from the HAADF-STEM analysis of the $[(PbSe)_{1+\delta}]_3(VSe_2)_1$ heterostructure were used as an initial model for a Rietveld refinement of the specular diffraction data. The diffraction data, calculated diffraction intensities from the refined structural model and the difference between them are shown in Figure IV.10, along with the refined structural model. The consistency between the structure derived from the HAADF-STEM and Rietveld refinement of the x-ray diffraction suggests that the majority of the film consists of the heterostructure. The Pb and Se planes are not coincident and there is an alternation of short and long distances between Pb (or Se) planes consistent with the formation of PbSe bilayers. This distortion is smaller than that observed in $[(PbSe)_{1+\delta}]_3(MoSe_2)$.[42]

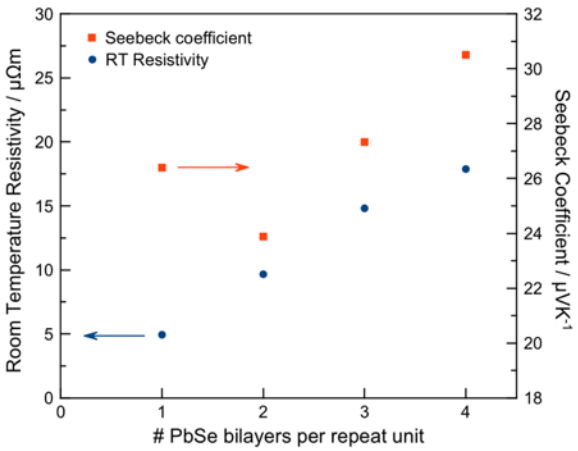

Figure IV.11. Room temperature Seebeck coefficients and resistivity graphed as a function of the number of PbSe bilayers in the respective compounds.

Resistivity, Hall coefficients and Seebeck coefficients were measured to investigate the impact of the increased PbSe thickness and associated structural changes on electrical transport properties. Since PbSe is semiconducting[46] and VSe_2 is metallic[44], conduction in the compounds studied here is expected to take place primarily in the VSe_2 layers as previously reported for $[(PbSe)_{1+\delta}]_m(NbSe_2)_1$ and $[(PbSe)_{1+\delta}]_1(VSe_2)_n$ ferecrystals and misfit layer compounds containing metallic dichalcogenides.[22,36] The room temperature resistivity of $[(PbSe)_{1+\delta}]_1(VSe_2)_1$ is consistent with previously published values,[22] and the resistivity values systematically increase as *m* increases (Figure IV.11). The differences in the resistivity between samples with adjacent *m* values decrease as *m* increases. The increase in resistivity as *m* increases was expected since a larger fraction of the film consists of semiconducting PbSe as *m* increases. The room temperature resistivity values for the $[(PbSe)_{1+\delta}]_m(VSe_2)_1$ compounds, however, are approximately twice as large as those reported for the analogous $[(SnSe)_{1+\delta}]_m(VSe_2)_1$ compounds.[21] We speculate that this is a consequence of the differences in the band gaps of SnSe and PbSe and a difference in the alignment of the VSe_2 bands with those of SnSe and PbSe. The room temperature Seebeck

coefficients are positive and the magnitude is typical for metallic behavior. The Seebeck coefficients, however, do not systematically increase as *m* is increased, which would be expected from the decrease in carrier concentration. The larger than expected Seebeck coefficient for the $[(PbSe)_{1+\delta}]_1(VSe_2)_1$ compound suggests that transport in this compound is more complicated, perhaps because only a 0.6 nm bilayer of PbSe separates the VSe_2 layers. The wave function tails of VSe_2 within the PbSe layer overlap more in $[(PbSe)_{1+\delta}]_1(VSe_2)_1$ than in the compounds with thicker PbSe layers.

The resistivity and carrier concentrations calculated from Hall coefficients assuming a single band are graphed in Figure IV.12 as a function of temperature. The room temperature Hall coefficients are all positive and change systematically as *m* is increased, indicating that holes are the majority carrier and that a decrease in carrier concentration causes the increase in resistivity as *m* increases. The carrier concentrations calculated assuming a single band model are in the range expected for a metal, consistent with the data presented in Figure IV.11. The sign of the Hall coefficient is opposite to that reported for bulk VSe_2. The temperature dependence of the resistivity of the different $[(PbSe)_{1+\delta}]_m(VSe_2)_1$ compounds are all very similar. Between 150 and 300 K, the resistivity slowly decreases with decreasing temperature as expected for a metal. The rate of the decrease is 2-3 times smaller than that found in bulk VSe_2, suggesting a reduced electron-phonon scattering. Between 90 and 105 K, depending on the value of *m*, the resistivity rapidly increases to a value at about 20 K that is 2-3 times larger than the room temperature value. This substantial increase in the resistivity is different from what is found in bulk VSe_2 and similar to the reported for the analogous $[(SnSe)_{1+\delta}]_m(VSe_2)_1$ compounds, which

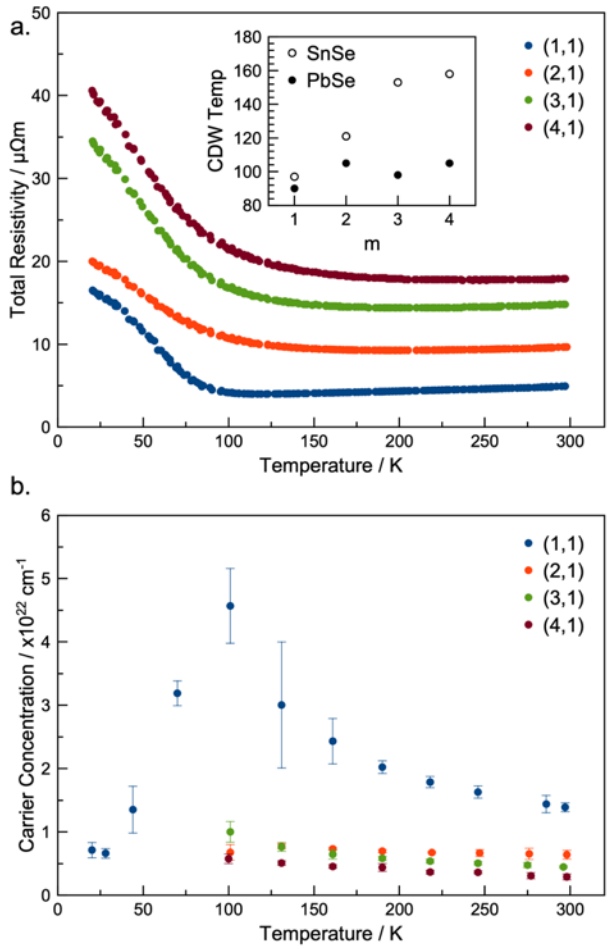

Figure IV.12. (a) Temperature dependence of resistivity and (b) carrier concentrations calculated from Hall coefficients assuming a single band model for $[(PbSe)_{1+\delta}]_m(VSe_2)_1$ (m = 1, 2, 3, 4) heterostructures. Inset of top plot shows a comparison of the CDW transition temperatures for $[(PbSe)_{1+\delta}]_m(VSe_2)_1$ and $[(SnSe)_{1+\delta}]_m(VSe_2)_1$ compounds.

was shown to be caused by a charge density wave transition.[21] The transition in $[(PbSe)_{1+\delta}]_1(VSe_2)_1$ is sharper than in the compounds with thicker PbSe layers and occurs at approximately 90 K. For the other three compounds, the transition is broader and the transition temperature occurs at slightly higher temperature. The addition of PbSe bilayers to the $[(PbSe)_{1+\delta}]_1(VSe_2)_1$ does not systematically increase the charge density wave transition temperature (Figure IV.12a inset), as was observed in $[(SnSe)_{1+\delta}]_m(VSe_2)_1$

compounds.[21] The ~10 K increase in the CDW onset temperature as m is increased is also significantly smaller than the increase observed for $[(SnSe)_{1+\delta}]_m(VSe_2)_1$ compounds.[21]

The temperature dependence of the carrier concentrations provides additional information, although we unfortunately were not able to measure the Hall coefficient for the higher m compounds below the CDW onset temperature. For the $m = 1$ compound, the carrier concentration has a strong temperature dependence, increasing as temperature is decreased from room temperature and then decreasing abruptly at the CDW onset. The temperature dependence suggests that a simple single band, free electron model is probably not appropriate for this compound. A similar temperature dependence was observed for $[(SnSe)_{1+\delta}]_1(VSe_2)_1$. The carrier concentrations of the samples with thicker PbSe layers increase slightly as temperature decreases. The carrier concentration decreases as m is increased as the semiconducting PbSe dilutes the carriers from the metallic VSe_2 layer.

A simple model for the electrical properties of the $[(PbSe)_{1+\delta}]_m(VSe_2)_1$ compounds is to consider the sample to be a composite consisting of non-interacting parallel conductors. If we assume that the resistivity of the PbSe layer is much higher than the resistivity of the VSe_2 layer, then it can be shown that

$$\rho_{VSe2} = \rho_{exp}\,[n/(m + n)] \qquad \text{Equation IV.1}$$

where ρ_{exp} is the measured resistivity, n is the number of VSe_2 layers in the repeating unit (one for this set of samples), and m is the number of PbSe bilayers.[36] If Equation IV.1 is valid, then the resistivity obtained for a monolayer of VSe_2 from each compound will be

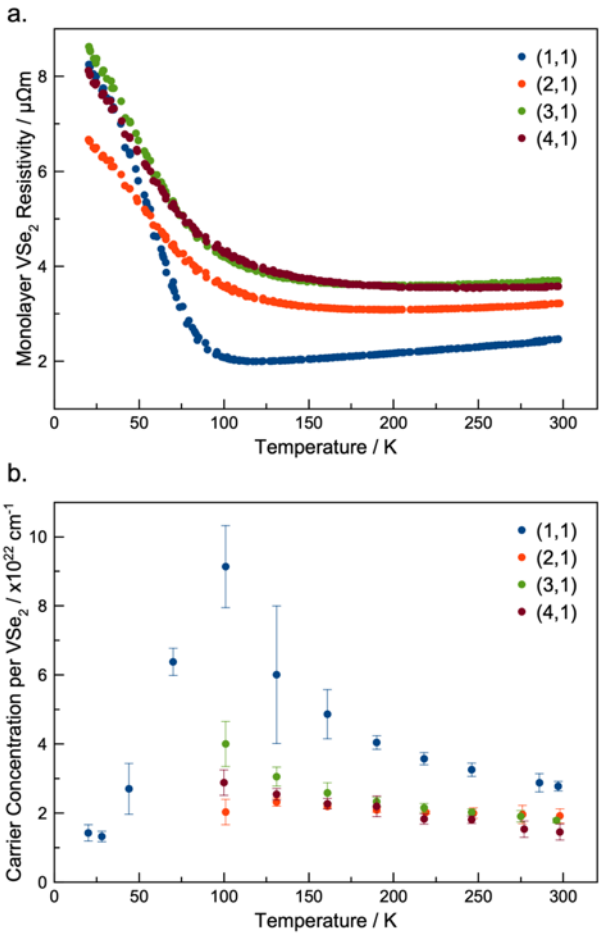

Figure IV.13. Calculated (a) resistivity and (b) carrier concentrations for a monolayer of VSe_2 using Equation 1 and the data in Figure IV.11. If Equation1 is valid, the resistivity and carrier concentration calculated from each of the compounds should be the same.

the same. Equation IV.1 also describes the expected change in carrier concentration assuming composite behavior. Figure IV.13 graphs the temperature dependence of the resistivity and carrier concentration of a VSe_2 monolayer obtained from each compound using this equation. The calculated resistivity of the VSe_2 monolayer increases as m increases, with the m = 3 and 4 samples having very similar resistivity values. The calculated carrier concentration for a monolayer of VSe_2 from $[(PbSe)_{1+\delta}]_1(VSe_2)_1$ data is higher than those calculated from the higher m compounds. The carrier concentrations are

very similar for the higher *m* compounds between 200 and 300 K. There is an increase in the carrier concentrations as the CDW transition temperature is approached. This suggests that the electrical properties can be described as that of a composite of a metallic VSe_2 monolayer separated by a non-conducting PbSe layer when *m* is 3 or greater. Though composite behavior is observed higher values of m, the electrical transport properties of $[(PbSe)_{1+\delta}]_m(VSe_2)_1$ is still distinctly different from its bulk constituents. The CDW wave of the heterostructures is also distinctly different from bulk VSe_2, with holes being the majority carrier and markedly different temperature dependences of resistivity and Hall coefficients, suggesting a distinctly different CDW in the VSe_2 monolayers.

Since the wave function of the metallic VSe_2 monolayer will extend into the semiconducting PbSe, which acts as a dielectric,[45] this composite behavior suggests that when *m* is 3 the distance between adjacent VSe_2 monolayers is large enough that the wavefunction tails in adjacent layers do not significantly overlap. The lower resistivity observed for the VSe_2 monolayer in $[(PbSe)_{1+\delta}]_1(VSe_2)_1$ would then result from the overlap of the wave function tails of adjacent VSe_2 monolayers, as the bilayer of PbSe that separates them is only 0.6 nm thick.

It is interesting to compare the electrical properties of the $[(PbSe)_{1+\delta}]_m(VSe_2)_1$ compounds presented here with those reported previously for $[(SnSe)_{1+\delta}]_m(VSe_2)_1$ compounds[21] and members of both families with thicker VSe_2 layers. In both sets of compounds, the electrical data indicate that VSe_2 monolayers are metallic and have a distinctly different charge density wave than that found in thicker VSe_2 layers. Both compounds with m = n = 1 have similar changes in the carrier concentration calculated from the Hall coefficient assuming a single band model, increasing significantly as

temperature is decreased and then dropping precipitously at the CDW onset temperature. $[(PbSe)_{1+\delta}]_m(VSe_2)_1$ compounds with m = 3 and 4 have composite behavior, however, while the analogous $[(SnSe)_{1+\delta}]_m(VSe_2)_1$ compounds[21] do not. This is perhaps related to the structural changes in the MSe layers as a function of thickness. In both PbSe and SnSe, there are two distortions that occur from a rock salt structure; a puckering distortion of the layers where the metal atoms are above and the Se atoms below the average plane, and an alternating long and short interlayer distance between MSe bilayers. Both of these distortions change systematically as m is increased. In the $[(SnSe)_{1+\delta}]_m(VSe_2)_1$ compounds[21] the puckering distortion increases as m increases as the SnSe. In $[(PbSe)_{1+\delta}]_m(VSe_2)_1$ compounds, however, both the puckering distortion and the difference between the inter- and intra- bilayers decrease as m increases. This difference in behavior is related to the different structures of SnSe and PbSe. SnSe has an orthorhombic structure at room temperature that becomes cubic as temperature is raised.[47] A single bilayer of SnSe has a structure close to the cubic high temperature structure, and the structure approaches the bulk low temperature structure as layer thickness is increased.[48] As many as 30 bilayers of SnSe are required to obtain lattice parameters that are consistent with the bulk struture.[49] PbSe, however, has a simple rock salt structure. A single bilayer of PbSe distorts from the rock salt structure and the distortion decreases as m increases and approaches the bulk structure when m is typically around 5 or 6.[42] In the $[(PbSe)_{1+\delta}]_m(VSe_2)_1$ series, however, the structure seems to be approaching the bulk quicker. The transition from a new material, with properties distinct from the constituent layers, to a composite of VSe_2 monolayers separated by a PbSe nonconducting layer occurs at 3 to 4 PbSe bilayers based on electrical properties.

IV.4 Conclusions

In this work we showed that the compounds $[(PbSe)_{1+\delta}]_m(VSe_2)_1$ with m from 1 to 4 could be prepared from designed precursors. The correct local number of atoms per unit area per repeating unit and the correct nanoarchitecture was necessary for the precursor to self-assemble into the targeted metastable products during low temperature annealing. The compounds with larger m values are less kinetically stable than $[(PbSe)_{1+\delta}]_1(VSe_2)_1$ and the precursors need to be closer to the targeted number of atoms per unit area. Diffraction data and HAADF-STEM images indicate that PbSe in the heterostructures has a lower symmetry structure than face centered cubic, presumably due to the interface and interlayer interactions. All of the $[(PbSe)_{1+\delta}]_m(VSe_2)_1$ compounds have an abrupt increase in resistivity as temperature is decreased, which is consistent with a charge density wave. The onset temperature of the CDW transition does not change significantly as *m* is increased. The transport behavior for the *m* = 3 and 4 compounds can be described using a composite model consisting of a conducting monolayer of VSe_2 and a non-conducting PbSe layer that do not interact. The difference in the rock salt layer thickness dependence of the CDW transition temperature between members of $[(PbSe)_{1+\delta}]_m(VSe_2)_1$ and $[(SnSe)_{1+\delta}]_m(VSe_2)_1$ which have approximately the same VSe_2 inter-layer distance, suggests that the identity of the intervening constituent and its interaction with the VSe_2 monolayer determines the CDW onset temperature.

IV.5 Bridge

The charge density wave properties of VSe_2-containing heterostructures is not strongly dependent on the inter-VSe_2 separation. Rather, it is strongly dependent on the

identity and chemistry of the intervening material separating VSe_2 monolayers. We highlight the importance of controlling nanoarchitecture and the number of atoms per square Angstrom in the successful targeting of $[(PbSe)_{1+\delta}]_m(VSe_2)_1$ compounds. This work opens up opportunities for targeting other PbSe- and VSe_2- containing heterostructures. The next chapter discusses our work on the synthesis and stability of $[(PbSe)_{1+\delta}]_q(VSe_2)_1$ compounds, where q is 1 to 11 and the number of PbSe monolayers, which is made possible by the ability to measure sub-monolayer quantities by XRF and precise control over precursor nanoarchitecture.

CHAPTER V

THE INSTABILITY OF MONOLAYER THICK PbSe ON VSe_2

Authorship Statement

At the time of writing this manuscript is unpublished. A paper is to be submitted with me as the primary author, Mina Buchanan, Taryn M. Kam, Shannon S. Fender, Renae F. Gannon, Robert Fischer, Dr. Ping Lu, Dr. Benjamin Hanken, and Dr. Mark Asta, and Dr. David C. Johnson. Mina Buchanan performed annealing studies for the precursors. Taryn M. Kam and Shannon S. Fender assisted in the analysis of x-ray diffraction data. Renae N. Gannon, Robert Fischer, and Dr. Ping Lu collected HAADF-STEM data. Dr. Benjamin Hanken and Dr. Mark Asta provided the computational data. Dr. David C. Johnson is my advisor and consulted in preparation of the manuscript.

V.1 Introduction

The discovery of 2-dimensional materials with so called emergent properties, those not observed in the constituent bulk compounds, has resulted in a boom in research on monolayers, heterostructures and ultrathin materials.[1] The expansion of this field is fueled by predictions of unusual quantum states and properties that might be observable in 2D materials, including unusual quantum spin Hall states,[2,3] Weyl Fermions,[4] indirect to direct band gap transitions,[5] and topological states.[6] The surfaces and interfaces in 2D materials are responsible for many of the observed emergent properties. In monolayers, the lack of adjacent layers removes bonding and antibonding interactions between layers, which can result in property changes such as the transition from an indirect to a direct band gap in MoS_2.[5] Interlayer coupling at the non-epitaxial interface between constituents in

heterostructures can produce new properties, for example charge transfer can cause modulation doping in heterostructures.[7,8] The interaction between layers can also prompt structural changes, such as the formation of octahedrally coordinated $MoSe_2$ when layered with BiSe.[9] The rapid development of this field experimentally was initially driven by the ability to obtain monolayers of naturally layered compounds via mechanical cleaving[10,11] and the ability to detect thicknesses rapidly using optical techniques.[12] The large interest in 2D materials as potentially important components of new technologies has resulted in the development of additional approaches to synthesizing films with precise control of thickness and heterostructures with controlled nanoarchitecture.[11,13]

While initially focused on materials with layered structures with obvious cleavage planes, recent theoretical papers have predicted unusual properties associated with 2D layers of materials with three dimensional structures.[14–19] Preparing 2D layers of materials with 3D structures, however, is synthetically more challenging than for structurally 2D or layered compounds. As a material becomes more 3D, cleaving thin layers in desired directions becomes increasingly more difficult. During vapor phase growth, the strength of the interaction between the growing layer and the substrate is very important. If the interaction between the layer and the substrate is too strong, it will modify the electronic structure that is being targeted synthetically. If the interaction between the layer and the substrate is too weak during, there will be a tendency to form islands rather than continuous thin films of uniform thickness. Recent calculations have predicted that a free-standing monolayer PbSe could be a 2D topological crystalline insulator, with Dirac-cone-like edge states.[20] PbSe ultra thin films have been grown on $SrTiO_3$ substrates by co-depositing Se and Pb atoms, forming crystalline PbSe islands after post-annealing.[21] A large compressive

strain exists in the epitaxial few-layers PbSe islands, with the lattice parameters changing from 5.85 Å for a 3 monolayer thick island to 6.1 Å for a 9 monolayer thick island compared to 6.14 Å for bulk PbSe. The large change in lattice parameters indicates a strong interaction between the substrate and the PbSe. The data presented suggest that the PbSe islands have Dirac-cone-like edge states. The distortion of the lattice with thickness also impacts properties, in addition to layer thicknesses.

Here we report our investigation of the growth of monolayer and controlled thickness PbSe layers between transition metal dichalcogenide layers, prompted by the thermodynamic stability of misfit layered compounds containing well defined bilayers of PbSe alternating with dichalcogenides.[22,23] Precursors were deposited to mimic the nanoarchitecture of $[(PbSe)_{1+y}]_q(VSe_2)_1$ heterostructures where q is an integer number of PbSe monolayers. The precursors with even layer and with $q \geq 7$ thicknesses had the expected as deposited nanoarchitecture and evolved into the desired heterostructures. Surface diffusion during the deposition process of the q = 1, 3 and 5 precursors, however, resulted in more complex initial nanoarchitectures, which impacted the resulting self-assembly of products. Consistent with the as deposited nanorarchtecture, the q = 5 sample formed the $[(PbSe)_{1+\delta}]_4(VSe_2)_1[(PbSe)_{1+\delta}]_6(VSe_2)_1$, heterostructure, the q = 3 sample formed $[(PbSe)_{1+\delta}]_2(VSe_2)_1[(PbSe)_{1+\delta}]_4(VSe_2)_1$ and the q = 1 sample disproportionated into regions of $[(PbSe)_{1+\delta}]_2(VSe_2)_1$ and VSe_2. DFT calculation of PbSe rock salt blocks of various thickness separated by vacuum yielded structural distortions that matched the experimental data and an odd-even alternation in energy as a function of layer thickness. The computational and experimental reveal that for small values of odd q, the formation of the PbSe rock salt block on a dichalcogenide is not kinetically stable and has a higher

energy compared to disproportionation its adjacent (q+1 and q-1) even counterparts. The preparation of monolayer thick PbSe will require finding a substrate that has a stronger film-substrate interaction.

V.2 Experimental

Precursors were deposited on <100> Si wafers with the native oxide using a custom-built physical deposition chamber described by Fister et al.[31] Elemental V (99.995% Alfa Aesar), and Pb (99.8% Alfa Aesar) were deposited using 6 keV electron beam guns while elemental Se (99.99% Alfa Aesar) was deposited using a Knudsen effusion cell. Elemental layers were deposited by exposing the substrate to a plum of atoms from the heated sources. The time the substrate is exposed is controlled by pneumatic shutters that close after the desired thickness has been deposited. The desired thickness was measured using a quartz crystal microbalance and the sequence and thickness of elemental layers can be controlled by custom LabView software. The number of atoms of each element deposited is optimized by measuring the x-ray fluorescence (XRF) of the films ex-situ using a Rigaku Primus II ZSX spectrometer. The measured XRF intensities are converted into the number of atoms per unit area for each constituent as described by Hamman et al.[24] The period of the deposited sequence of layers was measured using X-ray reflectivitiy (XRR).

Ex-situ annealing was performed on a hot plate in an inert N_2 atmosphere (O_2 < 0.8 ppm). The changes as a function of annealing temperature and time were followed using x-ray diffraction. Specular x-ray diffraction (XRD) and X-ray reflectivity (XRR) were collected on a Bruker D8 Diffractometer with Cu-Kα radiation (λ = 0.15418 nm). Grazing

incidence in-plane x-ray diffraction (GIPXRD) was collected on a Rigaku Smartlab Diffractometer, also with Cu-Kα radiation (λ = 0.15418 nm). LeBail fitting of the GIPXRD data was performed on the FullProf Suite.[32]

An FEI Titan™ G2 80-200 STEM with a Cs probe corrector and ChemiSTEM™ technology (X-FEG™ and SuperX™ EDS with four windowless silicon drift detectors) operated at 200 kV was used in this study. HAADF images were recorded with an electron probe of size (FWHM) of about 0.13 nm, convergence angle of 18.1 mrad and current of ~75 pA, and an annular dark-field detector with a collection range of 60-160 mrad.

V.3 Results and Discussion

A sequence of precursors was designed that mimics the targeted structures that contain the correct number of atoms of each element in a repeating sequence of elemental layers. We calculated the number of atoms needed to form a monolayer of rock salt structured PbSe in a <001> plane and a VSe_2 trilayer from the in-plane lattice parameters of each constituent in $[(PbSe)_{1+\delta}]_1(VSe_2)_1$, which contains a bilayer of PbSe alternating with VSe_2.[23] Figure V.1 shows the number of atoms of each element required to form $[(PbSe)_{1+\delta}]_q(VSe_2)_1$ compounds plotted as a function of q, where q is the number of PbSe monolayers. To prepare the compounds where q is even, we deposited a repeating unit (RU) of the sequence of elemental layers [V|Se + q/2(Pb|Se)] r times, where each V|Se bilayer is targeted to have the number of atoms required to form a VSe_2 layer and each Pb|Se layer is targeted to have the number of atoms required to form a PbSe bilayer. To prepare the compounds where q is 1, 3, 5, 7 or 9 monolayers (1.5, 2.5, 3.5 and 4.5 bilayers), we deposited a similar sequence of elemental layers, where each Pb|Se layer contained the

either the number of atoms required to form a monolayer or a bilayer of PbSe such that the total number of layers atoms deposited equaled the value needed for q monolayers. For example, to prepare a 7-1 precursor, we deposited the RU sequence [V|Se + 3(Pb|Se)$_{bilayer}$+ 1(Pb|Se)$_{monolayer}$].

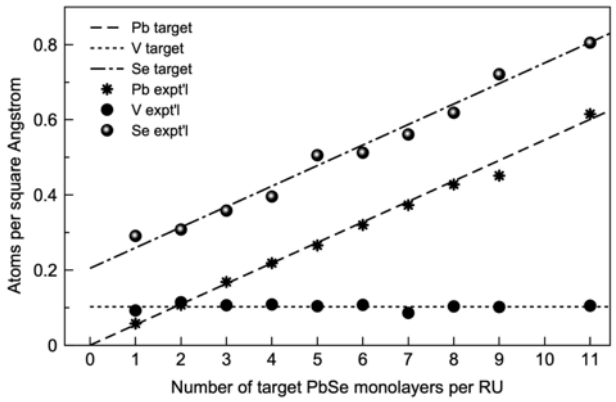

Figure V.1. The targeted number of atoms per square Angstrom for each element per repeat unit for each of the designed precursors are shown as lines. The circles are the amounts determined using XRF data.

The compositions and structures of the deposited precursors were determined using XRF, XRR and XRD. The total number of atoms of each element deposited in each precursor was measured using XRF and the average number of atoms per repeating unit was obtained by dividing the total by the number of repeating units deposited.[24] The measured number of atoms per unit area deposited for each precursor are shown as circles in Figure V.1. The number of V and Pb atoms per unit area of all of the odd number precursors are within 5% of the calculated values. The deviations from the calculated lines are a consequence of the challenges of depositing targeted numbers of atoms per unit area that are on the order of a monolayer of each element. Excess Se is observed in some precursors, but the excess was anticipated to evaporate during the annealing process. The

precursors all contain close to the number of atoms of each element in the repeating sequence of layers to form the targeted compounds.

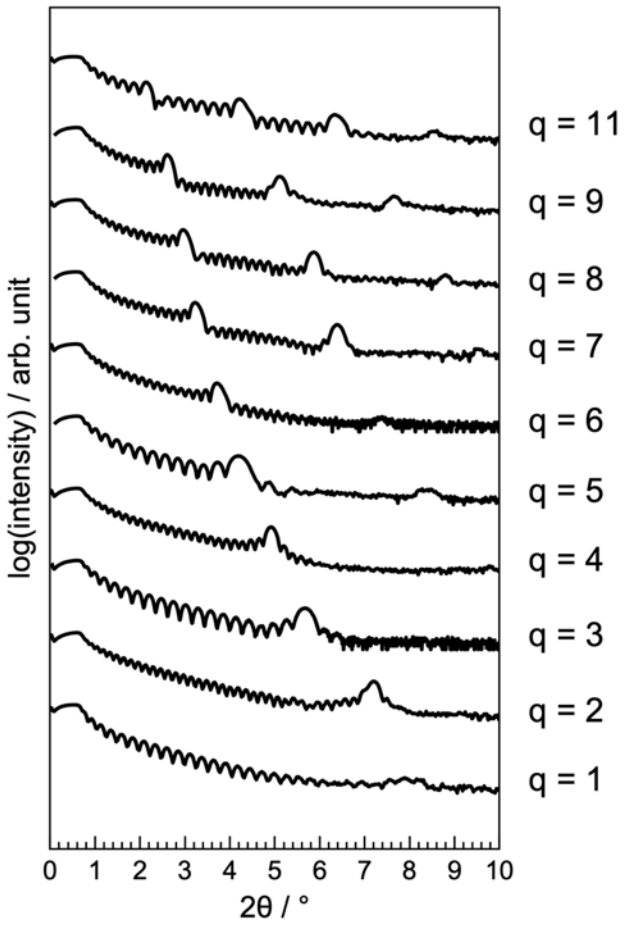

Figure V.2. X-ray reflectivity patterns show that all precursors are smooth and the modulation is retained upon deposition.

The XRR patterns of the precursors contain intensity oscillations (Kiessig fringes) due to the finite thickness of the entire film and Bragg maxima due to the repeating sequence of elemental layers in the precursor (Figure V.2). The position of the first order Bragg reflection due to the layering of the precursor systematically shifts to lower angle as the thickness of the PbSe layer (q) is increased. For the q = 1 sample, the Bragg maxima is

much broader than for the other samples and shifted to lower angle than expected, indicating that the repeating period is thicker than the targeted value. The precursor modulation length, calculated from the total thickness divided by the divided by the number of repeating units deposited, is as expected from the deposition process (Figure V.4). This discrepancy suggests that there must have been long range surface diffusion during the deposition that resulted in the precursor consisting of domains with different structures.

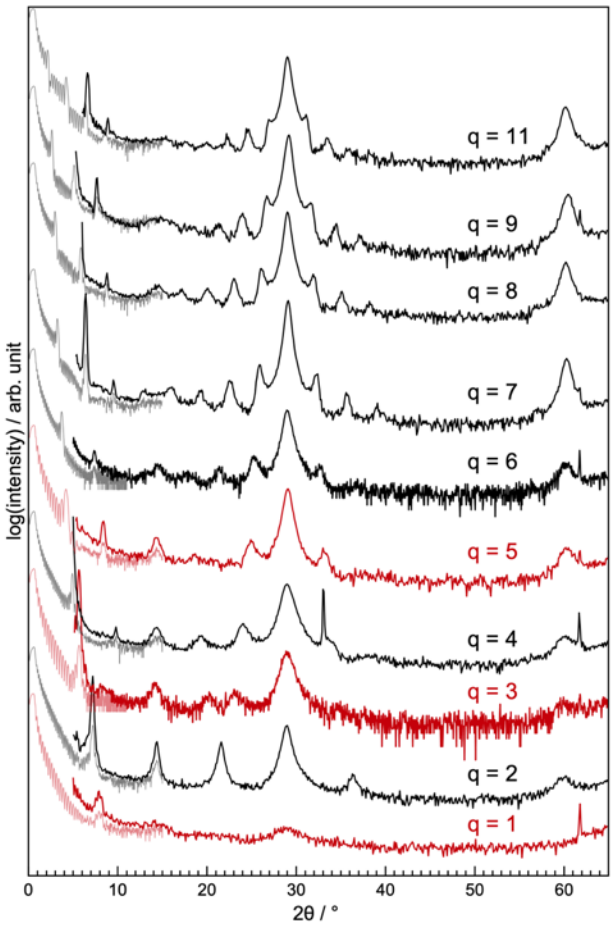

Figure V.3. X-ray diffraction patterns of all precursors show two different groups based on the relationship of the high angle peaks with the precursor modulation length.

The high angle diffraction patterns (Figure V.3) of the as deposited samples have high angle reflections that indicate that the samples have already begun to self-assemble

during the depositions. The positions of these weak reflections divide the precursors into two groups. The weak reflections for the precursors with even order q and odd q ≥ 7 monolayers thick are at positions consistent with their being indexed as 00l reflections yielding a *c*-axis unit cell size consistent with the precursor modulation length and the targeted nanoarchitecture. The precursors with q = 1, 3 and 5 all have weak reflections in the high angle scans that cannot be indexed as *00l* reflections from the precursor modulation length. For q = 3 and 5, the positions of the weak reflections indicate that the precursor modulation length is double that expected from the deposition sequence. For the q = 1 sample, the weak reflections are not related at all to the precursor modulation length, consistent with disproportionation during the deposition process.

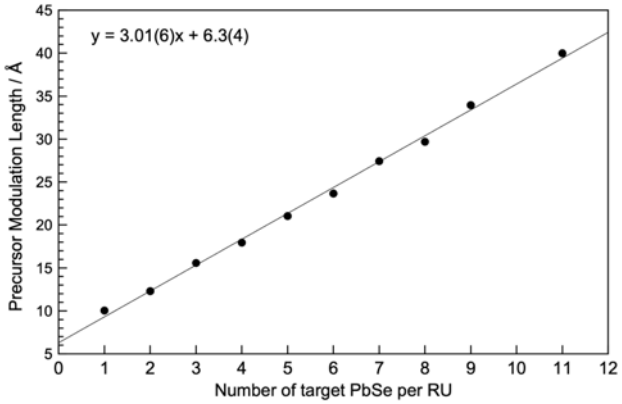

Figure V.4. The dependence of the precursor modulation length on the number targeted number of PbSe monolayers per RU.

The XRF, XRR and XRD data indicate that the precursors with q of 2, 4 and six or larger all have the correct the number of atoms of each element and the targeted nanoarchitecture. The precursor with q = 1 has the required number of atoms, however the XRR and XRD data indicates that nanoarchitecture is more complicated that the desired

sequence of a Pb|Se monolayer and a V|Se bilayer. The XRD data for the precursors with q = 3 and 5 indicates that these precursors have a modulation length that is twice that expected from the deposited sequence of layers. The precursor modulation length (λ) calculated from indexing the 00*l* reflections for samples with q greater than 1 and plotted versus q, the number of PbSe monolayer per repeat unit are shown in Figure V.4. For the q = 3 and 5 samples, ½ of modulation length calculated falls where expected based on the deposition parameters, our XRF measurements and the thicknesses of the even layer thickness samples q = 2, 4 and 6. For the q = 1 sample, the modulation length calculated from the total thickness divided by the number of repetitions of the elemental layer sequence deposited is close to the extrapolated value from the even PbSe layer thickness samples. The linear relationship between the precursor modulation length and target number of PbSe monolayers has a slope of (3.01(6) Å), which is the thickness of an elemental Pb|Se layer with the number of Pb and Se atoms calculated to yield a monolayer of PbSe. The intercept (6.3(4) Å) is the thickness of the elemental V|Se bilayer with the number of atoms calculated to yield a VSe_2 unit. The intercept is slightly thicker than the thickness of a crystalline VSe_2 trilayer because the precursors do not fully crystallize during deposition and are less dense than fully crystallized layers. The linear relationship in Figures 1 and 4 reflects the reproducibility of the precursor preparation.

X-ray reflectivity (XRR) and specular x-ray diffraction (XRD) scans were collected after annealing the precursors at different temperatures to obtain information on how the structure of the precursors evolve. Three different behaviors were observed that depend on the number of target PbSe monolayers per repeating unit of the precursor.

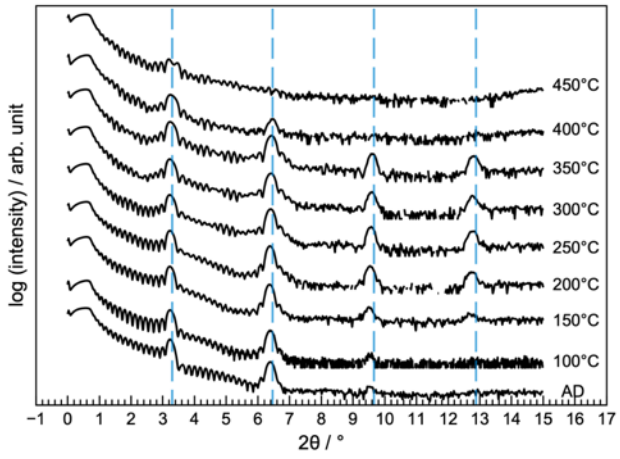

Figure V.5. X-ray reflectivity data collected after annealing the q = 7 precursor at the designated temperatures. The blue dashed lines (---) are the expected peak positions for a $[(PbSe)_{1+\delta}]_7(VSe_2)_1$ heterostructure.

Precursors with even order q and odd q ≥ 7 monolayers thick evolved to form the targeted heterostructures. The x-ray reflectivity scans collected on the q = 7 precursor (Figure 5) collected as a function of temperature illustrates this behavior. The *001* and *002* reflections change in intensity and shift to lower angles as the annealing temperature is increased. The *003* reflection increases in intensity when the precursor is annealed between 150 and 350 °C. The *004* reflection first appears after the 150ºC annealing and grows in intensity up to and including the 350°C annealing temperature. These changes all indicate that the nanoarchitecture is preserved and long range order increases as the sample self-assembles into the targeted heterostructure. The Kiessig fringes due to the reflection of x-rays from the top and bottom of the films and the Laue interference pattern due to the finite number of unit cells in the films are present at each step, suggesting that the films remain smooth throughout the annealing process. The film thickness decreases a small amount (<5%) as long range order develops. The number of diffraction orders decreases when the

precursors are annealed above 350°C as the sample, indicating that the initial nanoarchitecture is being lost.

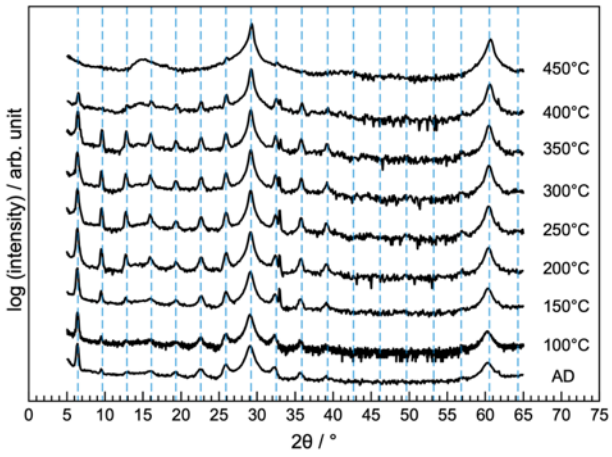

Figure V.6. Specular x-ray diffraction data collected after annealing the q = 7 precursor at the designated temperatures. The blue dashed lines (---) are the expected peak positions for $[(PbSe)_{1+\delta}]_7(VSe_2)_1$.

The specular diffraction patterns collected at higher angles as a function of annealing temperature support the conclusions drawn from the XRR data. Figure V.6 contains the data collected on the q = 7 precursor. Broad high order *00l* reflections (>15º) are observed in the as deposited precursor, indicating that the sample forms domains with significant long range order during the deposition. The higher angle reflections have the same periodicity (27.62(8) Å) as the low order (<15º) *00l* reflections (27.6(3) Å), suggesting that the nucleated structure has the same layering of the precursor. As the temperature is increased to 350ºC, the low and high order *00l* reflections increase in intensity and converge to have similar peak widths and to positions that give a c-lattice parameter of 27.52(6) Å. At 400ºC, the *00l* reflections start to diminish and we see the growth of a broad VSe_2 reflection at ~13°. At 450 ºC, the high angle scan contains only the

001 VSe_2, and *002* and *004* PbSe reflections, while the XRR scan shows a very reduced intensity of the *001* reflection from the heterostructure. This suggests that the superlattice is decomposing to its thermodynamic products.

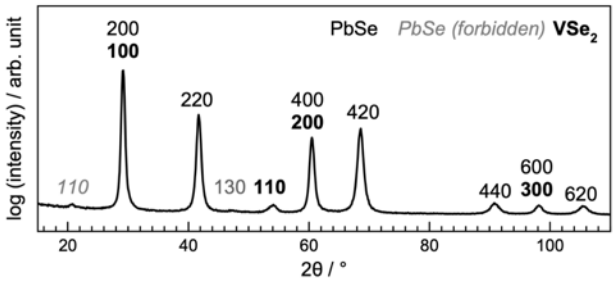

Figure V.7. In-plane x-ray diffraction pattern of a q = 7 precursor annealed at 300ºC.

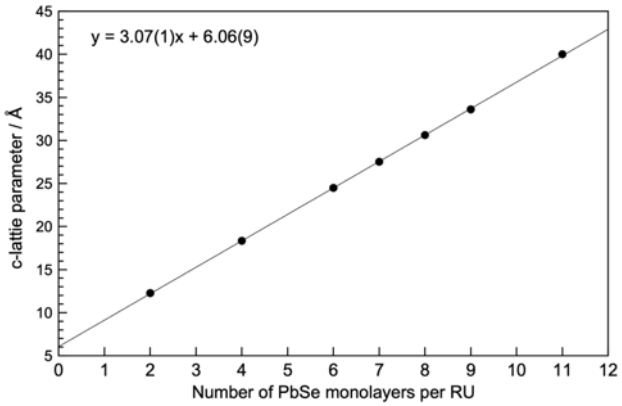

Figure V.8. The c-lattice parameters of even and odd samples with q ≥ 7 monolayers as a function of q.

Further evidence for the formation of the targeted heterostructures at moderate annealing temperatures comes from grazing incidence in-plane x-ray diffraction (GIPXRD) of the precursors after annealing to 300°C and the systematic change in *c*-axis lattice parameters of the products as q is varied. The in-plane diffraction of the q = 7 precursor after annealed at 300ºC, shown in Figure V.7, is representative of the samples

with even order q and odd q ≥ 7. All the observed reflections can be indexed as *hk0* reflections from either a hexagonal or a square unit cell. The in plane lattice parameter of the hexagonal unit cell (3.40(1) Å) is close to those reported for bulk VSe_2 (3.359 Å). The lattice parameter of the square unit cell (6.12(1) Å) is close to that reported for bulk PbSe (6.122 Å). Since only *00l* and *hk0* reflections are observed in the specular and in-plane x-ray diffraction respectively, the heterostructure is crystallographically-aligned to the substrate with the PbSe <*100*> and VSe_2 <*100*> planes parallel to substrate. The *c*-lattice parameters of the annealed q = even and q ≥ 7 precursors are plotted against q and shown in Figure 8. The linear relationship between the *c*-lattice parameters and q suggests that heterostructures in this category can be predictably synthesized with the correct precursor. The slope (3.07(1) Å) is close to the value of half of a PbSe unit cell (6.117 Å).[25] The y-intercept (6.06(9) Å) is close to the *c*-lattice parameters of bulk VSe_2 (5.96-6.11 Å).[26]

HAADF-STEM images were collected on annealed precursors to provide additional structural information on the products formed. Figure V.9 contains representative images from the q = 7 sample. The whole film image (Figure V.9a) shows that there is a consistent layered structure over the entire sample. The higher magnification (Figure V.9b) shows that most of the sample consists of a repeating unit cell containing 1 VSe_2 and 7 PbSe monolayers. There are local regions, however, where a repeating sequence of 6 PbSe monolayers - VSe_2 - 8 PbSe monolayers - VSe_2 (Figure V.9b, white box) replaces two 7 PbSe monolayers -VSe_2 sequences. This replacement is random and does not occur very often. The local information obtained from the HAADF-STEM data is consistent with the diffraction data discussed previously. The q = 7 sample forms mostly

$[(PbSe)_{1+\delta}]_7(VSe_2)_1$ with local regions consisting of $[(PbSe)_{1+\delta}]_6(VSe_2)_1[(PbSe)_{1+\delta}]_8(VSe_2)_1$.

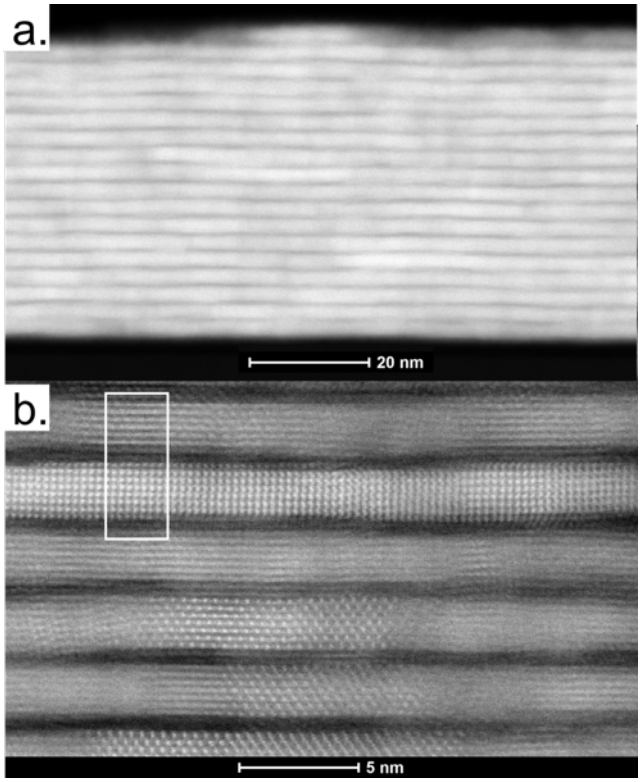

Figure V.9. Representative HAADF-STEM image of an annealed q = 7 precursor.

A different behavior as a function of annealing was observed for the q = 3 and 5 precursors, where the as deposited precursors have reflections that suggest a doubling of the modulation length. XRR scans for the q = 3 precursor collected as a function of annealing temperature are shown in Figure V.10. Superimposed on the diffraction scan are blue vertical lines locating angles where reflections are expected from the targeted q = 3 product and red lines vertical lines showing where additional reflections are expected for a

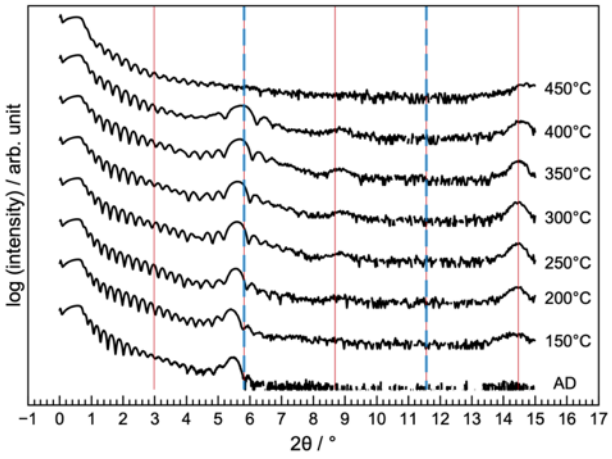

Figure 10. X-ray reflectivity data collected after annealing the q = 3 precursor at the designated temperatures. The blue dashed lines (---) are the expected peak positions for a $[(PbSe)_{1+\delta}]_3(VSe_2)_1$ heterostructure and the red solid lines are the expected positions for twice the unit cell size of the aforementioned.

precursor with a doubled modulation length. The 001 reflection of the precursor persists up to 400°C, but the expected second order reflection from the precursor does not appear (at the blue vertical dashed line at ~5.5 degrees). Reflections do grow in, however, at the approximate locations expected for the third and fifth order reflections from a doubled modulation length. The diffraction intensities decrease when annealed at 400°C and only Kiessig fringes from the interference between the front and back of the film remain after the 450°C anneal. Specular diffraction data collected on the q = 3 sample, shown in Figure V.11, provides additional information about the structural changes that occur during annealing. The diffraction pattern of the as deposited sample contains several higher angle reflections indicating long range ordering occurs during the deposition process to form a modulation length twice that which was expected. The high angle *00l* reflections intensify for annealing temperatures between 150°C and 400°C and all of the observed reflections

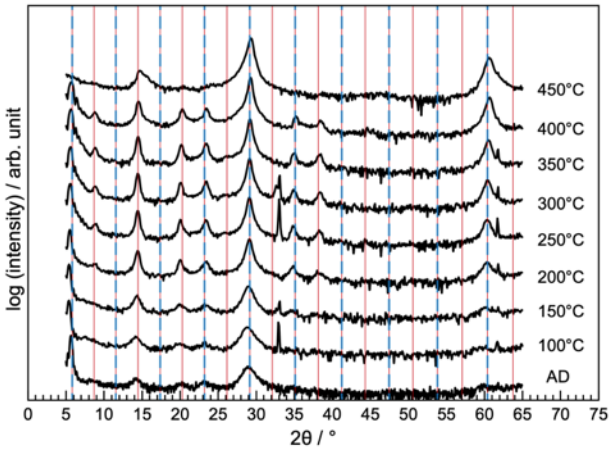

Figure 11. Specular x-ray diffraction data collected after annealing the q = 3 precursor at the designated temperatures. The blue dashed lines (---) are the expected peak positions for a $[(PbSe)_{1+\delta}]_3(VSe_2)_1$ heterostructure and the red solid lines are the expected positions for twice the unit cell size of the aforementioned.

can be indexed as *00l* reflections of a unit cell with twice the repeating period expected from the deposited elemental layers. The positions of several reflections deviate from that calculated from the average *c*-axis lattice parameter (30.5(1) Å at 350°C), which is probably a consequence of stacking faults apparent in the HAADF-STEM data discussed in a later paragraph. Only *001* VSe_2 and *002* and *004* PbSe reflections are observed in the specular scan after annealing at 450°C, indicating that the sample has disproportionated. In-plane x-ray diffraction data collected on a q = 3 precursor annealed at 300°C contains maxima that can be indexed as *hk0* reflections from a hexagonal base (a = 3.42(1) Å) and square base (a = 6.12(1) Å) (See Figure B.1). These lattice parameters are consistent with the formation of VSe_2 and PbSe respectively. The XRR, specular and in-plane diffraction data indicate that the q = 3 and 5 precursors self-assemble to form superlattices with twice the expected *c*-axis lattice parameter. The unit cell consists of twice the number of

crystallographically-aligned VSe_2 and PbSe layers per repeating unit expected from the deposition sequence used to form the precursor.

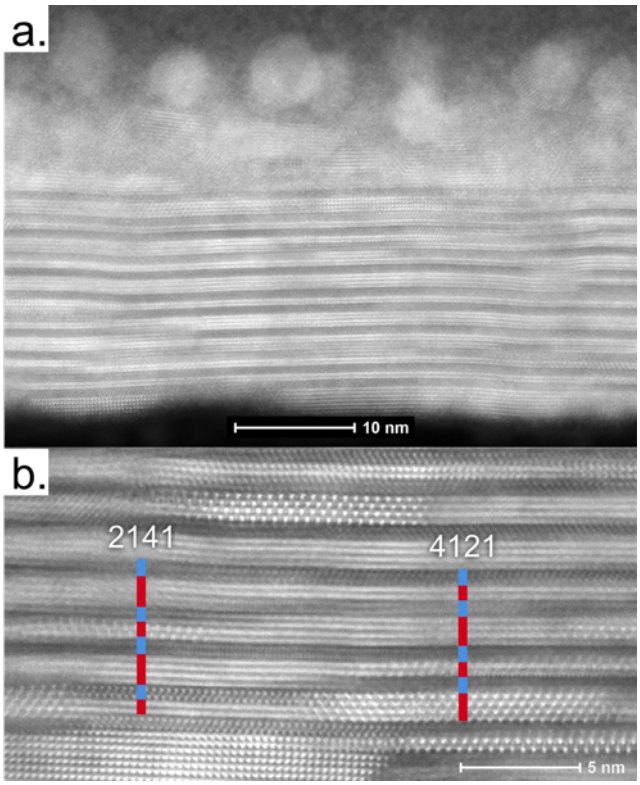

Figure V.12. Representative HAADF-STEM image of an annealed q = 3 precursor.

HAADF-STEM images were collected to corroborate on the structure of the self-assembled q = 3 precursor. The sample (Figure V.12a) contains a surface region containing light and dark regions without regular order above a layered film that contains light layers (PbSe) of various thicknesses separate by dark layers (VSe_2). Large Pb-rich and V-rich areas are observed at the top of the film indicating that some of the film has already disproportionated. Within the layered part of the film, there are small domains that contain a regular local stacking pattern. The higher magnification image (Figure V.12b) shows that the light layers are rock salt PbSe and the dark layers are CdI_2-structured VSe_2. Small

regions with different stacking sequences appear adjacent to one another. For example $[(PbSe)_{1+\delta}]_2(VSe_2)_1[(PbSe)_{1+\delta}]_4(VSe_2)_1$ regions labelled as '2141' and $[(PbSe)_{1+\delta}]_4(VSe_2)_1[(PbSe)_{1+\delta}]_2(VSe_2)_1$ regions labelled as '4121' are adjacent to one another. These observed "isomer" regions in the film cannot be distinguished using diffraction alone. Presence of these regions suggests that there is lateral diffusion during the deposition process. The HAADF-STEM image is consistent with the diffraction data.

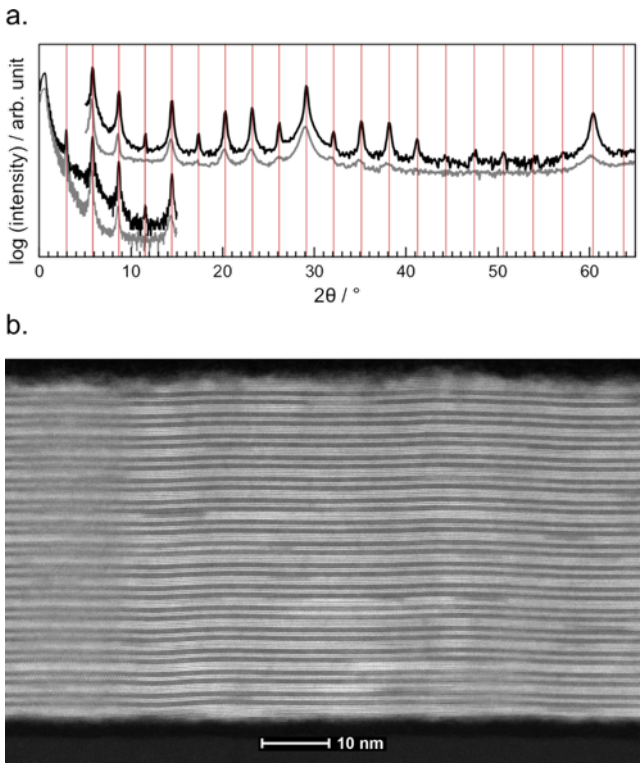

Figure V.13. (a) Specular x-ray diffraction and x-ray reflectivity patterns of the as-deposited (gray) and annealed (black) ‘2141’ precursor (b) HAADF-STEM image of the annealed precursor film.

We prepared a precursor for one of the q = 3 products, ’2141’ to demonstrate the importance of designing a precursor such that only short range diffusion are required to form the targeted. Specular diffraction and x-ray reflectivity pattern of the as-deposited and

annealed precursors are shown in Figure V.13a. The as deposited precursor has significantly more long range order that the q = 3 precursor discussed previously. The self-assembled heterostructure forms at lower temperatures and the diffraction maxima are significantly more intense and narrower than those shown in Figure V.10 and V.11, reflecting a more coherent structure. The cross section HAADF-STEM image of the entire film thickness shown in Figure V.13b contains very distinct PbSe and VSe_2 layers and a regular stacking pattern across the entirety of the film. This image is similar to those obtained on films with even order q and odd $q \geq 7$ monolayers, where also only short range diffusion in the precursor was required during self-assembly.

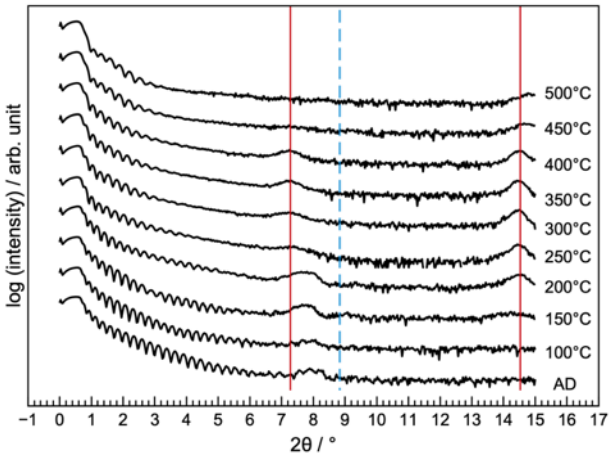

Figure V.14. X-ray reflectivity data collected after annealing the q = 1 precursor at the designated temperatures. The blue dashed lines (---) are the expected peak positions for the calculated modulation length and the red solid lines are the expected positions for a $[(PbSe)_{1+\delta}]_2(VSe_2)_1$ heterostructure.

The precursor with q = 1 evolves differently than all of the other samples. The XRR data as a function of annealing temperature is shown in Figure V.14. Vertical blue lines indicate the reflections expected from a period calculated from the total thickness divided

by the total number of layers deposited. Vertical red lines indicate the reflections expected for $[(PbSe)_{1+\delta}]_2(VSe_2)_1$. The angle of the first reflection observed is significantly smaller than expected in the as deposited sample and shifts further to lower angles as the precursor is annealed at increasing temperatures. A second reflection appears after annealing at 150°C and its intensity increases after annealing at higher temperatures. At 300°C, both of these reflections can be indexed as 00*l* reflections of a heterostructures with a 12.24(3) Å *c*-axis lattice parameter (red lines), which matches that expected for $[(PbSe)_{1+\delta}]_2(VSe_2)_1$.

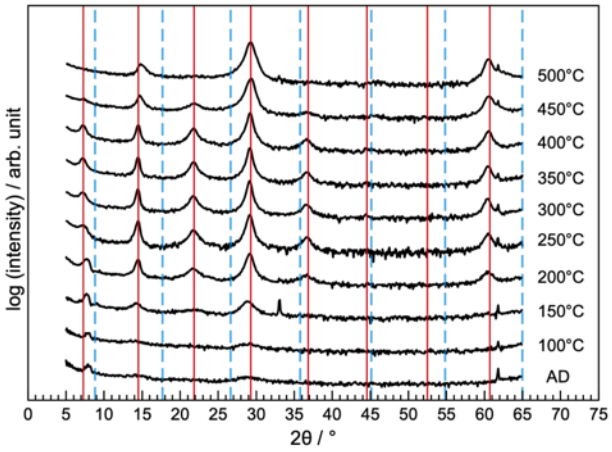

Figure 15. Specular x-ray diffraction data collected after annealing the q = 1 precursor at the designated temperatures. The blue dashed lines (---) are the expected peak positions for the calculated modulation length and the red solid lines are the expected positions for a $[(PbSe)_{1+\delta}]_2(VSe_2)_1$ heterostructure.

The specular diffraction data, Figure V.15, contains additional maxima that increase in intensity as annealing temperatures are increased. All of the reflections can be indexed as 00*l* reflections from $[(PbSe)_{1+\delta}]_2(VSe_2)_1$ after annealing at 250°C. The even order reflections appear to have a narrower peak width than the other reflections and higher intensities compared to what is expected from $[(PbSe)_{1+\delta}]_2(VSe_2)_1$, suggesting that a

second phase, VSe_2, is likely present. This is consistent with the XRF-determined composition of the film. After annealing at 500°C, the XRR pattern contains only Kiessig fringes and the diffraction pattern contains maxima that can be indexed as the *001* reflection from VSe_2 and the *002* and *004* reflections from PbSe.

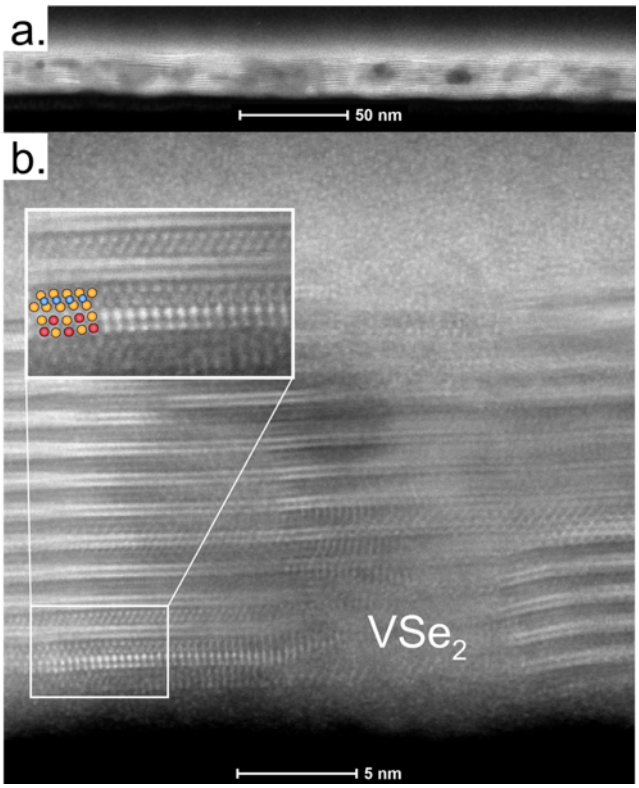

Figure V.16. Representative HAADF-STEM image of an annealed q = 1 precursor.

The structure of the self-assembled q = 1 precursor was further probed by collecting HAADF-STEM data. The whole film cross section (Figure V.16a) clearly demonstrates a different behavior as the others as the sample contains dark regions laterally separated from bright regions. This indicates segregation of large grains of VSe_2 from PbSe. Figure 16b shows that the brighter regions consist of alternate layers of VSe_2 and PbSe bilayers while the darker regions are VSe_2. A closer look at the bright region (white box in Figure V.16b)

suggests that the local structure of the film consists of a mixture of $[(PbSe)_{1+\delta}]_2(VSe_2)_1$ and VSe_2.The segregation into these two distinct regions suggests that there is lateral diffusion taking place during deposition. A consistent theme from the HAADF-STEM data is that the formation of an even number of monolayers of PbSe appears to be favored over odd layers, especially for small odd q. The as-deposited XRR and XRD suggests that the formation of even number of monolayers stems from the initial structure of the precursor. Based on the data presented above, all the precursors deposited only had PbSe bilayers.

The underlying assumption of the MER synthesis approach is that preparing a precursor with the nanoarchitecture of a specific target compound enables its synthesis because atoms do not need to move large distances to form this product relative to more stable alternatives. The nanoarchitecture of the precursor is experimentally controlled by the sequence of elements and the amount of each element deposited. In the system investigated here, the deposition sequence produced precursors with close to the desired structure for q = even and $q \geq 7$, but the nanoarchitecture of the precursors with q = 1, 3, and 5 were different than expected from the deposition process. The data presented above suggest that the atoms in the Pb|Se layer in the q = 1, 3, and 5 samples underwent significant lateral diffusion during the deposition process to form PbSe layers containing an even number of PbSe monolayers. For the q = 1 sample, lateral diffusion of atoms in the V|Se layer is also required to explain the uniform thickness and the observed modulation length of the precursor. The precursors preferred to form a defect-rich film with bilayers rather than a fully ordered film with a PbSe layer containing an odd number of monolayers.

DFT calculations shed light on the underlying reason for this behavior. Different thickness layers (q = 2-6) of PbSe with ideal rock salt atomic positions and 001 surfaces

separated by a nanometer of vacuum were allowed to relax to minimize the energy. Figure 17 contains the minimum energies obtained as a function of q, the number of monolayers of PbSe in the block. Energies of odd numbered blocks are greater than the convex hull

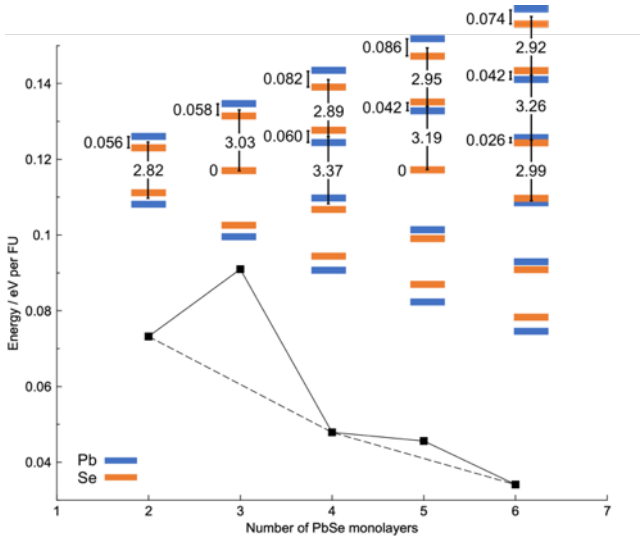

Figure V.17. DFT calculated energies and structures of PbSe blocks in vacuum with varying numbers of monolayers (q). Shown above are visual representations of the relative Pb and Se atom positions in the z-axis direction.

created by the even numbered blocks, indicating that it is more favorable to form a mixture of adjacent even numbered blocks than an odd numbered blocks. The difference in energy between the convex hull and the odd numbered block decreases as the thickness of the odd numbered block increases. There is also a general decrease in energy as the thickness of the block is increased, which is due to the larger number of internal atoms compared to those on the surface. Inter- and intra-layer distortions are observed due to the termination of the 3D rock salt structure at the interfaces, as illustrated by the images of each structure shown in Figure V.17. Within a monolayer, Pb and Se atoms deviate from the ideal rock salt positions by a shift along the z-axis, with the Pb atoms moved to the outside and the

Se atoms moved towards the center. There is also a distinct alternation of short and long distances between monolayers in the even thickness PbSe blocks, resulting in bilayers. The largest puckering occurs in the surface layer, regardless of the thickness of the PbSe block, but the distortion in the surface layer decreases in magnitude as the PbSe monolayers approach the interior. This reflects the trade-off between the surface reconstruction to lower the surface energy and distortions in the interior layers due to the surface reconstruction. In blocks with an odd number of monolayers the bulk cannot form bilayers as the surface reconstructs resulting in their higher energy relative to the even thickness PbSe layers. These energy calculations provide an explanation for the observed as deposited structure and the final structures formed. For the q = 1 sample, the energy difference between a single PbSe monolayer between VSe_2 layers versus ½ the surface being a bilayer and ½ without PbSe is high enough that the system reconstructs during the deposition as the atoms diffuse on the surface. Annealing results in continued disproportionation of the sample into $[(PbSe)_{1+\delta}]_2(VSe_2)_1$ and VSe_2. High temperatures and long times are required due to the significant diffusion distances. For the q = 3 and 5 samples, the energy difference between regions with an odd monolayer thickness q versus alternating layers with q-1 and q+1 is still large enough to reconstruct the PbSe layer during the deposition. Annealing continues the self-assembly of the favored even layer thickness PbSe regions, since the precursor already has bilayer nanoarchitecture. For q = 7, the energy difference is not enough to drive the system to disproportionate a layer with a thickness of q monolayers into q-1 and q+1 layers during the deposition.

V.4 Conclusions

The data presented in this paper illustrates the importance of the nanoarchitecture of precursors in the self-assembly of the precursors and presents surprising evidence for significant lateral diffusion of atoms during the room temperature deposition of precursors. Precursors with nanoarchitecture close to a specific product self-assemble during the deposition and subsequent low temperature annealing via a near diffusionless process. Precursors that have a nanoarchitecture that differs from a potential product require longer diffusion distances to self-assemble into specific products, which requires higher annealing temperatures and longer annealing times. Atoms can undergo long range surface diffusion during the deposition process to form more favorable configurations than those targeted using the sequence of elemental layers. Surprisingly, even though long range diffusion is occurring, the precursors evolve into metastable products rather than completely disproportionating. Limiting diffusion via low temperatures restricts the topology of the free energy landscape that can be explored, making the structure of the precursor critical in determining what products form.

In the specific system investigated here, the stability of puckered PbSe bilayers drives the lateral diffusion of Pb and Se atoms during both deposition and when annealing the films to form coherent bilayers. Precursors with an odd number of PbSe planes (q = 1, 3, and 5) cannot be prepared with room temperature deposition because long range surface diffusion occurs during deposition to form precusors with regions of even number of PbSe planes. The higher energy of odd monolayer thick PbSe blocks is associated with the inability to retain the puckering distortion found in even monolayer thick blocks. Lowering the temperature of the substrate during deposition might decrease surface diffusion enough

to prepare precursors with odd monolayer thick blocks. Similar odd-even alternation based on energy differences between even and odd conformations has been observed in self assembled alkane monolayers and the melting points and dynamical behavior of alkanes.[27–30] The results obtained herein suggest that calculations on the properties of monolayers and thin layers of 3D materials should include the relative energy as a function of thickness to aid experimentalists in choosing substrates and synthetic conditions.

V.5 Bridge

This chapter builds on the foundation of MER synthesis established from previous chapters: the importance of controlling the number of atoms and nanoarchitecture of the precursor. We expand this concept in the succeeding chapter by targeting the compound $[(SnSe_2)_{1+\delta}]_1(VSe_2)_1$, another charge density wave material candidate. The new target material is closely related to a previously studied, highly kinetically stable compound $[(SnSe)_{1+\delta}]_1(VSe_2)_1$. In order to drive the self-assembly towards the desired reaction pathway, the precursor must be precisely designed so that the $SnSe_2$ compound forms and not the SnSe compound.

CHAPTER VI

CONTROLLING THE SELF-ASSEMBLY OF NEW METASTABLE TIN VANADIUM SELENIDES USING COMPOSITION AND NANOARCHITECTURE OF PRECURSORS

Authorship Statement

This chapter has been submitted for publication, with me as the primary author. Taryn M. Kam collected x-ray diffraction data. Renae N. Gannon and Dr. Ping Lu collected HAADF-STEM data. Dr. David C. Johnson, my adviser and group leader, and assisted in the preparation of this manuscript.

VI.1 Introduction

Molecular synthesis is powerful, with chemists being able to perform total syntheses of complex molecules through a series of carefully designed steps beginning from simple precursors.[1] Several important factors have contributed to the development and success of this field. One factor is the ability to predict the structure of potential kinetically stable compounds using simple bonding rules (the octet rule and the 18-electron rule).[2,3] A second factor is the diversity of reagents and catalysts that can be used to transform a single functional group, allowing a reaction to be possible for a large number of substrates. A third factor is the typically homogeneous nature of reacting systems, where reactants dissolve in solvents while maintaining their structure. Most of the structure of the different reactants is preserved in the product molecules, as targeted reactions break and make specific bonds. NMR and other spectroscopies give detailed information about speciation, enabling the kinetics of the transformation from reactants to products can be investigated.[4,5] This has enabled molecular chemists to develop rules based on reaction

mechanisms to modify reaction parameters to control reaction pathways.[6] Since intermediates in a multistep synthesis can be purified, a sequence of specific reactions can be planned using retrosynthetic analysis to synthesize complicated molecules.[7]

In contrast, solid state synthesis is considered "as much art as science", since the process is mainly experience- and intuition-driven.[8] This reflects important differences between the synthesis of extended structures and molecules. For example, it is much more challenging to predict the structure of potential products, because many metallic elements can have a variety of oxidation states and coordination numbers.[9] The formation of an extended structure also involves the repeated formation of specific bonds to form crystals with macroscopic amounts of atoms. This self-assembly of the crystal structure cannot be done using stepwise reactions. Hence, synthesis approaches are less developed and the analytical techniques used to follow reactions often require specialized instrumentation.[10] While the synthesis approach of extended solids using fluids (fluxes, mineralizers, or supercritical fluids) as solvents is similar in many respects to molecular synthesis,[11–13] the reactants typically do not maintain their structure upon dissolution, and very little is typically known about the speciation that occurs in the liquid phase.[14] Spectroscopy and other reaction monitoring methods are also more difficult to implement due to typically higher reaction temperatures, opaque fluid phases, and more challenging NMR nuclei.[15,16] Diffusion is the rate-limiting step in the direct reaction of solids at high temperature,[17] where reactions occur at the interfaces between particles. Since many different interfaces with different crystallographic orientations are reacting between different elements (A-B, B-C, A-C), different reactions will be occurring at different interfaces forming different products at different rates.[18] Most analytical approaches only provide the sum of all of these

reactions, making kinetic studies challenging. In most reactions to form extended solids, high temperatures and long times are typically used, resulting in the formation of only thermodynamically stable compounds.[19,20] While the importance of solid state reaction mechanisms to develop kinetically controlled synthesis approaches has been recognized, the field remains understudied.[21,22]

Here we use precursors made of a repeating sequence of Sn|Se|V|Se elemental layers to selectively form the metastable solids $[(SnSe_2)_{0.80}]_1(VSe_2)_1$ and $Sn_xV_{1-x}Se_2$. X-ray reflectivity and x-ray diffraction (specular and in-plane) were used to follow the self-assembly of $[(SnSe_2)_{0.80}]_1(VSe_2)_1$. Laue oscillations observed in the XRR patterns enable us to determine the number of unit cells of $[(SnSe_2)_{0.80}]_1(VSe_2)_1$ perpendicular to the substrate as a function of annealing temperature. In-plane XRD patterns enable us to independently follow the lateral growth of $SnSe_2$ and VSe_2. This data was used to develop an atomic scale picture of the reaction mechanism. The proposed reaction mechanism was tested by modifying the nanoarchitecture of the initial precursor to synthesize the new metastable alloy, $Sn_xV_{1-x}Se_2$. Using an energy landscape, we rationalized why local composition and nanoarchitecture allowed us to discriminate between different reaction pathways.

VI.2 Experimental

Thin film multilayer precursors were deposited on (100) oriented Si wafers with native oxide using a custom-built high vacuum physical vapor deposition (PVD) chamber with pressures maintained below 2 x 10^{-7} torr. Se (Alfa-Aesar, 99.999%) was deposited using a Knudsen effusion cell, while V (Alfa-Aesar, 99.7%) and Sn (Alfa-Aesar, 99.98%)

were deposited using 6 keV electron beam guns. More detailed information about the instrument setup is found elsewhere.[23] The thickness of each element deposited at each step was monitored by quartz crystal microbalances found above each elemental source. A custom-made LabView code controls the opening and closing of pneumatic shutters to control the sequence and amount of each element deposited.

The areal density (in atoms/Å^2) of each element was measured using x-ray fluorescence (XRF) on a Rigaku ZSX Primus II spectrometer. For each sample, the background signal was subtracted using the actual measurement from blank substrates as described by Hamann and co-workers.[24]

Precursors were annealed on a hotplate in a drybox with an inert atmosphere (O_2 < 0.8 ppm). X-ray reflectivity (XRR) and specular x-ray diffraction (XRD) patterns were collected on a Bruker D8 diffractometer equipped with Cu Kα radiation. One piece of Precursor I was annealed for 5 minutes at various temperatures to determine the processing conditions to form $[(SnSe_2)_{0.80}]_1(VSe_2)_1$. A second piece of Precursor I and Precursor II were annealed at the optimum processing conditions. The Kiessig and Laue oscillations observed in the XRR pattern were used to calculate the thickness of the film via a modified form of Bragg's Law and the size of the coherently scattering domains, respectively. Grazing incidence in-plane diffraction (GIXRD) patterns were collected on a Rigaku Smartlab diffractometer also equipped with Cu Kα radiation. A model for the position of the atomic planes along the c axis was optimized by Rietveld refinement of the specular x-ray diffraction patterns using the GSAS-II.[25] LeBail fitting of the in plane x-ray diffraction using the FullProf Suite was used to refine lattice parameters.[26]

A thin cross-section of the film was prepared with an FEI Helios NanoLab^{TM} 600i DualBeam FIB-SEM using standard lift-out procedures. Scanning transmission electron microscopy data was collected on FEI Titan^{TM} G2 80-200 STEM with a Cs probe corrector and ChemiSTEM^{TM} technology (X-FEG^{TM} and SuperX^{TM} EDS with four windowless silicon drift detectors) operated at 200 kV. High angle annular dark field (HAADF) images were taken with an electron probe of size (FWHM) of about 0.13 nm, current of ~75 pA, convergence angle of 18.1 mrad and using an annular dark-field detector with a collection range of 60-160 mrad.

VI.3 Results

Two multilayer precursors (I and II) with repeating structure Sn|Se|V|Se were deposited. The lattice parameters of bulk VSe_2 and $SnSe_2$ were used to calculate the required number of atoms in each Sn|Se|V|Se sequence to form Se-M-Se trilayers of both VSe_2 and $SnSe_2$.[27,28] Precursor I used these targets and the Sn|Se|V|Se sequence was repeated 41 times. Precursor II contained the Sn|Se|V|Se sequence repeated 82 times, with each sequence containing one half the number of atoms needed to form each Se-M-Se trilayer. The two precursors containing the same number of atoms but with a different nanoarchitecture. The total number of atoms of Sn, V, and Se per $Å^2$ (areal density) were measured using XRF and summarize in Table VI.1 along with the targeted values. The measured values of Sn and V for both precursors are within error of the target amounts. There is a slight excess in the amount of Se in Precursor II.

The evolution of a piece of precursor I was followed as a function of annealing temperature using XRF, XRR and XRD to determine the conditions to form a single-phase

Table VI.1. Number of atoms per unit area determined using XRF compared to target values based on the lattice constants of bulk $SnSe_2$ and VSe_2

Material	Repeating Units	Total number of atoms /Å^2		
		Sn	V	Se
Precursor I	41	3.3(1)	4.3(1)	14.6(4)
Precursor II	82	3.13(9)	4.1(1)	16.6(5)
VSe_2	41	0	4.203(3)	8.406(6)
$SnSe_2^{ref}$	41	3.256(5)	0	6.52(1)

$[(SnSe_2)_{1+\delta}]_1(VSe_2)_1$ sample (Figure VI.1). The XRR scan contains Kiessig fringes from the interference between the front and the back of the deposited film.[30] The spacing of the Kiessig fringes yield a film thickness of 550.8(6) Å and the angle where the Kiessig fringes can no longer be observed yields a surface roughness of ~6 Å. The number of Kiessig fringes observed before the Bragg maxima from the modulation of the electron density in the precursor is consistent with the presence of 41 repeating sequences of Sn|Se|V|Se layers. The position of the first two Bragg reflections from the Sn|Se|V|Se sequence of layers yields a modulation length of 13.5 Å. This is slightly larger than the sum of the *c*-axis lattice parameters of bulk VSe_2 and $SnSe_2$, 12.247(2) Å, since amorphous layers have a lower density than their crystalline counterparts. There is also a broad maximum at ~14° suggesting that nucleation and coherent stacking of dichalcogenide layers occurs during deposition. Scherrer analysis of the linewidth suggests that the thickness of the coherent stacking is only a few layers thick. The XRR and XRF data indicate that the nanoarchitecture of the precursor is close to what was targeted and resembles the desired product.

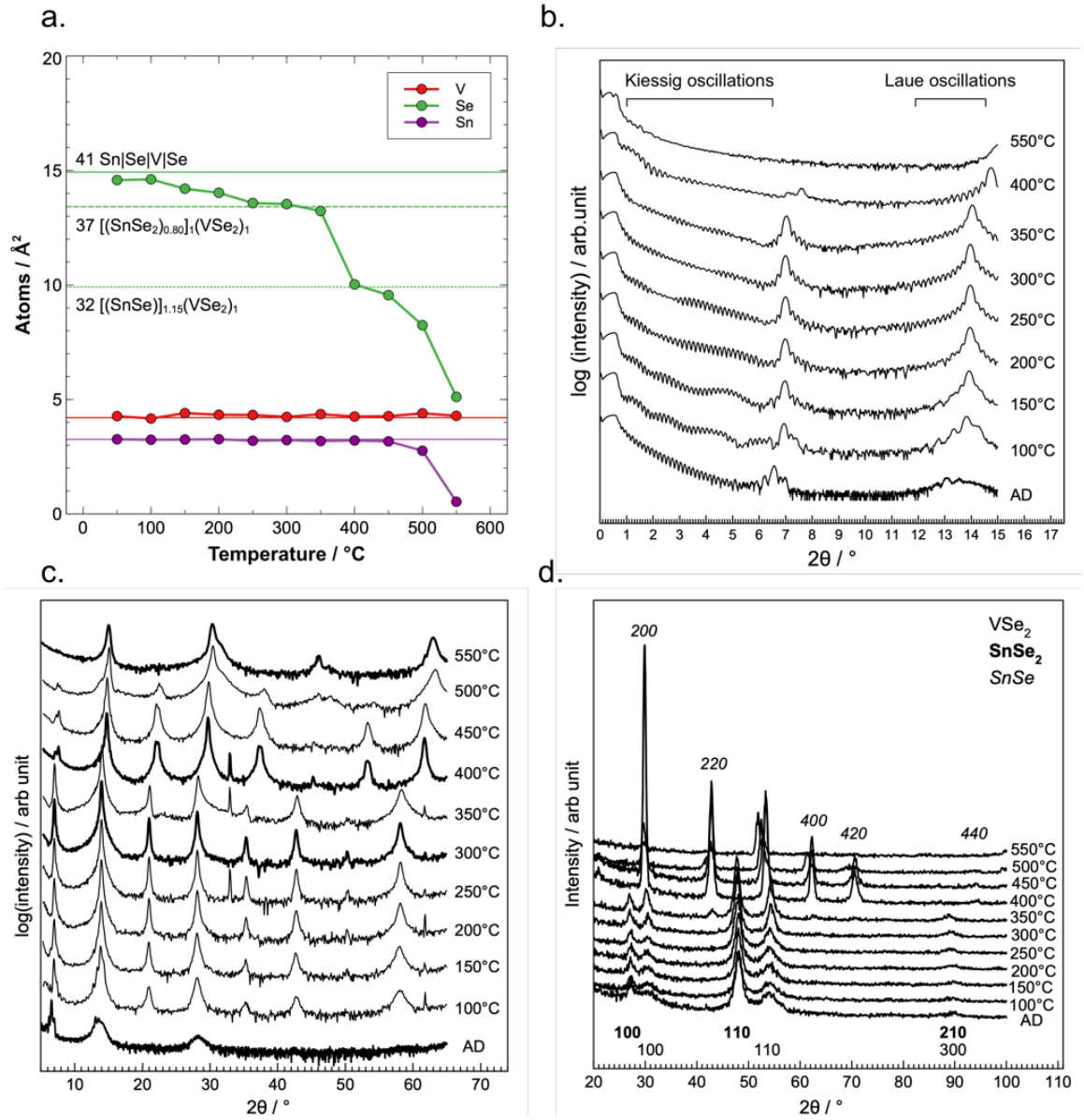

Figure VI.1. Evolution of Sn|Se|V|Se precursor annealed at different temperature steps. (a) The number of atoms per Å^2 of each element measured by XRF at each temperature step and calculated from number of unit cells and a-lattice parameters at RT, 250°C, and 400°C. (b) X-ray reflectivity patterns showing the evolution of the overall film structure (c) Specular x-ray diffraction showing the evolution of the structure perpendicular to the substrate (d) Grazing incidence in-plane x-ray diffraction showing the evolution of the structure in the plane parallel to the substrate.

The diffraction data collected on the as deposited precursor is consistent with the XRR discussion. The specular XRD pattern contains two narrow Bragg reflections from the repeating Sn|Se|V|Se sequence of layers and broad reflections from self-assembly occurring during the deposition of the precursor. The broad reflections at ~14 and 28° indicate that coherent domains have formed. The in plane XRD pattern contains *hk*0 peaks that can be indexed to two hexagonal unit cells, $SnSe_2$ and VSe_2, with a-lattice parameters of 3.78(1) and 3.39(1) Å. The peak widths of $SnSe_2$ is narrower than VSe_2, indicating that there are larger in-plane grains of $SnSe_2$ than VSe_2.

The data collected between 100 and 300°C show that $[(SnSe_2)_{1+\delta}]_1(VSe_2)_1$ gradually self-assembles during this temperature range. The XRF data indicates that there is a small decrease in the amount of Se in this temperature range, which results from evaporation of Se while annealing. The XRR patterns contain an additional low frequency Kiessig oscillation due to the growth of an oxide at the surface of the film. The film thickness calculated from the high frequency Kiessig fringes in the XRR indicate that the film thickness gradually decreases as annealing temperature increases, which is a consequence of both the loss of Se and the increasing density of the film. The first two diffraction maxima shift in angle on annealing at 100°C and then increase in intensity and become narrower as annealing temperature increases. Laue fringes,[31,32] which originate from the finite number of unit cells in the coherently diffracting coherent domains of the film are clearly visible on the diffraction maxima at 14°, and become closer together as annealing temperature increases. This indicates that majority of the coherent domains are the identical thickness, which can be calculated from the frequency of the Laue oscillations. During the growth process, the low angle Bragg reflections from the artificial layering of

the precursor disappears. The specular XRD patterns confirm the formation of $[(SnSe_2)_{1+\delta}]_1(VSe_2)_1$ and corroborate growth of the coherent domains perpendicular to the substrate. Starting at 100°C, long range order starts to develop as additional 00*l* reflections appear at higher angles. These 00*l* reflections increase in intensity, reaching a maximum at 250-300°C. The positions of the 00*l* Bragg reflections yield a c-axis lattice parameter of 12.69(1) Å, which is slightly larger than the sum of the *c*-axis lattice parameters of bulk VSe_2 and $SnSe_2$, 12.247(2) Å, presumably due to the in-plane lattice mismatch preventing nesting of one constituent layer in the other. Laue oscillations, indicating a common size for the different $[(SnSe_2)_{1+\delta}]_1(VSe_2)_1$ domains after each annealing temperature, are observed on the first several Bragg reflections and will be discussed more fully in the next paragraph. The in-plane diffraction patterns reflect the in-plane crystal growth that also occurs during annealing. The $SnSe_2$ *hk*0 reflections exhibited only small changes in peak width and intensity, indicating that most of the $SnSe_2$ is crystalline as deposited and the crystallite size does not increase during the annealing. The VSe_2 *hk*0 reflections, however, noticeable increase in peak intensity and decrease in peak width as annealing temperature increases, indicating an increase in the amount of crystalline VSe_2 and growth of the in plane grain sizes.

The characterization data in this temperature range provide a coherent picture of the self-assembly of $[(SnSe_2)_{1+\delta}]_1(VSe_2)_1$ from the as deposited precursor. Figure VI.2a contains a closer view of the Laue oscillations visible on the 002 reflection of $[(SnSe_2)_{1+\delta}]_1(VSe_2)_1$ after each annealing temperature. The presence of these oscillations indicates that a large majority of the suite of $[(SnSe_2)_{1+\delta}]_1(VSe_2)_1$ domains at each temperature are the identical size and an integral number of unit cells thick, which can be

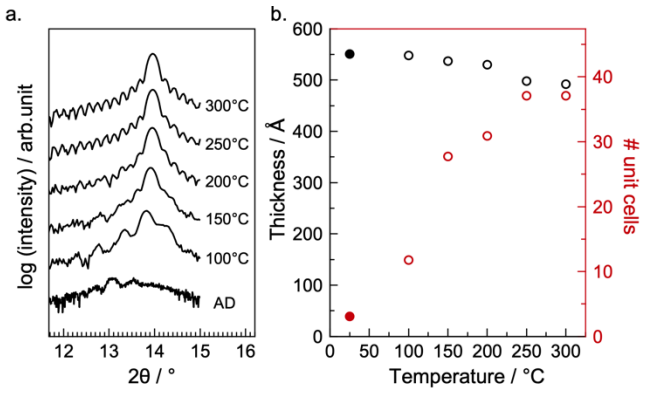

Figure VI.2. (a) Laue oscillations coming from the coherent film thickness at different temperatures. (b) Kiessig (black circles) and Laue (red circles, left axis) film thickness, and the number of unit cells (red circles, right axis) formed at each annealing temperature. The size of the coherent domain in the as deposited sample (filled red circle) is estimated from the line width of the 002 reflection.

calculated from the spacing of the Laue oscillations. Figure VI.2b graphs the change in the size of the domains as a function of annealing temperature. At 250°C, the number of unit cells reach its maximum value of 37. The number of unit cells formed is smaller than expected due to loss of Se and oxidation at the film surface. The overall film thickness (calculated from Kiessig oscillations) decreases by a small amount as the target product grows, due to densification of the film as it self-assembles and loss of some Se. The difference between the total film thickness and the thickness of 37 unit cells of $[(SnSe_2)_{1+\delta}]_1(VSe_2)_1$ at 250°C is due to an oxide layer on the surface of the film. The areal density of Se measure using XRF is consistent with that expected for 37 unit cells of $[(SnSe_2)_{1+\delta}]_1(VSe_2)_1$ at 250°C (solid green line, Figure VI.1a).

A growth mechanism consistent with the characterization data is shown in Figure VI.3. The most difficult fact to explain is that the majority of the film consists of domains of $[(SnSe_2)_{1+\delta}]_1(VSe_2)_1$ that are exactly the same integral number of unit cells throughout the annealing process. One possible explanation is that the coherent domains in the as

deposited film grow out from the substrate film interface as the film is deposited. This would provide a common starting point for all of the domains. The domains would stop growing as the film is deposited since metal atoms would need to diffuse through a thicker layer of amorphous Se and the increasing accumulated roughness as the film becomes thicker would decrease the coherence of the later deposited layers. The in plane diffraction patterns suggest that most of the $SnSe_2$ forms large 2D grains during the deposition. There are fewer and smaller domains of VSe_2 and unreacted V|Se layers between the $SnSe_2$ grains. As the precursor is annealed, the number of unit cells in the coherent domains near the substrate increase and an oxide layer forms at the film surface. The coherent domains grow at the same rates because the diffusion distances for atoms to arrive at the growth fronts are similar as a result of the nanoarchitecture of the precursor. During this process lateral growth of existing VSe_2 layers in the precursor occurs and additional VSe_2 layers self-assemble between existing $SnSe_2$ layers as charge transfer between the layers stabilize the intergrowth. Excess Se diffuses to the surface and evaporates. The difference in the self-assembly behavior of $SnSe_2$ and VSe_2 results in an interesting dynamic between lateral and perpendicular growth of $[(SnSe_2)_{1+\delta}]_1(VSe_2)_1$.

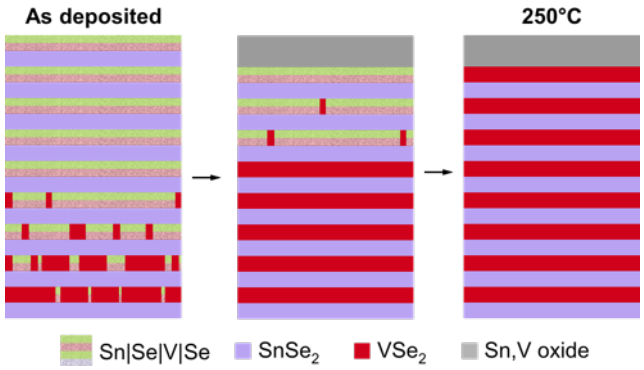

Figure VI.3. Proposed formation and growth mechanism for $[(SnSe_2)_{1+\delta}]_1(VSe_2)_1$.

Further annealing to 400°C results in the decomposition of $[(SnSe_2)_{0.80}]_1(VSe_2)_1$ as Se is lost and $[(SnSe)_{1.15}]_1(VSe_2)_1$ forms. The XRF data shows a substantial drop in the number of Se atoms per Å^2 starting at 350°C. This is close to the decomposition temperature of bulk $SnSe_2$ to SnSe (340°C).[33] Changes in the XRR pattern from 300-400°C demonstrate that the $SnSe_2$ layers have indeed decomposed. The decrease in the Kiessig fringe amplitude point to a change in the density of the film. The number of unit cells also decrease to 32, suggesting that not all of the $[(SnSe_2)_{1+\delta}]_1(VSe_2)_1$ layers were converted to $[(SnSe)_{1.15}]_1(VSe_2)_1$. This is not at all surprising since SnSe has a higher atomic areal density of Sn than $SnSe_2$. The $SnSe_2$ decomposition does not reduce the number of VSe_2 layers, since VSe_2 is kinetically stable up to 400°C.[34] The VSe_2 layers that are not in the heterostructure likely exists as small VSe_2 grains within the film. The retention of the Kiessig fringes in the XRR pattern shown that film remains smooth during this transition. The *c*-axis lattice parameter of 12.02(1) Å after the 400°C anneal is consistent with previously reported $[(SnSe)_{1.15}]_1(VSe_2)_1$.[35] The odd order reflections are broader than the even order reflections, presumably due to peak splitting from extra planes of VSe_2 separating domains of $[(SnSe)_{1.15}]_1(VSe_2)_1$ by half of a unit cell's thickness within the interior of the film.[36] The in-plane diffraction data supports the formation of SnSe.[35] After the 350°C anneal, *hk*0 reflections from VSe_2, $SnSe_2$ and SnSe are present. After the 400°C anneal the $SnSe_2$ *hk*0 reflections are no longer present. The *a*-axis lattice parameter of the VSe_2 phase is 3.43(1) Å, consistent with previously studied $[(SnSe)_{1.15}]_1(VSe_2)_1$ (VSe_2 a = 3.414(3) Å).[35] SnSe has a square unit cell and an *a* axis-lattice parameter of 5.94(1) Å, which is also consistent with previous reports for $[(SnSe)_{1.15}]_m(VSe_2)_1$ (SnSe a = 5.91-5.92 Å).[37]

The last phase transition involves the disproportionation and subsequent oxidation of $[(SnSe)_{1.15}]_1(VSe_2)_1$ at temperatures greater than 450°C, even though the sample was annealed in a drybox with low oxygen concentration. Another dramatic drop in Se atoms per $Å^2$ is observed during this last transition. This transition coincides with an increase in oxygen XRF intensity and decrease in Sn atoms per $Å^2$. These stoichiometry changes suggest that the disproportionation is accompanied by the oxidation of Sn into volatile species. The XRR data shows that the film roughness significantly increases. The 00*l* peaks in the XRD shift to higher angles and broaden starting at 500°C. Odd order 00*l* reflections are completely diminished at 550°C, what remains are 00*l* reflections coming from a structure with a c-lattice parameter of 5.90(1) Å, consistent with some non-stoichiometric VSe_2 remaining in the film.[27] At the highest temperature studied, only hk0 reflections from two closely related hexagonal lattices are observed, with a-lattice parameters of 3.46 Å and 3.52 Å, suggesting that the major phase present is VSe_2 with different values of x and y in the formula $V_{1+x}Sn_ySe_2$.

A second piece of precursor I was annealed at 250°C for 5 minutes based on the annealing data and its XRR pattern is shown in Figure VI.4. The Laue oscillations around the first order Bragg maximum are consistent with 39 layers of $[(SnSe_2)_{1+\delta}]_1(VSe_2)_1$ self-assembling during the anneal. Fewer layers oxidized during this single annealing step compared to the sequential annealing done on the first piece of precursor I. The total thickness determined from the Kiessig fringes is larger than 39 times the unit cell parameter of $[(SnSe_2)_{0.80}]_1(VSe_2)_1$, as two of the deposited precursor layers did not form the intended product. We modeled the XRR data using the program GenX to calculate the XRR pattern from our proposed structural model.[38]

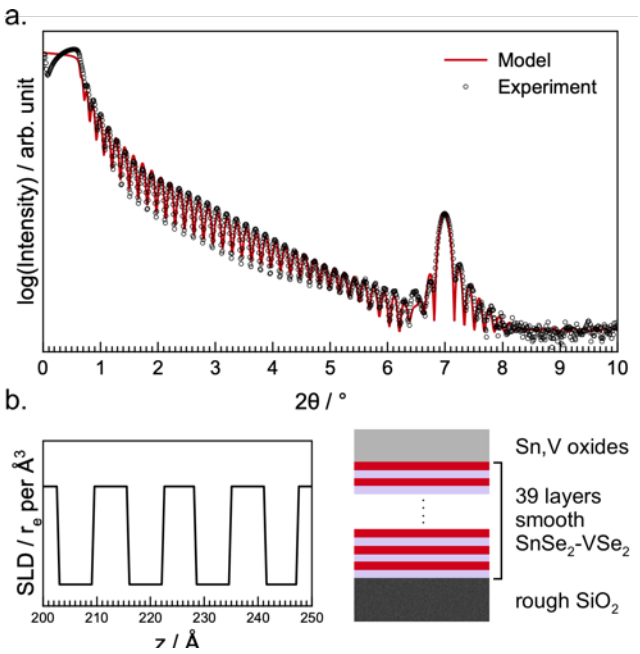

Figure VI.4. (a) XRR modelling of the optimized $[(SnSe_2)_{1+\delta}]_1(VSe_2)_1$ heterostructure. (b) Electron density profile and schematic of the film based on the model.

Table VI.2. Thin film layer parameters obtained from XRR modelling (FOM = 0.141).

Layer	# layers	Thickness / Å	Density / FU per Å^3 x10^{-2}	Roughness / Å	Interdiffusion / Å
Sn/V oxides	1	24.1(6)	1.6(1)	3.4(4)	-
VSe_2	39	6.31(4)	1.55(4)	-	-
$SnSe_2$		6.38(2)	1.28(4)	-	-
SiO_2	1	50(20)	1.7(5)	2(1)	4(1)

The calculated pattern, shown in Figure VI.4, matches the experimental pattern and the film parameters in the model are summarized in Table VI.2. The model contained 39 unit cells of $[(SnSe_2)_{0.80}]_1(VSe_2)_1$ with atomically smooth interfaces between the constituents, a rough layer of SiO_2 below the $[(SnSe_2)_{0.80}]_1(VSe_2)_1$ block and a rough layer of tin/vanadium oxides above it. The thickness of the top oxide layer is approximately equal to that of the two missing unit cells, suggesting they were mostly lost to oxidation.

A thin interdiffusion region was required in the model to match the experimental pattern, which is consistent with a small amount of initially deposited Sn reacting with the SiO_2 surface during deposition.

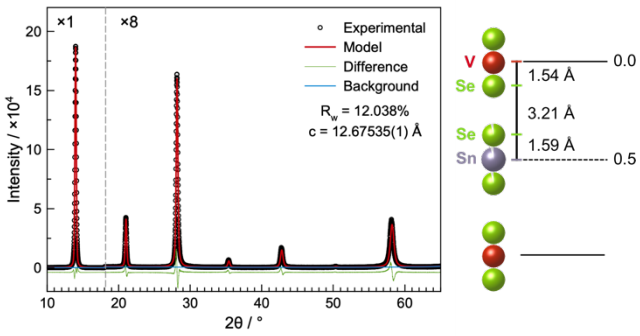

Figure VI.5. Rietveld refinement result of the specular x-ray diffraction of $[(SnSe_2)_{1+\delta}]_1(VSe_2)_1$ and the atomic z-plane model of the average structure.

Rietveld analysis of the specular x-ray diffraction of $[(SnSe_2)_{0.80}]_1(VSe_2)_1$ is shown in Figure VI.5. Since only 00*l* reflections are observed, a Rietveld analysis only provides information of the atomic positions of the atomic planes in the heterostructures that are parallel to the substrate. To simplify the analysis, a model with V at zero and Sn at half the *c*-axis lattice parameter was used, with a mirror plane at the halfway point. The refined V-Se distance of 1.54 Å is close to those observed in other VSe_2-heterostructures like $[(SnSe)_{1+\delta}]_1(VSe_2)_1$ (1.48(2) Å),[35] $[(PbSe)_{1+\delta}]_1(VSe_2)_1$ (1.54 Å),[39] $[(BiSe)_{1+\delta}]_1(VSe_2)_1$ (1.52(1) Å),[40] and bulk VSe_2 (1.57 Å).[29] The refined Sn-Se distance (1.59 Å) is close to that observed in $[(SnSe_2)_{1+\delta}]_1(MoSe_2)_1$ (1.57 Å)[41] and bulk $SnSe_2$ (1.53 Å).[28] The refined van der Waals gap of 3.21 Å is larger than those observed in either VSe_2 or $SnSe_2$, but smaller than the gap found in $[(SnSe_2)_{1+\delta}]_1(MoSe_2)_1$ (3.35(1) Å).[41] The large van der Waals gap is a consequence of the large difference between the in-plane lattice parameters of

VSe_2 and $SnSe_2$, which prevents the Se atoms on either side of the van der Waals gap from nesting in between the Se atoms of the adjacent layers.

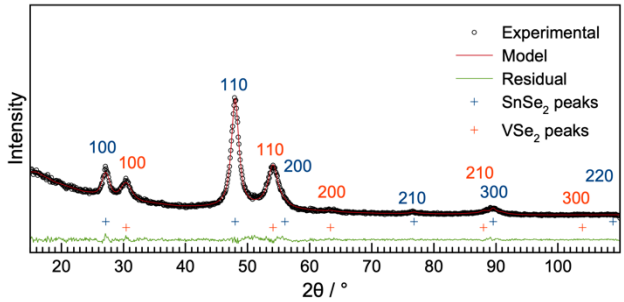

Figure VI.6. LeBail fit of the grazing incidence in-plane x-ray diffraction pattern of the optimized $[(SnSe_2)_{1+\delta}]_1(VSe_2)_1$ heterostructure.

A LeBail fit of the in-plane x-ray diffraction data of the second piece of Precursor I is shown in Figure VI.6. All reflections can be indexed as *hk*0 reflections from to two different hexagonal unit cells. The calculated *a*-axis lattice parameter for the $SnSe_2$ constituent (3.79(1) Å) is only slightly lower than what is observed for bulk $SnSe_2$ (3.811 Å),[28] and in $[(SnSe)_{1+\delta}]_1(MoSe_2)_1$ (3.81 Å).[41] The calculated *a*-axis lattice parameter for the VSe_2 constituent (3.39(1) Å) is between the bulk value for stoichiometric VSe_2 (3.358 Å),[29] and that reported for $[(SnSe)_{1+\delta}]_1(VSe_2)_1$ (3.414 Å).[35] The difference in the in plane lattice parameters results in a stoichiometry of $[(SnSe_2)_{0.80}]_1(VSe_2)_1$.

HAADF-STEM data was obtained on a cross section of the $[(SnSe_2)_{0.80}]_1(VSe_2)_1$ film from the second annealed piece of precursor I to obtain information about the relative orientation of the dichalcogenide layers. Figure VI.7a contains an image of the entirety of the film, which shows that the film is homogenous and smooth, consistent with the modelling of specular XRD and XRR. There are 38 layers of $[(SnSe_2)_{0.80}]_1(VSe_2)_1$ clearly

visible, with another layer occasionally found at the top or bottom of the film. A closer look of the

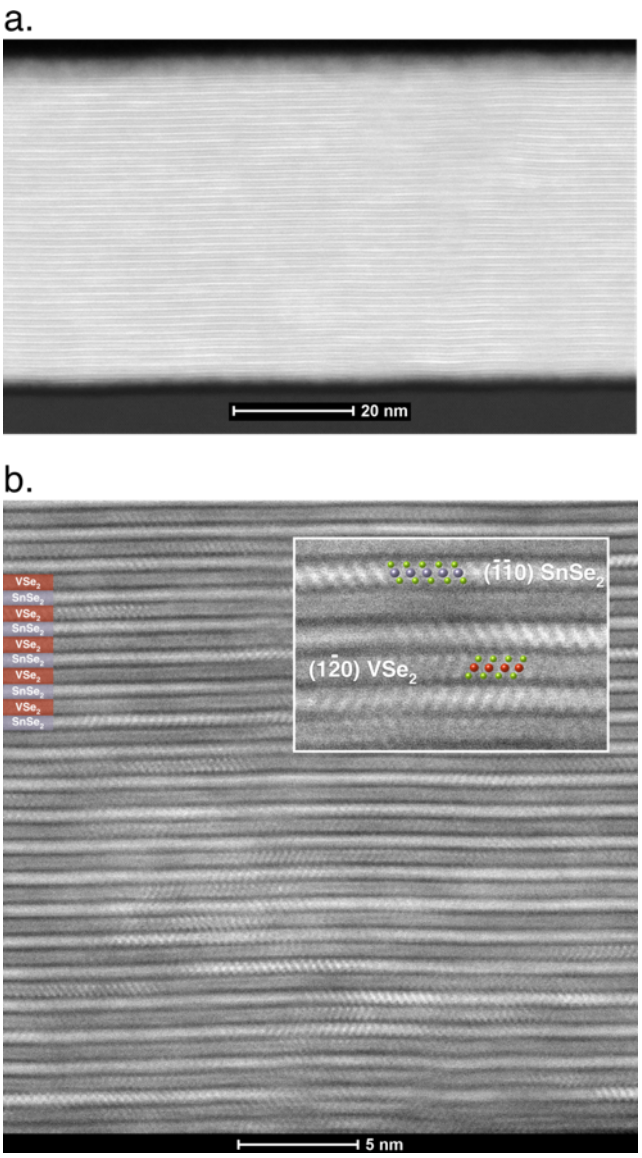

Figure VI.7. HAADF-STEM image of the (a) entirety and (b) large section of the film shows that it consists of $[(SnSe_2)_{0.80}]_1(VSe_2)_1$.

film at higher magnification, Figure VI.7b, contains alternating dark and bright layers that can be identified as VSe_2 and $SnSe_2$, respectively, since heavier elements appear brighter in HAADF-STEM data.[42] There are noticeably dark regions between at the interfaces of

the $SnSe_2$ andVSe_2 layers due to the van der Waals gap between the two constituents. The inset of Figure VI.7b shows a region of layers with high atomic resolution that happen to show zone axis views of both constituent layers. Only the <110> and <1$\bar{2}$0> orientations of the two constituents are clearly resolved in the images. Both the VSe_2 and $SnSe_2$ layers exhibit octahedral coordination, which is consistent with the bulk structures of $SnSe_2$ and VSe_2. It is apparent from the microscopy data that there is a large degree of turbostratic disorder and lack of long range order in the heterostructure. A close inspection of the entirety of the cross section reveals that there are no large grains containing multiple repeating units crystallizing with a consistent orientation. Qualitative analysis of Figure 7b gives an estimated grain size of 5 nm, smaller than the grain sizes observed from other heterostructures that have long range order.[43] These features can be traced to the large lattice mismatch and weak interaction between the constituents.

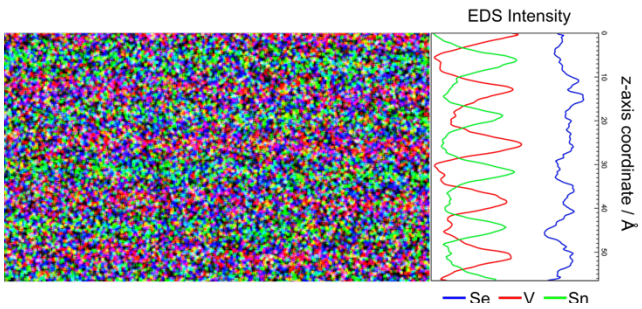

Figure VI.8. EDX elemental analysis of a section of the film showing atomic plane position of the elements.

More information on the elemental distribution of the atoms within the layers was collected by EDX analysis of a small section of the film (Figure VI.8). The elemental EDX map confirms that there are alternating atomic layers of Sn and V separated by Se. However, there are regions where there are V-intensity in the Sn positions and vice versa.

Since the unexpected intensities are not uniform across the analyzed region, it is likely due to inhomogeneous cross substitution (e.g. VSe_2 replacing $SnSe_2$ or vice versa) across layers rather than homogenous alloying (e.g. $Sn_xV_{1-x}Se_2$) within the layers. Substitutional defects of this type have been observed in non-stoichiometric $[(SnSe)_{1+\delta}]_1(VSe_2)_1$ when there are deliberate variations in global composition.[44] Homogenous alloys like $[(SnSe)_{1+\delta}]_1(Ta_xV_{1+x}Se_2)_1[(SnSe)_{1+\delta}]_1(V_yTa_{1-y}Se_2)_1$ have clearly resolved V intensity peaks in Ta positions and vice versa.[45] In $[(SnSe_2)_{0.80}]_1(VSe_2)_1$, we speculate this result comes from variations in local composition that are difficult to control during the deposition process.

The data presented above on precursor I and the mechanism for growth prompted us to prepare precursor II to probe the relative importance of composition versus nanoarchitecture on product formation. We intended precursor II to have the same composition as precursor 1 but half the initial modulation length of the deposited sequence of Sn|Se|V|Se layers. Our question was, "what would form from this precursor?". Only short range diffusion would be required to form the metastable alloy $Sn_xV_{1-x}Se_2$ and roughly twice that diffusion distance would be required to form the metastable compound $[(SnSe_2)_{0.80}]_1(VSe_2)_1$,. Alternatively, small domains of VSe_2 interwoven with larger domains of $SnSe_2$ might form, or Se might segregate enabling the thermodynamically stable compound $[(SnSe)_{1.15}]_1(VSe_2)_1$ to form. Based on the data from precursor I, we expected $SnSe_2$ would nucleate first, but the formation of large in plane grains of $SnSe_2$ would be inhibited by increasing concentrations of vanadium atoms at the growth front.

Figure VI.9 contains diffraction data on precursor II. The experimental modulation length of the layering in the as deposited precursor II was 7.27 Å, close to the *c*-axis lattice

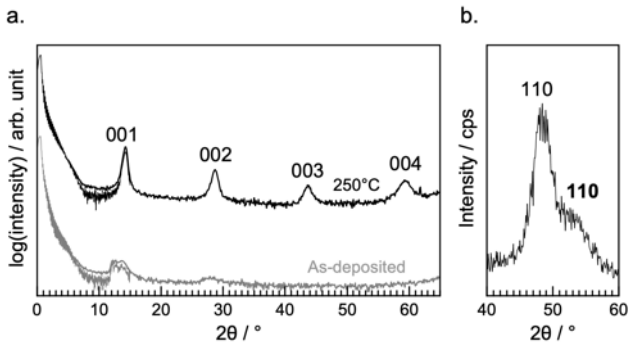

Figure VI.9. Synthesis of a new $Sn_xV_{1-x}Se_2$ alloy. (a) Specular x-ray diffraction of a precursor with half the number of required atoms per layer (b) In-plane x-ray diffraction of the tin and vanadium diselenide alloy showing the presence of alloys with two different values of x.

parameters of tin and vanadium diselenides. Figure VI.9a contains the specular and in plane diffraction patterns of precursor II after it was annealed at 250°C. The specular diffraction pattern contains 4 reflections that can be indexed as 00l reflections, yield a *c*-axis lattice parameter of 6.23(1) Å. The 110 reflection from the in-plane diffraction pattern (Figure VI.9b) of this sample is split suggesting the products are a vanadium rich and a tin rich dichalcogenide alloy. Vegard's law can be used to estimate the composition of the majority components from the resulting *a*-axis lattice parameters of a = 3.49(1) and 3.75(1) Å. The calculated compositions of the two phases observed are $Sn_{0.86}V_{0.14}Se_2$ and $Sn_{0.29}V_{0.71}Se_2$. We suggest that $SnSe_2$ nucleates and grows, but incorporates some V due to the increasing concentration of V at the growth front. The increased concentration of V results in the nucleation of the vanadium rich dichalcogenide. These events occur randomly results in the random intergrowth of the two alloys rather than a precisely layered nanoarchitecture.

VI.4 Discussion

Traditional materials synthesis approaches have few parameters that can be used to control a reaction pathway to a specific product, instead relying on changing the system

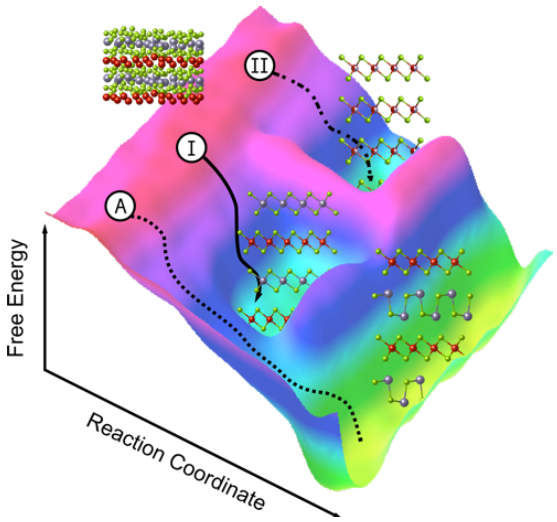

Figure VI.10. Schematic of the free energy landscape of tin vanadium selenides.

conditions (temperature, pressure, composition) to make the desired product thermodynamically stable. The results presented herein indicate that both the local composition and nanoarchitecture of precursors, which controls the initial distribution of atoms, provides a means to choose between different self-assembly pathways. An energy landscape provides a useful tool to visualize key aspects reaction pathways and Figure VI.10 contains an energy landscape consistent with the results of our study. Figure VI.10 shows the two kinetically stable phases formed in this study, $[(SnSe_2)_{0.80}]_1(VSe_2)_1$ and $Sn_{1-x}V_xSe_2$ exists as local minima and the misfit layer compound $[(SnSe)_{1.15}]_1(VSe_2)_1$ as the thermodynamic global minimum. Three different starting points are shown, corresponding to precursors I and II, and precursor A containing less Se with the nanoarchitecture designed to form the misfit layer compound $[(SnSe)_{1.15}]_1(VSe_2)_1$. As the layers in precursor I self-assemble to form $[(SnSe_2)_{1+\delta}]_1(VSe_2)_1$, the free energy drops as the system falls into the local minima (solid black line from site I). The formation of $SnSe_2$ during the deposition, facilitated by the local composition and nanoarchitecture of precursor I, selects

this reaction pathway. Precursor II, while having the same overall composition, has a nanoarchitecture that does not provide enough Sn in any single elemental layer to form large grains of $SnSe_2$. When $SnSe_2$ nucleates, the growth front quickly becomes enriched in V, resulting in the formation of the metastable alloy, $Sn_{1-x}V_xSe_2$ (black dash dot line from site II). Precursor A, reported by Atkins and coworkers, had a nanoarchitecture similar to precursor I, containing alternating Sn and V rich layers, but ~25% less Se. This precursor forms $[(SnSe)_{1.15}]_1(VSe_2)_1$, as there was not sufficient Se to nucleate $SnSe_2$ during the deposition. There are large activation barriers between the different products initially formed because it would be necessary to create regions with the local composition required to nucleate the different alternatives, and this would require long range solid state diffusion which has a high activation energy.[35] The importance of local composition is also seen in a paper by Falmbigl and coworkers, which involved the reaction of a Sn|Se|V|Se precursor with a nanoarchitecture similar to that of precursors I and A, but with an intermediate amount of Se.[46] In this precursor, annealing at 100°C resulted in the simultaneous crystallization of $SnSe_2$, SnSe, and VSe_2 and all of these exhibited significant in-plane grain growth between 100-300°C. The simultaneous formation of all three constituents suggests that the difference between the nucleation barriers for the three phases is small and controlled by the local Sn and Se composition.

VI.5 Conclusions

In this work, in-plane diffraction measurements and Laue oscillations present in x-ray reflectivity scans of a designed precursor as it evolved into a metastable heterostructure, enabled us to determine the absolute size of the growing crystal as a function of

temperature. This data provided insights into the self-assembly mechanism and defined optimum processing conditions to form a new kinetically stable misfit layer compound, $[(SnSe_2)_{0.80}]_1(VSe_2)_1$, with minimum oxidation. Controlling the local composition of the precursor enabled $[(SnSe_2)_{0.80}]_1(VSe_2)_1$ to preferentially form over $[(SnSe)_{1.15}]_1(VSe_2)_1$. Preparing a precursor with the same overall composition but different nanoarchitecture resulted in the formation of a new kinetically stable $Sn_xV_{1-x}Se_2$ alloy instead of $[(SnSe_2)_{0.80}]_1(VSe_2)_1$. The different reactions encountered from annealing studies of closely related multilayer systems were discussed in terms of an energy landscape as an effort to rationalize the different self-assembly pathways observed. The results show that nanoarchitecture and local composition are complementary design parameters to direct the self-assembly of new kinetically stable compounds along different reaction pathways in the energy landscape.

CHAPTER VII

CONCLUSIONS AND SUMMARY

Authorship Statement

This chapter was written with the editorial assistance of my advisor, Dr David C. Johnson.

VII.1 Concluding Remarks

As the existing paradigm of solid state synthesis shifts from serendipitous discovery to materials-by-design, the need for synthesis planning has become more increasingly apparent. This dissertation focused on understanding the self-assembly behavior of Modulated Elemental Reactants (MER) synthesis in order to uncover new aspects and consequential factors that go beyond the generally accepted simple mechanism.

The first chapter introduced the concept of an energy landscape applied to bulk systems, molecular systems, solid interfaces, and eventually, ultrathin layers. We emphasize the need to study reaction mechanisms in order to explore more reaction pathways in an energy landscape. Chapter II discussed important structural and compositional techniques essential to guiding the deliberate synthesis of heterostructures. A novel method of analyzing and utilizing XRF data based on manual background correction and thin film limit considerations is introduced. Two new methods of calibrating XRF intensities and converting values to atom density (in atoms per square Angstrom) are presented. XRF and XRD would later be demonstrated as foundational methods for MER synthesis. Chapter III shed light on a fundamental requirement of misfit layered compounds and ferecrystalline heterostructures: the presence of a strong interaction between

constituent layers. A strong interaction exists if a thick rock salt layer (PbSe) crystallizes crystallographically aligned on transition metal dichalcogenide layers (VSe_2). This approach serves as a test to determine the compatibility of two layered constituents as a heterostructure or misfit layer compound.

As Chapter III addressed the compatibility of PbSe and VSe_2 as a combined heterostructure, Chapter IV discussed the synthesis of $[(PbSe)_{1+\delta})]_m(VSe_2)_1$ heterostructures, where m = 1, 2, 3, 4, as potential charge density wave materials. The synthesis was driven by the ability to precisely control the number of atoms and nanoarchitecture of a designed precursor, guided by XRF and XRD. It was determined that the distinct charge density wave behavior in VSe_2 heterostructures is strongly influenced by the identity of the intervening constituent rather than VSe_2-separation. This worked also highlighted the importance of having the correct number of atoms in the precursor and presented alternate pathways in the energy landscape when this condition is not met. Chapter V built on the foundations established in Chapter III and IV by using designed precursors to investigate the limit of the interaction between PbSe and VSe_2 by targeting the synthesis of $[(PbSe)_{1+\delta}]_q(VSe_2)_1$ where q = 1 - 11 and the number of PbSe monolayers. The designed precursors exhibited vastly different self-assembly behaviors depending on the number of PbSe monolayers targeted. Unexpected room temperature lateral diffusion of atoms was observed for precursors with q = 1, 3, and 5, all of which were targeted to form PbSe monolayers. DFT calculations further demonstrated that the low temperatures rearrangements were driven by the stability of PbSe bilayers over monolayers.

Finally, Chapter VI described the synthesis of new metastable compounds $[(SnSe_2)_{1+\delta}]_1(VSe_2)_1$ and $Sn_xV_{1-x}Se_2$, by precisely controlling the nanoarchitecture of the

precursor and using XRR and XRD reaction monitoring the elucidate the growth mechanism from the precursor to the target product.

VII.2 Outlook

Overall, the goal of this work is to establish foundations for a toolbox of methods and concepts for rational synthesis planning of heterostructures via modulated elemental reactants. So far, we recognize the following ideas and methods as valuable tools in for rational synthesis.

1. X-ray Fluorescence (XRF)

   The ability of measure the number of atoms on a film with submonolayer accuracy opens up multiple opportunities in the thin film community. The convenience, low-cost, and non-destructive approach make it suitable to investigate compositional evolution of films made by various deposition methods. At the moment, active collaborations with groups with expertise in atomic layer deposition are ongoing as an effort to make the method more widespread.

2. Compatibility Test

   The compatibility test based on crystallographic alignment when combined with XRF, provides a quick and systematic approach for preliminary testing of new materials. Additionally, it also acts as a means for synthesizing crystallographically aligned rock salt films. As of the time of writing, the thermodynamic counterpart of PbSe-VSe_2 has been confirmed, consistent with the compatibility test.

3. Precise Precursor Design

   One of the most important and consequential aspects of MER synthesis is the design of the precursor. This work has demonstrated how the number of atoms and the modulation length can dictate the reaction pathway and impact the reaction product. The renewed emphasis in the precursor have contributed to recent successes in the group such as a synthesis of the very first three layer rock salt heterostructure. The ability to precisely control these two parameters have allowed us to test and investigate the generally accepted MER mechanism and reveal consequential features that were previously overlooked.

4. Energy Landscape

   In the synthesis of heterostructures, the energy landscape framework helps motivate the exploration of reaction pathways by traversing the experimental parameter space. Being cognizant of activation barriers that trap local minima containing metastable products helps one make logical experimental decisions. Computational tools that can predict kinetically stable structures as local minima can expedite synthesis.

These tools potentially move us closer to the ultimate goal of mechanistic solid state synthesis. The more we develop and establish new tools to guide synthesis planning, the closer we get to more deliberate chemistry and the less we have to rely on serendipity.

APPENDICES

A. SUPPLEMENTAL MATERIAL TO CHAPTER IV

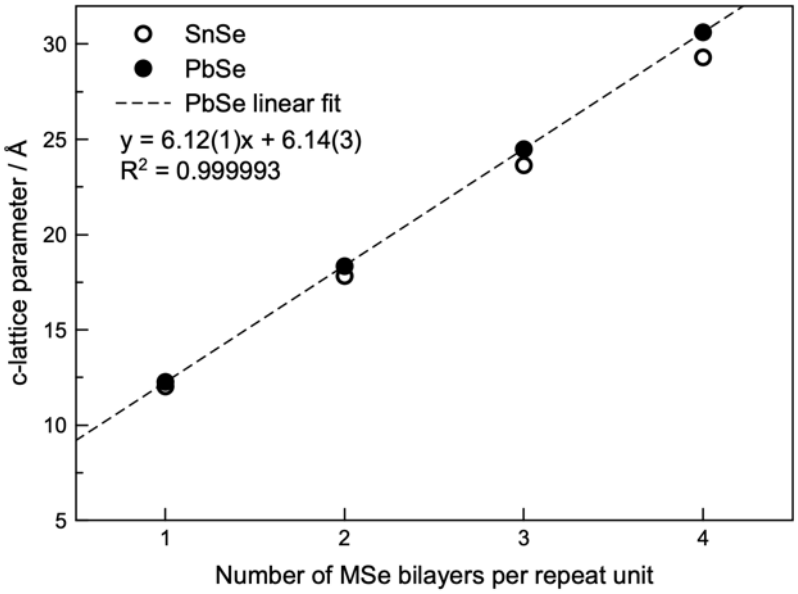

Figure A.1. Plot of c-lattice parameter of the $[(PbSe)_{1+\delta}]_m(VSe_2)_1$ heterostructures and m, showing that the lattice parameter increases linearly as a PbSe bilayer is added to the repeat unit.

Table A.1: Rietveld refinement results from GSAS analysis of the $[(PbSe)_{1+\delta}]_3(VSe_2)_1$ heterostructure

Parameter	Value
Atom Fractional Coordinate (occ)	
V (1.00)	0
Se (1.00)	0.6385(6)
Pb (0.517)	0.18246(7)
Se (0.517)	0.2053(2)
Se (0.517)	0.2965(2)
Pb (0.517)	0.31638(9)
Pb (0.517)	0.43339(9)
Se (0.517)	0.4510(2)
U_{iso}	0.026(1)
Profile coefficients: Histogram type 1	
U	$8.6(2) \times 10^{2}$
V	-1.0×10^{0}
W	$4.9(2) \times 10^{1}$
X	$1.549(9) \times 10^{1}$
R_p	0.0955

B. SUPPLEMENTAL MATERIAL TO CHAPTER V.

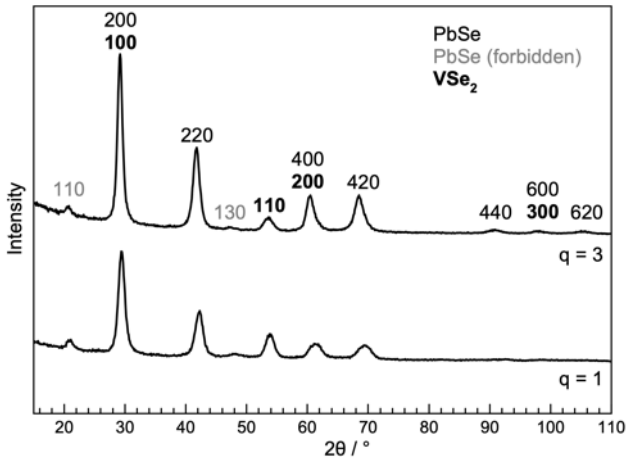

Figure B.1 In plane x-ray diffraction patterns of the annealed q = 1 and 3 precursors.

REFERENCES CITED

Chapter I

(1) Jansen, M. A Concept for Synthesis Planning in Solid-State Chemistry. *Angew. Chemie - Int. Ed.* **2002**, *41* (20), 3746–3766. https://doi.org/10.1002/1521-3773(20021018)41:20<3746::AID-ANIE3746>3.0.CO;2-2.

(2) Kanatzidis, M. G. Structural Evolution and Phase Homologies for "Design" and Prediction of Solid-State Compounds. *Acc. Chem. Res.* **2005**, *38* (4), 359–368. https://doi.org/10.1021/ar040176w.

(3) Curtarolo, S.; Hart, G. L. W.; Nardelli, M. B.; Mingo, N.; Sanvito, S.; Levy, O. The High-Throughput Highway to Computational Materials Design. *Nat. Mater.* **2013**, *12* (3), 191–201. https://doi.org/10.1038/nmat3568.

(4) Jain, A.; Ong, S. P.; Hautier, G.; Chen, W.; Richards, W. D.; Dacek, S.; Cholia, S.; Gunter, D.; Skinner, D.; Ceder, G.; et al. Commentary: The Materials Project: A Materials Genome Approach to Accelerating Materials Innovation. *APL Mater.* **2013**, *1*, 011002. https://doi.org/10.1063/1.4812323.

(5) Narayan, A.; Bhutani, A.; Rubeck, S.; Eckstein, J. N.; Shoemaker, D. P.; Wagner, L. K. Computational and Experimental Investigation for New Transition Metal Selenides and Sulfides: The Importance of Experimental Verification for Stability. *Phys. Rev. B* **2016**, *94* (4), 1–15. https://doi.org/10.1103/PhysRevB.94.045105.

(6) Regus, M.; Mankovsky, S.; Polesya, S.; Kuhn, G.; Ditto, J.; Schürmann, U.; Jacquot, A.; Bartholomé, K.; Näther, C.; Winkler, M.; et al. Characterization of Cr-Rich Cr-Sb Multilayer Films: Syntheses of a New Metastable Phase Using Modulated Elemental Reactants. *J. Solid State Chem.* **2015**, *230*, 254–265. https://doi.org/10.1016/j.jssc.2015.06.038.

(7) Schöllhorn, R. Solid-State Chemistry: Restoring the Balance. *Angew. Chemie Int. Ed. English* **1996**, *35* (20), 2338–2338. https://doi.org/10.1002/anie.199623381.

(8) Hemminger, J. *A Report from the Basic Energy Sciences Advisory Committee*; **2007**.

(9) Schön, J. C.; Jansen, M. First Step Towards Planning of Syntheses in Solid-State Chemistry: Determination of Promising Structure Candidates by Global Optimization. *Angew. Chemie Int. Ed. English* **1996**, *35* (12), 1286–1304. https://doi.org/10.1002/anie.199612861.

(10) Wales, D. J.; Bogdan, T. V. Potential Energy and Free Energy Landscapes. *J. Phys. Chem. B* **2006**, *110* (42), 20765–20776. https://doi.org/10.1021/jp0680544.

(11) West, A. *Solid State Chemistry and Its Applications*; John Wiley & Sons, Ltd: New York City, 1984.

(12) Martinolich, A. J.; Neilson, J. R. Pyrite Formation via Kinetic Intermediates through Low-Temperature Solid-State Metathesis. *J. Am. Chem. Soc.* **2014**, *136* (44), 15654–15659. https://doi.org/10.1021/ja5081647.

(13) Lowe, M. A.; Gao, J.; Abruña, H. D. In Operando X-Ray Studies of the Conversion Reaction in Mn 3O4 Lithium Battery Anodes. *J. Mater. Chem. A* **2013**, *1* (6), 2094–2103. https://doi.org/10.1039/c2ta01270g.

(14) Skjærvø, S. L.; Wells, K. H.; Sommer, S.; Vu, T. D.; Tolchard, J. R.; Van Beek, W.; Grande, T.; Iversen, B. B.; Einarsrud, M. A. Rationalization of Hydrothermal Synthesis of NaNbO3 by Rapid in Situ Time-Resolved Synchrotron X-Ray Diffraction. *Cryst. Growth Des.* **2018**, *18* (2), 7770–7774. https://doi.org/10.1021/acs.cgd.7b01192.

(15) Venna, S. R.; Jasinski, J. B.; Carreon, M. A. Structural Evolution of Zeolitic Imidazolate Framework-8. *J. Am. Chem. Soc.* **2010**, *132* (51), 18030–18033. https://doi.org/10.1021/ja109268m.

(16) Shoemaker, D. P.; Chung, D. Y.; Mitchell, J. F.; Bray, T. H.; Soderholm, L.; Chupas, P. J.; Kanatzidis, M. G. Understanding Fluxes as Media for Directed Synthesis: In Situ Local Structure of Molten Potassium Polysulfides. *J. Am. Chem. Soc.* **2012**, *134* (22), 9456–9463. https://doi.org/10.1021/ja303047e.

(17) Kanatzidis, M. G.; Pöttgen, R.; Jeitschko, W. The Metal Flux: A Preparative Tool for the Exploration of Intermetallic Compounds. *Angew. Chemie - Int. Ed.* **2005**, *44* (43), 6996–7023. https://doi.org/10.1002/anie.200462170.

(18) Saha, D.; Jensen, K. M. Ø.; Tyrsted, C.; Bøjesen, E. D.; Mamakhel, A. H.; Dippel, A. C.; Christensen, M.; Iversen, B. B. In Situ Total X-Ray Scattering Study of WO3 Nanoparticle Formation under Hydrothermal Conditions. *Angew. Chemie - Int. Ed.* **2014**, *53* (14), 3667–3670. https://doi.org/10.1002/anie.201311254.

(19) DiSalvo, F. J. Solid State Chemistry. *Solid State Commun.* **1997**, *102* (2–3), 79–85. https://doi.org/10.1016/S0038-1098(96)00713-2.

(20) Nicolaou, K. C. The Emergence of the Structure of the Molecule and the Art of Its Synthesis. *Angew. Chemie - Int. Ed.* **2013**, *52*, 131–136. https://doi.org/10.1002/anie.201207081.

(21) Kocienski, P. J. *Protecting Groups*; Georg Thieme Verlag: Stuttgart, 2005.

(22) Price, S. L. Predicting Crystal Structures of Organic Compounds. *Chem. Soc. Rev.* **2014**, *43*, 2098–2111. https://doi.org/10.1039/c3cs60279f.

(23) Price, S. L. Computed Crystal Energy Landscapes for Understanding and Predicting Organic Crystal Structures and Polymorphism. *Acc. Chem. Res.* **2009**, *42* (1), 117–126. https://doi.org/10.1021/ar800147t.

(24) Morrison, R. T.; Boyd, R. N. *Organic Chemistry, 3rd Edition*, 3rd ed.; Allyn and Bacon, Inc: Boston, 1973.

(25) Disalvo, F. J. Solid-State Chemistry: A Rediscovered Chemical Frontier. *Science (80-.).* **1990**, *27*, 649–655. https://doi.org/10.1126/science.247.4943.649.

(26) Wendt, M.; Mahnke, L. K.; Heidenreich, N.; Bensch, W. Nucleation and Crystal Growth of a {V14Sb8O42} Cluster from a {V15Sb6O42} Polyoxovanadate: In Situ XRD Studies. *Eur. J. Inorg. Chem.* **2016**, *2016* (34), 5393–5398. https://doi.org/10.1002/ejic.201601025.

(27) Ostwald, W. Studien Über Die Bildung Und Umwandlung Fester Körper. *Zeitschrift für Phys. Chemie* **1897**, *22* (1), 289–330. https://doi.org/10.1515/zpch-1897-2233.

(28) Van Santen, R. A. The Ostwald Step Rule. *J. Phys. Chem.* **1984**, *88* (24), 5768–5769. https://doi.org/10.1021/j150668a002.

(29) Baumgartner, J.; Dey, A.; Bomans, P. H. H.; Le Coadou, C.; Fratzl, P.; Sommerdijk, N. A. J. M.; Faivre, D. Nucleation and Growth of Magnetite from Solution. *Nat. Mater.* **2013**, *12*, 310–314. https://doi.org/10.1038/nmat3558.

(30) Pienack, N.; Bensch, W. In-Situ Monitoring of the Formation of Crystalline Solids. *Angew. Chemie - Int. Ed.* **2011**, *50* (9), 2014–2034. https://doi.org/10.1002/anie.201001180.

(31) Cho, A. Y.; Arthur, J. R. Molecular Beam Epitaxy. *Prog. Solid State Chem.* **1975**, *10*, 157–192.

(32) Joyce, B. A. Molecular Beam Epitaxy. *Reports Prog. Phys.* **1985**, *48* (12), 1637. https://doi.org/10.1088/0034-4885/48/12/002.

(33) Farrow, R. F. C. *Molecular Beam Epitaxy, Applications to Key Materials*; Noyes Publications: Park Ridge, NJ, 1995.

(34) Volmer, M.; Weber, A. Keimbildung in Übersättigten Gebilden. *Zeitschrift für Phys. Chemie* **1925**, *119* (1), 277–301. https://doi.org/10.1515/zpch-1926-11927.

(35) Franck, C. F.; Van Der Merwe, J. H. One-Dimensional Dislocations. II. Misfitting Monolayers and Oriented Overgrowth. *Proc. R. Soc. London. Ser. A. Math. Phys. Sci.* **1949**, *198* (1053), 216–225. https://doi.org/10.1098/rspa.1949.0096.

(36) Stranski, I. N.; Krastanow, L. Zur Theorie Der Orientierten Ausscheidung von Ionenkristallen Aufeinander. *Abhandlungen der Math. Klasse IIb. Akad. der Wissenschaften Wien* **1938**, *146*, 797–810.

(37) Schöllhorn, R. Reversible Topotactic Redox Reactions of Solids by Electron/Ion Transfer. *Angewandte Chemie International Edition in English*. John Wiley & Sons, Ltd December 1, 1980, pp 983–1003. https://doi.org/10.1002/anie.198009831.

(38) Hayward, M. Soft Chemistry Synthesis of Oxides. In *Comprehensive Inorganic Chemistry II (Second Edition) From Elements to Applications*; 2013; pp 417–453.

(39) McIntyre, R. A.; Falster, A. U.; Li, S.; Simmons, J.; O'Connor, C. J.; Wiley, J. B. Opening a Perovskite to Valence Manipulation: Two-Step Topotactic Route to a New Mixed-Valence Titanate, Na(1-X+y)Ca(x/2)LaTiO4. *J. Am. Chem. Soc.* **1998**, *120* (1), 217–218. https://doi.org/10.1021/ja971299x.

(40) Kodentsov, A. A.; Bastin, G. F.; Van Loo, F. J. J. The Diffusion Couple Technique in Phase Diagram Determination. *J. Alloys Compd.* **2001**, *320* (2), 207–217. https://doi.org/10.1016/S0925-8388(00)01487-0.

(41) Gösele, U.; Tu, K. N. Growth Kinetics of Planar Binary Diffusion Couples: "Thin-Film Case" versus "Bulk Cases." *J. Appl. Phys.* **1982**, *53* (4), 3252–3260. https://doi.org/10.1063/1.331028.

(42) Walser, R. M.; Bené, R. W. First Phase Nucleation in Silicon-Transition-Metal Planar Interfaces. *Appl. Phys. Lett.* **1976**, *28*, 624–625. https://doi.org/10.1063/1.88590.

(43) Schwarz, R. B.; Johnson, W. L. Formation of an Amorphous Alloy by Solid-State Reaction of the Pure Polycrystalline Metals. *Phys. Rev. Lett.* **1983**, *51* (5), 415–418. https://doi.org/10.1103/PhysRevLett.51.415.

(44) Gösele, U.; Tu, K. N. "Critical Thickness" of Amorphous Phase Formation in Binary Diffusion Couples. *J. Appl. Phys.* **1989**, *66* (6), 2619–2626. https://doi.org/10.1063/1.344229.

(45) Novet, T.; Johnson, D. C. New Synthetic Approach to Extended Solids: Selective Synthesis of Iron Silicides via the Amorphous State. *J. Am. Chem. Soc.* **1991**, *113* (9), 3398–3403. https://doi.org/10.1021/ja00009a027.

(46) Hornbostel, M. D.; Hyer, E. J.; Thiel, J.; Johnson, D. C. Rational Synthesis of Metastable Skutterudite Compounds Using Multilayer Precursors. *J. Am. Chem. Soc.* **1997**, *119* (11), 2665–2668. https://doi.org/10.1021/ja964084g.

(47) Bené, R. W. A Kinetic Model for Solid-State Silicide Nucleation. *J. Appl. Phys.* **1987**, *61* (5), 1826–1833. https://doi.org/10.1063/1.338025.

(48) Anderson, M. D.; Thompson, J. O.; Johnson, D. C. Avoiding Binary Compounds as Reaction Intermediates in Solid State Reactions. *Chem. Mater.* **2013**, *25* (20), 3996–4002. https://doi.org/10.1021/cm4019259.

(49) Oyelaran, O.; Novet, T.; Johnson, C. D.; Johnson, D. C. Controlling Solid-State Reaction Pathways: Composition Dependence in the Nucleation Energy of InSe. *J. Am. Chem. Soc.* **1996**, *118* (10), 2422–2426. https://doi.org/10.1021/ja953560k.

(50) Williams, J. R.; Johnson, M.; Johnson, D. C. Composition Dependence of the Nucleation Energy of Iron Antimonides from Modulated Elemental Reactants. *J. Am. Chem. Soc.* **2001**, *123* (8), 1645–1649. https://doi.org/10.1021/ja003791d.

(51) Williams, J. R.; Johnson, M. B.; Johnson, D. C. Suppression of Binary Nucleation in Amorphous La-Fe-Sb Mixtures. *J. Am. Chem. Soc.* **2003**, *125* (12), 3589–3592. https://doi.org/10.1021/ja0205380.

(52) Curtarolo, S.; Setyawan, W.; Wang, S.; Xue, J.; Yang, K.; Taylor, R. H.; Nelson, L. J.; Hart, G. L. W.; Sanvito, S.; Buongiorno-Nardelli, M.; et al. AFLOWLIB.ORG: A Distributed Materials Properties Repository from High-Throughput Ab Initio Calculations. *Comput. Mater. Sci.* **2012**, *58*, 227–235. https://doi.org/10.1016/j.commatsci.2012.02.002.

(53) Saal, J. E.; Kirklin, S.; Aykol, M.; Meredig, B.; Wolverton, C. Materials Design and Discovery with High-Throughput Density Functional Theory: The Open Quantum Materials Database (OQMD). *JOM* **2013**, *65* (11), 1501–1509. https://doi.org/10.1007/s11837-013-0755-4.

(54) Computational Materials Repository https://cmr.fysik.dtu.dk/.

(55) Electronic Structure Project http://gurka.fysik.uu.se/ESP.

(56) Hadland, E. C.; Jang, H.; Wolff, N.; Fischer, R.; Lygo, A. C.; Mitchson, G.; Li, D.; Kienle, L.; Cahill, D. G.; Johnson, D. C. Ultralow Thermal Conductivity of Turbostratically Disordered MoSe2 Ultra-Thin Films and Implications for Heterostructures. *Nanotechnology* **2019**, *30*, 285401. https://doi.org/10.1088/1361-6528/aafea2.

(57) Liebold-Ribeiro, Y.; Fischer, D.; Jansen, M. Experimental Substantiation of the "Energy Landscape Concept" for Solids: Synthesis of a New Modification of LiBr. *Angew. Chemie - Int. Ed.* **2008**, *47* (23), 4428–4431. https://doi.org/10.1002/anie.200800333.

(58) Regus, M.; Kuhn, G.; Polesya, S.; Mankovsky, S.; Alemayehu, M.; Stolt, M.; Johnson, D. C.; Ebert, H.; Bensch, W. Experimental and Theoretical Investigation of the New, Metastable Compound Cr3Sb. *Zeitschrift fur Krist. - Cryst. Mater.* **2014**, *229* (7), 505–515. https://doi.org/10.1515/zkri-2014-1744.

(59) Ditto, J.; Merrill, D. R.; Mitchson, G.; Gabriel, J. J.; Mathew, K.; Hennig, R. G.; Medlin, D. L.; Browning, N. D.; Johnson, D. C. Interface-Driven Structural Distortions and Composition Segregation in Two-Dimensional Heterostructures. *Angew. Chemie - Int. Ed.* **2017**, *56* (46), 14448–14452. https://doi.org/10.1002/anie.201707270.

(60) Sun, W.; Dacek, S. T.; Ong, S. P.; Hautier, G.; Jain, A.; Richards, W. D.; Gamst, A. C.; Persson, K. A.; Ceder, G. The Thermodynamic Scale of Inorganic Crystalline Metastability. *Sci. Adv.* **2016**, *2* (11), e1600225. https://doi.org/10.1126/sciadv.1600225.

(61) Aykol, M.; Dwaraknath, S. S.; Sun, W.; Persson, K. A. Thermodynamic Limit for Synthesis of Metastable Inorganic Materials. *Sci. Adv.* **2018**, *4* (4), eaaq0148. https://doi.org/10.1126/sciadv.aaq0148.

(62) Ohta, H.; Seo, W. S.; Koumoto, K. Thermoelectric Properties of Homologous Compounds in the ZnO-In2O3 System. *J. Am. Ceram. Soc.* **1996**, *79* (8), 2193–2196. https://doi.org/10.1111/j.1151-2916.1996.tb08958.x.

(63) Merrill, D. R.; Sutherland, D. R.; Ditto, J. J.; Moore, D. B.; Falmbigl, M.; Medlin, D. L.; Johnson, D. C. The Synthesis of (PbSe)(1+delta) (m)(TiSe2)(n) (SnSe2)(1+gamma) (m)(TiSe2)(n) Heterostructures with Designed Nanoarchitectures by Self Assembly of Amorphous Precursors. *Nanoscale* **2016**, *8* (28), 13646–13651. https://doi.org/10.1039/c6nr03406c.

(64) Wiegers, G. A. Misfit Layer Compounds: Structures and Physical Properties. *Prog. Solid State Chem.* **1996**, *24* (1–2), 1–139. https://doi.org/10.1016/0079-6786(95)00007-0.

(65) Heideman, C.; Nyugen, N.; Hanni, J.; Lin, Q.; Duncombe, S.; Johnson, D. C.; Zschack, P. The Synthesis and Characterization of New [(BiSe)1.10]m[NbSe2]n, [(PbSe)1.10]m[NbSe2]n, [(CeSe)1.14]m[NbSe2]n and [(PbSe)1.12]m[TaSe2]n Misfit Layered Compounds. *J. Solid State Chem.* **2008**, *181* (7), 1701–1706. https://doi.org/10.1016/j.jssc.2008.06.017.

(66) Atkins, R.; Wilson, J.; Zschack, P.; Grosse, C.; Neumann, W.; Johnson, D. C. Synthesis of [(SnSe)1.15]m(TaSe2)Nferecrystals: Structurally Tunable Metallic Compounds. *Chem. Mater.* **2012**, *24* (23), 4594–4599. https://doi.org/10.1021/cm302948x.

(67) Alemayehu, M. B.; Ta, K.; Falmbigl, M.; Johnson, D. C. Structure, Stability, and Properties of the Intergrowth Compounds ([SnSe]1+δ)m(NbSe2)n, Where m = n = 1-20. *J. Am. Chem. Soc.* **2015**, *137* (14), 4831–4839. https://doi.org/10.1021/jacs.5b01556.

(68) Esters, M.; Alemayehu, M. B.; Jones, Z.; Nguyen, N. T.; Anderson, M. D.; Grosse, C.; Fischer, S. F.; Johnson, D. C. Synthesis of Inorganic Structural Isomers by Diffusion-Constrained Self-Assembly of Designed Precursors: A Novel Type of Isomerism. *Angew. Chemie - Int. Ed.* **2015**, *54* (4), 1130–1134. https://doi.org/10.1002/anie.201409714.

(69) Shabunina, G. G.; Kireeva, E. V.; Aminov, T. Reaction of Bi2Se3 with Cr2Sei3. *Russ. J. Inorg. Chem.* **1996**, *41*, 1496–1498.

(70) Clarke, S. M.; Freedman, D. E. (BiSe)1.23CrSe2 and (BiSe)1.22(Cr1.2Se2)2: Magnetic Anisotropy in the First Structurally Characterized Bi-Se-Cr Ternary Compounds. *Inorg. Chem.* **2015**, *54* (6), 2765–2771. https://doi.org/10.1021/ic5029178.

(71) Lin, Q.; Smeller, M.; Heideman, C. L.; Zschack, P.; Koyano, M.; Anderson, M. D.; Kykyneshi, R.; Keszler, D. A.; Anderson, I. M.; Johnson, D. C. Rational Synthesis and Characterization of a New Family of Low Thermal Conductivity Misfit Layer Compounds $[(PbSe)_{0.99}]_m(WSe_2)_n$†. *Chem. Mater.* **2010**, *22* (3), 1002–1009. https://doi.org/10.1021/cm901952v.

(72) Heideman, C. L.; Tepfer, S.; Lin, Q.; Rostek, R.; Zschack, P.; Anderson, M. D.; Anderson, I. M.; Johnson, D. C. Designed Synthesis, Structure, and Properties of a Family of Ferecrystalline Compounds $[(PbSe)_{1.00}]_m(MoSe_2)_N$. *J. Am. Chem. Soc.* **2013**, *135* (30), 11055–11062. https://doi.org/10.1021/ja402819q.

(73) Beekman, M.; Disch, S.; Gunning, N.; Johnson, D. C. Preparation, Formation, and Structure of [(SnSe)1.04]m(MoSe2)Nintergrowth Compounds (0 < m and n < 32) from Designed Precursors. *Inorg. Chem.* **2015**, *54* (3), 1091–1099. https://doi.org/10.1021/ic502427c.

(74) Moore, D. B.; Beekman, M.; Disch, S.; Johnson, D. C. Telluride Misfit Layer Compounds: [(PbTe)1.17] m(TiTe2)N. *Angew. Chemie - Int. Ed.* **2014**, *53* (22), 5672–5675. https://doi.org/10.1002/anie.201401022.

(75) Westover, R. D.; Ditto, J.; Falmbigl, M.; Hay, Z. L.; Johnson, D. C. Synthesis and Characterization of Quaternary Monolayer Thick MoSe<inf>2</Inf>/SnSe/NbSe<inf>2</Inf>/SnSe Heterojunction Superlattices. *Chem. Mater.* **2015**, *27* (18), 6411–6417. https://doi.org/10.1021/acs.chemmater.5b02588.

(76) Westover, R. D.; Atkins, R. A.; Ditto, J. J.; Johnson, D. C. Synthesis of [(SnSe) $_{1.16–1.09}$] $_1$ [(Nb $_x$ Mo $_{1-x}$)Se $_2$] $_1$ Ferecrystal Alloys. *Chem. Mater.* **2014**, *26* (11), 3443–3449. https://doi.org/10.1021/cm500720x.

(77) Falmbigl, M.; Hay, Z.; Ditto, J.; Mitchson, G.; Johnson, D. C. Modifying a Charge Density Wave Transition by Modulation Doping: Ferecrystalline Compounds ([Sn $_{1-x}$ Bi $_x$ Se] $_{1.15}$) $_1$ (VSe $_2$) $_1$ with $0 \leq x \leq 0.66$. *J. Mater. Chem. C* **2015**, *3* (47), 12308–12315. https://doi.org/10.1039/C5TC03130C.

(78) Merrill, D. R.; Sutherland, D. R.; Ditto, J.; Bauers, S. R.; Falmbigl, M.; Medlin, D. L.; Johnson, D. C. Kinetically Controlled Site-Specific Substitutions in Higher-Order Heterostructures. *Chem. Mater.* **2015**, *27* (11), 4066–4072. https://doi.org/10.1021/acs.chemmater.5b01071.

(79) Noh, M.; Thiel, J.; Johnson, D. C. Synthesis of Crystalline Superlattices by Controlled Crystallization of Modulated Reactants. *Science (80-.).* **1995**, *270* (5239), 1181–1184. https://doi.org/10.1126/science.270.5239.1181.

(80) Noh, M.; Thiel, J.; Johnson, D. C. Crystalline Superlattices with Designed Structure from Elementally Modulated Reactants. *Adv. Mater.* **1996**, *8* (7), 596–599. https://doi.org/10.1002/adma.19960080715.

(81) Noh, M.; Johnson, D. C. Designed Synthesis of Solid State Structural Isomers from Modulated Reactants. *J. Am. Chem. Soc.* **1996**, *118* (38), 9117–9122. https://doi.org/10.1021/ja9617653.

(82) Hughes, T. A.; Kevan, S. D.; Cox, D. E.; Johnson, D. C. Synthesis of Superlattices of Intercalated Transition Metal Dichalcogenides. *J. Am. Chem. Soc.* **2000**, *122* (37), 8910–8915. https://doi.org/10.1021/ja994140o.

(83) Nguyen, N. T.; Howe, B.; Hash, J. R.; Liebrecht, N.; Johnson, D. C. Synthesis of [(VSe2)n]1.06[(TaSe 2)n] Superlattices Using a Hybrid Approach: Self-Assembly of Amorphous Nanostructured Reactants. *Adv. Mater.* **2006**, *18* (1), 118–122. https://doi.org/10.1002/adma.200501400.

(84) Hadland, E.; Jang, H.; Falmbigl, M.; Fischer, R.; Medlin, D. L.; Cahill, D. G.; Johnson, D. C. Synthesis, Characterization, and Ultralow Thermal Conductivity of a Lattice-Mismatched SnSe2(MoSe2)1.32 Heterostructure. *Chem. Mater.* **2019**, *31* (15), 5699–5705. https://doi.org/10.1021/acs.chemmater.9b01637.

(85) Harris, F. R.; Standridge, S.; Feik, C.; Johnson, D. C. Design and Synthesis of [(Bi2Te3) x(TiTe2)y] Superlattices. *Angew. Chemie - Int. Ed.* **2003**, *42* (43), 5296–5299. https://doi.org/10.1002/anie.200351724.

(86) Harris, F. R.; Standridge, S.; Johnson, D. C. The Synthesis of [(Bi2Te3)X{(TiTe 2)Y}1.36] Superlattices from Modulated Elemental Reactants. *J. Am. Chem. Soc.* **2005**, *127* (21), 7843–7848. https://doi.org/10.1021/ja050799k.

(87) Alemayehu, M. B.; Falmbigl, M.; Ta, K.; Ditto, J.; Medlin, D. L.; Johnson, D. C. Designed Synthesis of van Der Waals Heterostructures: The Power of Kinetic Control. *Angew. Chemie - Int. Ed.* **2015**, *54* (51), 15468–15472. https://doi.org/10.1002/anie.201506152.

(88) Gunning, N. S.; Dankwort, T.; Falmbigl, M.; Ross, U.; Mitchson, G.; Hamann, D. M.; Lotnyk, A.; Kienle, L.; Johnson, D. C. Expanding the Concept of van Der Waals Heterostructures to Interwoven 3D Structures. *Chem. Mater.* **2017**, *29* (19), 8292–8298. https://doi.org/10.1021/acs.chemmater.7b02605.

(89) Lygo, A. C.; Wood, S. R.; Ditto, J.; Johnson, D. C. Synthesis of (BiSe)1+δ(Bi2Se3)1+γ(BiSe)1+δTiSe2 by Directed Self-Assembly of a Designed Precursor. *Chem. Mater.* **2019**, *31* (1), 216–223. https://doi.org/10.1021/acs.chemmater.8b04229.

(90) Neumann, W.; Kirmse, H.; Hausler, I.; Grosse, C.; Moeck, P.; Rouyimov, S.; Beekman, M.; Atkins, R.; Johnson, D. C.; Volz, K. Methods of Electron Crystallography as Tools for Materials Analysis. *Solid State Phenom.* **2012**, *186*, 1–6.

(91) Nguyen, N. T.; Berseth, P. A.; Lin, Q.; Chiritescu, C.; Cahill, D. G.; Mavrokefalos, A.; Shi, L.; Zschack, P.; Anderson, M. D.; Anderson, I. M.; et al. Synthesis and Properties of Turbostratically Disordered, Ultrathin WSe 2 Films. *Chem. Mater.* **2010**, *22* (9), 2750–2756. https://doi.org/10.1021/cm903633w.

(92) Atkins, R.; Moore, D. B.; Johnson, D. C. Insights into the Self-Assembly of Ferecrystalline Compounds from Designed Amorphous Precursors. *Chem. Mater.* **2013**, *25* (9), 1744–1750. https://doi.org/10.1021/cm400218z.

(93) Esters, M.; Johnson, D. C. Targeted Synthesis of Metastable Compounds and Intergrowths: The Modulated Elemental Reactants Method. In *Crystal Growth: Concepts, Mechanisms and Applications*; Li, J., Li, J., Chu, Y., Eds.; Nova Publishers: Hauppauge, NY, 2017.

(94) Beekman, M.; Cogburn, G.; Heideman, C.; Rouvimov, S.; Zschack, P.; Neumann, W.; Johnson, D. C. New Layered Intergrowths in the Sn-Mo-Se System. *J. Electron. Mater.* **2012**, *41* (6), 1476–1480. https://doi.org/10.1007/s11664-012-1971-3.

(95) Hamann, D. M.; Merrill, D. R.; Bauers, S. R.; Mitchson, G.; Ditto, J.; Rudin, S. P.; Johnson, D. C. Long-Range Order in [(SnSe) 1.2] 1 [TiSe 2] 1 Prepared from Designed Precursors. *Inorg. Chem.* **2017**, *56* (6), 3499–3505. https://doi.org/10.1021/acs.inorgchem.6b03063.

(96) Novet, T.; McConnell, J. M.; Johnson, D. C. Low-Temperature Reaction of Buried Metal-Silicon Interfaces: The Evolution of Interfacial Structure. *Chem. Mater.* **1992**, *4* (2), 473–478. https://doi.org/10.1021/cm00020a043.

(97) Sutherland, D. R.; Merrill, D. R.; Ditto, J.; Moore, D. B.; Medlin, D.; Johnson, D. C. Kinetics of the Topochemical Transformation of (PbSe) m (TiSe 2) n (SnSe 2) m (TiSe 2) n to (Pb 0.5 Sn 0.5 Se) m (TiSe 2) N. *J. Am. Chem. Soc.* **2019**, *141* (2), 922–927. https://doi.org/10.1021/jacs.8b10681.

(98) Westover, R. D.; Mitchson, G.; Ditto, J. J.; Johnson, D. C. Synthesis of a Family of ([SnSe] 1+ δ) m -([{Mo x Nb 1 x }Se 2] 1+ γ) 1 ([SnSe] 1+ δ) m -({Nb x -Mo 1-x }Se 2) 1 Superlattice -Heterostructures (m = 0, 1, 2, 3, 4 -and 0.8 ≤ x ≤ 1). *Eur. J. Inorg. Chem.* **2016**, *2016* (8), 1225–1231. https://doi.org/10.1002/ejic.201501324.

(99) Wood, S. R.; Merrill, D. R.; Mitchson, G.; Lygo, A. C.; Bauers, S. R.; Hamann, D. M.; Sutherland, D. R.; Ditto, J.; Johnson, D. C. Modulation Doping in Metastable Heterostructures via Kinetically Controlled Substitution. *Chem. Mater.* **2017**, *29* (2), 773–779. https://doi.org/10.1021/acs.chemmater.6b04688.

(100) Westover, R. D.; Mitchson, G.; Hite, O. K.; Hill, K.; Johnson, D. C. Suppression of a Charge Density Wave in ([SnSe]1.15)1(VSe2)1 Ferecrystals Via Isoelectronic Doping with Ta. *J. Electron. Mater.* **2016**, *45* (10), 4898–4902. https://doi.org/10.1007/s11664-016-4662-7.

(101) Hamann, D. M.; Bardgett, D.; Cordova, D. L. M.; Maynard, L. A.; Hadland, E. C.; Lygo, A. C.; Wood, S. R.; Esters, M.; Johnson, D. C. Sub-Monolayer Accuracy in Determining the Number of Atoms per Unit Area in Ultrathin Films Using X-Ray Fluorescence. *Chem. Mater.* **2018**, *30* (18), 6209–6216. https://doi.org/10.1021/acs.chemmater.8b02591.

(102) Cordova, D. L. M.; Fender, S. S.; Kam, T. M.; Seyd, J.; Albrecht, M.; Lu, P.; Fischer, R.; Johnson, D. C. Designed Synthesis and Structure-Property Relationships of Kinetically Stable [(PbSe)1+Î´]m(VSe2)1 (m = 1, 2, 3, 4) Heterostructures. *Chem. Mater.* **2019**, *31* (20), 8473–8483. https://doi.org/10.1021/acs.chemmater.9b02826.

(103) Fischer-Colbrie, A.; Bienenstock, A.; Fuoss, P. H.; Marcus, M. A. Structure and Bonding in Photodiffused Amorphous Ag-GeSe2 Thin Films. *Phys. Rev. B* **1988**, *38* (17), 12388–12403. https://doi.org/10.1103/PhysRevB.38.12388.

(104) Tyrsted, C.; Pauw, B. R.; Jensen, K. M. Ø.; Becker, J.; Christensen, M.; Iversen, B. B. Watching Nanoparticles Form: An in Situ (Small-/Wide-Angle x-Ray Scattering/Total Scattering) Study of the Growth of Yttria-Stabilised Zirconia in Supercritical Fluids. *Chem. - A Eur. J.* **2012**, *18* (18), 5759–5766. https://doi.org/10.1002/chem.201102826.

(105) Bøjesen, E. D.; Iversen, B. B. The Chemistry of Nucleation. *CrystEngComm* **2016**, *18* (43), 8332–8353. https://doi.org/10.1039/c6ce01489e.

(106) Rigden, J. S.; Newport, R. J.; Bushnell-Wye, G. The Structural Characterization of Amorphous Thin Films and Coatings in Their As-Deposited State Using x-Rays at Shallow Angles of Incidence. *J. Mater. Res.* **1997**, *12* (1), 264–276. https://doi.org/10.1557/JMR.1997.0034.

(107) Jensen, K. M. Ø.; Blichfeld, A. B.; Bauers, S. R.; Wood, S. R.; Dooryhée, E.; Johnson, D. C.; Iversen, B. B.; Billinge, S. J. L. Demonstration of Thin Film Pair Distribution Function Analysis (TfPDF) for the Study of Local Structure in Amorphous and Crystalline Thin Films. *IUCrJ* **2015**, *2*, 481–489. https://doi.org/10.1107/S2052252515012221.

(108) Shyam, B.; Stone, K. H.; Bassiri, R.; Fejer, M. M.; Toney, M. F.; Mehta, A. Measurement and Modeling of Short and Medium Range Order in Amorphous Ta2O5 Thin Films. *Sci. Rep.* **2016**, *6* (1), 1–7. https://doi.org/10.1038/srep32170.

(109) Bauers, S. R.; Wood, S. R.; Jensen, K. M. Ø.; Blichfeld, A. B.; Iversen, B. B.; Billinge, S. J. L.; Johnson, D. C. Structural Evolution of Iron Antimonides from Amorphous Precursors to Crystalline Products Studied by Total Scattering Techniques. *J. Am. Chem. Soc.* **2015**, *137* (30), 9652–9658. https://doi.org/10.1021/jacs.5b04838.

(110) Wood, S. R.; Woods, K. N.; Plassmeyer, P. N.; Marsh, D. A.; Johnson, D. W.; Page, C. J.; Jensen, K. M. Ø.; Johnson, D. C. Same Precursor, Two Different Products: Comparing the Structural Evolution of In-Ga-O "Gel-Derived" Powders and Solution-Cast Films Using Pair Distribution Function Analysis. *J. Am. Chem. Soc.* **2017**, *139* (15), 5607–5613. https://doi.org/10.1021/jacs.7b02097.

(111) Permien, S.; Hansen, A. L.; Van Dinter, J.; Indris, S.; Neubüser, G.; Kienle, L.; Doyle, S.; Mangold, S.; Bensch, W. Unveiling the Reaction Mechanism during Li Uptake and Release of Nanosized "NiFeMnO4": Operando X-Ray Absorption, X-Ray Diffraction, and Pair Distribution Function Investigations. *ACS Omega* **2019**, *4* (1), 2398–2409. https://doi.org/10.1021/acsomega.8b03276.

(112) Hansen, A. L.; Dankwort, T.; Groß, H.; Etter, M.; König, J.; Duppel, V.; Kienle, L.; Bensch, W. Structural Properties of the Thermoelectric Material CuCrS2 and of Deintercalated Cu: XCrS2 on Different Length Scales: X-Ray Diffraction, Pair Distribution Function and Transmission Electron Microscopy Studies. *J. Mater. Chem. C* **2017**, *5* (36), 9331–9338. https://doi.org/10.1039/c7tc02983g.

(113) Hansen, A. L.; Dietl, B.; Etter, M.; Kremer, R. K.; Johnson, D. C.; Bensch, W. Temperature-Dependent Synchrotron X-Ray Diffraction, Pair Distribution Function and Susceptibility Study on the Layered Compound CrTe3. *Zeitschrift fur Krist. - Cryst. Mater.* **2017**, *233* (6), 361–370. https://doi.org/10.1515/zkri-2017-2100.

(114) Kohlmann, H. Looking into the Black Box of Solid-State Synthesis. *Eur. J. Inorg. Chem.* **2019**, No. 39–40, 4174–4180. https://doi.org/10.1002/ejic.201900733.

(115) Shoemaker, D. P.; Hu, Y. J.; Chung, D. Y.; Halder, G. J.; Chupas, P. J.; Soderholm, L.; Mitchell, J. F.; Kanatzidis, M. G. In Situ Studies of a Platform for Metastable Inorganic Crystal Growth and Materials Discovery. *Proc. Natl. Acad. Sci. U. S. A.* **2014**, *111* (30), 10922–10927. https://doi.org/10.1073/pnas.1406211111.

(116) Scarlett, N. V. Y.; Grey, I. E.; Brand, H. E. A. In Situ Synchrotron Diffraction Studies on the Formation Kinetics of Jarosites. *J. Synchrotron Radiat.* **2013**, *20* (2), 366–375. https://doi.org/10.1107/S0909049513000101.

(117) Rudin, S. P. A Density Functional Theory Calculations-Based Approach that Predicts Layered Materials with Emergent Structures. arXiv:1611.07510v1

(118) Kisielowski, C.; Freitag, B.; Bischoff, M.; Van Lin, H.; Lazar, S.; Knippels, G.; Tiemeijer, P.; Van Der Stam, M.; Von Harrach, S.; Stekelenburg, M.; et al. Detection of Single Atoms and Buried Defects in Three Dimensions by Aberration-Corrected Electron Microscope with 0.5-Å Information Limit. *Microsc. Microanal.* **2008**, *14* (5), 469–477. https://doi.org/10.1017/S1431927608080902.

(119) Egoavil, R.; Gauquelin, N.; Martinez, G. T.; Van Aert, S.; Van Tendeloo, G.; Verbeeck, J. Atomic Resolution Mapping of Phonon Excitations in STEM-EELS Experiments. *Ultramicroscopy* **2014**, *147*, 1–7. https://doi.org/10.1016/j.ultramic.2014.04.011.

(120) Delobbe, A.; Salord, O.; Hrncir, T.; David, A.; Sudraud, P.; Lopour, F. High Speed TEM Sample Preparation by Xe FIB. *Microsc. Microanal.* **2014**, *20* (3), 298–299. https://doi.org/10.1017/S1431927614003213.

(121) Zhang, Y.; Keller, D.; Rossell, M. D.; Erni, R. Formation of Au Nanoparticles in Liquid Cell Transmission Electron Microscopy: From a Systematic Study to Engineered Nanostructures. *Chem. Mater.* **2017**, *29* (24), 10518–10525. https://doi.org/10.1021/acs.chemmater.7b04421.

(122) Yuan, Y.; Amine, K.; Lu, J.; Shahbazian-Yassar, R. Understanding Materials Challenges for Rechargeable Ion Batteries with in Situ Transmission Electron Microscopy. *Nat. Commun.* **2017**, *8* (1), 1–14. https://doi.org/10.1038/ncomms15806.

(123) Allen, L. J.; D'Alfonso, A. J.; Freitag, B.; Klenov, D. O. Chemical Mapping at Atomic Resolution Using Energy-Dispersive X-Ray Spectroscopy. *MRS Bull.* **2012**, *37* (1), 47–52. https://doi.org/10.1557/mrs.2011.331.

Chapter II

(1) West, A. R. *Solid State Chemistry and Its Applications*, 2nd ed.; John Wiley & Sons, Ltd: West Sussex, UK, 2014.

(2) Merrill, D. R.; Moore, D. B.; Mark, N.; Beekman, M.; Heideman, C. L.; Johnson, D. C. Ferecrystals : Non-Epitaxial Layered Intergrowths. **2014**. https://doi.org/10.1088/0268-1242/29/6/064012.

(3) Parratt, L. G. Surface Studies of Solids by Total Reflection of X-Rays. *Phys. Rev.* **1954**, *95* (2), 359–369. https://doi.org/10.1103/PhysRev.95.359.

(4) Phung, T. M.; Jensen, J. M.; Johnson, D. C.; Donovan, J. J.; Mcburnett, B. G. Determination of the Composition of Ultra-Thin Ni-Si Films on Si: Constrained Modeling of Electron Probe Microanalysis and x-Ray Reflectivity Data. **2008**, *37*, 608–614. https://doi.org/10.1002/xrs.1102.

(5) Zeppenfeld, A. C.; Fiddler, S. L.; Ham, W. K.; Klopfenstein, B. J.; Page, C. J. Variation of Layer Spacing in Self-Assembled Hafnium-1,10-Decanediylbis(Phosphonate) Multilayers As Determined by Ellipsometry and Grazing Angle X-Ray Diffraction. *J. Am. Chem. Soc.* **1994**, *116* (20), 9158–9165. https://doi.org/10.1021/ja00099a034.

(6) Falmbigl, M.; Alemayehu, M. B.; Merrill, D. R.; Beekman, M.; Johnson, D. C. In-Plane Structure of Ferecrystalline Compounds. *Cryst. Res. Technol.* **2015**, *50* (6), 464–472. https://doi.org/10.1002/crat.201500019.

(7) Tanner, B. K.; Hase, T. P. A.; Lafford, T. A.; Goorsky, M. S. Grazing Incidence In-Plane X-Ray Diffraction in the Laboratory. *Powder Diffr.* **2004**, *19* (1), 45–48. https://doi.org/10.1154/1.1649319.

(8) Lygo, A. C.; Wood, S. R.; Ditto, J.; Johnson, D. C. Synthesis of (BiSe)1+δ(Bi2Se3)1+γ(BiSe)1+δTiSe2 by Directed Self-Assembly of a Designed Precursor. *Chem. Mater.* **2019**, *31* (1), 216–223. https://doi.org/10.1021/acs.chemmater.8b04229.

(9) Haschke, M. *Laboratory Micro-X-Ray Fluorescence Spectroscopy: Instrumentation and Applications*; Springer International Publishing: Eggersdorf, Germany, 2014.

(10) Hamann, D. M.; Bardgett, D.; Cordova, D. L. M.; Maynard, L. A.; Hadland, E. C.; Lygo, A. C.; Wood, S. R.; Esters, M.; Johnson, D. C. Sub-Monolayer Accuracy in Determining the Number of Atoms per Unit Area in Ultrathin Films Using X-Ray Fluorescence. *Chem. Mater.* **2018**, *30* (18), 6209–6216. https://doi.org/10.1021/acs.chemmater.8b02591.

(11) Frey, H.; Khan, H. R. *Handbook of Thin-Film Technology*; Springer-Verlag, 2015. https://doi.org/10.1007/978-3-642-05430-3.

(12) Sze, S. M.; Lee, M. K. *Semiconductor Devices*, 3rd ed.; John Wiley & Sons, Ltd: New York City, NY, 2012.

(13) Heaney, M. B. Electrical Conductivity and Resistivity. In *Electrical Measurement, Signal Processing, and Displays*; Webster, J. G., Ed.; CRC Press, 2003; pp 1–14.

(14) van der Pauw, L. J. A Method of Measuring the Resistivity and Hall Coefficient on Lamellae of Arbitrary Shape. *Philips Technical Review*. 1958, pp 220–224. https://doi.org/537.723.1:53.081.7+538.632:083.9.

Chapter III.

(1) Schön, J. C.; Jansen, M. First Step Towards Planning of Syntheses in Solid-State Chemistry: Determination of Promising Structure Candidates by Global Optimization. *Angew. Chemie Int. Ed. English* **1996**, *35* (12), 1286–1304. https://doi.org/10.1002/anie.199612861.

(2) Shoemaker, D. P.; Chung, D. Y.; Mitchell, J. F.; Bray, T. H.; Soderholm, L.; Chupas, P. J.; Kanatzidis, M. G. Understanding Fluxes as Media for Directed Synthesis: In Situ Local Structure of Molten Potassium Polysulfides. *J. Am. Chem. Soc.* **2012**, *134* (22), 9456–9463. https://doi.org/10.1021/ja303047e.

(3) Curtarolo, S.; Hart, G. L. W.; Nardelli, M. B.; Mingo, N.; Sanvito, S.; Levy, O. The High-Throughput Highway to Computational Materials Design. *Nat. Mater.* **2013**, *12* (3), 191–201. https://doi.org/10.1038/nmat3568.

(4) Saal, J. E.; Kirklin, S.; Aykol, M.; Meredig, B.; Wolverton, C. Materials Design and Discovery with High-Throughput Density Functional Theory: The Open Quantum Materials Database (OQMD). *JOM* **2013**, *65* (11), 1501–1509. https://doi.org/10.1007/s11837-013-0755-4.

(5) Trimarchi, G.; Zunger, A. Global Space-Group Optimization Problem: Finding the Stablest Crystal Structure without Constraints. *Phys. Rev. B - Condens. Matter Mater. Phys.* **2007**, *75* (10), 1–8. https://doi.org/10.1103/PhysRevB.75.104113.

(6) Narayan, A.; Bhutani, A.; Rubeck, S.; Eckstein, J. N.; Shoemaker, D. P.; Wagner, L. K. Computational and Experimental Investigation for New Transition Metal Selenides and Sulfides: The Importance of Experimental Verification for Stability. *Phys. Rev. B* **2016**, *94* (4), 1–15. https://doi.org/10.1103/PhysRevB.94.045105.

(7) Kalläne, M.; Rossnagel, K.; Marczynski-Bühlow, M.; Kipp, L.; Starnberg, H. I.; Stoltz, S. E. Stabilization of the Misfit Layer Compound (PbS)1.13TaS2 by Metal Cross Substitution. *Phys. Rev. Lett.* **2008**, *100* (6), 13–16. https://doi.org/10.1103/PhysRevLett.100.065502.

(8) Wiegers, G. A. Misfit Layer Compounds: Structures and Physical Properties. *Prog. Solid State Chem.* **1996**, *24* (1–2), 1–139. https://doi.org/10.1016/0079-6786(95)00007-0.

(9) Oosawa, Y.; Gotoh, Y.; Akimoto, J.; Tsunoda, T.; Sohma, M.; Onoda, M. Three Types of Ternary Selenides with Layered Composite Crystal Structures Formed in the PbNbSe System. *Jpn. J. Appl. Phys* **1992**, *31*, 1096–1099.

(10) Wiegers, G. A.; Meetsma, A.; Haange, R. J.; De Boer, J. L. Structure, Electrical Transport, and Magnetic Properties of the Misfit Layer Compound (CeS)1.16NbS2, "CeNbS3." *J. Solid State Chem.* **1990**, *89*, 328–339. https://doi.org/10.1016/0022-4596(90)90274-2.

(11) Ohno, Y. Electronic Structure of the Misfit-Layer Compounds PbTiS3 and SnNbS3. *Phys. Rev. B* **1991**, *44* (3), 1281–1291. https://doi.org/10.1103/PhysRevB.44.1281.

(12) Ettema, A. R. H. F.; Haas, C. An X-Ray Photoemission Spectroscopy Study of Interlayer Charge Transfer in Some Misfit Layer Compounds. *J. Phys. Condens. Matter* **1993**, *5* (23), 3817–3826. https://doi.org/10.1088/0953-8984/5/23/008.

(13) Fang, C. M.; Ettema, A. R. H. F.; Haas, C.; Wiegers, G. A. Electronic Structure of the Misfit-Layer Compound (SnS)1.17NbS2 Deduced from Band-Structure Calculations and Photoelectron Spectra. *Phys. Rev. B* **1995**, *52* (4), 2336–2347.

(14) Moelo, Y.; Meerschaut, A.; Rouxel, J.; Auriel, C. Precise Analytical Characterization of Incommensurate Sandwiched Layered Compounds [(Pb,Sn)S]1+x[(Nb,Ti)S2]m (0.08<= x <= 0.28, m = 1-3). Role of Cationic Coupling on the Properties and the Structural Modulation. *Chem. Mater.* **1995**, *7*, 1759–1771.

(15) Mariano, A. N.; Chopra, K. L. Polymorphism in Some IV-VI Compounds Induced by High Pressure and Thin-Film Epitaxial Growth. *Appl. Phys. Lett.* **1967**, *10* (10), 282–284. https://doi.org/10.1063/1.1754812.

(16) Wiegers, G. A. The Characterisation of VSe2: A Study of the Thermal Expansion. *J. Phys. C Solid State Phys* **1981**, *14*, 4225–4235.

(17) Hamann, D. M.; Bardgett, D.; Cordova, D. L. M.; Maynard, L. A.; Hadland, E. C.; Lygo, A. C.; Wood, S. R.; Esters, M.; Johnson, D. C. Sub-Monolayer Accuracy in Determining the Number of Atoms per Unit Area in Ultrathin Films Using X-Ray Fluorescence. *Chem. Mater.* **2018**, *30* (18), 6209–6216. https://doi.org/10.1021/acs.chemmater.8b02591.

(18) Zeppenfeld, A. C.; Fiddler, S. L.; Ham, W. K.; Klopfenstein, B. J.; Page, C. J. Variation of Layer Spacing in Self-Assembled Hafnium-1,10-Decanediylbis(Phosphonate) Multilayers As Determined by Ellipsometry and Grazing Angle X-Ray Diffraction. *J. Am. Chem. Soc.* **1994**, *116* (20), 9158–9165. https://doi.org/10.1021/ja00099a034.

(19) Hite, O. K.; Falmbigl, M.; Alemayehu, M. B.; Esters, M.; Wood, S. R.; Johnson, D. C. Charge Density Wave Transition in (PbSe) 1+δ (VSe 2) n Compounds with n = 1, 2, and 3. *Chem. Mater.* **2017**, *29*, 5646–5653. https://doi.org/10.1021/acs.chemmater.7b01383.

Chapter IV

(1) Hamann, D. M.; Hadland, E. C.; Johnson, D. C. Heterostructures Containing Dichalcogenides-New Materials with Predictable Nanoarchitectures and Novel Emergent Properties. *Semicond. Sci. Technol.* **2017**, *32* (9), 093004. https://doi.org/10.1088/1361-6641/aa7785.

(2) Geim, A. K.; Grigorieva, I. V. Van Der Waals Heterostructures. *Nature* **2014**, *499* (7459), 419–425. https://doi.org/10.1038/nature12385.

(3) Wang, H.; Huang, X.; Lin, J.; Cui, J.; Chen, Y.; Zhu, C.; Lui, F.; Zeng, Q.; Zhou, J.; Yu, P.; et al. High-Quality Monolayer Superconductor NbSe2 Grown by Chemical Vapour Deposition. *Nat. Commun.* **2017**, *8* (394). https://doi.org/10.1038/s41467-017-00427-5.

(4) Tsen, A. W.; Hovden, R.; Wang, D.; Kim, Y. D.; Okamoto, J.; Spoth, K. A.; Liu, Y.; Lu, W.; Sun, Y.; Hone, J. C.; et al. Structure and Control of Charge Density Waves in Two-Dimensional 1T-TaS2. *Proc. Natl. Acad. Sci. U. S. A.* **2015**, *112* (49), 15054–15059. https://doi.org/10.1073/pnas.1512092112.

(5) Yang, J.; Wang, W.; Liu, Y.; Du, H.; Ning, W.; Zheng, G.; Jin, C.; Han, Y.; Wang, N.; Yang, Z.; et al. Thickness Dependence of the Charge-Density-Wave Transition Temperature in VSe2. *Appl. Phys. Lett.* **2014**, *105* (6). https://doi.org/10.1063/1.4893027.

(6) Xi, X.; Zhao, L.; Wang, Z.; Berger, H.; Forró, L.; Shan, J.; Mak, K. F. Strongly Enhanced Charge-Density-Wave Order in Monolayer NbSe2. *Nat. Nanotechnol.* **2015**, *10* (9), 765–769. https://doi.org/10.1038/nnano.2015.143.

(7) Grosse, C.; Alemayehu, M. B.; Falmbigl, M.; Mogilatenko, A.; Chiatti, O.; Johnson, D. C.; Fischer, S. F. Superconducting Ferecrystals: Turbostratically Disordered Atomic-Scale Layered (PbSe)1.14(NbSe2) n Thin Films. *Sci. Rep.* **2016**, *6* (1), 33457. https://doi.org/10.1038/srep33457.

(8) Goli, P.; Khan, J.; Wickramaratne, D.; Lake, R. K.; Balandin, A. A. Charge Density Waves in Exfoliated Films of van Der Waals Materials: Evolution of Raman Spectrum in TiSe2. *Nano Lett.* **2012**, *12* (11), 5941–5945. https://doi.org/10.1021/nl303365x.

(9) Yan, Z.; Jiang, C.; Pope, T. R.; Tsang, C. F.; Stickney, J. L.; Goli, P.; Renteria, J.; Salguero, T. T.; Balandin, A. A. Phonon and Thermal Properties of Exfoliated $TaSe_2$ Thin Films. *J. Appl. Phys.* **2013**, *114* (20), 204301. https://doi.org/10.1063/1.4833250.

(10) Li, F.; Tu, K.; Chen, Z. Versatile Electronic Properties of VSe2 Bulk, Few-Layers, Monolayer, Nanoribbons, and Nanotubes: A Computational Exploration. *J. Phys. Chem. C* **2014**, *118* (36), 21264–21274. https://doi.org/10.1021/jp507093t.

(11) Wasey, A. H. M. A.; Chakrabarty, S.; Das, G. P. Quantum Size Effects in Layered VX_2 (X = S, Se) Materials: Manifestation of Metal to Semimetal or Semiconductor Transition. *J. Appl. Phys.* **2015**, *117* (6), 064313. https://doi.org/10.1063/1.4908114.

(12) Lebègue, S.; Björkman, T.; Klintenberg, M.; Nieminen, R. M.; Eriksson, O. Two-Dimensional Materials from Data Filtering and *Ab Initio* Calculations. *Phys. Rev. X* **2013**, *3* (3), 031002. https://doi.org/10.1103/PhysRevX.3.031002.

(13) Thompson, A. H.; Silbernagel, B. G. Correlated Magnetic and Transport Properties in the Charge-Density-Wave States of VSe2. *Phys. Rev. B* **1979**, *19* (7), 3420–3426. https://doi.org/10.1103/PhysRevB.19.3420.

(14) Xu, K.; Chen, P.; Li, X.; Wu, C.; Guo, Y.; Zhao, J.; Wu, X.; Xie, Y. Ultrathin Nanosheets of Vanadium Diselenide: A Metallic Two-Dimensional Material with Ferromagnetic Charge-Density-Wave Behavior. *Angew. Chemie Int. Ed.* **2013**, *52* (40), 10477–10481. https://doi.org/10.1002/anie.201304337.

(15) Pásztor, Á.; Scarfato, A.; Renner, C. Mechanical in Situ Exfoliation of van Der Waals Materials. *Rev. Sci. Instrum.* **2017**, *88* (7), 076104. https://doi.org/10.1063/1.4993738.

(16) Feng, J.; Biswas, D.; Rajan, A.; Watson, M. D.; Mazzola, F.; Clark, O. J.; Underwood, K.; Marković, I.; McLaren, M.; Hunter, A.; et al. Electronic Structure and Enhanced Charge-Density Wave Order of Monolayer VSe_2. *Nano Lett.* **2018**, *18* (7), 4493–4499. https://doi.org/10.1021/acs.nanolett.8b01649.

(17) Duvjir, G.; Choi, B. K.; Jang, I.; Ulstrup, S.; Kang, S.; Thi Ly, T.; Kim, S.; Choi, Y. H.; Jozwiak, C.; Bostwick, A.; et al. Emergence of a Metal–Insulator Transition and High-Temperature Charge-Density Waves in VSe_2 at the Monolayer Limit. *Nano Lett.* **2018**, *18* (9), 5432–5438. https://doi.org/10.1021/acs.nanolett.8b01764.

(18) Chen, P.; Pai, W. W.; Chan, Y.-H.; Madhavan, V.; Chou, M. Y.; Mo, S.-K.; Fedorov, A.-V.; Chiang, T.-C. Unique Gap Structure and Symmetry of the Charge Density Wave in Single-Layer VSe 2. *Phys. Rev. Lett.* **2018**, *121* (19), 196402. https://doi.org/10.1103/PhysRevLett.121.196402.

(19) Bonilla, M.; Kolekar, S.; Ma, Y.; Diaz, H. C.; Kalappattil, V.; Das, R.; Eggers, T.; Gutierrez, H. R.; Phan, M.-H.; Batzill, M. Strong Room-Temperature Ferromagnetism in VSe2 Monolayers on van Der Waals Substrates. *Nat. Nanotechnol.* **2018**, *13* (4), 289–293. https://doi.org/10.1038/s41565-018-0063-9.

(20) Cao, Q.; Yun, F. F.; Sang, L.; Xiang, F.; Liu, G.; Wang, X. Defect Introduced Paramagnetism and Weak Localization in Two-Dimensional Metal VSe_2. *Nanotechnology* **2017**, *28* (47), 475703. https://doi.org/10.1088/1361-6528/aa8f6c.

(21) Atkins, R.; Dolgos, M.; Fiedler, A.; Grosse, C.; Fischer, S. F.; Rudin, S. P.; Johnson, D. C. Synthesis and Systematic Trends in Structure and Electrical Properties of [(SnSe) 1.15]m(VSe2)1, m = 1,2,3, and 4. *Chem. Mater.* **2014**, *26*, 2862–2872. https://doi.org/10.1021/cm5004774.

(22) Hite, O. K.; Falmbigl, M.; Alemayehu, M. B.; Esters, M.; Wood, S. R.; Johnson, D. C. Charge Density Wave Transition in (PbSe) 1+δ (VSe 2) n Compounds with n = 1, 2, and 3. *Chem. Mater.* **2017**, *29*, 5646–5653. https://doi.org/10.1021/acs.chemmater.7b01383.

(23) Falmbigl, M.; Fiedler, A.; Atkins, R. E.; Fischer, S. F.; Johnson, D. C. Suppressing a Charge Density Wave by Changing Dimensionality in the Ferecrystalline Compounds ([SnSe]1.15)1(VSe2)n with n = 1, 2, 3, 4. *Nano Lett.* **2015**, *15* (2), 943–948. https://doi.org/10.1021/nl503708j.

(24) Lin, Q.; Smeller, M.; Heideman, C. L.; Zschack, P.; Koyano, M.; Anderson, M. D.; Kykyneshi, R.; Keszler, D. A.; Anderson, I. M.; Johnson, D. C. Rational Synthesis and Characterization of a New Family of Low Thermal Conductivity Misfit Layer Compounds $[(PbSe)_{0.99}]_m(WSe_2)_n$ †. *Chem. Mater.* **2010**, *22* (3), 1002–1009. https://doi.org/10.1021/cm901952v.

(25) Heideman, C. L.; Rostek, R.; Anderson, M. D.; Herzing, A. A.; Anderson, I. M.; Johnson, D. C. Synthesis and Electronic Properties of the Misfit Layer Compound [(PbSe)1.00]1[MoSe2]1. *J. Electron. Mater.* **2010**, *39* (9), 1476–1481. https://doi.org/10.1007/s11664-010-1303-4.

(26) Fister, L.; Li, X.; McConnell, J.; Novet, T.; Johnson, D. C. Deposition System for the Synthesis of Modulated, Ultrathin-film Composites. *J. Vac. Sci. Technol. A Vacuum, Surfaces, Film.* **1993**, *11* (6), 3014–3019. https://doi.org/10.1116/1.578290.

(27) Hamann, D. M.; Bardgett, D.; Cordova, D. L. M.; Maynard, L. A.; Hadland, E. C.; Lygo, A. C.; Wood, S. R.; Esters, M.; Johnson, D. C. Sub-Monolayer Accuracy in Determining the Number of Atoms per Unit Area in Ultrathin Films Using X-Ray Fluorescence. *Chem. Mater.* **2018**, *30* (18), 6209–6216. https://doi.org/10.1021/acs.chemmater.8b02591.

(28) Rodríguez-Carvajal, J. FULLPROF: A Program for Rietveld Refinement and Pattern Matching Analysis. In *Abstracts of the Satellite Meeting on Powder Diffraction of the XV Congess of the IUCr, Toulouse, France*; 1990; p 127. https://doi.org/SDI: 0921-4526(93)E0113-U.

(29) Toby, B. H. EXPGUI, a Graphical User Interface for GSAS. *J. Appl. Crystallogr.* **2001**, *34*, 210–213. https://doi.org/10.1107/S0021889801002242.

(30) Smeller, M. Structural Studies of [(PbSe)0.99]m[WSe2]n, [(PbSe)1.00]m[MoSe2]n, and [(SnSe)1.03]m[MoSe2]n Misfit Layered Compounds, Dissertation, University of Oregon, Eugene, OR, 2011.

(31) Mariano, A. N.; Chopra, K. L. Polymorphism in Some IV-VI Compounds Induced by High Pressure and Thin-Film Epitaxial Growth. *Appl. Phys. Lett.* **1967**, *10* (10), 282–284. https://doi.org/10.1063/1.1754812.

(32) Schneemeyer, L. F.; Stacy, A.; Sienko, M. J. Effect of Nonstoichiometry on the Periodic Lattice Distortion in Vanadium Diselenide. *Inorg. Chem.* **1980**, *19* (9), 2659–2662. https://doi.org/10.1021/ic50211a036.

(33) Zeppenfeld, A. C.; Fiddler, S. L.; Ham, W. K.; Klopfenstein, B. J.; Page, C. J. Variation of Layer Spacing in Self-Assembled Hafnium-1,10-Decanediylbis(Phosphonate) Multilayers As Determined by Ellipsometry and Grazing Angle X-Ray Diffraction. *J. Am. Chem. Soc.* **1994**, *116* (20), 9158–9165. https://doi.org/10.1021/ja00099a034.

(34) Parratt, L. G. Surface Studies of Solids by Total Reflection of X-Rays. *Phys. Rev.* **1954**, *95* (2), 359–369. https://doi.org/10.1103/PhysRev.95.359.

(35) Cordova, D. L. M.; Kam, T. M.; Fender, S. S.; Tsai, Y. H.; Johnson, D. C. Strong Non-Epitaxial Interactions: Crystallographically Aligned PbSe on VSe2. *Phys. Status Solidi* **2019**, *1800896*, 1800896. https://doi.org/10.1002/pssa.201800896.

(36) Alemayehu, M. B.; Mitchson, G.; Ditto, J.; Hanken, B. E.; Asta, M.; Johnson, D. C. Charge Transfer between PbSe and NbSe2 in [(PbSe) 1.14]m(NbSe2)1 Ferecrystalline Compounds. *Chem. Mater.* **2014**, *26* (5), 1859–1866. https://doi.org/10.1021/cm404018a.

(37) Moore, D. B.; Beekman, M.; Zschack, P.; Johnson, D. C. Synthesis of Four New Members of the Ferecrystals. *Nanotechnol. (IEEE-NANO), 2011 11th IEEE Conf. on, 15-18 Aug. 2011* **2011**, *16*, 1363–1366. https://doi.org/10.1109/NANO.2011.6144586.

(38) Heideman, C. L.; Tepfer, S.; Lin, Q.; Rostek, R.; Zschack, P.; Anderson, M. D.; Anderson, I. M.; Johnson, D. C. Designed Synthesis, Structure, and Properties of a Family of Ferecrystalline Compounds $[(PbSe)_{1.00}]_m(MoSe_2)_N$. *J. Am. Chem. Soc.* **2013**, *135* (30), 11055–11062. https://doi.org/10.1021/ja402819q.

(39) Grosse, C.; Alemayehu, M. B.; Falmbigl, M.; Mogilatenko, A.; Chiatti, O.; Johnson, D. C.; Fischer, S. F. Superconducting Ferecrystals: Turbostratically Disordered Atomic-Scale Layered (PbSe)1.14(NbSe2)n Thin Films. *Sci. Rep.* **2016**, *6* (August), 33457. https://doi.org/10.1038/srep33457.

(40) Atkins, R.; Moore, D. B.; Johnson, D. C. Insights into the Self-Assembly of Ferecrystalline Compounds from Designed Amorphous Precursors. *Chem. Mater.* **2013**, *25* (9), 1744–1750. https://doi.org/10.1021/cm400218z.

(41) Lin, Q.; Smeller, M.; Heideman, C. L.; Zschack, P.; Koyano, M.; Anderson, M. D.; Kykyneshi, R.; Keszler, D. A.; Anderson, I. M.; Johnson, D. C. Rational Synthesis and Characterization of a New Family of Low Thermal Conductivity Misfit Layer Compounds [(PbSe)0.99]m(WSe2)n'. *Chem. Mater.* **2010**, *22* (3), 1002–1009. https://doi.org/10.1021/cm901952v.

(42) Anderson, M. D.; Heideman, C. L.; Lin, Q.; Smeller, M.; Kokenyesi, R.; Herzing, A. A.; Anderson, I. M.; Keszler, D. A.; Zschack, P.; Johnson, D. C. Size-Dependent Structural Distortions in One-Dimensional Nanostructures. *Angew. Chemie - Int. Ed.* **2013**, *52* (7), 1982–1985. https://doi.org/10.1002/anie.201207825.

(43) Eftekhari, A. Molybdenum Diselenide (MoSe2) for Energy Storage, Catalysis, and Optoelectronics. *Appl. Mater. Today* **2017**, *8*, 1–17. https://doi.org/10.1016/j.apmt.2017.01.006.

(44) Bayard, M.; Sienko, M. J. Anomalous Electrical and Magnetic Properties of Vanadium Diselenide *. *J. Solid State Chem.* **1976**, *19*, 325–329.

(45) Heine, V. Theory of Surface States. *Phys. Rev.* **1965**, *138* (6A), A1689–A1696. https://doi.org/10.1103/PhysRev.138.A1689.

(46) Dalven, R. A Review of the Semiconductor Properties of PbTe, PbSe, PbS and PbO. *Infrared Phys.* **1969**, *9* (4), 141–184. https://doi.org/10.1016/0020-0891(69)90022-0.

(47) Chattopadhyay, T.; Pannetier, J.; Von Schnering, H. G. Neutron Diffraction Study of the Structural Phase Transition in SnS and SnSe. *J. Phys. Chem. Solids* **1986**, *47* (9), 879–885. https://doi.org/10.1016/0022-3697(86)90059-4.

(48) Falmbigl, M.; Alemayehu, M. B.; Merrill, D. R.; Beekman, M.; Johnson, D. C. In-Plane Structure of Ferecrystalline Compounds. *Cryst. Res. Technol.* **2015**, *50* (6), 464–472. https://doi.org/10.1002/crat.201500019.

(49) Beekman, M.; Disch, S.; Rouvimov, S.; Kasinathan, D.; Koepernik, K.; Rosner, H.; Zschack, P.; Neumann, W. S.; Johnson, D. C. Controlling Size-Induced Phase Transformations Using Chemically Designed Nanolaminates. *Angew. Chemie Int. Ed.* **2013**, *52* (50), 13211–13214. https://doi.org/10.1002/anie.201305377.

Chapter V

(1) Hamann, D. M.; Hadland, E. C.; Johnson, D. C. Heterostructures Containing Dichalcogenides-New Materials with Predictable Nanoarchitectures and Novel Emergent Properties. *Semicond. Sci. Technol.* **2017**, *32* (9), 093004. https://doi.org/10.1088/1361-6641/aa7785.

(2) Bernevig, B. A.; Zhang, S. C. Quantum Spin Hall Effect. *Phys. Rev. Lett.* **2006**, *96* (10), 106802. https://doi.org/10.1103/PhysRevLett.96.106802.

(3) Marrazzo, A.; Gibertini, M.; Campi, D.; Mounet, N.; Marzari, N. Prediction of a Large-Gap and Switchable Kane-Mele Quantum Spin Hall Insulator. *Phys. Rev. Lett.* **2018**, *120* (11), 117701. https://doi.org/10.1103/PhysRevLett.120.117701.

(4) Burkov, A. A.; Balents, L. Weyl Semimetal in a Topological Insulator Multilayer. *Phys. Rev. Lett.* **2011**, *107* (12), 127205. https://doi.org/10.1103/PhysRevLett.107.127205.

(5) Mak, K. F.; Lee, C.; Hone, J.; Shan, J.; Heinz, T. F. Atomically Thin MoS2: A New Direct-Gap Semiconductor. *Phys. Rev. Lett.* **2010**, *105* (13), 2–5. https://doi.org/10.1103/PhysRevLett.105.136805.

(6) Müchler, L.; Zhang, H.; Chadov, S.; Yan, B.; Casper, F.; Kübler, J.; Zhang, S. C.; Felser, C. Topological Insulators from a Chemist's Perspective. *Angew. Chemie - Int. Ed.* **2012**, *51* (29), 7221–7225. https://doi.org/10.1002/anie.201202480.

(7) Ju, L.; Velasco, J.; Huang, E.; Kahn, S.; Nosiglia, C.; Tsai, H. Z.; Yang, W.; Taniguchi, T.; Watanabe, K.; Zhang, Y.; et al. Photoinduced Doping in Heterostructures of Graphene and Boron Nitride. *Nat. Nanotechnol.* **2014**, *9* (5), 348–352. https://doi.org/10.1038/nnano.2014.60.

(8) Xu, K.; Wang, Y.; Zhao, Y.; Chai, Y. Modulation Doping of Transition Metal Dichalcogenide/Oxide Heterostructures. *J. Mater. Chem. C* **2017**, *5* (2), 376–381. https://doi.org/10.1039/C6TC04640A.

(9) Hadland, E. C.; Göhler, F.; Mitchson, G.; Fender, S. S.; Schmidt, C.; Zahn, D. R. T.; Seyller, T.; Johnson, D. C. Synthesis and Properties of (BiSe)0.97MoSe2: A Heterostructure Containing Both 2H-MoSe2 and 1T-MoSe2. *Chem. Mater.* **2019**, *31* (15), 5824–5831. https://doi.org/10.1021/acs.chemmater.9b01899.

(10) Frindt, R. F. Superconductivity in Ultrathin NbSe2 Layers. *Phys. Rev. Lett.* **1972**, *28* (5), 299–301. https://doi.org/10.1103/PhysRevLett.28.299.

(11) Novoselov, K. S.; Geim, A. K.; Morozov, S. V.; Jiang, D.; Zhang, Y.; Dubonos, S. V.; Grigorieva, I. V.; Firsov, A. A. Electric Field in Atomically Thin Carbon Films. *Science (80-.).* **2004**, *306* (5696), 666–669. https://doi.org/10.1126/science.1102896.

(12) Roddaro, S.; Pingue, P.; Piazza, V.; Pellegrini, V.; Beltram, F. The Optical Visibility of Graphene: Interference Colors of Ultrathin Graphite on SiO2. *Nano Lett.* **2007**, *7* (9), 2707–2710. https://doi.org/10.1021/nl0711581.

(13) Li, M. Y.; Chen, C. H.; Shi, Y.; Li, L. J. Heterostructures Based on Two-Dimensional Layered Materials and Their Potential Applications. *Materials Today*. Elsevier B.V. July 1, 2016, pp 322–335. https://doi.org/10.1016/j.mattod.2015.11.003.

(14) Wang, J.; Zhang, Y. Topologic Connection between 2-D Layered Structures and 3-D Diamond Structures for Conventional Semiconductors. *Sci. Rep.* **2016**, *6* (1), 1–9. https://doi.org/10.1038/srep24660.

(15) Wang, F. Q.; Zhang, S.; Yu, J.; Wang, Q. Thermoelectric Properties of Single-Layered SnSe Sheet. *Nanoscale* **2015**, *7* (38), 15962–15970. https://doi.org/10.1039/c5nr03813h.

(16) Tyagi, K.; Waters, K.; Wang, G.; Gahtori, B.; Haranath, D.; Pandey, R. Thermoelectric Properties of SnSe Nanoribbons: A Theoretical Aspect. *Mater. Res. Express* **2016**, *3*, 035013. https://doi.org/10.1088/2053-1591/3/3/035013.

(17) Zhang, L. C.; Qin, G.; Fang, W. Z.; Cui, H. J.; Zheng, Q. R.; Yan, Q. B.; Su, G. Tinselenidene: A Two-Dimensional Auxetic Material with Ultralow Lattice Thermal Conductivity and Ultrahigh Hole Mobility. *Sci. Rep.* **2016**, *6* (1), 1–9. https://doi.org/10.1038/srep19830.

(18) Sun, Y.; Luo, S.; Zhao, X. G.; Biswas, K.; Li, S. L.; Zhang, L. InSe: A Two-Dimensional Material with Strong Interlayer Coupling. *Nanoscale* **2018**, *10* (17), 7991–7998. https://doi.org/10.1039/c7nr09486h.

(19) Yuan, X.; Tang, L.; Liu, S.; Wang, P.; Chen, Z.; Zhang, C.; Liu, Y.; Wang, W.; Zou, Y.; Liu, C.; et al. Arrayed van Der Waals Vertical Heterostructures Based on 2d GaSe Grown by Molecular Beam Epitaxy. *Nano Lett.* **2015**, *15* (5), 3571–3577. https://doi.org/10.1021/acs.nanolett.5b01058.

(20) Wrasse, E. O.; Schmidt, T. M. Prediction of Two-Dimensional Topological Crystalline Insulator in PbSe Monolayer. *Nano Lett.* **2014**, *14* (10), 5717–5720. https://doi.org/10.1021/nl502481f.

(21) Shao, Z.; Zheng, F.; Zhang, Z.; Sun, H.; Li, S.; Yuan, H.; Li, Q.; Zhang, P.; Pan, M. Epitaxial Growth of PbSe Few-Layers on SrTiO3: The Effect of Compressive Strain and Potential Two-Dimensional Topological Crystalline Insulator. *ACS Nano* **2019**, *13* (2), 2615–2623. https://doi.org/10.1021/acsnano.9b00072.

(22) Wang, N. Z.; Yuan, S. F.; Cong, R.; Lu, X. F.; Meng, F. B.; Shang, C.; Chen, X. H. Structure and Physical Properties of the Misfit Compounds (PbSe)1.16(TiSe2)m (m = 1, 2). *Epl* **2015**, *112* (6). https://doi.org/10.1209/0295-5075/112/67007.

(23) Cordova, D. L. M.; Fender, S. S.; Kam, T. M.; Seyd, J.; Albrecht, M.; Lu, P.; Fischer, R.; Johnson, D. C. Designed Synthesis and Structure-Property Relationships of Kinetically Stable [(PbSe)1+Î´]m(VSe2)1 (m = 1, 2, 3, 4) Heterostructures. *Chem. Mater.* **2019**, *31* (20), 8473–8483. https://doi.org/10.1021/acs.chemmater.9b02826.

(24) Fister, L.; Li, X.; McConnell, J.; Novet, T.; Johnson, D. C. Deposition System for the Synthesis of Modulated, Ultrathin-film Composites. *J. Vac. Sci. Technol. A Vacuum, Surfaces, Film.* **1993**, *11* (6), 3014–3019. https://doi.org/10.1116/1.578290.

(25) Hamann, D. M.; Bardgett, D.; Cordova, D. L. M.; Maynard, L. A.; Hadland, E. C.; Lygo, A. C.; Wood, S. R.; Esters, M.; Johnson, D. C. Sub-Monolayer Accuracy in Determining the Number of Atoms per Unit Area in Ultrathin Films Using X-Ray Fluorescence. *Chem. Mater.* **2018**, *30* (18), 6209–6216. https://doi.org/10.1021/acs.chemmater.8b02591.

(26) Rodríguez-Carvajal, J. FULLPROF: A Program for Rietveld Refinement and Pattern Matching Analysis. In *Abstracts of the Satellite Meeting on Powder Diffraction of the XV Congess of the IUCr, Toulouse, France*; 1990; p 127. https://doi.org/SDI: 0921-4526(93)E0113-U.

(27) Mariano, A. N.; Chopra, K. L. Polymorphism in Some IV-VI Compounds Induced by High Pressure and Thin-Film Epitaxial Growth. *Appl. Phys. Lett.* **1967**, *10* (10), 282–284. https://doi.org/10.1063/1.1754812.

(28) Schneemeyer, L. F.; Stacy, A.; Sienko, M. J. Effect of Nonstoichiometry on the Periodic Lattice Distortion in Vanadium Diselenide. *Inorg. Chem.* **1980**, *19* (9), 2659–2662. https://doi.org/10.1021/ic50211a036.

(29) Tao F.; Bernasek, S. L. Understanding Odd−Even Effects in Organic Self-Assembled Monolayers. **2007**. https://doi.org/10.1021/CR050258D.

(30) Burnett, E. K.; Ai, Q.; Cherniawski, B. P.; Parkin, S. R.; Risko, C.; Briseno, A. L. Even-Odd Alkyl Chain-Length Alternation Regulates Oligothiophene Crystal Structure. *Chem. Mater.* **2019**, *31* (17), 6900–6907. https://doi.org/10.1021/acs.chemmater.9b01317.

(31) Thuo, M. M.; Reus, W. F.; Nijhuis, C. A.; Barber, J. R.; Kim, C.; Schulz, M. D.; Whitesides, G. M. Odd-Even Effects in Charge Transport across Self-Assembled Monolayers. *J. Am. Chem. Soc.* **2 011**, *133* (9), 2962–2975. https://doi.org/10.1021/ja1090436.

(32) Yang, K.; Cai, Z.; Jaiswal, A.; Tyagi, M.; Moore, J. S.; Zhang, Y. Dynamic Odd-Even Effect in Liquid *n* -Alkanes near Their Melting Points. *Angew. Chemie Int. Ed.* **2016**, *55* (45), 14090–14095. https://doi.org/10.1002/anie.201607316.

Chapter VI

(1) Trost, B. M.; Dong, G. Total Synthesis of Bryostatin 16 Using Atom-Economical and Chemoselective Approaches. *Nature* **2008**, *456* (7221), 485–488. https://doi.org/10.1038/nature07543.

(2) Langmuir, I. The Arrangement of Electrons in Atoms and Molecules. *J. Am. Chem. Soc.* **1919**, *41* (6), 868–934. https://doi.org/10.1021/ja02227a002.

(3) Pyykkö, P. Understanding the Eighteen-Electron Rule. *J. Organomet. Chem.* **2006**, *691* (21), 4336–4340. https://doi.org/10.1016/j.jorganchem.2006.01.064.

(4) Wu, Y.; D'Agostino, C.; Holland, D. J.; Gladden, L. F. In Situ Study of Reaction Kinetics Using Compressed Sensing NMR. *Chem. Commun.* **2014**, *50* (91), 14137–14140. https://doi.org/10.1039/c4cc06051b.

(5) Capocasa, G.; Sessa, F.; Tavani, F.; Monte, M.; Olivo, G.; Pascarelli, S.; Lanzalunga, O.; Di Stefano, S.; D'Angelo, P. Coupled X-Ray Absorption/UV-Vis Monitoring of Fast Oxidation Reactions Involving a Nonheme Iron-Oxo Complex. *J. Am. Chem. Soc.* **2019**, *141* (6), 2299–2304. https://doi.org/10.1021/jacs.8b08687.

(6) Huang, Z.; Dong, G. Site-Selectivity Control in Organic Reactions: A Quest to Differentiate Reactivity among the Same Kind of Functional Groups. *Accounts of Chemical Research*. 2017, pp 465–471. https://doi.org/10.1021/acs.accounts.6b00476.

(7) Corey, E. J. The Logic of Chemical Synthesis: Multistep Synthesis of Complex Carbogenic Molecules (Nobel Lecture). *Angew. Chemie Int. Ed. English* **1991**, *30* (5), 455–465. https://doi.org/10.1002/anie.199104553.

(8) Disalvo, F. J. Solid-State Chemistry: A Rediscovered Chemical Frontier. *Science (80-.).* **1990**, *27*, 649–655. https://doi.org/10.1126/science.247.4943.649.

(9) Jansen, M. A Concept for Synthesis Planning in Solid-State Chemistry. *Angew. Chemie - Int. Ed.* **2002**, *41* (20), 3746–3766. https://doi.org/10.1002/1521-3773(20021018)41:20<3746::AID-ANIE3746>3.0.CO;2-2.

(10) Pienack, N.; Bensch, W. In-Situ Monitoring of the Formation of Crystalline Solids. *Angew. Chemie - Int. Ed.* **2011**, *50* (9), 2014–2034. https://doi.org/10.1002/anie.201001180.

(11) Kanatzidis, M. G.; Pöttgen, R.; Jeitschko, W. The Metal Flux: A Preparative Tool for the Exploration of Intermetallic Compounds. *Angew. Chemie - Int. Ed.* **2005**, *44* (43), 6996–7023. https://doi.org/10.1002/anie.200462170.

(12) Xu, Y.; Musumeci, V.; Aymonier, C. Chemistry in Supercritical Fluids for the Synthesis of Metal Nanomaterials. *Reaction Chemistry and Engineering*. 2019. https://doi.org/10.1039/c9re00290a.

(13) Hagenmuller, P. *Preparative Methods in Solid State Chemistry*; Academic Press: New York, 1972.

(14) Shoemaker, D. P.; Chung, D. Y.; Mitchell, J. F.; Bray, T. H.; Soderholm, L.; Chupas, P. J.; Kanatzidis, M. G. Understanding Fluxes as Media for Directed Synthesis: In Situ Local Structure of Molten Potassium Polysulfides. *J. Am. Chem. Soc.* **2012**, *134* (22), 9456–9463. https://doi.org/10.1021/ja303047e.

(15) Kohlmann, H. Looking into the Black Box of Solid-State Synthesis. *Eur. J. Inorg. Chem.* **2019**, No. 39–40, 4174–4180. https://doi.org/10.1002/ejic.201900733.

(16) Marbella, L. E.; Millstone, J. E. NMR Techniques for Noble Metal Nanoparticles. *Chem. Mater.* **2015**, *27* (8), 2721–2739. https://doi.org/10.1021/cm504809c.

(17) West, A. R. *Solid State Chemistry and Its Applications*, 2nd ed.; John Wiley & Sons, Ltd: West Sussex, UK, 2014.

(18) Lau, S. S.; Feng, J. S. Y.; Olowolafe, J. O.; Nicolet, M. A. Iron Silicide Thin Film Formation at Low Temperatures. *Thin Solid Films* **1975**, *25* (2), 415–422. https://doi.org/10.1016/0040-6090(75)90059-0.

(19) Stein, A.; Keller, S. W.; Mallouk, T. E. Turning down the Heat: Design and Mechanism in Solid-State Synthesis. *Science (80-.).* **1993**, *259* (5101), 1558–1564. https://doi.org/10.1126/science.259.5101.1558.

(20) Chamorro, J. R.; Mcqueen, T. M. Progress toward Solid State Synthesis by Design. *Acc. Chem. Res.* **2018**, *51*, 2918–2925. https://doi.org/10.1021/acs.accounts.8b00382.

(21) Schäfer, H. Preparative Solid State Chemistry: The Present Position. *Angew. Chemie Int. Ed. English* **1971**, *10* (1), 43–50. https://doi.org/10.1002/anie.197100431.

(22) De Yoreo, J.; Mandrus, D.; Soderholm, L.; Forbes, T.; Kanatzidis, M.; Wiesner, U.; Xu, T.; Tolbert, S.; Zawarotko, M.; Chan, J.; et al. *Report of the Basic Energy Sciences Workshop on Synthesis Science for Energy Relevant Technology*; 2016.

(23) Fister, L.; Li, X.; McConnell, J.; Novet, T.; Johnson, D. C. Deposition System for the Synthesis of Modulated, Ultrathin-film Composites. *J. Vac. Sci. Technol. A Vacuum, Surfaces, Film.* **1993**, *11* (6), 3014–3019. https://doi.org/10.1116/1.578290.

(24) Hamann, D. M.; Bardgett, D.; Cordova, D. L. M.; Maynard, L. A.; Hadland, E. C.; Lygo, A. C.; Wood, S. R.; Esters, M.; Johnson, D. C. Sub-Monolayer Accuracy in Determining the Number of Atoms per Unit Area in Ultrathin Films Using X-Ray Fluorescence. *Chem. Mater.* **2018**, *30* (18), 6209–6216. https://doi.org/10.1021/acs.chemmater.8b02591.

(25) Toby, B. H.; Von Dreele, R. B. GSAS-II: The Genesis of a Modern Open-Source All Purpose Crystallography Software Package. *J. Appl. Crystallogr.* **2013**, *46* (2), 544–549. https://doi.org/10.1107/S0021889813003531.

(26) Rodríguez-Carvajal, J. FULLPROF: A Program for Rietveld Refinement and Pattern Matching Analysis. In *Abstracts of the Satellite Meeting on Powder Diffraction of the XV Congess of the IUCr, Toulouse, France*; 1990; p 127. https://doi.org/SDI: 0921-4526(93)E0113-U.

(27) Schneemeyer, L. F.; Stacy, A.; Sienko, M. J. Effect of Nonstoichiometry on the Periodic Lattice Distortion in Vanadium Diselenide. *Inorg. Chem.* **1980**, *19* (9), 2659–2662. https://doi.org/10.1021/ic50211a036.

(28) Evans, B. L.; Hazelwood, R. A. Optical and Electrical Properties of SnSe2. *J. Phys. D. Appl. Phys.* **1969**, *2* (11), 1507–1516. https://doi.org/10.1088/0022-3727/2/11/304.

(29) Holy, V.; Pietsch, U.; Baumbach, T. *High-Resolution X-Ray Scattering from Thin Films and Multilayers*; Springer Berlin Heidelberg: Germany, 1999.

(30) Stierle, A.; Vlieg, E. Surface Sensitive X-Ray Diffraction Methods. In *Modern Diffraction Methods*; Mittemeijer, E. J., Welsel, U., Eds.; Wiley-VCH Verlag & Co.: Weinheim, Germany, 2013; pp 221–258.

(31) Woolfson, M. M. *An Introduction to X-Ray Crystallography*, 2nd ed.; Cambridge University Press: Cambridge, UK, 1997.

(32) Shimada, T.; Ohuchi, F. S.; Parkinson, B. A. Thermal Decomposition of SnS_2 and $SnSe_2$: Novel Molecular-beam Epitaxy Sources for Sulfur and Selenium. *J. Vac. Sci. Technol. A Vacuum, Surfaces, Film.* **1992**, *10* (3), 539–542. https://doi.org/10.1116/1.578184.

(33) Cordova, D. L. M.; Kam, T. M.; Fender, S. S.; Tsai, Y. H.; Johnson, D. C. Strong Non-Epitaxial Interactions : Crystallographically Aligned PbSe on VSe 2. *Phys. Status Solidi* **2019**, *1800896* (1800896), 1–7. https://doi.org/10.1002/pssa.201800896.

(34) Atkins, R.; Disch, S.; Jones, Z.; Haeusler, I.; Grosse, C.; Fischer, S. F.; Neumann, W.; Zschack, P.; Johnson, D. C. Synthesis, Structure and Electrical Properties of a New Tin Vanadium Selenide. *J. Solid State Chem.* **2013**, *202*, 128–133. https://doi.org/10.1016/j.jssc.2013.03.008.

(35) Beekman, M.; Rodriguez, G.; Atkins, R.; Kunert, J.; Moore, D. B.; Johnson, D. C.; Beekman, M.; Rodriguez, G.; Atkins, R.; Kunert, J.; et al. Detection of Nanoscale Embedded Layers Using Laboratory Specular X-Ray Diffraction Detection of Nanoscale Embedded Layers Using Laboratory Specular X-Ray Diffraction. **2016**, *185306* (2015). https://doi.org/10.1063/1.4920928.

(36) Atkins, R.; Dolgos, M.; Fiedler, A.; Grosse, C.; Fischer, S. F.; Rudin, S. P.; Johnson, D. C. Synthesis and Systematic Trends in Structure and Electrical Properties of [(SnSe)1.15]m(VSe2)1 , m = 1, 2, 3, and 4. *Chem. Mater.* **2014**, *26* (9), 2862–2872. https://doi.org/10.1021/cm5004774.

(37) Björck, M.; Andersson, G. GenX: An Extensible X-Ray Reflectivity Refinement Program Utilizing Differential Evolution. *J. Appl. Crystallogr.* **2007**, *40* (6), 1174–1178. https://doi.org/10.1107/S0021889807045086.

(38) Hite, O. K.; Falmbigl, M.; Alemayehu, M. B.; Esters, M.; Wood, S. R.; Johnson, D. C. Charge Density Wave Transition in (PbSe)1+δ(VSe2)n Compounds with n = 1, 2, and 3. *Chem. Mater.* **2017**, *29* (13), 5646–5653. https://doi.org/10.1021/acs.chemmater.7b01383.

(39) Hite, O. K.; Nellist, M.; Ditto, J.; Falmbigl, M.; Johnson, D. C. Transport Properties of VSe 2 Monolayers Separated by Bilayers of BiSe. *J. Mater. Res.* **2015**, *31* (7), 886–892. https://doi.org/10.1557/jmr.2015.354.

(40) Bayard, M.; Sienko, M. J. Anomalous Electrical and Magnetic Properties of Vanadium Diselenide *. *J. Solid State Chem.* **1976**, *19*, 325–329.

(41) Hadland, E.; Jang, H.; Falmbigl, M.; Fischer, R.; Medlin, D. L.; Cahill, D. G.; Johnson, D. C. Synthesis, Characterization, and Ultralow Thermal Conductivity of a Lattice-Mismatched SnSe2(MoSe2)1.32 Heterostructure. *Chem. Mater.* **2019**, *31* (15), 5699–5705. https://doi.org/10.1021/acs.chemmater.9b01637.

(42) Van Aert, S.; Verbeeck, J.; Erni, R.; Bals, S.; Luysberg, M.; Dyck, D. Van; Tendeloo, G. Van. Quantitative Atomic Resolution Mapping Using High-Angle Annular Dark Field Scanning Transmission Electron Microscopy. *Ultramicroscopy* **2009**, *109* (10), 1236–1244. https://doi.org/10.1016/j.ultramic.2009.05.010.

(43) Hamann, D. M.; Merrill, D. R.; Bauers, S. R.; Mitchson, G.; Ditto, J.; Rudin, S. P.; Johnson, D. C. Long-Range Order in [(SnSe) $_{1.2}$] $_1$ [TiSe $_2$] $_1$ Prepared from Designed Precursors. *Inorg. Chem.* **2017**, *56* (6), 3499–3505. https://doi.org/10.1021/acs.inorgchem.6b03063.

(44) Falmbigl, M.; Putzky, D.; Ditto, J.; Esters, M.; Bauers, S. R.; Ronning, F.; Johnson, D. C. Influence of Defects on the Charge Density Wave of ([SnSe]1+δ)1(VSe2)1 Ferecrystals. *ACS Nano* **2015**, *9* (8), 8440–8448. https://doi.org/10.1021/acsnano.5b03361.

(45) Westover, R.; Atkins, R. A.; Falmbigl, M.; Ditto, J. J.; Johnson, D. C. Self-Assembly of Designed Precursors: A Route to Crystallographically Aligned New Materials with Controlled Nanoarchitecture. *J. Solid State Chem.* **2016**, *236*, 173–185. https://doi.org/10.1016/j.jssc.2015.08.018.

(46) Falmbigl, M.; Esters, M.; Johnson, D. C. Formation of a Selenide-Based Heterostructure From a Designed Precursor†. *Cryst. Res. Technol.* **2017**, *52* (10), 1–6. https://doi.org/10.1002/crat.201700067.